

Department of Physics and Astronomy
Heidelberg University

Master's Thesis in Physics
submitted by

Alexander Kunkel

born in Freital (Germany)

May, 2022

An investigation of the Madelung formulation of the Fuzzy Dark Matter model

This Master's thesis has been carried out by Alexander Kunkel
under the supervision of
Prof. *Björn Malte Schäfer*
at the Institute for Theoretical Physics at Heidelberg University,
and
Prof. *Tzihong Chiueh*
at the Institute of Astrophysics and Center of Theoretical Physics at National
Taiwan University
and
Prof. *Hsi-Yu Schive*
at the Institute of Astrophysics and Center of Theoretical Physics at National
Taiwan University and at the National Center of Theoretical Sciences in Taiwan.

Abstract

The Fuzzy Dark Matter (FDM) model posits that dark matter consists of ultralight bosons with a mass $m \sim 10^{-22}$ eV. FDM has the potential to solve the small-scale crisis of the standard Cold Dark Matter (CDM) model by suppressing structure growth below its astrophysically relevant de Broglie wavelength. Yet, cosmological simulations of FDM are extremely time-consuming because of the oscillatory behaviour of FDM. They need to spatially resolve the potentially very small de Broglie wavelength of FDM even in regions where the mass density is low and smooth.

Fortunately, the non-relativistic equations of motion of FDM - the Schrödinger-Poisson system (SPS) - admit a fluid formulation via the Madelung transform that does not share this restriction. This thesis studies the fluid formulation of the SPS in two ways:

Firstly, we employ non-linear time-dependent Eulerian perturbation theory to predict structure formation and give a *weak lensing view on FDM*. We find that a Euclid-like weak lensing survey can potentially be used to distinguish a FDM-dominated universe from a CDM-dominated universe up to a mass of $m = 10^{-22}$ eV. FDM models with higher masses are not distinguishable from CDM in our weak lensing survey.

Secondly, we present a *proof-of-concept for a hybrid scheme* that solves the fluid formulation of the SPS on large scales and switches to solving the wave formulation of the SPS in regions of interference. This approach enables larger simulation volumes by eliminating the need to resolve the de Broglie wavelength on large scales. Our code correctly recovers FDM dynamics in a 3D simulation where a large fraction of the simulation volume uses the fluid formulation.

Zusammenfassung

Das Fuzzy Dark Matter-Modell (FDM) postuliert, dass dunkle Materie aus ultraleichten Bosonen mit einer Masse von $m \sim 10^{-22}$ eV besteht. FDM kann potenziell die Probleme des Cold Dark Matter-Modells (CDM) auf kleinen Skalen lösen: In FDM ist das Wachstum von Strukturen auf Skalen unterhalb der astronomisch relevanten de Broglie-Wellenlänge unterdrückt. Eine Schwierigkeit des FDM-Modells besteht darin, dass astronomische Simulationen von FDM außerordentlich rechenaufwendig sind. Das liegt daran, dass FDM auf kleinen Skalen oszilliert und Standardsimulationen die de Broglie-Wellenlänge von FDM auch dort räumlich auflösen müssen, wo die Massendichte gering und glatt ist.

Glücklicherweise erlauben die nichtrelativistischen Bewegungsgleichungen von FDM - die Schrödinger-Poisson-Gleichungen (SPS) - eine Formulierung als System von Fluidgleichungen: den sogenannten Madelunggleichungen. Diese Arbeit nutzt die Madelunggleichungen, um die numerischen Schwierigkeiten bei der Simulation des SPS auf zwei Arten zu umgehen:

Im ersten Teil der Arbeit wenden wir Eulersche Störungstheorie auf die Madelunggleichungen an, um kosmologische Strukturbildung in FDM und CDM zu vergleichen. Wir zeigen, dass *Beobachtungen des schwachen Gravitationslinseneffektes* von Galaxien in einer Messung wie der des Weltraumteleskops Euklid genutzt werden können, um FDM und CDM bis zu einer Masse von $m = 10^{-22}$ eV zu unterscheiden. Höhere Massen im FDM-Modell führen zu einer kleineren de Broglie-Wellenlänge und zu Unterschieden zum Standard-CDM-Modell außerhalb des mithilfe des schwachen Gravitationslinseneffektes messbaren Bereichs.

Im zweiten Teil der Arbeit entwickeln wir den *Prototypen eines Hybrid-Codes*, der kosmologische Strukturbildung im FDM-Modell simuliert. Er löst auf großen Skalen die Madelunggleichungen und auf kleinen Skalen die Wellengleichungen vom FDM. Ein solcher Ansatz erlaubt größere Simulationsvolumina, da die de Broglie-Wellenlänge auf großen Skalen nicht aufgelöst werden muss. Unser Demonstrationscode beschreibt in einer 3-D-Simulation Interferenzeffekte von FDM auf kleinen Skalen korrekt, während ein Großteil des Simulationsvolumens die Madelunggleichungen nutzt.

Contents

Contents	i
Notations and Conventions	iii
1 Introduction	1
2 Schrödinger-Poisson System	4
2.1 Derivation	4
2.2 Madelung Transform	7
2.3 Symmetries	11
2.4 Thermodynamics	12
2.5 Numerical Experiments	15
2.5.1 Gaussian Wave Packet	15
2.5.2 Gravity	17
3 Eulerian Perturbation Theory	18
3.1 Eulerian Linear Perturbation Theory	18
3.1.1 CDM	18
3.1.2 FDM	20
3.2 Eulerian Non-Linear Perturbation Theory	26
3.2.1 Goroff's Method	27
3.2.2 Scoccimarro's Method	29
3.2.3 FDM for EdS Cosmology	37
3.2.4 CDM for General Cosmology	40
3.2.5 FDM for General Cosmology	43
4 A Weak Lensing View on FDM	45
4.1 Statistics of Cosmic Fields	46
4.1.1 Power Spectrum	48
4.1.2 Bispectrum	49
4.1.3 Trispectrum	52
4.2 Weak Lensing	52
4.3 Experimental Setup	58
4.3.1 Choice of FDM Masses	58
4.3.2 Lensing Survey Parameters	59
4.3.3 Initial Power Spectra	60
4.4 Results	62

4.4.1	Spectra	62
4.4.2	Signal-To-Noise Ratios and χ^2 -Functionals	67
4.5	Discussion	73
5	Hybrid Simulation of FDM	75
5.1	Boundary Matching Problem	77
5.1.1	Evolution of the Velocity Field	77
5.1.2	Parallel Evolution of the Velocity and Phase Fields	78
5.1.3	Evolution of the Phase Field	78
5.2	Introduction to CFD	79
5.2.1	Finite Difference Method	79
5.2.2	Finite Volume Method	88
5.3	Simulating the Hamilton-Jacobi Equation	91
5.4	Simulating Gravity	93
5.5	Simulating the Schrödinger Equation	96
5.6	The Phase Scheme	97
5.6.1	Design	98
5.6.2	Testing and Validation	99
5.7	The Hybrid Scheme	112
5.7.1	Design	112
5.7.2	Testing and Validation	114
5.8	Discussion	117
6	Conclusions and Outlook	119
	References	121
A	Appendix	I
A.1	Newtonian Cosmology	I
A.2	Explicit Symmetrisation of FDM PT Kernels	III
A.3	Linear Growth in FDM	VI
A.4	Lensing Integrals	XII
A.5	CDM PT with FDM IC	XIV
A.6	Method of Characteristics	XVII
A.7	Slope Limiters in Phase Scheme	XIX
	Statement of Authorship	XXII

Notations and Conventions

SPS	Schrödinger-Poisson system;
CDM	Cold Dark Matter (model);
Λ CDM	Flat CDM model with cosmological constant;
FDM	Fuzzy Dark Matter (model);
EdS	Einstein-de Sitter cosmology with $\Omega_m = 1$;
FC	Fiducial Cosmology;
IC	Initial Conditions;
MC	Monte Carlo;
CFD	Computational Fluid Dynamics;
AMR	Adaptive Mesh Refinement;
FDM	Finite Difference Method;
FVM	Finite Volume Method;
ODE	Ordinary Differential Equation;
PDE	Partial Differential Equation;
CFL	Courant-Friedrichs-Lewy;
TVD	Total Variation Diminishing;
RK	Runge-Kutta;
FTCS	Forward-in-Time-Centered-in-Space;
MUSCL	Monotone Upstream Scheme for Conservation Laws;

Table 1: Abbreviations

Ω_m	Total matter density in units of the critical density;
Λ	Cosmological constant;
Ω_Λ	Reduced cosmological constant;
H_0	Hubble constant at present time;
w	Dark energy equation of state parameter;
a	Scale factor;
a_{osc}	Time where linear density fluctuations stop oscillating;
τ	Conformal time, $dt = a d\tau$;
\mathcal{H}	Conformal expansion rate, $\mathcal{H} = aH$;
η	Modified conformal time $\eta = 2\sqrt{a}$ in EdS where $\tau = H_0\Omega_{m,0}^{1/2}2\sqrt{a}$;
D	Linear growth factor;
$k_J(a)$	Comoving Jeans scale;
$\lambda_J(a)$	Comoving Jeans wavelength;
$\ell_J(a)$	Jeans multipole order;

Table 2: Notation for Various Cosmological Variables

\mathbf{x}	Comoving position in real space;
$\rho(\mathbf{x})$	Local cosmic density;
$\rho_b(t)$	Background density;
$\delta(\mathbf{x})$	Local density contrast, $\delta = \rho/\rho_b - 1$;
$\phi(\mathbf{x})$	Newtonian gravitational potential;
$\mathbf{v}(\mathbf{x})$	Local peculiar velocity field;
$\theta(\mathbf{x})$	Local velocity divergence in units of $\mathcal{H} = aH$;
F_n	n^{th} order density field kernel;
G_n	n^{th} order velocity divergence field kernel;

Table 3: Notation for the Cosmic Fields

$P(k)$	Density power spectrum;
$B(k_1, k_2, k_3)$	Matter bispectrum;
$T(k_1, k_2, k_4, k_4)$	Matter trispectrum;
$P_\kappa(\ell)$	Lensing spectrum;
$B_\kappa(\ell_1, \ell_2, \ell_3)$	Lensing bispectrum;
$T_\kappa(\ell_1, \ell_2, \ell_4, \ell_4)$	Lensing trispectrum;
$\Sigma_P(\ell)$	Cumulative signal-to-noise ratio of lensing spectrum;
$\Sigma_B(\ell)$	Cumulative signal-to-noise ratio of lensing bispectrum;
$\Sigma_T(\ell)$	Cumulative signal-to-noise ratio of lensing trispectrum;
$\chi_P^2(\ell)$	χ^2 -functional for distinguishing CDM and FDM using the lensing spectrum;
$\chi_B^2(\ell)$	χ^2 -functional for distinguishing CDM and FDM using the lensing bispectrum;
$\chi_T^2(\ell)$	χ^2 -functional for distinguishing CDM and FDM using the lensing trispectrum;

Table 4: Notation for Statistical Quantities

Momentum Sums	$\mathbf{k}_{ijk\dots} \equiv \mathbf{k}_i + \mathbf{k}_j + \mathbf{k}_k + \dots$
Fourier Integrations	$f(\mathbf{k}) = \int \frac{d^3\mathbf{x}}{(2\pi)^3} \exp(-i\mathbf{k} \cdot \mathbf{x}) f(\mathbf{x})$
Momentum Integrations	$\delta_D(\mathbf{k} - \mathbf{k}_{12}) f(\mathbf{k}_1) g(\mathbf{k}_2) \equiv \int \frac{d^3\mathbf{k}_1 d^3\mathbf{k}_2}{(2\pi)^6} \delta_D(\mathbf{k} - \mathbf{k}_{12}) f(\mathbf{k}_1) g(\mathbf{k}_2)$

Table 5: Conventions

$H(a)$	$H_0 \sqrt{\Omega_m a^{-3} + \Omega_\Lambda a^{-3(1+w)}}$
H_0	$67.3 \frac{\text{km}}{\text{s}} \frac{1}{\text{Mpc}}$
$\Omega_{m,0}$	0.3159
Ω_Λ	$1 - \Omega_{m,0}$
w	-0.9

Table 6: Fiducial Cosmology (FC) used in chapters 3 and 4.

f_{sky}	Fraction of sky covered by survey; 0.5
ℓ_{min}	Minimum multipole moment considered; 10
ℓ_{max}	Maximum multipole moment considered; 10000
σ_{ϵ}	Standard deviation of intrinsic ellipticities of galaxies; 0.4 ²
\bar{n}	Average number of galaxies per steradian; $4.727 \cdot 10^8$
z_0	Mean redshift; 0.9

Table 7: Parameter set used for Euclid-like weak lensing survey in chapter 4.

1

Introduction

The standard Cold Dark Matter (CDM) model with a non-zero cosmological constant Λ , commonly referred to as Λ CDM, assumes that the largest contributions to the mass-energy of the universe are dark energy and dark matter that respectively make up $68 \pm 1\%$ and $27 \pm 1\%$ of the total energy content of the universe (Collaboration et al. 2018). There are a number of experimental confirmations of the Λ CDM model such as observations of the mass-to-light-ratio of clusters of galaxies (Bahcall, Lubin and Dorman 1995), the rotation curves of galaxies, (Einasto, Kaasik and Saar 1974), the Bullet cluster (Clowe et al. 2006), the cosmic microwave background (CMB) (Collaboration et al. 2018) and the large-scale structure of the universe (Tegmark et al. 2004). While cosmological simulations in the Λ CDM model allow the prediction of structure growth in the deeply nonlinear regime, there are significant discrepancies between numerical predictions and the observed structures on small scales of ~ 10 kpc or less. This fact is referred to as *small-scale crisis* of CDM. Actually one can distinguish a number of small scale crises (Weinberg et al. 2013; Bullock and Boylan-Kolchin 2017):

The *missing satellites problem* describes that CDM predicts more small Milky Way satellite galaxies than are observed. Halos in CDM simulations contain thousands of sub-halos, some of which would host galaxies. This is in conflict with observations of the Milky Way which indicate around 50 satellite galaxies.

The *too-big-to-fail problem* refers to the fact that the local universe contains too few galaxies indicative of very massive halos ($M \sim 10^{10} M_{\odot}$). Such halos are abundant in CDM simulations and believed to be too massive to have failed to form stars. It is unclear why they are missing in the local universe.

Finally, the *cusp-core-problem* is related to the predicted density profile of CDM halos. CDM halos have a universal shape well approximated by the so-

called Navarro–Frenk–White profile (Navarro, Frenk and White 1995). At small radii, the NFW profile predicts that the halo density scales as $\rho(r) \propto r^{-1}$, whereas dark matter-dominated, dwarf spherical galaxies favour a flat halo center.

There are a number of different proposed solutions to the small-scale crises of CDM. On the one hand, they may be solved by properly modelling astrophysical processes like supernova explosions that may smooth out small-scale structure. On the other hand, there are a number of different modifications of the CDM model like the Warm Dark Matter model (Colin, Avila-Reese and Valenzuela 2000), dark matter models with self-interactions (Spergel and Steinhardt 2000) or the Decaying Dark Matter model (Cheng, Chu and Tang 2015).

Another such model is the *Fuzzy Dark Matter* (FDM) model first proposed by Hu, Barkana and Gruzinov (2000). It describes dark matter as a bosonic, scalar field composed of very light particles with mass $m \sim 10^{-22}$ eV with negligible self interactions and a macroscopic de Broglie wavelength. The FDM bosons are also called *axions*¹. Axions are a well-motivated addition to the standard-model of particle physics. They can explain the CP-violation and are naturally generated in supersymmetric theories and theories with extra-dimensions including string theory (Marsh 2016). In the following, it will not be important that the FDM particle is an axion or an axion-like particle. We only assume that the particle is bosonic, non-relativistic and has negligible self-interaction.

The dynamics of FDM in the non-relativistic limit are governed by the Schrödinger-Poisson equation (SPS). Because of its small mass, the FDM axion has an astrophysically relevant de Broglie wavelength at the order of a few kiloparsecs. Its wave-like behaviour suppresses structure formation on small scales while one recovers CDM behaviour on large scales. The FDM model therefore has the potential to solve the small-scale crisis of CDM. One problem in the study of the FDM model is that cosmological simulations of FDM are computationally very demanding. For this reason, they are limited to small simulation volumes compared to CDM simulations. The underlying reason is that the SPS suggests an inherently Eulerian view and requires the spatial resolution of the de Broglie wavelength of the FDM even where the matter density is low and smooth. In contrast, the spatial grid in N -body simulations of CDM does not have any resolution limits because N -body methods are inherently Lagrangian. Fortunately, one can recast the SPS into a hydrodynamical form: the Madelung equations. The Madelung equations are Euler-Poisson equations with an additional scale-dependent modification, the so-called *quantum pressure* term. On large scales,

¹The term *axion* is used to refer to a number of scalar particles with different masses. It was first proposed as a solution to the strong CP problem in QCD (Peccei 1996) and owes its name to an American laundry detergent.

this term vanishes and one recovers the ideal fluid equations for CDM. One might wonder why one would exchange a single linear differential equation for a coupled nonlinear system of differential equations. One of the appeals of the Madelung transform lies in being able to apply standard cosmological perturbation theory to the SPS. Another advantage lies in being able to apply hydrodynamics codes that have less stringent spatial resolution requirements than Schrödinger-Poisson solvers.

This thesis makes *two contributions* to better understanding cosmological structure formation in the FDM model: In the first part of the thesis, we study the role of FDM in structure formation by applying Eulerian perturbation theory to the Madelung equations. We compute the lensing spectra, bispectra and trispectra in CDM and FDM and determine the attainable cumulative signal-to-noise ratios in a Euclid-like *weak lensing survey*. Finally, we give an estimate of the attainable χ^2 -functionals for distinguishing CDM and FDM at three different masses. In the second part of this thesis, we combine the wave and fluid formulations of the SPS to create a *hybrid scheme* that uses the fluid formulation on large scales and the wave formulations in regions of destructive interference.

The plan of the thesis is as follows: In chapter 2 we derive the SPS as well as equivalent formulations of the SPS using the Madelung transform. In chapter 3, we introduce linear and non-linear Eulerian perturbation theory for CDM and develop a framework for time-dependent perturbation theory for FDM. In chapter 4, we use perturbation theory to compare CDM and FDM in a weak lensing survey. Finally, chapter 5 gives an introduction to the numerical methods used for solving partial differential equations and develops a proof-of-concept code for the hybrid scheme.

2

Schrödinger-Poisson System

This chapter gives a motivation of the dynamical equations governing FDM: the Schrödinger-Poisson system (SPS) of equations. The SPS emerges as the non-relativistic limit of the Klein-Gordon-Einstein equation in a geometry described by the perturbed Friedmann-Lemaître-Robertson-Walker (FLRW) metric in Newtonian gauge. After deriving the SPS, we introduce the Madelung transform and discuss its interpretation as well as other equivalent forms of the SPS. We draw heavily on the review paper by Marsh (2016).

2.1 Derivation

Consider a (pseudo-)scalar field φ minimally coupled to gravity

$$S = \frac{1}{\hbar c^2} \int d^4x \sqrt{-g} \left[\frac{1}{2} g^{\mu\nu} \nabla_\mu \varphi \nabla_\nu \varphi - \frac{1}{2} \frac{m^2 c^2}{\hbar^2} \varphi^2 \right], \quad (1)$$

where we follow the convention in (Hui et al. 2017). The scalar field φ has units of energy and m is the axion mass. This action is invariant under parity- and time-inversion because it is quadratic in φ . For QCD axions, this action is valid after symmetry breaking and after non-perturbative effects have been switched on. Further, we neglect possible self-interactions of the axion. The equations of motion are obtained by varying the action with respect to φ

$$\square\varphi + \frac{\partial V}{\partial\varphi} = 0, \quad (2)$$

where the d'Alembertian is

$$\square = \frac{1}{\sqrt{-g}} \partial_\mu (\sqrt{-g} g^{\mu\nu} \partial_\nu). \quad (3)$$

If the background metric is given by the flat FLRW metric, the background evolution of the axion reads

$$\ddot{\varphi} + 3H\dot{\varphi} + \frac{m^2 c^2}{\hbar^2} \varphi = 0. \quad (4)$$

In a matter- or radiation-dominated universe, the scale factor evolves as a power law $a \propto t^p$ and Eq. (4) admits the analytical solution

$$\varphi = a^{-\frac{3}{2}} \left(\frac{t}{t_i} \right)^{\frac{1}{2}} \left[C_1 J_n \left(\frac{mc}{\hbar} t \right) + C_2 Y_n \left(\frac{mc}{\hbar} t \right) \right], \quad (5)$$

where $n = (3p-1)/2$, $J_n(x)$, $Y_n(x)$ are Bessel functions of the first and second kind and t_i is the initial time. The dimensionful coefficients C_1 and C_2 are determined by initial conditions.

In the next step, one can study solutions of the relativistic axion e.o.m. (2) by allowing perturbations of the flat FLRW metric. Further, we can apply a non-relativistic approximation for studying structure formation. This is because the virial velocity in a typical galaxy $v_{vir} \sim 100 \frac{km}{s} \ll c$ and galaxies are much smaller than the Hubble horizon. On the lower scale end, we are concerned with scales above the axion Compton wave length $\frac{\hbar}{m}c$ which would correspond to relativistic scales in the Klein-Gordon equation. Except in the vicinity of black holes, the Newtonian potential ϕ obeys $|\phi|/c^2 \ll 1$. Therefore, the Newtonian limit is appropriate and we can adopt the perturbed FLRW metric

$$ds^2 = \left(1 + \frac{2\phi}{c^2} \right) c^2 dt^2 - a^2(t) \left(1 - \frac{2\phi}{c^2} \right) d\mathbf{x}^2 \quad (6)$$

in Newtonian gauge. To leading order in ϕ , the d'Alembertian is then given by

$$\square = -(1 - 2\phi)(\partial_t^2 + 3H\partial_t) + a^{-2}(1 + 2\phi)\Delta - 4\dot{\phi}\partial_t, \quad (7)$$

and the axion energy density is

$$\rho_a = \frac{1}{2}((1 - 2\phi)\dot{\varphi}^2 + m^2\varphi^2 + a^{-2}(1 + 2\phi)\partial^i\varphi\partial_i\varphi). \quad (8)$$

To study the clustering of axions on non-linear scales, we can take the WKB-approximation of the form

$$\varphi = \sqrt{\frac{\hbar^3 c}{2m}} (\psi e^{-\frac{imc^2 t}{\hbar}} + \psi^* e^{\frac{imc^2 t}{\hbar}}), \quad (9)$$

where ψ is a complex scalar field because axions that cluster on galactic scales

began oscillating in the very early universe. We apply the previous considerations by taking $\phi \sim \epsilon^2$, $k/m \sim \epsilon$ and $H/m \sim \epsilon$ and work to order $\mathcal{O}(\epsilon^2)$. Further, we assume the non-relativistic approximation $|\dot{\psi}| \ll \frac{mc^2}{\hbar}|\psi|$. The assumption $\partial_t \ll m$ is non-relativistic because we have $\partial_t \sim \Delta/m \sim k^2/m$ and therefore $k^2/m \ll m$. With these simplifications, we obtain the

Comoving Schrödinger-Poisson Equation

$$i\hbar \left(\partial_t \psi(\mathbf{x}, t) + \frac{3}{2} H \psi(\mathbf{x}, t) \right) = \left(-\frac{\hbar^2}{2ma^2} \Delta + m\phi(\mathbf{x}, t) \right) \psi(\mathbf{x}, t), \quad (10)$$

$$\Delta\phi(\mathbf{x}, t) = 4\pi G a^2 (|\psi(\mathbf{x}, t)|^2 - \rho_b(t)), \quad (11)$$

where $\rho_b(t)$ is the background density and $|\psi|^2$ measures the density in a proper volume.

We supplement the Schrödinger-Poisson equation by the normalisation condition

$$\int \rho(\mathbf{x}, t) d^3x = Nm, \quad (12)$$

which fixes the density $\rho = |\psi|^2$ for N axions of mass m . In Eq. (10), positions of particles are described using comoving coordinates \mathbf{x} . Substituting back physical coordinates yields the familiar Schrödinger equation in a static universe. See appendix A.1 for a brief introduction into Newtonian cosmology. The imaginary, dissipative term on the left hand side of Eq. (10) is due to the Hubble flow. We can decompose the density field into the background density $\bar{\rho}(t)$ and the density perturbation $\delta\rho(\mathbf{x}, t)$ as

$$\rho(\mathbf{x}, t) = \rho_b(t) + \delta\rho(\mathbf{x}, t) = \rho_b(t)(1 + \delta(\mathbf{x}, t)), \quad (13)$$

where

$$\delta(\mathbf{x}, t) = \frac{\delta\rho(\mathbf{x}, t)}{\rho_b(t)} \quad (14)$$

is the matter density contrast. We know that $\rho_b(t) \propto a^{-3}$ where a^{-3} is the conversion to proper space density. In other words, the Hubble friction term in Eq. (10) expresses the fact that the matter density is measured in a proper volume. Fortunately, we can restore hermiticity of the Hamiltonian by substituting $\psi \rightarrow$

$a^{-\frac{3}{2}}\psi'$ to obtain

$$i\hbar\partial_t\psi'(\mathbf{x}, t) = \left(-\frac{\hbar^2}{2ma^2}\Delta + m\phi(\mathbf{x}, t)\right)\psi'(\mathbf{x}, t), \quad (15)$$

$$\Delta\phi(\mathbf{x}, t) = \frac{4\pi G}{a}\rho'_b\delta'(\mathbf{x}, t), \quad (16)$$

where $|\psi'|^2$ measures the density in a comoving volume. Following (Schive, Chiueh and Broadhurst 2014), we can further recast Eq. (10) into a more familiar form via the transformation

$$dt \rightarrow a^2 dt' \quad (17)$$

yielding the set of equations

$$i\hbar\partial_{t'}\psi'(\mathbf{x}, t') = \left(-\frac{\hbar^2}{2m}\Delta + m\phi(\mathbf{x}, t')\right)\psi'(\mathbf{x}, t'), \quad (18)$$

$$\Delta\phi'(\mathbf{x}, t') = 4\pi Ga\rho'_b\delta'(\mathbf{x}, t'), \quad (19)$$

where the cosmological expansion shows through the scale factor a acting as a time-dependent coupling strength for the gravitational potential. The coupling increases monotonically with time². At this point, a remark about the physical interpretation of the Schrödinger-Poisson equation in the context of FDM is in order. Even though the above equations share the structure of the quantum-mechanical Schrödinger equation, they are not quantum-mechanical results. We only required the constant \hbar to have dimensions of an action, but did not fix it to any particular value. In fact, \hbar and the mass m appear only in the form of the ratio \hbar/m in the SPS which is why one can also interpret \hbar/m as the free parameter of the theory. Hence, we must interpret Eq. (10) as e.o.m. of a classical field theory in the non-relativistic limit that happen to coincide with their quantum-mechanical counterpart. Interference effects in FDM are classical in nature.

2.2 Madelung Transform

We can make contact with standard perturbation theory and non-linear simulation tools by recasting the nonlinear Schrödinger equation into a fluid form. To this end we substitute

$$\psi(\mathbf{x}, t) =: \sqrt{\frac{\rho(\mathbf{x}, t)}{m}}e^{iS(\mathbf{x}, t)}, \quad (20)$$

²This formulation is very useful in developing numerical schemes for describing FDM dynamics since there is no need to include terms resulting from the Hubble flow.

for real fields $\rho(x, t)$ and $S(x, t)$ into Eq. (10). Computing the e.o.m for the newly defined fields in comoving coordinates under the assumption that $\rho \neq 0$, one obtains the

Hamilton-Jacobi-Madelung Equations

$$\partial_t \rho + 3H\rho + \frac{1}{a} \nabla \cdot \left(\rho \frac{\hbar}{ma} \nabla S \right) = 0, \quad (21)$$

$$\partial_t S + HS + \frac{\hbar}{2ma^2} (\nabla S)^2 + \frac{m}{\hbar} \phi + \frac{m}{\hbar a^2} Q_P = 0, \quad (22)$$

$$\Delta \phi(\mathbf{x}, t) - 4\pi G a^2 \rho_b(t) \delta(\mathbf{x}, t) = 0, \quad (23)$$

where Q_P is usually referred to as *quantum pressure* and is defined as

$$\frac{2m^2}{\hbar^2} Q_P = -\frac{\Delta \sqrt{\rho}}{\sqrt{\rho}} = -\frac{1}{2} \Delta \log \rho - \frac{1}{4} (\nabla \log \rho)^2. \quad (24)$$

Bohm (1952) first derived this set of equations in a static universe on a static, flat spacetime in the context of quantum mechanics. He was trying to find a new physical interpretation for Schrödinger's equation. We note that for $\hbar \rightarrow 0$, in other words in the classical limit in the context of the quantum-mechanical Schrödinger equation, Eq. (22) reduces to the classical Hamilton-Jacobi equation. If we understand the quantum pressure term Eq. (24) as a potential that acts on particles in addition to the gravitational potential ϕ , we can still consider Eq. (21) as a Hamilton-Jacobi equation for an ensemble of particles, with

$$\mathbf{v} = \frac{\hbar}{ma} \nabla S = \frac{i\hbar}{2am|\psi|^2} (\psi \nabla \psi^* - \psi^* \nabla \psi) \quad (25)$$

giving the particle velocity. This interpretation immediately leads to the so-called *Madelung transform* (Madelung 1927) where one takes the gradient of Eq. (21) and thereby obtains the

Madelung equations

$$\begin{aligned} \partial_t \rho + 3H\rho + \frac{1}{a} \nabla \cdot (\rho \mathbf{v}) &= 0, \\ \partial_t \mathbf{v} + H\mathbf{v} + \frac{1}{a} (\mathbf{v} \cdot \nabla) \mathbf{v} + \frac{1}{a} \nabla \phi + \frac{1}{a^3} \nabla Q_P &= 0, \\ \Delta \phi(\mathbf{x}, t) - 4\pi G a^2 \rho_b(t) \delta(\mathbf{x}, t) &= 0. \end{aligned} \quad (26)$$

The Madelung equations describe the Schrödinger equation via a system of fluid equations for frictionless, compressible flow in an external potential ϕ . The flow gets modified by the quantum pressure Q_P that accounts for the underlying wave dynamics in FDM. For a narrowly located source, the quantum pressure is large and reflects the Heisenberg uncertainty principle in quantum mechanics. For large scales, on the other hand, the Madelung equations reduce to the Euler equations of a pressureless fluid and we recover the dynamics of standard cold dark matter ³:

Euler-Poisson equations

$$\partial_t \rho + 3H\rho + \frac{1}{a} \nabla \cdot (\rho \mathbf{v}) = 0, \quad (27)$$

$$\partial_t \mathbf{v} + H\mathbf{v} + \frac{1}{a} (\mathbf{v} \cdot \nabla) \mathbf{v} + \frac{1}{a} \nabla \phi = 0. \quad (28)$$

$$\Delta \phi(\mathbf{x}, t) - 4\pi G a^2 \rho_b(t) \delta(\mathbf{x}, t) = 0. \quad (29)$$

This underlines once again that FDM represents a modification of CDM on small scales and therefore has the potential to resolve the small-scale crisis in CDM. A few remarks about the mathematical structure of the Madelung equations: Firstly, the quantum pressure Q_P is not technically a pressure since it arises from the off-diagonal elements of a stress-tensor. It is therefore equivalent to an anisotropic pressure stress ⁴. This can be seen from the equivalent form of the Euler equation in Eq. (26)

$$\frac{\partial(\rho v_i)}{\partial t} + 4H\rho v_i + \frac{1}{a} \frac{\partial}{\partial x_j} (\rho v_i v_j + P_{ij}) = -\rho \frac{\partial \phi}{\partial x_i}, \quad (30)$$

where

$$\frac{1}{m} \nabla Q_P = \frac{a^2}{\rho} \partial_j P_{ij}, \quad (31)$$

with

$$P_{ij} = -\frac{\hbar^4}{2m^2 a^2} \rho \partial_i \partial_j \log(\rho) = \frac{\hbar^4}{4m^2 a^2} \left(\frac{1}{\rho} \partial_i \rho \partial_j \rho - \delta_{ij} \Delta \rho \right). \quad (32)$$

³The Euler equations for CDM are derived assuming that the scales of typical structure are much larger than the typical inter-particle spacing and typical timescales are much larger than the 2-body relaxation time of the system. In this case, a system of $N \gg 1$ collisionless particles of mass m interacting gravitationally in an expanding universe can be described using the Vlasov equation (Widrow and Kaiser 1993). Taking momentum moments of the Vlasov equation then yields the continuity and Euler equation. Higher-order moments can be neglected before virialisation and shell-crossing occur.

⁴However, unlike pressure in a real fluid, the quantum pressure can also become negative which poses problems when incorporating it into standard hydrodynamics codes.

This form also suggests the definition of the momentum-flux-density tensor

$$\begin{aligned}\Pi_{ij} &= \rho v_i v_j - P_{ij} \\ &= \frac{\hbar^2}{4ma^2} (\partial_i \psi^* \partial_j \psi + \partial_i \psi \partial_j \psi^* - \psi^* \partial_i \partial_j \psi - \psi \partial_i \partial_j \psi^*),\end{aligned}\tag{33}$$

up to the addition of a divergence-free tensor. As before, we can account for the effects of cosmological expansion via a change of variables:

$$dt \rightarrow a^2 dt', \quad \rho \rightarrow a^{-3} \rho',\tag{34}$$

and obtain the set of equations

$$\begin{aligned}\partial_{t'} \rho' + \nabla \cdot (\rho' \mathbf{v}) &= 0, \\ \partial_{t'} \mathbf{v} + (\mathbf{v} \cdot \nabla) \mathbf{v} + \nabla \phi + \nabla Q'_P &= 0, \\ \Delta \phi - 4\pi G a \rho'_b \delta' &= 0.\end{aligned}\tag{35}$$

To sum up, we have derived the fluid description of the Schrödinger-Poisson system. It states that the dynamics of the Schrödinger equation can be thought of as that of a frictionless flow with a special type of pressure that accounts for the Heisenberg uncertainty principle. The fluid description is amenable to fluid perturbation theory and can be integrated into existing hydrodynamics codes. However, it suffers from a significant drawback that we have neglected so far: In deriving the phase and fluid descriptions, we assumed that the density ρ was non-vanishing everywhere. For this reason, Eqs. (21) and (22) are not equivalent to Eq. (10) unless supplemented by the quantisation condition

$$\oint \mathbf{v} \cdot d\mathbf{x} = n \frac{\hbar}{m} \quad n \in \mathbb{N},\tag{36}$$

first derived by Wallstrom (1994).⁵ This quantisation condition guarantees that the wave function obtained by inverting the Madelung transform is single-valued everywhere in its domain. In practice, the phase/fluid formulation of the SPS is valid unless the wave function develops points with $\psi = 0$. Yet, this is quite common in wave dynamics. Think of the destructive interference of two waves, for instance. Therefore, we shall always check whether the application of the fluid formulation is justified in the following. In perturbation theory, for instance, the

⁵Note the similarity to the Bohr-Sommerfeld-quantisation condition for quantum systems

$$\oint_{H(\mathbf{p}, \mathbf{q})=E} \mathbf{p} d\mathbf{q} = 2\pi n \hbar, \quad n \in \mathbb{N},\tag{37}$$

where H is the Hamiltonian \mathbf{p} and \mathbf{q} are canonically conjugate variables.

fluid formulation remains valid as long as the perturbation theory itself remains valid. At the same time, evolving FDM dynamics using standard fluid dynamics codes will in general give incorrect results. Li, Hui and Bryan (2018) and Zhang, Liu and Chu (2019) give a discussion the of the limitations of fluid solvers for simulating FDM dynamics.

2.3 Symmetries

In this section, we briefly recapitulate symmetries of the Schrödinger-Poisson system in the form given by Eqs. (18) and (19):

$$i\hbar\partial_t\psi = \left(-\frac{\hbar^2}{2m}\Delta + m\phi\right)\psi, \quad (38)$$

$$\Delta\phi = 4\pi aG(|\psi|^2 - \rho_b). \quad (39)$$

We find *conservation of the norm of the wave function*

$$\frac{d}{dt} \left(\int dx |\psi(x, t)|^2 \right) = 0, \quad (40)$$

because of invariance of the action under global phase changes $\psi(x, t) \rightarrow e^{i\phi}\psi(x, t)$, *momentum conservation*

$$\frac{d}{dt} \left(-i \int dx \psi^* \partial_x \psi \right) = \frac{d}{dt} \left(\text{Im} \int dx \psi \partial_x \psi^* \right) = 0, \quad (41)$$

because of spatial translation invariance $\psi(x, t) \rightarrow \psi(x - x', t)$ and *conservation of angular momentum* due to rotational invariance of the gravitational potential. The SPS also retains invariance under inertial frame changes of the form

$$\psi(x, t) \rightarrow e^{i(vx - \frac{1}{2}v^2t)}\psi(x - vt, t), \quad (42)$$

and *conserves the Galileian boost operator*. In a static universe, we also find time translation invariance and therefore conservation of total energy. The Madelung equations Eqs. (35) provide a different view on the symmetries of the SPS. Norm conservation translates into mass conservation and momentum conservation immediately follows because the Euler equation is obtained as gradient of the Hamilton-Jacobi equation. Note that the flow described by the Madelung equations is therefore irrotational. ⁶

⁶The SPS can, however, develop vortices which is why we require the quantisation condition (36).

2.4 Thermodynamics

Heifetz and Cohen (2015) provide a thermodynamic view on the Madelung fluid by comparing it to a fluid with classical barotropic conservative flow. We consider the first law of thermodynamics $dI = -PdV$, where I is the thermal internal energy of a barotropic, frictionless fluid. When following a fluid parcel in motion, the adiabatic first law transform into

$$\rho \frac{D}{Dt} I = -P \log(\delta V) = -P \nabla \cdot \mathbf{v}, \quad (43)$$

where $\frac{D}{Dt} = \frac{\partial}{\partial t} + \mathbf{v} \cdot \nabla$ is the convective derivative. Multiplying the Euler equation for a compressible, potential flow

$$\frac{\partial \mathbf{v}}{\partial t} + (\mathbf{v} \cdot \nabla) \mathbf{v} = -\frac{1}{\rho} \nabla P, \quad (44)$$

by $\rho \mathbf{v}$ and combining it with Eq. (43), one obtains

$$\rho \frac{D}{Dt} (K + I + U) = -\nabla \cdot (\mathbf{v} P), \quad (45)$$

where K is the kinetic energy, I is the internal energy and U is an external potential. The total energy of a fluid parcel per unit mass $E = (K + I + U)$, is not materially conserved because of the surrounding pressure. Nevertheless, the overall total energy of the fluid is conserved in the domain averaged sense

$$\langle E \rangle = \langle K \rangle + \langle I \rangle + \langle U \rangle = -\nabla \cdot (\mathbf{v} P). \frac{\partial}{\partial t} \int E d^3x = 0. \quad (46)$$

We can now compare this to the energy expectation value of the Schrödinger equation which can be expressed via the quantum pressure as ⁷

$$\langle E \rangle = \frac{1}{2} \int \psi^* \left(-\frac{\hbar^2}{2m} \Delta + m\phi \right) \psi d^3x = \left\langle \frac{\mathbf{v}^2}{2} + Q_P + m\phi \right\rangle. \quad (47)$$

This view suggests that the expectation value of the internal energy of the fluid could be identified with the expectation value of the quantum pressure term $\langle Q \rangle = \langle I \rangle$, an interpretation also suggested in (Dennis, Gosson and Hiley 2014).

⁷This can also be seen via defining the energy as time-derivative of the Hamilton-Jacobi equation $E(\mathbf{x}, t) = -\frac{\partial S}{\partial t}$ and then taking the spatial average with integration by parts assuming vanishing boundary terms:

$$\langle E \rangle = \int \rho \left(\frac{(\nabla S)^2}{2m} + m\phi - \frac{\hbar^2}{2m} \frac{(\nabla \sqrt{\rho})^2}{\sqrt{\rho}^2} \right) d^3x.$$

Note that while the quantum pressure itself is not positive-definite, its expectation value after integration by parts can be expressed as

$$\langle Q_P \rangle = \left\langle \frac{1}{2} \left(\frac{\hbar}{2m} \nabla(\ln \rho) \right)^2 \right\rangle \equiv I, \quad (48)$$

where I is the internal energy per unit mass. Recami and Salesi (1998) therefore suggest the following partition

$$S_r = \log \left(\sqrt{\frac{\rho}{m}} \right), \quad S_i = S \quad (49)$$

$$\mathbf{v}_r = -\frac{\hbar}{ma} \nabla S_r, \quad \mathbf{v}_i = \frac{\hbar}{ma} \nabla S_i. \quad (50)$$

It has been used by Szapudi and Kaiser (2003) to derive Eulerian perturbation theory from the Schrödinger equation in terms of the logarithm of the density contrast (see Coles and Jones (1991) for more information on the lognormal model for cosmological mass distribution). The energy can now be expressed as

$$\langle E \rangle = \int \rho \left(\frac{v_i^2}{2} + \frac{v_r^2}{2} - \frac{m}{\hbar} \phi \right) d^3x \quad (51)$$

In this interpretation, the macroscopic energy of the flow is $\frac{v_r^2}{2}$ and the microscopic thermal motion is $\frac{v_i^2}{2}$. We can derive the corresponding equations of motions from Eq. (11) by substituting $\psi(\mathbf{x}, t) = e^{S_r(\mathbf{x}, t) + iS_i(\mathbf{x}, t)}$:

Convective form of the Madelung equations

$$\begin{aligned} \frac{D}{Dt} S_r + \frac{3}{2} H + \frac{\hbar}{2ma^2} \Delta S_i &= 0, \\ \frac{D}{Dt} S_i + S_i H - \frac{\hbar}{2ma^2} \Delta S_r &= \frac{am}{2\hbar} (v_i^2 + av_r^2) - \frac{m}{\hbar} \phi, \end{aligned} \quad (52)$$

where we define the convective derivative $\frac{D}{Dt} = \frac{\partial}{\partial t} + \mathbf{v}_i \cdot \nabla$.

This set of equations expresses that S_r and S_i both obey a type of coupled convection-diffusion equation where the convection of the phase S_i is driven by the energy of the system as source. Contrast this with the usual form of the Schrödinger equation where $\Re(\psi)$ and $\Im(\psi)$ obey a coupled diffusion equation ⁸.

⁸In fact, there are two coupled diffusion processes with opposite sign between the real and imaginary part of the wave function that exactly balance each other out to preserve the norm

Remark 1: Advection and waves

Consider the one-dimensional linear convection equation

$$u_t + au_x = 0. \quad (54)$$

This equation describes the transport of the quantity u by the constant convection velocity a . Given an arbitrary initial profile $u(x, t = 0) = u_0(x)$, the solution to the advection equation Eq. (54) is given by

$$u(x, t) = u_0(x - at). \quad (55)$$

This equation can be understood as a wave propagation equation where a wave of amplitude u propagates with the phase propagation speed a . A plane wave of amplitude \hat{u} , wavelength λ , and frequency ω

$$u = \hat{u}e^{i(kx - \omega t)}, \quad (56)$$

where $k = 2\pi/\lambda$ is a solution of the advection equation if $\omega = ak$. Hence, plane wave solutions of the advection equation satisfy the basic relation between wavelength and frequency $f = a/\lambda$. In other words, pure convection and wave propagation are equivalent (Hirsch 2007).

We call PDEs admitting solutions that describe wave-like phenomena *hyperbolic*. This is in contrast to *parabolic* PDEs that describe damped spatial waves and *elliptic* PDEs that do not admit wave-like solutions. The heat diffusion equation of Fourier

$$\frac{\partial u}{\partial t} = \alpha \frac{\partial^2 u}{\partial x^2} \quad (57)$$

is an example of a parabolic PDE. It describes heat conduction in solids or fluids at rest and admits the solution

$$u = \hat{u}e^{ikx}e^{-\alpha k^2 t}. \quad (58)$$

This solution represents an exponentially damped spatial wave for positive α . The Poisson equation

$$\Delta u = q \quad (59)$$

of the wave function:

$$\Re\left(\frac{\partial \psi}{\partial t}\right) = -\frac{\hbar}{2m}\Im(\Delta\psi), \quad \Im\left(\frac{\partial \psi}{\partial t}\right) = \frac{\hbar}{2m}\Re(\Delta\psi). \quad (53)$$

is an example of an elliptic PDE. It describes pure diffusion in space and does not admit wave-like solutions. The Schrödinger equation is similar to the heat equation, but with an imaginary diffusion coefficient and is therefore hyperbolic. This is reflected by the fact that the Madelung equations are a set of hyperbolic conservation laws.

2.5 Numerical Experiments

Below, we describe a number of one-dimensional tests in order to study the SPS system as well as the quantum pressure and convection terms in the Hamilton-Jacobi-Madelung equation. This section draws on (Li, Hui and Bryan 2018) for the first test without gravity and adds a second test with gravity to demonstrate the absence of cusps in FDM simulations first pointed out by Hu, Barkana and Gruzinov (2000). All figures and animations in this and the following sections were created using the wonderful MATPLOTLIB-library (Hunter 2007).

2.5.1 Gaussian Wave Packet

The 1D free Schrödinger equation is solved by a Gaussian wave packet with

$$\psi(x, t) = \sqrt{\frac{1}{\alpha + i\frac{\hbar t}{m}}} \exp\left(-\frac{x^2}{2(\alpha + i\frac{\hbar t}{m})}\right), \quad (60)$$

where α is a constant that specifies the width of the wave packet. The density and velocity follow as

$$\rho = \frac{1}{\sqrt{\alpha^2 + \frac{\hbar^2 t^2}{m^2}}} \exp\left(-\frac{\alpha x^2}{\alpha^2 + \frac{\hbar^2 t^2}{m^2}}\right), \quad v = \frac{x}{\alpha^2 + \frac{\hbar^2 t^2}{m^2}} \frac{\hbar^2 t}{m^2}. \quad (61)$$

Figure 1 shows the comparison between the numerical solution with and without quantum pressure and terms in the Euler equation (26). The simulation starts at $t = 0$ with $\alpha = 1/20$. On the one hand, the quantum pressure term drives the dispersion of the wave packet. In the absence of quantum pressure, the wave packet remains unchanged. The absence of convection in the Euler equation, on the other hand, accelerates the dispersion of the wave packet.

The free Schrödinger equation also admits a solution where a single Gaussian wave packet moves with momentum $\hbar k$:

$$\psi(x, t) = \sqrt{\frac{\alpha}{\alpha + i\frac{\hbar}{m}t}} \exp\left(-\frac{(x + x_0 - ik\alpha)^2}{2(\alpha + i\frac{\hbar}{m}t)}\right) \exp\left(-\frac{\alpha k^2}{2}\right). \quad (62)$$

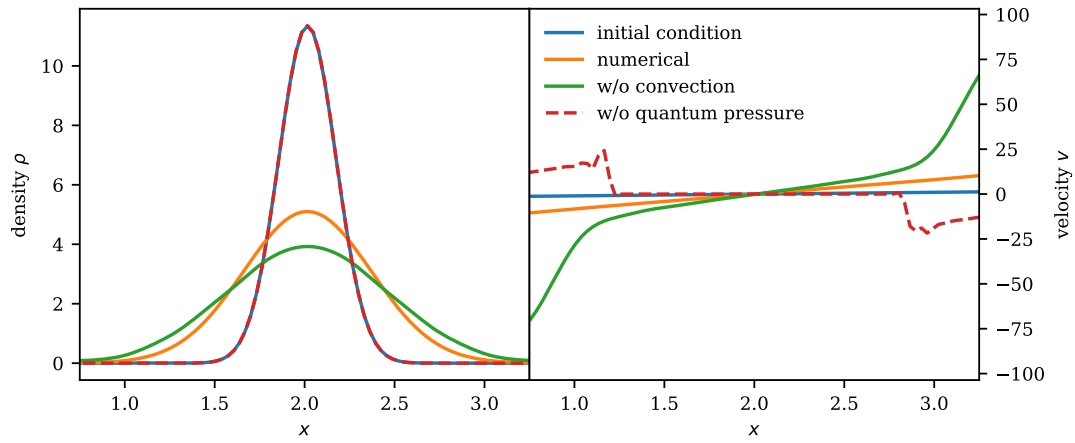


Figure 1: Comparison of analytical and numerical results for density evolution of a standing Gaussian wave packet at time $t = 0.1$ in code units.

Figure 2 shows this situation for $\alpha = 1/500$ and $k = 20\pi$. As before, the quantum pressure term drives the dispersion of the wave packet and interestingly, the absence of the convective term in the Hamilton-Jacobi equation modifies the dispersion of the wave packet.

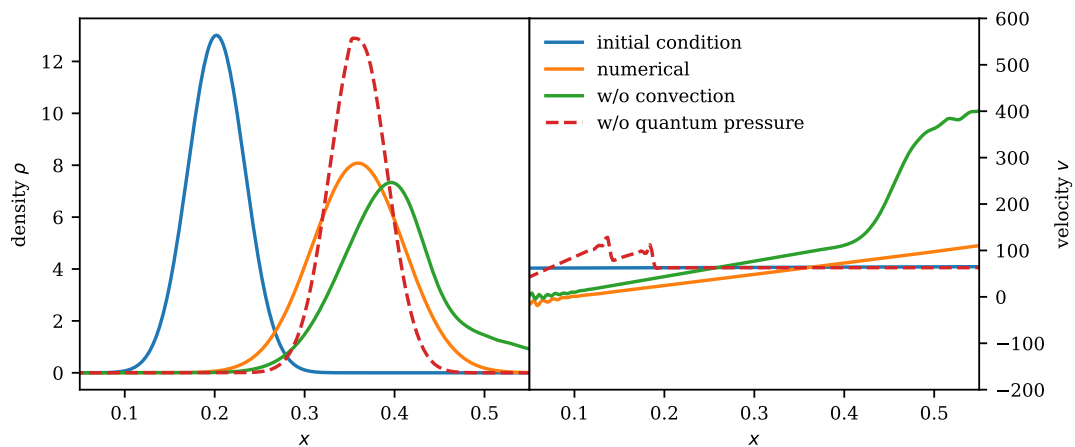


Figure 2: Comparison of analytical and numerical results for density evolution of a travelling Gaussian wave packet at time $t = 0.0025$ in code units.

2.5.2 Gravity

In this example, we consider the superposition of plane waves and a constant background density as initial conditions for a simulation with gravity:⁹

$$\psi(x, t = 0) = 1 + \sum_{n=0}^N (\alpha_n \cos(2\pi(n+1)x/L) + \beta_n \sin(2\pi(n+1)x/L)), \quad (63)$$

where $N = 1$, $L = 10$, α_n and β_n are uniform, random numbers between 0 and $5 \cdot 10^{-3}$. The gravitational constant is set to $G = 1$, but cosmological expansion is still turned off ($a = 1$). Figure 3 shows the evolution of these initial conditions. Without quantum pressure, cuspy profiles form. They are characteristic of N -Body CDM simulations. The quantum pressure term flattens these cusps. In the following chapter, we will study the suppression of structures in FDM below the characteristic *Jeans scale* in detail. For this example, the absence of the convection term in the Hamilton-Jacobi equation leads to high-frequency oscillations superposed with the expected large scale dynamics.

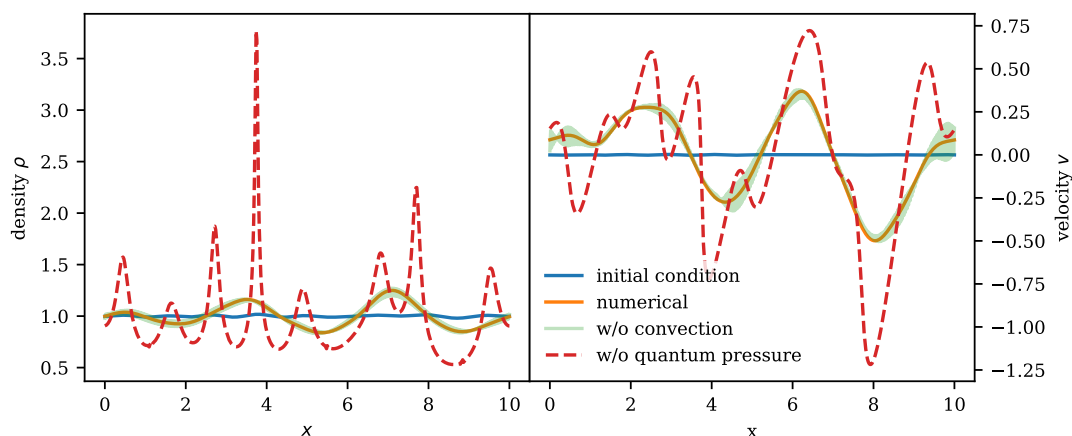


Figure 3: Comparison of the numerical evolution of a constant $\mathcal{O}(1)$ density background with $\mathcal{O}(10^{-3})$ density perturbations under the influence of gravity up to $t = 1.25$ in code units.

For more examples and possible interpretations of the Madelung equations see (Tsekov 2009; Bohm 1952).

⁹Note while the superposition principle holds for the linear Schrödinger equation, the velocity and density fields do not obey the superposition principle because of the nonlinearity introduced by the Madelung transform. Therefore, even a superposition of plane waves with vanishing velocity and constant density fields will of course lead to non-trivial velocity and density fields reflecting wave interference.

3

Eulerian Perturbation Theory

The goal of cosmological perturbation theory is to describe the departure of matter evolution from the homogeneous Hubble expansion perturbatively. In *Eulerian perturbation theory* (PT), one describes the nonlinear gravitational dynamics in terms of solutions of the linearised fluid equations in a fixed laboratory frame. We will see that linear analysis predicts that all scales are unstable in CDM models. This serves to explain the over-abundance of low mass halos and cuspy dark matter halo profiles observed in numerical CDM simulations. FDM can alleviate these problems because the quantum pressure term counteracts gravitational collapse below a non-zero *Jeans scale*. In the second part of this chapter, we will introduce nonlinear Eulerian perturbation theory. The fundamental objects of nonlinear PT are the *coupling kernels* F_n and G_n . They encode how linear modes couple in the full, nonlinear theory and therefore act as nonlinear transfer functions. We will first present recursion relations that allow to compute the kernels F_n and G_n in CDM following (Bernardeau et al. 2001). Afterwards, we will develop a general framework for time-dependent PT based on the approach suggested in (Li, Hui and Bryan 2018). We then use it to compute the kernels F_2 , F_3 and F_4 in CDM and FDM.

3.1 Eulerian Linear Perturbation Theory

In the following, we assume $\delta \ll 1$ and $|\mathbf{v}| \ll 1$ for the fluctuation fields and neglect higher-order perturbations of the form $\mathcal{O}(\delta^2, \mathbf{v} \cdot \delta, \mathbf{v}^2)$.

3.1.1 CDM

In order to linearise the Euler-Poisson equations, we substitute the density contrast into the comoving continuity equation (27) and use that the background

density evolution is governed by

$$\partial_t \rho_b(t) + 3H(t)\rho_b(t) = 0, \quad (64)$$

to obtain

$$\partial_t \delta + \frac{1}{a} \nabla \cdot ((1 + \delta)\mathbf{v}) = 0. \quad (65)$$

Neglecting higher-order terms $\mathcal{O}(\delta^2, \mathbf{v}\delta, \mathbf{v}^2)$, we find the

Linearised Euler-Poisson Equations

$$\partial_t \delta(\mathbf{x}, t) = -\frac{1}{a} \nabla \cdot \mathbf{v}(\mathbf{x}, t), \quad (66)$$

$$\partial_t \mathbf{v}(\mathbf{x}, t) + H\mathbf{v}(\mathbf{x}, t) = -\frac{1}{a} \nabla \phi(\mathbf{x}, t), \quad (67)$$

$$\Delta \Phi(\mathbf{x}, t) = 4\pi G a^2 \rho_b(t) \delta(\mathbf{x}, t). \quad (68)$$

Using the fact that \mathbf{v} can be decomposed into its divergence $\theta := \nabla \cdot \mathbf{v}$ and its vorticity $\mathbf{w} := \nabla \times \mathbf{v}$, we obtain

$$\partial_t \mathbf{w}(\mathbf{x}, t) = -\frac{1}{a} \mathbf{w}(\mathbf{x}, t). \quad (69)$$

Since $a(t) > 0 \forall t$, any initial vorticity decays away due to the expansion of the universe. Note that this linear result will in general not hold true in the nonlinear regime. In contrast, the velocity in FDM is derived as gradient of the phase and therefore irrotational by definition. Next, we study the time evolution of linear density perturbations. To this end, we assume that the time dependence of the density contrast can be separated from its spatial dependence

$$\delta(\mathbf{x}, t) = D(t)\delta(\mathbf{x}, 0), \quad (70)$$

where $D(t)$ is called the *linear growth factor*. Its evolution is governed by the linear growth equation

$$\ddot{D} + 2H\dot{D} - 4\pi G \rho_b D = 0. \quad (71)$$

Since Eq. (71) is a second-order ODE, there are two independent solutions, i.e. $D_+(t)$ and $D_-(t)$. They respectively describe the time-evolution of growing and decaying modes. Other common forms of this linear growth equation can be found by parameterising the time dependence of the growth factor via the conformal

time τ

$$D''(\tau) + \mathcal{H}(\tau)D'(\tau) - \frac{3}{2}\Omega_m(\tau)\mathcal{H}^2(\tau)D(\tau) = 0, \quad (72)$$

or via the scale factor a

$$D''(a) + \frac{1}{a} \left(3 + \frac{d \ln H(a)}{d \ln a} \right) D'(a) - \frac{3}{2} \frac{\Omega_{m,0}}{a^5} \frac{H_0^2}{H^2(a)} D(a) = 0, \quad (73)$$

where we made use of the relation

$$\frac{\Omega_m(a)}{\Omega_{m,0}} = \frac{1}{a^3} \frac{H_0^2}{H^2(a)}. \quad (74)$$

For an Einstein-de Sitter model with $\Omega_m = 1$ (EdS) at small a , the cosmological equation reduces to

$$\frac{\dot{a}^2}{a^2} = \frac{8}{3}\pi G\rho_b a^2, \quad (75)$$

and is solved by

$$a \propto t^{2/3}, \quad 6\pi G\rho_b t^2 = 1. \quad (76)$$

The linear growth equation (73) then becomes

$$D'' + \frac{3}{2a}D' = \frac{3}{2a^2}D, \quad (77)$$

with the solutions

$$D_+(a) = a, \quad D_-(a) = a^{-\frac{3}{2}}. \quad (78)$$

Note that the growing modes approximately grow with a on large scales even in cosmologies where $\Omega_m < 1$ as shown in Fig. 4.

3.1.2 FDM

As in the CDM case, we substitute the density contrast into the comoving continuity equation and linearise the Madelung equations (26) by neglecting higher-order terms $\mathcal{O}(\delta^2, \mathbf{v} \cdot \delta, \mathbf{v}^2)$ to obtain the

Linearised Madelung Equations

$$\partial_t \delta(\mathbf{x}, t) = -\frac{1}{a} \nabla \cdot \mathbf{v}, \quad (79)$$

$$\partial_t \mathbf{v}(\mathbf{x}, t) + H \mathbf{v}(\mathbf{x}, t) = -\frac{1}{a} \nabla \Phi(\mathbf{x}, t) + \frac{\hbar^2}{4m^2 a^3} \Delta(\Delta \delta), \quad (80)$$

$$\Delta \Phi = 4\pi G a^2 \rho_b \delta. \quad (81)$$

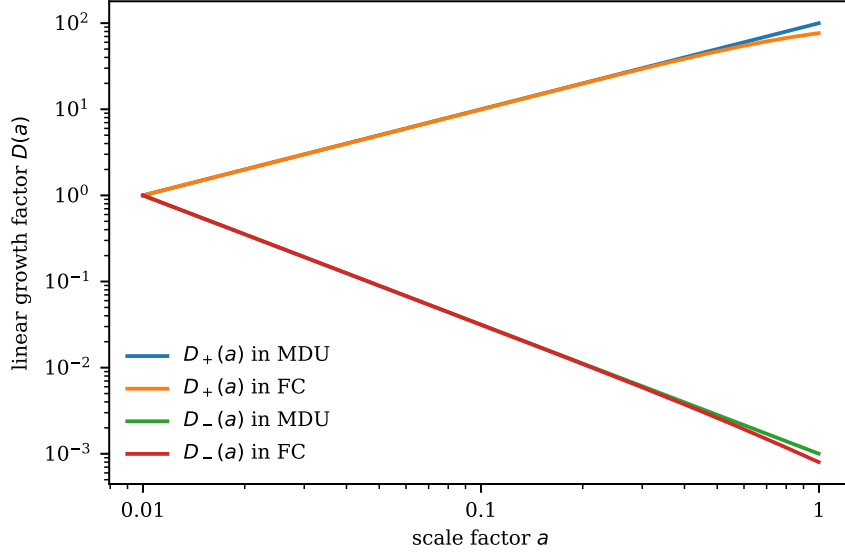


Figure 4: Comparison of analytical solutions of growth equation in EdS or matter-dominated universe (MDU) with solution in [fiducial cosmology](#) (FC) obtained by numerical integration of Eq. (73). Growth factors are normalised to $D_{\pm}(a_0) = 1$ at $a_0 = 0.01$.

Eliminating the velocity field yields the evolution of the density field δ

$$\ddot{\delta} + 2H\dot{\delta} = 4\pi G\rho_b\delta - \frac{\hbar^2}{4m^2a^4}\Delta(\Delta\delta). \quad (82)$$

A Fourier transform then gives:

$$\ddot{\delta}_k + 2H\dot{\delta}_k - \left(4\pi G\rho_b - \frac{\hbar^2 k^4}{4m^2 a^4}\right)\delta_k = 0. \quad (83)$$

Unlike in the CDM case, linear growth in FDM is scale-dependent because of the quantum pressure term. Modes at different scales still evolve independently because we linearised the Madelung equations. Mode coupling and the transfer of power from large to small scales are a purely nonlinear phenomenon. Note that the term in brackets $\frac{\hbar^2 k^4}{4m^2 a^4}$ contains the FDM sound speed $c_{s,\text{eff}}^2 \approx \frac{k^2}{4m^2 a^2}$ in the limit $\frac{k}{ma} < 1$ ¹⁰. For each mode k , Eq. (83) describes a harmonic oscillator with time-dependent dampening $H(t)$ and frequency

$$\omega(k, t) = \sqrt{\frac{\hbar^2 k^4}{4m^2 a^4} - \frac{4\pi G\rho_b}{a^3}}. \quad (85)$$

¹⁰A relativistic treatment of the effective sound speed in the gauge comoving with the time-averaged axion fluid yields

$$c_{s,\text{eff,full}}^2 = \frac{k^2/(4m^2 a^2)}{1 + k^2/(4m^2 a^2)}. \quad (84)$$

Scale factor a	$m = 10^{-21}$ eV	$m = 10^{-22}$ eV	$m = 10^{-23}$ eV
0.01	70	22	7
1	221	70	22

Table 8: Comoving quantum Jeans scales $k_J \propto a^{\frac{1}{4}} m^{\frac{1}{2}}$ for 3 different axion masses m and redshifts in units h/Mpc . The respective Jeans wavelengths λ_J range from 30 kpc/h to 900 kpc/h .

The condition $\omega = 0$ defines the *comoving quantum Jeans scale* k_J as

$$\begin{aligned}
k_J &= \left(\frac{16\pi G m^2 \rho_b a}{\hbar^2} \right)^{\frac{1}{4}} \\
&= 44.7 \text{Mpc}^{-1} \left(6a \frac{\Omega_{m,0}}{0.3} \right)^{\frac{1}{4}} \left(\frac{H_0}{70 \frac{\text{km}}{\text{s}} \frac{1}{\text{Mpc}}} \frac{m}{10^{-22} \text{eV}} \right)^{\frac{1}{2}}, \tag{86}
\end{aligned}$$

or equivalently the *comoving quantum Jeans wavelength* λ_J as

$$\begin{aligned}
\lambda_J &= \frac{2\pi}{k_J} = \left(\frac{\hbar^2 \pi^3}{m^2 G \rho_b a} \right)^{\frac{1}{4}} \\
&= 141 \text{kpc} \left(6a \frac{\Omega_{m,0}}{0.3} \right)^{-\frac{1}{4}} \left(\frac{H_0}{70 \frac{\text{km}}{\text{s}} \frac{1}{\text{Mpc}}} \frac{m}{10^{-22} \text{eV}} \right)^{-\frac{1}{2}}. \tag{87}
\end{aligned}$$

Table 8 lists a few examples of comoving Jeans scales for different FDM masses. The Jeans scale describes a force balance between gravity and quantum pressure. For $k < k_J$, i.e. scales larger than λ_J , $\omega(k, t)$ becomes imaginary and we recover a growing and a decaying mode just like for CDM. Perturbations on these scales are unstable and will gravitationally collapse. For $k > k_J$, i.e. scales smaller than λ_J , the frequency $\omega(k, t)$ becomes real. Perturbations on small scales therefore undergo oscillations. Physically speaking, the quantum pressure counteracts gravity and perturbations do not collapse under their own gravity. The comoving Jeans wavelength decreases with time as $\lambda_J \sim a^{-\frac{1}{4}}$ which is why more small-scale features can develop as the universe evolves.

As in the CDM case, we find an analytical solution of the linear FDM growth equation (83) in the EdS case. To this end, we rewrite Eq. (83) in terms of the

scale factor a

$$D''(a) + \frac{1}{a} \left(3 + \frac{d \ln H}{d \ln a} \right) D'(a) - \frac{1}{a^2 H(a)^2} \left(\frac{3 \Omega_{m,0} H_0^2}{2 a^3} - \frac{\hbar^2 k^4}{2 m^2 a^4} \right) D(a) = 0. \quad (88)$$

Simplifying with $\Omega_{m,0} = 1$ gives

$$D''(a) + \frac{3}{2a} D'(a) - \left(\frac{3}{2a^2} - \frac{\hbar^2 k^4}{4m^2 a^3 H_0^2} \right) D(a) = 0. \quad (89)$$

Following the convention in (Li, Hui and Bryan 2018), we further introduce the conformal time η that is related to the standard conformal time τ via

$$\eta \equiv 2\sqrt{a} = H_0 \tau, \quad (90)$$

as well as the momentum scale $b(k)$ as

$$b(k) = \frac{2\hbar k^2}{m H_0}. \quad (91)$$

With these definitions in place, we obtain

$$\partial_\eta^2 D(k, \eta) + \frac{2}{\eta} \partial_\eta D(k, \eta) - \left(\frac{6}{\eta^2} - \frac{b(k)^2}{\eta^4} \right) D(k, \eta) = 0. \quad (92)$$

The analytical solutions to Eq. (92) take the form

$$D_\pm(k, \eta) = \eta^{-\frac{1}{2}} J_{\mp 5/2} \left(\frac{b(k)}{\eta} \right), \quad (93)$$

where $J_{\mp 5/2}$ are cylindrical Bessel functions of fractional order:

$$J_{-5/2} = \sqrt{\frac{2}{\pi z}} \left(\frac{3 \cos z}{z^2} + \frac{3 \sin z}{z} - \cos z \right), \quad (94)$$

$$J_{+5/2} = \sqrt{\frac{2}{\pi z}} \left(\frac{3 \sin z}{z^2} - \frac{3 \cos z}{z} - \sin z \right). \quad (95)$$

We recover the CDM solutions (78) in the limit of small arguments for the Bessel functions:

$$J_{-5/2} \rightarrow \sqrt{\frac{2}{\pi}} \frac{3}{z^{\frac{5}{2}}}, \quad J_{5/2} \rightarrow \sqrt{\frac{2}{\pi}} \frac{z^{\frac{5}{2}}}{15}. \quad (96)$$

This limit physically corresponds to the quantum pressure becoming small which happens at late times, at large scales and for large masses. We can also study the CDM limit of Eq. (92) directly. The ansatz $D \propto \eta^\alpha$ solves Eq. (92) if the coefficient α obeys

$$\alpha_{+/-} = -\frac{1}{2} \pm \sqrt{\frac{25}{4} - \frac{b(k)^2}{\eta^2}}. \quad (97)$$

For vanishing quantum pressure, the exponents $\alpha_+ = 2$ and $\alpha_- = 3$ correspond to the CDM solutions defined in Eq. (78). If $\frac{b(k)^2}{\eta^2} > \frac{25}{4}$, that is, if we consider scales smaller than the quantum Jeans wavelength, we obtain complex exponents corresponding to growing and decaying oscillations of the density perturbations. Figs. 5 and 6 show the growing and decaying solutions respectively.

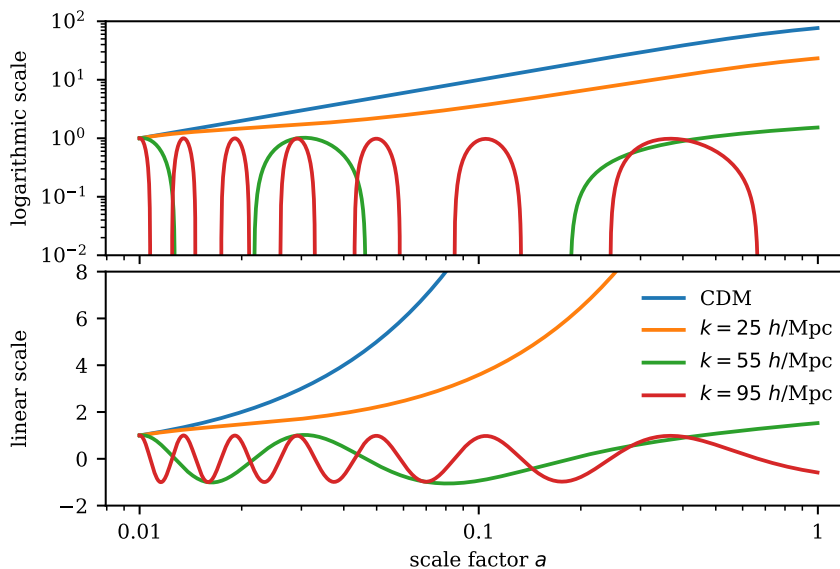


Figure 5: Growing modes $D_+(a)$ in CDM and $D_+(k, a)$ in FDM in fiducial cosmology obtained by numerical integration of Eqs. (73) and (89) for a mass of $m = 10^{-22}$ eV at three different scales k . Growth factors are normalised to $D_+(a_0) = 1$ at $a_0 = 0.01$.

The existence of a natural length scale in FDM can also be understood on purely dimensional grounds. The most apparent scale in the SPS is the static *Compton wavelength* $\lambda = \frac{h}{mc}$. It gives the wavelength of a photon whose energy equals the axion mass. For an ultra-light axion with a mass of $m \sim 10^{-22}$ eV, the Compton wavelength is at the order of 10^{-1} pc and therefore much smaller than a typical galaxy. Therefore, we turn towards the *de Broglie wavelength*:

$$\lambda_{dB} = \frac{h}{mv} = 1.92 \text{kpc} \left(\frac{10^{-22} \text{eV}}{m} \right) \left(\frac{10 \frac{\text{km}}{\text{s}}}{v} \right). \quad (98)$$

It represents the wavelength of solutions of the Schrödinger equation. For galactic velocities v with $v \sim 10^4 \frac{\text{m}}{\text{s}}$, we find the astronomically relevant de Broglie

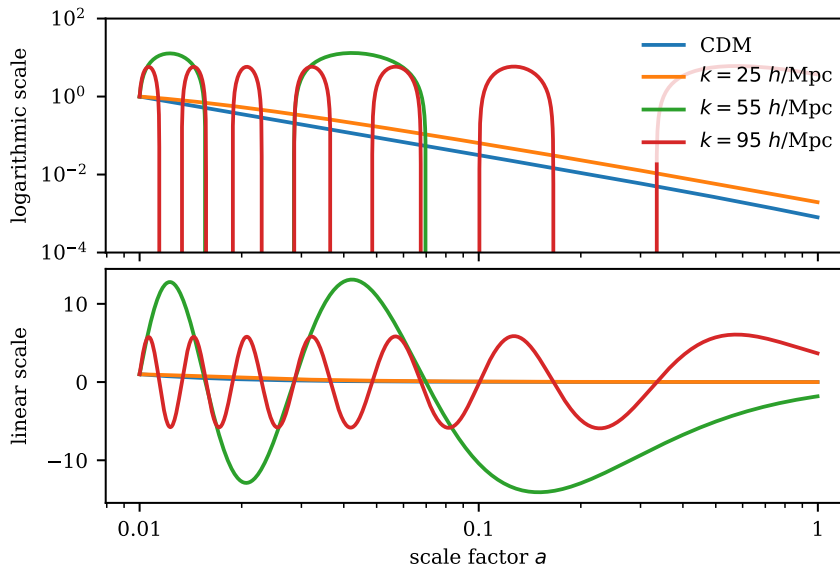


Figure 6: Decaying modes $D_-(k, a)$ in CDM and FDM in [fiducial cosmology](#) obtained by numerical integration of Eqs. (73) and (89) for a mass of $m = 10^{-22}$ eV at three different scales k . Growth factors are normalised to $D_-(a_0) = 1$ at $a_0 = 0.01$.

wavelength $\lambda_{dB} \sim 1$ kpc. Roughly speaking, the de Broglie wavelength cannot exceed the virial radius $r \sim \frac{GM}{v^2}$ of an equilibrium self-gravitating system of mass M ¹¹. Thus,

$$r \gtrsim \frac{\hbar^2}{m^2} \frac{1}{GM}. \quad (99)$$

The *Buckingham-II theorem* now ensures that Eq. (99) defines the unique length scale that can be formed using the input parameters

$$\left[\frac{\hbar}{m} \right] = \frac{L^2}{T}, \quad [G] = \frac{L^3}{MT^2}, \quad [M] = M, \quad [a] = 1. \quad (100)$$

These are three dimensionful and one dimensionless input parameter expressed in terms of the three fundamental dimensions time T , length L and mass M . The Buckingham-II theorem now states that there is no dimensionless product of rational powers of the dimensionful input parameters. Therefore, any length scale of interest λ must be of the form

$$\lambda = f(a) \frac{\hbar^2}{m^2} \frac{1}{GM}. \quad (101)$$

If we now assume that M is the mass of a sphere of radius λ with density ρ_b , we

¹¹This statement can be made rigorous by showing that the SPS admits a stable ground state solution that is the long-term attractor of any FDM system. For a proof, see for instance (Chavanis 2011).

find

$$\lambda = \left(f(a) \frac{\hbar^2}{m^2} \frac{1}{G\rho_b} \right)^{\frac{1}{4}}, \quad (102)$$

which is, up to factors of order unity, the expression for the comoving quantum Jeans length defined in Eq. (87).

To sum up, the *key difference between CDM and FDM in linear perturbation theory* is the existence of a unique length scale in FDM. Whereas all scales are gravitationally unstable in CDM, the perturbations below the quantum Jeans scale are stabilised in FDM. Nevertheless, nonlinear perturbation theory may alter these conclusions since the quantum Jeans scale is a concept only valid within linear perturbation theory. This can be seen by taking the first few terms of the Taylor expansion of the quantum pressure Eq. (24):

$$\frac{2m^2}{\hbar^2} \Delta Q_P = -\Delta \frac{\Delta \sqrt{\rho}}{\sqrt{\rho}} = \Delta \left(-\Delta \delta + \frac{1}{4} \Delta \delta^2 + \frac{1}{2} \delta \Delta \delta + \mathcal{O}(\delta^2) \right) \quad (103)$$

The linear contribution $-\Delta^2 \delta$ counteracts gravity since they have opposite signs in Eq. (82). However, the quadratic terms acts in the same direction as gravity and could therefore potentially enhance gravitational collapse (Li, Hui and Bryan 2018). This is related to the fact that the interference of waves can lead to structures that are smaller than their wavelength. As a matter of fact, halos in FDM simulations often have large density fluctuations below the Jeans scale. In order to estimate the effect of nonlinearities on cosmological structure formation, we develop nonlinear perturbation theory for CDM and FDM in the next section.

3.2 Eulerian Non-Linear Perturbation Theory

We will now consider the evolution of CDM and FDM beyond the linear approximation using *Eulerian Non-Linear Perturbation Theory*. The fundamental assumption of Eulerian perturbation theory is that we can expand the density contrast and velocity fields in terms of the solutions $\delta^{(1)}$ and $\mathbf{v}^{(1)}$ of the linearised equations (66) and (79):

$$\delta(\mathbf{x}, a) = \sum_{n=1}^{\infty} \delta^{(n)}(\mathbf{x}, a), \quad \theta(\mathbf{x}, a) = \sum_{n=1}^{\infty} \theta^{(n)}(\mathbf{x}, a), \quad (104)$$

where $\theta = \nabla \cdot \mathbf{v}$ and the n^{th} -order fluctuation fields $\delta^{(n)}$ and $\theta^{(n)}$ are proportional to the n^{th} power of the linear fluctuation fields:

$$\delta^{(n)} \sim (\delta^{(1)})^n, \quad \theta^{(n)} \sim (\theta^{(1)})^n. \quad (105)$$

In addition, we have $\partial_a \delta^{(1)} = \theta^{(1)}$ from the linearised continuity equation. Therefore, both the velocity and the density field are fully determined by the linear density fluctuations. The goal of perturbation theory is now to describe how linear modes couple in the full, nonlinear theory. To this end, we introduce the nonlinear coupling kernels F_n and G_n . They describe how the n^{th} -order fluctuation fields are sourced by the linear fluctuation fields via

$$\begin{aligned} \delta^{(n)}(\mathbf{k}) &= \int \frac{d^3 \mathbf{q}_1}{(2\pi)^3} \cdots \int \frac{d^3 \mathbf{q}_n}{(2\pi)^3} \delta_D(\mathbf{k} - \mathbf{q}_{1,\dots,n}) \\ &\quad \times F_n(\mathbf{q}_1, \dots, \mathbf{q}_n) \delta^{(1)}(\mathbf{q}_1) \dots \delta^{(1)}(\mathbf{q}_n), \end{aligned} \quad (106)$$

$$\begin{aligned} \theta^{(n)}(\mathbf{k}) &= \int \frac{d^3 \mathbf{q}_1}{(2\pi)^3} \cdots \int \frac{d^3 \mathbf{q}_n}{(2\pi)^3} \delta_D(\mathbf{k} - \mathbf{q}_{1,\dots,n}) \\ &\quad \times G_n(\mathbf{q}_1, \dots, \mathbf{q}_n) \delta^{(1)}(\mathbf{q}_1) \dots \delta^{(1)}(\mathbf{q}_n), \end{aligned} \quad (107)$$

where F_n and G_n are homogeneous functions of the wave vectors $\mathbf{q}_1, \dots, \mathbf{q}_n$ with degree zero and $\mathbf{q}_{1,\dots,n} \equiv \mathbf{q}_1 + \dots + \mathbf{q}_n$. Note that in the following, we employ a convention where integration over momenta $\mathbf{k}_i, \mathbf{k}_j$ with equal indices i, j is understood, e.g.:

$$\begin{aligned} \delta_D(\mathbf{k} - \mathbf{k}_{12}) \beta(\mathbf{k}_1, \mathbf{k}_2) \theta(\mathbf{k}_1) \theta(\mathbf{k}_2) &\equiv \\ \int \frac{d^3 \mathbf{k}_1 d^3 \mathbf{k}_2}{(2\pi)^6} \delta_D(\mathbf{k} - \mathbf{k}_{12}) \beta(\mathbf{k}_1, \mathbf{k}_2) \theta(\mathbf{k}_1) \theta(\mathbf{k}_2). \end{aligned} \quad (108)$$

With this convention in place, Eqs. (106) and (107) take the form:

$$\delta^{(n)}(\mathbf{k}) = \delta_D(\mathbf{k} - \mathbf{q}_{1,\dots,n}) F_n(\mathbf{q}_1, \dots, \mathbf{q}_n) \delta^{(1)}(\mathbf{q}_1) \dots \delta^{(1)}(\mathbf{q}_n), \quad (109)$$

$$\theta^{(n)}(\mathbf{k}) = \delta_D(\mathbf{k} - \mathbf{q}_{1,\dots,n}) G_n(\mathbf{q}_1, \dots, \mathbf{q}_n) \delta^{(1)}(\mathbf{q}_1) \dots \delta^{(1)}(\mathbf{q}_n). \quad (110)$$

3.2.1 Goroff's Method

We start by reminding the reader of the Euler-Poisson equations expressed in terms of the conformal time τ :

$$\partial_\tau \delta + \nabla \cdot ((1 + \delta) \mathbf{v}) = 0, \quad (111)$$

$$\partial_\tau \mathbf{v} + \mathcal{H} \mathbf{v} + (\mathbf{v} \cdot \nabla) \mathbf{v} + \nabla \phi = 0, \quad (112)$$

$$\Delta \phi - \frac{3}{2} \Omega_{m,0} \mathcal{H}^2 \delta = 0. \quad (113)$$

We characterise the velocity field \mathbf{v} only by its divergence θ and neglect vorticity degrees of freedom. This is a valid assumption as long as multi-streaming and shocks do not occur. After taking the divergence of Eq. (112) and Fourier

transforming, we obtain

$$\partial_\tau \delta(\mathbf{k}, \tau) + \theta(\mathbf{k}, \tau) = -\delta_D(\mathbf{k} - \mathbf{k}_{12})\alpha(\mathbf{k}_1, \mathbf{k}_2)\theta(\mathbf{k}_1, \tau)\delta(\mathbf{k}_2, \tau), \quad (114)$$

as well as the Euler equation

$$\begin{aligned} \partial_\tau \theta(\mathbf{k}, \tau) + \mathcal{H}(\tau)\theta(\mathbf{k}, \tau) + \frac{3}{2}\Omega_{m,0}\mathcal{H}^2(\tau)\delta(\mathbf{k}, \tau) \\ = -\delta_D(\mathbf{k} - \mathbf{k}_{12})\beta(\mathbf{k}_1, \mathbf{k}_2)\theta(\mathbf{k}_1, \tau)\theta(\mathbf{k}_2, \tau), \end{aligned} \quad (115)$$

where the following mode-coupling functions were defined:

$$\alpha(\mathbf{k}_1, \mathbf{k}_2) \equiv \begin{cases} \frac{\mathbf{k}_{12} \cdot \mathbf{k}_1}{k_1^2}, & \text{if } k_1 \neq 0, \\ 0, & \text{otherwise,} \end{cases} \quad (116)$$

$$\beta(\mathbf{k}_1, \mathbf{k}_2) \equiv \begin{cases} \frac{k_{12}^2(\mathbf{k}_1 \cdot \mathbf{k}_2)}{2k_1^2 k_2^2}, & \text{if } k_1 \neq 0 \text{ and } k_2 \neq 0, \\ 0, & \text{otherwise.} \end{cases} \quad (117)$$

We now consider an EdS universe where $a(\tau) \propto \tau^2$ and $\mathcal{H}(\tau) = \frac{2}{\tau}$. In this situation, we can bring the system of equations (114) and (115) into a form which is homogeneous in the scale factor. It can then be solved using the perturbative expansion

$$\delta(\mathbf{k}, \tau) = \sum_{n=1}^{\infty} a^n(\tau)\delta_n(\mathbf{k}), \quad (118)$$

$$\theta(\mathbf{k}, \tau) = -\mathcal{H}(\tau) \sum_{n=1}^{\infty} a^n(\tau)\theta_n(\mathbf{k}). \quad (119)$$

With the help of this expansion, one can derive recursion relations for the mode coupling kernels:

$$\begin{aligned} F_n(\mathbf{q}_1, \dots, \mathbf{q}_n) &= \sum_{m=1}^{n-1} \frac{G_n(\mathbf{q}_1, \dots, \mathbf{q}_m)}{(2n+3)(n-1)} ((2n+1)\alpha(\mathbf{k}_1, \mathbf{k}_2) \\ &\quad \times F_{n-m}(\mathbf{q}_{m+1}, \dots, \mathbf{q}_n) \\ &\quad + 2\beta(\mathbf{k}_1, \mathbf{k}_2)G_{n-m}(\mathbf{q}_{m+1}, \dots, \mathbf{q}_n)), \\ G_n(\mathbf{q}_1, \dots, \mathbf{q}_n) &= \sum_{m=1}^{n-1} \frac{G_n(\mathbf{q}_1, \dots, \mathbf{q}_m)}{(2n+3)(n-1)} (3\alpha(\mathbf{k}_1, \mathbf{k}_2) \\ &\quad \times F_{n-m}(\mathbf{q}_{m+1}, \dots, \mathbf{q}_n) \\ &\quad + 2n\beta(\mathbf{k}_1, \mathbf{k}_2)G_{n-m}(\mathbf{q}_{m+1}, \dots, \mathbf{q}_n)), \end{aligned} \quad (120)$$

where $\mathbf{k}_1 = \mathbf{q}_1 + \dots + \mathbf{q}_m$, $\mathbf{k}_2 = \mathbf{q}_{m+1} + \dots + \mathbf{q}_n$, $\mathbf{k} = \mathbf{k}_1 + \mathbf{k}_2$, and $F_1 = G_1 = 1$. This method was developed in a series of papers (Fry 1984; Goroff et al. 1986; Jain and Bertschinger 1993). Following the convention in (Reimberg 2016), we will refer to this method of developing perturbative solutions to the Euler equations in an EdS universe as *Goroff's method* because of (Goroff et al. 1986). We further introduce the symmetrised recursion kernels

$$F_n^{(s)}(\mathbf{q}_1, \dots, \mathbf{q}_n) = \frac{1}{n!} \sum_{\pi \in \Pi(n)} F_n(\mathbf{q}_{\pi(1)}, \dots, \mathbf{q}_{\pi(n)}), \quad (121)$$

$$G_n^{(s)}(\mathbf{q}_1, \dots, \mathbf{q}_n) = \frac{1}{n!} \sum_{\pi \in \Pi(n)} G_n(\mathbf{q}_{\pi(1)}, \dots, \mathbf{q}_{\pi(n)}). \quad (122)$$

For instance, the symmetrised kernel $F_2^{(s)}$ reads:

$$F_2^{(s)}(\mathbf{q}_1, \mathbf{q}_2) = \frac{5}{7} + \frac{1}{2} \frac{\mathbf{q}_1 \cdot \mathbf{q}_2}{q_1 q_2} \left(\frac{q_1}{q_2} + \frac{q_2}{q_1} \right) + \frac{2}{7} \frac{(\mathbf{q}_1 \cdot \mathbf{q}_2)^2}{q_1^2 q_2^2}. \quad (123)$$

In a general cosmology, the PT expansion is more complicated because the solutions at each order become non-separable functions of τ and \mathbf{k} . In particular, the growing mode at order n does not scale as $D_1^n(\tau)$. Yet, it is possible to show that a simple approximation to the equations of motion for general Ω_m and Ω_Λ leads to separable solutions of arbitrary order in PT and the same recursion relations as in the EdS case. All the information of the PT solutions on the cosmological parameters Ω_m and Ω_Λ is then encoded in the linear growth factor (Bernardeau et al. 2001).

3.2.2 Scoccimarro's Method

The first attempt at using cosmological perturbation theory for the Schrödinger equation in the fluid picture can be found in Szapudi and Kaiser (2003). They derive the above recursion kernels in the correspondence limit of the Schrödinger equation ($\hbar \rightarrow 0$). This has the advantage that the PT remains valid even after shell crossing because the velocity field is irrotational by definition. However, including the quantum pressure for $\hbar \neq 0$ poses additional difficulties. In a CDM EdS universe, we have seen that it is possible to obtain algebraic recursion relations for the coupling kernels. This is because the Euler-Poisson system becomes homogeneous in the scaling factor a in this case. In FDM, the quantum pressure term has a different dependence on the scale factor a and the coupling kernels end up being time time-dependent, even in an EdS universe. Therefore, we were not able to obtain recursion relations for the couplings kernels in FDM. Just like for

a general cosmology in CDM, the solutions at each order become non-separable functions of time and scale. A method to obtain the PT kernels in this case is described in a series of papers (Scoccimarro 1998; Scoccimarro 2006). They develop a framework for time-dependent PT using Feynman diagrams. In the following, we will refer to their method as *Scoccimarro's method*. Li, Hui and Bryan (2018) use Scoccimarro's method for computing the kernels F_2 and F_3 in FDM. One treats the nonlinear terms in the Madelung equations as inhomogeneity $g(\eta)$ while solving the growth equation (92)

$$\partial_\eta^2 D(k, \eta) + \frac{2}{\eta} \partial_\eta D(k, \eta) - \left(\frac{6}{\eta^2} - \frac{b(k)^2}{\eta^4} \right) D(k, \eta) = g(\eta). \quad (124)$$

We end up with an integral equation that can be represented as a Dyson series. The Dyson series allows for a diagrammatic representation and can be recursively solved up to a given order in perturbation theory. In the following section, we will retrace the steps taken by Li, Hui and Bryan (2018) to apply Scoccimarro's method to FDM. We begin our discussion in a more general setting before we specialise to FDM and CDM.

We start with a system of two coupled equations of the form

$$\partial_\tau \delta = -\nabla \cdot ((1 + \delta)\mathbf{v}), \quad (125)$$

$$\partial_\tau \theta = f(\theta, \delta), \quad (126)$$

where f is a well-behaved functions that is allowed to depend on θ and δ and their spatial derivatives. Hence, Eq. (126) include both the ideal fluid equations with pressure if we neglect the vorticity degrees of freedom as well as the Madelung equations. Further, we introduce the two-component vector

$$\Psi = [\delta \quad \theta]^\top, \quad (127)$$

such that the density and velocity fields can be treated on equal footing. We now Taylor expand Eq. (126) in terms of δ and θ and then Fourier transform it:

$$\begin{aligned} \partial_\eta \Psi_a(\mathbf{k}) + \Omega_{ab}(\mathbf{k}, \eta) \Psi_b(\mathbf{k}) = \\ \sum_{n=2}^{\infty} \delta_D(\mathbf{k} - \mathbf{k}_{1\dots n}) \Gamma_{a,i_1\dots i_n}^n(\mathbf{k}, \mathbf{k}_1, \dots, \mathbf{k}_n, \eta) \Psi_{i_1}(\mathbf{k}_1, \eta) \times \dots \times \Psi_{i_n}(\mathbf{k}_n, \eta). \end{aligned} \quad (128)$$

where we introduced the time- and scale-dependent mode-coupling matrices Ω_{ab} and Γ_{a,i_1,\dots,i_n} for the indices $a, b, i_1, \dots, i_n \in \{1, 2\}$ and we employ the Einstein sum convention. The matrix Ω_{ab} encodes the linearised fluctuations, whereas the

matrices $\Gamma_{a,i_1\dots i_n}$ encode all nonlinearities. The meaning of the indices can be easily understood: The index a tells us whether we are looking at a contribution to the density contrast δ or the velocity divergence θ . The indices i tells us which fields couple to one another. The continuity equation Eq. (125) gives $\Omega_{11} = 0$ and $\Omega_{12} = 1$. We can therefore substitute

$$\begin{aligned} \Psi_2(\mathbf{k}, \eta) &= -\partial_\eta \Psi_1(\mathbf{k}, \eta) \\ &+ \sum_{n=2}^{\infty} \delta_D(\mathbf{k} - \mathbf{k}_{1\dots n}) \Gamma_{1,i_1\dots i_n}^n(\mathbf{k}, \mathbf{k}_1, \dots, \mathbf{k}_n, \eta) \Psi_{i_1}(\mathbf{k}_1, \eta) \times \dots \times \Psi_{i_n}(\mathbf{k}_n, \eta) \end{aligned} \quad (129)$$

into Eq. (126) for $a = 2$ to obtain

$$\partial_\eta^2 \Psi_1 + \Omega_{22} \partial_\eta \Psi_1 - \Omega_{21} \Psi_1 = g(\mathbf{k}, \eta), \quad (130)$$

where we omitted time and momentum variables and the inhomogeneity $g(\mathbf{k}, \eta)$ is defined as

$$\begin{aligned} g(\mathbf{k}, \eta) &\equiv \sum_{n=2}^{\infty} \delta_D(\mathbf{k} - \mathbf{k}_{1\dots n}) \\ &\left[\partial_\eta \left[\Gamma_{1,i_1\dots i_n}^n \Psi_{i_1}(\mathbf{k}_1, \eta) \times \dots \times \Psi_{i_n}(\mathbf{k}_n, \eta) \right] \right. \\ &\left. + (\Omega_{22} - 1) \Gamma_{2,i_1\dots i_n}^n \Psi_{i_1}(\mathbf{k}_1, \eta) \times \dots \times \Psi_{i_n}(\mathbf{k}_n, \eta) \right]. \end{aligned} \quad (131)$$

Linearising Eq. (130) gives the homogeneous, linear second-order ODE

$$\partial_\eta^2 \Psi_1^{(1)} + \Omega_{22} \partial_\eta \Psi_1^{(1)} - \Omega_{21} \Psi_1^{(1)} = 0, \quad (132)$$

whose solutions are the linear growth factors D_+ and D_- if we make the ansatz $\Psi_1^{(1)}(\mathbf{k}, \eta) = \delta(\mathbf{k}, \eta_0) D(\eta, \eta_0)$. A particular solution of an inhomogeneous second-order ODE can be found by the convolution of the inhomogeneity $g(k, a)$ with the Green's function $G_k(s, a)$

$$u(\mathbf{k}, \eta) = \int_{\eta_0}^{\eta} ds g(\mathbf{k}, s) G_k(s, \eta), \quad (133)$$

where the Green's function $G_k(s, a)$ of the ODE is given by a combination of two linearly independent solutions, i.e. D_+ and D_- , of the homogeneous equation

$$G(s, \eta) = \frac{D_-(s)D_+(\eta) - D_-(\eta)D_+(s)}{D_-(s)\partial_s D_+(s) - \partial_s D_-(s)D_+(s)}. \quad (134)$$

The Green's function has the following properties:

$$G_k(\eta, \eta) = 0, \quad \partial_\eta G_k(s, \eta)|_{s=\eta} = 1, \quad \partial_s G_k(s, \eta)|_{s=\eta} = -1. \quad (135)$$

Now comes the *crucial idea of the derivation* of the coupling kernels: If we write down the convolution in Eq. (133) for the inhomogeneity defined in Eq. (131), we obtain an integral equation for Ψ_a . This integral equation can be brought into the form of Eqs. (106) and (107). Finding the coupling kernels F_i and G_i is then simply a matter of comparing integrands. Pursuing this idea, we express the solution Ψ_1 of the full theory as sum of the homogeneous solution $\Psi_1^{(1)}$ and a particular solution

$$\Psi_1(\mathbf{k}, \eta) = \Psi_1^{(1)}(\mathbf{k}, \eta) + \int_{\eta_0}^{\eta} ds g(\mathbf{k}, s) G_k(s, \eta). \quad (136)$$

We now parameterise the inhomogeneous solution in terms of the *vertex couplings* $C_{a,i_1\dots i_n}^{(n)}(\mathbf{k}, \mathbf{k}_1, \dots, \mathbf{k}_n, s, \eta)$ and write

$$\begin{aligned} \Psi_a(\mathbf{k}, \eta) &= \Psi_a^{(1)}(\mathbf{k}, \eta) + \sum_{n=2}^{\infty} \delta_D(\mathbf{k} - \mathbf{k}_{1\dots n}) \\ &\times \int_{\eta_0}^{\eta} ds C_{a,i_1\dots i_n}^{(n)}(\mathbf{k}, \mathbf{k}_1, \dots, \mathbf{k}_n, s, \eta) \Psi_{i_1}(\mathbf{k}_1, s) \times \dots \times \Psi_{i_n}(\mathbf{k}_n, s). \end{aligned} \quad (137)$$

The vertex couplings for Ψ_1 can be immediately derived from Eq. (131) by partial integration of the derivative term $\partial_s [\Gamma_{1,i_1\dots i_n} \Psi_{i_1}(\mathbf{k}_1, s) \times \dots \times \Psi_{i_n}(\mathbf{k}_n, s)]$ using $G_k(\eta, \eta) = 0$:

$$\begin{aligned} C_{1,i_1\dots i_n}^{(n)}(\mathbf{k}, \mathbf{k}_1, \dots, \mathbf{k}_n, s, \eta) &= \\ &- \Gamma_{1,i_1\dots i_n}^n(\mathbf{k}, \mathbf{k}_1, \dots, \mathbf{k}_n, s) \partial_s G_k(s, \eta) \\ &+ [\Omega_{22}(\mathbf{k}, \mathbf{k}_1, \dots, \mathbf{k}_n, s) - 1] \Gamma_{2,i_1\dots i_n}^n(\mathbf{k}, \mathbf{k}_1, \dots, \mathbf{k}_n, s) G_k(s, \eta). \end{aligned} \quad (138)$$

The vertex couplings $C^{(n)}$ owe their name to the diagrammatic representation of Eq. (137) shown in Fig. 7. In the following, we will make use of this diagrammatic language to compute the higher-order coupling kernels. Equation (137) can be used to obtain the perturbative solution iteratively: We substitute $\Psi = \Psi^{(1)} + \mathcal{O}(\delta^2)$ into the RHS of Eq. (137) which gives an equation whose solution is $\Psi = \Psi^{(1)} + \Psi^{(2)} + \mathcal{O}(\delta^3)$. Substituting this expression back into the RHS of Eq. (137) gives an equation whose solution is $\Psi = \Psi^{(1)} + \Psi^{(2)} + \Psi^{(3)} + \mathcal{O}(\delta^4)$ and so on. In the following, we will give expressions for $\Psi_a(\mathbf{k}, \eta)$ up to quartic

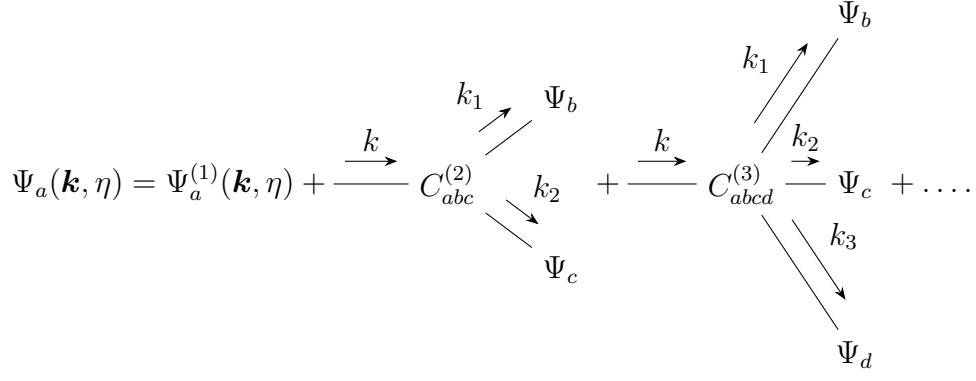


Figure 7: Diagrammatic representation of Eq. (137) in terms of trees. Outgoing momentum arrows express momentum integrations. The Dirac-Delta functions enforce momentum conservation at the vertices and we employ the Einstein sum convention for repeated indices. The depth of the tree, i.e. 1, denotes the number of time integrations.

order in order to compute the kernels F_2 , F_3 and F_4 :

$$\begin{aligned}
\Psi_a^{(2)}(\mathbf{k}, \eta) &= +\delta_D(\mathbf{k} - \mathbf{k}_{12}) \int_{\eta_0}^{\eta} ds C_{abc}^{(2)}(\mathbf{k}, \mathbf{k}_1, \mathbf{k}_2, s, \eta) \\
&\quad \times \Psi_b^{(1)}(\mathbf{k}_1, s) \Psi_c^{(1)}(\mathbf{k}_2, s), \\
\Psi_a^{(3)}(\mathbf{k}, \eta) &= +\delta_D(\mathbf{k} - \mathbf{k}_{12}) \int_{\eta_0}^{\eta} ds C_{abc}^{(2)}(\mathbf{k}, \mathbf{k}_1, \mathbf{k}_2, s, \eta) \\
&\quad \times \left(\Psi_b^{(1)}(\mathbf{k}_1, s) \Psi_c^{(2)}(\mathbf{k}_2, s) \right. \\
&\quad \left. + \Psi_b^{(2)}(\mathbf{k}_1, s) \Psi_c^{(1)}(\mathbf{k}_2, s) \right) \\
&\quad + \delta_D(\mathbf{k} - \mathbf{k}_{123}) \int_{\eta_0}^{\eta} ds C_{abcd}^{(3)}(\mathbf{k}, \mathbf{k}_1, \mathbf{k}_2, \mathbf{k}_3, s, \eta) \\
&\quad \times \Psi_b^{(1)}(\mathbf{k}_1, s) \Psi_c^{(1)}(\mathbf{k}_2, s) \Psi_d^{(1)}(\mathbf{k}_3, s), \\
\Psi_a^{(4)}(\mathbf{k}, \eta) &= +\delta_D(\mathbf{k} - \mathbf{k}_{12}) \int_{\eta_0}^{\eta} ds C_{abc}^{(2)}(\mathbf{k}, \mathbf{k}_1, \mathbf{k}_2, s, \eta) \\
&\quad \times \left(\Psi_b^{(2)}(\mathbf{k}_1, s) \Psi_c^{(2)}(\mathbf{k}_2, s) \right. \\
&\quad \left. + \Psi_b^{(1)}(\mathbf{k}_1, s) \Psi_c^{(3)}(\mathbf{k}_2, s) \right. \\
&\quad \left. + \Psi_b^{(3)}(\mathbf{k}_1, s) \Psi_c^{(1)}(\mathbf{k}_2, s) \right) \\
&\quad + \delta_D(\mathbf{k} - \mathbf{k}_{123}) \int_{\eta_0}^{\eta} ds C_{abcd}^{(3)}(\mathbf{k}, \mathbf{k}_1, \mathbf{k}_2, \mathbf{k}_3, s, \eta) \\
&\quad \times \left(\Psi_b^{(2)}(\mathbf{k}_1, s) \Psi_c^{(1)}(\mathbf{k}_2, s) \Psi_d^{(1)}(\mathbf{k}_3, s) \right. \\
&\quad \left. + \Psi_b^{(1)}(\mathbf{k}_1, s) \Psi_c^{(2)}(\mathbf{k}_2, s) \Psi_d^{(1)}(\mathbf{k}_3, s) \right. \\
&\quad \left. + \Psi_b^{(1)}(\mathbf{k}_1, s) \Psi_c^{(1)}(\mathbf{k}_2, s) \Psi_d^{(2)}(\mathbf{k}_3, s) \right) \\
&\quad + \delta_D(\mathbf{k} - \mathbf{k}_{1234}) \int_{\eta_0}^{\eta} ds C_{abcde}^{(4)}(\mathbf{k}, \mathbf{k}_1, \mathbf{k}_2, \mathbf{k}_3, \mathbf{k}_4, s, \eta) \\
&\quad \times \Psi_b^{(1)}(\mathbf{k}_1, s) \Psi_c^{(1)}(\mathbf{k}_2, s) \Psi_d^{(1)}(\mathbf{k}_3, s) \Psi_e^{(1)}(\mathbf{k}_4, s).
\end{aligned} \tag{139}$$

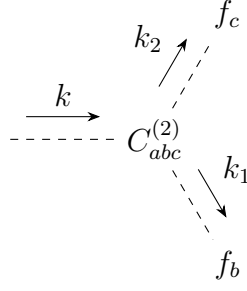


Figure 8: Diagrammatic representation of the coupling kernels F_2 and G_2 . There is one free index a that describes the density coupling kernel $F_2(\mathbf{k}, \mathbf{k}_1, \mathbf{k}_2)$ for $a = 1$ and the velocity coupling kernel $G_2(\mathbf{k}, \mathbf{k}_1, \mathbf{k}_2)$ for $a = 2$. The tree has depth 1 and therefore requires a single time integration.

We express Eq. (139) in terms of the linear density fluctuations only. They are related to the linear velocity divergence fluctuations via

$$\Psi_1^{(1)}(\mathbf{k}, \eta) = D_k(\eta)\Psi_1^{(1)}(\mathbf{k}, \eta_0), \quad \Psi_2^{(1)}(\mathbf{k}, \eta) = -\partial_\eta D_k(\eta)\Psi_1^{(1)}(\mathbf{k}, \eta_0) \quad (140)$$

We therefore define the two-component vector \mathbf{f} that relates the linear density and velocity divergence fluctuations at time s with the linear density fluctuations at time η :

$$\mathbf{f}(k, s, \eta) = \begin{bmatrix} D_k(s) & -\partial_s D_k(s) \\ D_k(\eta) & D_k(\eta) \end{bmatrix}^\top \quad (141)$$

With this definition in place we can rewrite $\Psi_a^{(2)}(\mathbf{k}, \eta)$ as

$$\begin{aligned} \Psi_a^{(2)}(\mathbf{k}, \eta) &= \delta_D(\mathbf{k} - \mathbf{k}_{12})\delta(\mathbf{k}_1, \eta)\delta(\mathbf{k}_2, \eta) \\ &\times \int_{\eta_0}^{\eta} ds C_{abc}^{(2)}(\mathbf{k}, \mathbf{k}_1, \mathbf{k}_2, s, \eta) f_b(k_1, s, \eta) f_c(k_2, s, \eta) \end{aligned} \quad (142)$$

Comparing this expression to the definition of F_n in Eq. (106), we can finally read off the coupling kernels. They can be expressed diagrammatically as shown in Fig. 8 or explicitly written as:

Second-order Time-dependent PT Kernels F_2 and G_2

$$F_2(\mathbf{k}_1, \mathbf{k}_2, \eta) = \int_{\eta_0}^{\eta} ds C_{1bc}^{(2)}(\mathbf{k}_{12}, \mathbf{k}_1, \mathbf{k}_2, s, \eta) f_b(k_1, s, \eta) f_c(k_2, s, \eta), \quad (143)$$

$$G_2(\mathbf{k}_1, \mathbf{k}_2, \eta) = \int_{\eta_0}^{\eta} ds C_{2bc}^{(2)}(\mathbf{k}_{12}, \mathbf{k}_1, \mathbf{k}_2, s, \eta) f_b(k_1, s, \eta) f_c(k_2, s, \eta). \quad (144)$$

Note that all the kernels derived in this section have yet to be symmetrised

w.r.t. exchange of momenta. We now proceed by deriving the kernels at third and fourth order in diagrammatic representation.

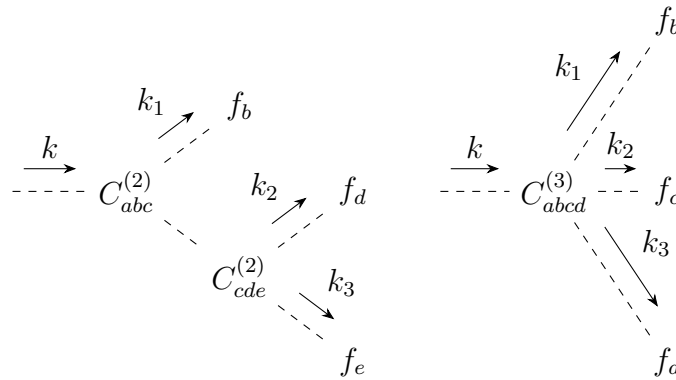


Figure 9: Diagrammatic representation of contributions to PT kernels F_3 and G_3 . The left diagrams describes two contributions with the permutation $b \leftrightarrow c$ and corresponds to the Eq. (145). The depth of the tree is 2. Accordingly it requires two time integrations. The right diagrams corresponds to the expression Eq. (146).

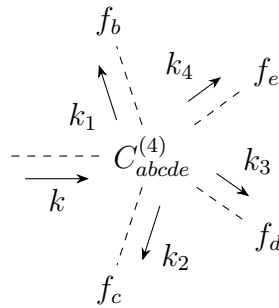


Figure 10: Diagrammatic representation of contributions to PT kernels F_4 and G_4 involving only the fourth-order vertex coupling $C^{(4)}$.

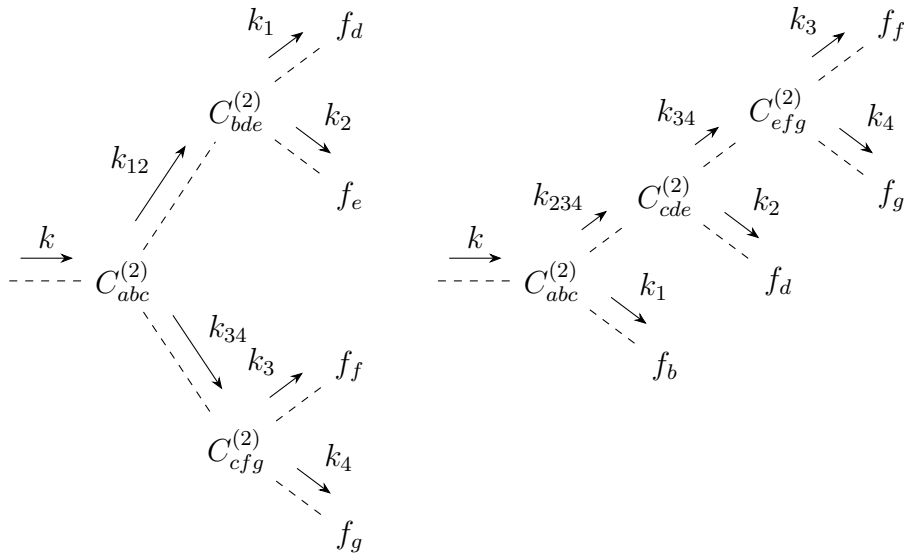


Figure 11: Diagrammatic representation of contributions to PT kernels F_4 and G_4 involving only the second-order vertex coupling $C^{(2)}$. There is one additional permutation $b \leftrightarrow c$ for the left diagram as well as three additional permutations $b \leftrightarrow c$ and $d \leftrightarrow e$ for the diagram on the right.

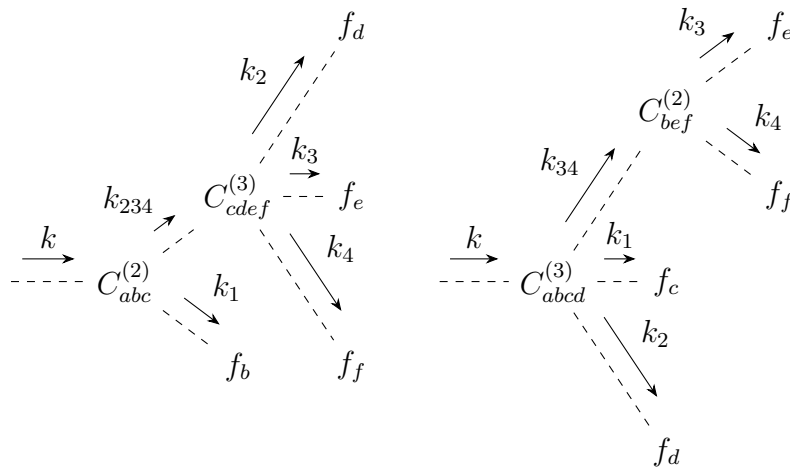


Figure 12: Diagrammatic representation of contributions to PT kernels F_4 and G_4 involving both the second- and third-order vertex couplings $C^{(2)}$ and $C^{(3)}$. There is one additional permutation $b \leftrightarrow c$ for the left diagram and two additional permutations for $b \leftrightarrow c \leftrightarrow d$ for the right diagram.

At third order, the diagrammatic representation of the coupling kernels F_3 and G_3 is given by the two types of diagrams shown in Fig. 9. Explicitly, we find the

Third-order Time-dependent PT Kernels F_3 and G_3

The time-dependent coupling kernels F_3 and G_3 in FDM are given by $F_3^{FDM} = I_1^{(3)} + J_1^{(3)}$ and $G_3^{FDM} = I_2^{(3)} + J_2^{(3)}$ with

$$I_a^{(3)} = \left(\int_{\eta_0}^{\eta} ds C_{abc}^{(2)}(\mathbf{k}, \mathbf{k}_1, \mathbf{k}_{23}, s, \eta) \times f_b(\mathbf{k}_1, s, \eta) \right. \\ \left. \times \int_{\eta_0}^s ds_1 C_{cde}^{(2)}(\mathbf{k}_{23}, \mathbf{k}_2, \mathbf{k}_3, s_1, s) f_d(\mathbf{k}_2, s_1, s) f_e(\mathbf{k}_3, s_1, s) \right) \\ + \left(\int_{\eta_0}^{\eta} ds C_{abc}^{(2)}(\mathbf{k}, \mathbf{k}_1, \mathbf{k}_{23}, s, \eta) \times f_c(\mathbf{k}_1, s, \eta) \right. \\ \left. \times \int_{\eta_0}^s ds_1 C_{bde}^{(2)}(\mathbf{k}_{23}, \mathbf{k}_2, \mathbf{k}_3, s_1, s) f_d(\mathbf{k}_2, s_1, s) f_e(\mathbf{k}_3, s_1, s) \right), \quad (145)$$

$$J_a^{(3)} = \int_{\eta_0}^{\eta} ds C_{abcd}^{(3)}(\mathbf{k}, \mathbf{k}_1, \mathbf{k}_2, \mathbf{k}_3, s, \eta) \\ \times f_b(\mathbf{k}_1, s, \eta) f_c(\mathbf{k}_2, s, \eta) f_d(\mathbf{k}_3, s, \eta). \quad (146)$$

Finally, at fourth order, we find the diagrams shown in figures 10, 11 and 12. This concludes our general discussion of time-dependent perturbation theory using Scoccimarro's method. Before we move on to the FDM case, we briefly review the steps we took to derive the PT kernels:

5 Steps Towards Time-dependent PT

- Step 1: Taylor expand fluid equations w.r.t δ and θ and Fourier transform;
- Step 2: Derive mode coupling matrices Ω_{ab} and $\Gamma_{ai_1, \dots, i_n}$;
- Step 3: Derive Green's function for second-order growth equation;
- Step 4: Use Eq. (138) to compute the vertex couplings $C^{(n)}$;
- Step 5: (Optional) Symmetrise the kernels F_n and G_n w.r.t. exchange of momenta.

3.2.3 FDM for EdS Cosmology

We can now apply the time-dependent perturbation theory framework developed in the last section to the FDM case. As in the CDM case, we start by

reviewing the Madelung equations (26) in terms of the conformal time τ

$$\partial_\tau \delta + \nabla \cdot ((1 + \delta)\mathbf{v}) = 0, \quad (147)$$

$$\partial_\tau \mathbf{v} + \mathcal{H}\mathbf{v} + (\mathbf{v} \cdot \nabla)\mathbf{v} + \nabla\phi = -\frac{\hbar^2}{2m^2 a^2} \nabla \left(\frac{(\Delta \sqrt{1 + \delta})}{\sqrt{1 + \delta}} \right), \quad (148)$$

$$\Delta\phi - \frac{3}{2}\Omega_{m,0}\mathcal{H}^2\delta = 0. \quad (149)$$

In the next step, we Fourier transform the Madelung equations. The Fourier transform of the quantum pressure term is computed by the Taylor expansion up to fourth order using *Mathematica* (Wolfram Research 2021). We obtain the same continuity equation as in the CDM case

$$\partial_\tau \delta(\mathbf{k}) + \theta(\mathbf{k}) = -\delta_D(\mathbf{k} - \mathbf{k}_{12}) \frac{\mathbf{k} \cdot \mathbf{k}_2}{k_2^2} \delta(\mathbf{k}_1) \theta(\mathbf{k}_2), \quad (150)$$

as well as the Euler equation with quantum pressure corrections

$$\begin{aligned} \partial_\tau \theta(\mathbf{k}) + \mathcal{H}\theta(\mathbf{k}) + \frac{3}{2}\Omega_{m,0}\mathcal{H}^2\delta(\mathbf{k}) - \frac{k^4}{4a^2 m^2} \delta(\mathbf{k}) = & \\ -\delta_D(\mathbf{k} - \mathbf{k}_{12}) \left(\frac{1}{2} k^2 \frac{\mathbf{k}_1 \cdot \mathbf{k}_2}{k_1^2 k_2^2} \theta(\mathbf{k}_1) \theta(\mathbf{k}_2) \right) & \\ -\delta_D(\mathbf{k} - \mathbf{k}_{12}) \delta(\mathbf{k}_1) \delta(\mathbf{k}_2) \frac{k^4}{16a^2 m^2} & \\ \times \left(1 + \frac{\sum_i k_i^2}{k^2} \right) & \\ +\delta_D(\mathbf{k} - \mathbf{k}_{123}) \delta(\mathbf{k}_1) \delta(\mathbf{k}_2) \delta(\mathbf{k}_3) \frac{k^4}{32a^2 m^2} & \\ \times \left(1 + \frac{\sum_i k_i^2}{k^2} + \frac{\sum_{i,j,i<j} k_{ij}^2}{3k^2} \right) & \\ -\delta_D(\mathbf{k} - \mathbf{k}_{1234}) \delta(\mathbf{k}_1) \delta(\mathbf{k}_2) \delta(\mathbf{k}_3) \delta(\mathbf{k}_4) \frac{3k^4}{128a^2 m^2} & \\ \times \left(1 + \frac{2\sum_i k_i^2}{3k^2} + \frac{1\sum_{i,j,i<j} k_{ij}^2}{3k^2} \right) & \\ + \mathcal{O}(\delta^5), & \end{aligned} \quad (151)$$

where we omitted the time dependence of all quantities and integrations over momenta with repeated indices are again understood. Comparing equations (150) and (151) to Eq. (128), we can now determine the mode coupling matrices: The

linear mode coupling matrix Ω_{ab} reads

$$\Omega(\mathbf{k}) = \begin{pmatrix} 0 & 1 \\ \frac{6}{\eta^2} - \frac{b(k)^2}{\eta^4} & \frac{2}{\eta} \end{pmatrix}, \quad (152)$$

where we remind the reader that $b(k)$ is defined as

$$b(k) = \frac{2k^2 \hbar}{mH_0 \Omega_m^{\frac{1}{2}}}, \quad (153)$$

and encodes the characteristic scale of the FDM system. Ω_{21} vanishes when k equals the comoving quantum Jeans scale k_J . We compute the non-linear mode coupling matrices Γ_{a,i_1,\dots,i_n} up to $n = 4$: At second order, the matrices Γ_{a,i_1,i_2} include the nonlinear contribution from the convection term as well as the second-order mode coupling from the quantum pressure term:

$$\begin{aligned} \Gamma_{112}(\mathbf{k}, \mathbf{k}_1, \mathbf{k}_2) &= -\alpha(\mathbf{k}, \mathbf{k}_2), \\ \Gamma_{121}(\mathbf{k}, \mathbf{k}_1, \mathbf{k}_2) &= -\alpha(\mathbf{k}, \mathbf{k}_1), \\ \Gamma_{211}(\mathbf{k}, \mathbf{k}_1, \mathbf{k}_2) &= -\frac{b(k)^2}{\eta^4} \frac{1}{4} \left(1 + \frac{\sum_i^2 k_i^2}{k^2} \right), \\ \Gamma_{222}(\mathbf{k}, \mathbf{k}_1, \mathbf{k}_2) &= -\beta(\mathbf{k}, \mathbf{k}_1, \mathbf{k}_2), \end{aligned} \quad (154)$$

where $\alpha(\mathbf{k}, \mathbf{k}_1)$ and $\beta(\mathbf{k}, \mathbf{k}_1, \mathbf{k}_2)$ were defined in Eqs. (116) and (117), and all other components vanish. All higher-order contributions to Γ_{a,i_1,\dots,i_n} stem solely from the quantum pressure term and therefore represent self-interactions of the density field:

$$\Gamma_{2111}(\mathbf{k}, \mathbf{k}_1, \mathbf{k}_2, \mathbf{k}_3) = +\frac{b(k)^2}{\eta^4} \frac{1}{8} \left(1 + \frac{\sum_i^3 k_i^2}{k^2} + \frac{\sum_{i,j,i<j}^3 \mathbf{k}_{ij}^2}{3k^2} \right), \quad (155)$$

$$\Gamma_{21111}(\mathbf{k}, \mathbf{k}_1, \mathbf{k}_2, \mathbf{k}_3, \mathbf{k}_4) = -\frac{b(k)^2}{\eta^4} \frac{3}{32} \left(1 + \frac{2 \sum_i^4 k_i^2}{3 k^2} + \frac{1 \sum_{i,j,i<j}^4 \mathbf{k}_{ij}^2}{3 k^2} \right), \quad (156)$$

and all other contributions at third and fourth order vanish. The linear growth equation in FDM for a general source $g(\mathbf{k}, a)$ reads

$$u''(\mathbf{k}, a) + 2H(a)u'(\mathbf{k}, a) + \left(\frac{\hbar^2 k^4}{2m^2 a^4} - 4\pi G \rho_b(a) \right) u(\mathbf{k}, a) = g(\mathbf{k}, a). \quad (157)$$

Using the analytical growth factors D_+ and D_- in an EdS universe derived in Eq. (93), we find the Green's function

$$G_k(s, \eta) = \frac{\pi s^{3/2}}{2\eta^{1/2}} \times \left[J_{5/2} \left(\frac{b(k)}{s} \right) J_{-5/2} \left(\frac{b(k)}{\eta} \right) - J_{5/2} \left(\frac{b(k)}{\eta} \right) J_{-5/2} \left(\frac{b(k)}{s} \right) \right]. \quad (158)$$

Using equation (138), we find the vertex couplings

$$C_{1bc}^{(2)}(\mathbf{k}, \mathbf{k}_1, \mathbf{k}_2, s, \eta) = -\Gamma_{1bc}(\mathbf{k}, \mathbf{k}_1, \mathbf{k}_2, s) \partial_s G_k(s, \eta) - \left(\Gamma_{2bc}(\mathbf{k}, \mathbf{k}_1, \mathbf{k}_2, s) - \frac{2}{s} \Gamma_{1bc}(\mathbf{k}, \mathbf{k}_1, \mathbf{k}_2, s) \right) G_k(s, \eta). \quad (159)$$

at second order as well as

$$C_{1111}^{(3)}(\mathbf{k}, \mathbf{k}_1, \mathbf{k}_2, \mathbf{k}_3, s, \eta) = -\Gamma_{2111}(\mathbf{k}, \mathbf{k}_1, \mathbf{k}_2, \mathbf{k}_3) G_k(s, \eta), \quad (160)$$

$$C_{11111}^{(4)}(\mathbf{k}, \mathbf{k}_1, \mathbf{k}_2, \mathbf{k}_3, \mathbf{k}_4, s, \eta) = -\Gamma_{21111}(\mathbf{k}, \mathbf{k}_1, \mathbf{k}_2, \mathbf{k}_3, \mathbf{k}_4) G_k(s, \eta), \quad (161)$$

at third and fourth order where all other vertex couplings vanish. This is because above order two in FDM there are only self-interactions of the density field stemming from the Taylor expansion of the quantum pressure term. This simplifies the computation and the symmetrisation of the kernels F_3^{FDM} and F_4^{FDM} significantly. A more detailed discussion can be found in appendix A.2. Since $\gamma_{abc}(\mathbf{k}, \mathbf{k}_1, \mathbf{k}_2, s, \eta)$ is symmetric w.r.t. exchange of \mathbf{k}_1 and \mathbf{k}_2 , $C_{1bc}^{(2)}(\mathbf{k}, \mathbf{k}_1, \mathbf{k}_2, s, \eta)$ inherits this property. As a consequence F_2^{FDM} as given by Eq. (143) is already symmetric under exchange of \mathbf{k}_1 and \mathbf{k}_2 .

Fig. 13 shows a comparison of the symmetrised kernels $F_2^{(s)}$ in FDM and CDM. As expected, the two agree on large large scales. Moreover, the FDM kernel is suppressed and shows oscillations on small scales. At the same time, we also observe that FDM enhances mode coupling for orthogonal configurations even on small scales. This is in agreement with our observation that the next-to-leading order term in the Taylor expansion of the quantum pressure term can potentially enhance gravitational collapse.

3.2.4 CDM for General Cosmology

In this section, we compare the PT kernels obtained with the help of the recursion relations in Eq. (120) with the time-dependent PT for EdS and the *fiducial cosmology*. The time-dependent coupling kernels in CDM for a general cosmology immediately follow from the FDM case in the limit $b(k) \rightarrow 0$. The

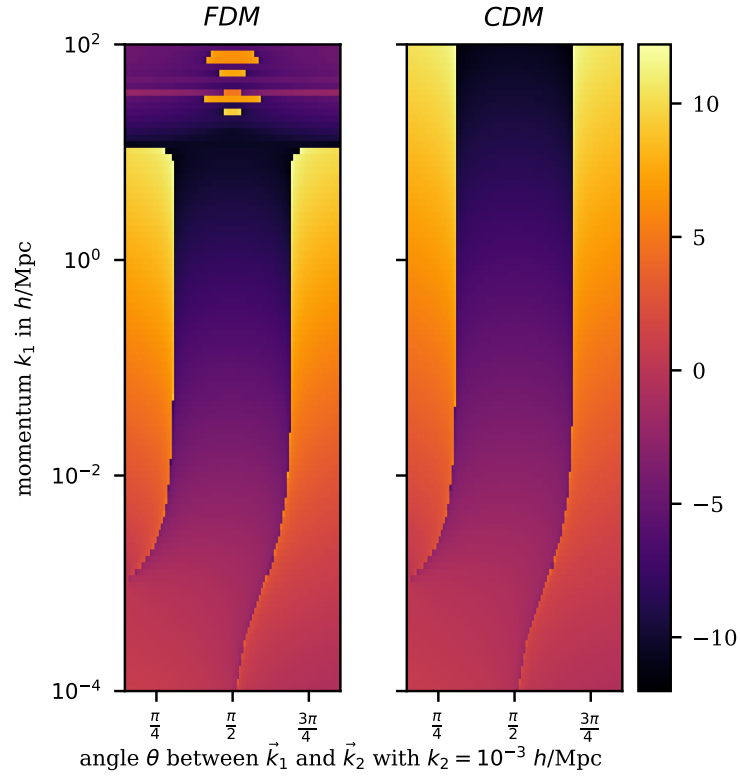


Figure 13: Comparison of symmetrised PT kernels $F_2^{(s)}(\mathbf{k}_1, \mathbf{k}_2)$ in FDM and CDM in EdS. The figure shows the quantity $\text{sgn}(F_2) \log_{10}(|F_2|)$ for different scales and angular configurations. The kernel in FDM was obtained by numerical integration using the analytical Green's function in Eq. (158).

linear mode coupling matrix Ω_{ab} reads

$$\Omega(\mathbf{k}) = \begin{pmatrix} 0 & 1 \\ \frac{6}{\eta^2} & \frac{2}{\eta} \end{pmatrix}. \quad (162)$$

The matrices Γ_{a,i_1,i_2} are given as

$$\begin{aligned} \Gamma_{112}(\mathbf{k}, \mathbf{k}_1, \mathbf{k}_2) &= -\alpha(\mathbf{k}, \mathbf{k}_2), \\ \Gamma_{121}(\mathbf{k}, \mathbf{k}_1, \mathbf{k}_2) &= -\alpha(\mathbf{k}, \mathbf{k}_1), \\ \Gamma_{211}(\mathbf{k}, \mathbf{k}_1, \mathbf{k}_2) &= 0, \\ \Gamma_{222}(\mathbf{k}, \mathbf{k}_1, \mathbf{k}_2) &= -\beta(\mathbf{k}, \mathbf{k}_1, \mathbf{k}_2), \end{aligned} \quad (163)$$

and all higher-order mode-coupling matrices vanish. Consequently, the only non-zero vertex coupling is

$$C_{1bc}^{(2)}(\mathbf{k}, \mathbf{k}_1, \mathbf{k}_2, s, \eta) = -\Gamma_{1bc}(\mathbf{k}, \mathbf{k}_1, \mathbf{k}_2, s) \partial_s G_k(s, \eta) - \left(\Gamma_{2bc}(\mathbf{k}, \mathbf{k}_1, \mathbf{k}_2, s) - \frac{2}{s} \Gamma_{1bc}(\mathbf{k}, \mathbf{k}_1, \mathbf{k}_2, s) \right) G_k(s, \eta). \quad (164)$$

We can compute the Green's function in Eq. (134) using the analytical growth factors in an EdS universe:

$$D_+(\eta) = a(\eta) = \frac{\eta^2}{4}, \quad D_-(\eta) = a^{-\frac{3}{2}}(\eta) = \left(\frac{\eta^2}{4} \right)^{-\frac{3}{2}}, \quad (165)$$

leading to

$$G_k(s, \eta) = \frac{1}{5} \left(\frac{\eta^2}{s} - \frac{s^4}{\eta^3} \right). \quad (166)$$

Alternatively, we can numerically find two linearly independent solutions to the CDM growth equation (73). The advantage of the EdS case is that we can analytically integrate the time-dependent expressions PT kernels.¹² Integration of Eq. (143) gives for example:

$$F_{2,td}^{(s)}(\mathbf{k}_1, \mathbf{k}_2) = \frac{25a^{\frac{7}{2}} - 21a^{\frac{5}{2}}a_0 - 4(a_0)^{\frac{7}{2}}}{70a^{\frac{7}{2}}} (2 + \alpha(\mathbf{k}_1, \mathbf{k}_2) + \alpha(\mathbf{k}_2, \mathbf{k}_1)) + \frac{4(5a^{\frac{7}{2}} - 7a^{\frac{5}{2}}a_0 + 2(a_0)^{\frac{7}{2}})}{70a^{\frac{7}{2}}} \beta(\mathbf{k}_1, \mathbf{k}_2). \quad (167)$$

This expression differs from the kernel $F_2^{(s)}$ in Eq. (123) derived using the recursion relations according to Goroff's method:

$$F_2^{(s)}(\mathbf{k}_1, \mathbf{k}_2) = \frac{5}{7} + \frac{5}{14} (\alpha(\mathbf{k}_1, \mathbf{k}_2) + \alpha(\mathbf{k}_2, \mathbf{k}_1)) + \frac{2}{7} \beta(\mathbf{k}_1, \mathbf{k}_2). \quad (168)$$

In fact the two only agree in the limit $a_0 \rightarrow 0$. The mismatch between the two kernels at $a = 1$ is shown in Fig. 14. Fig. 14 also indicates that we should use the CDM PT kernels obtained using time-dependent PT for comparison with the FDM kernels since they do not exhibit any mismatch (besides numerical errors) on large scales. Computing the CDM kernel numerically for the **fiducial cosmology** reveals a much more significant discrepancy. As Fig. 15 shows, the time-dependent PT kernels in an EdS and the fiducial cosmology disagree by more than 30%. This could be because the time-dependent PT kernels carry

¹²A Mathematica notebook performing these computations is available on <https://github.com/KunkelAlexander/fdm-eulerpt>.

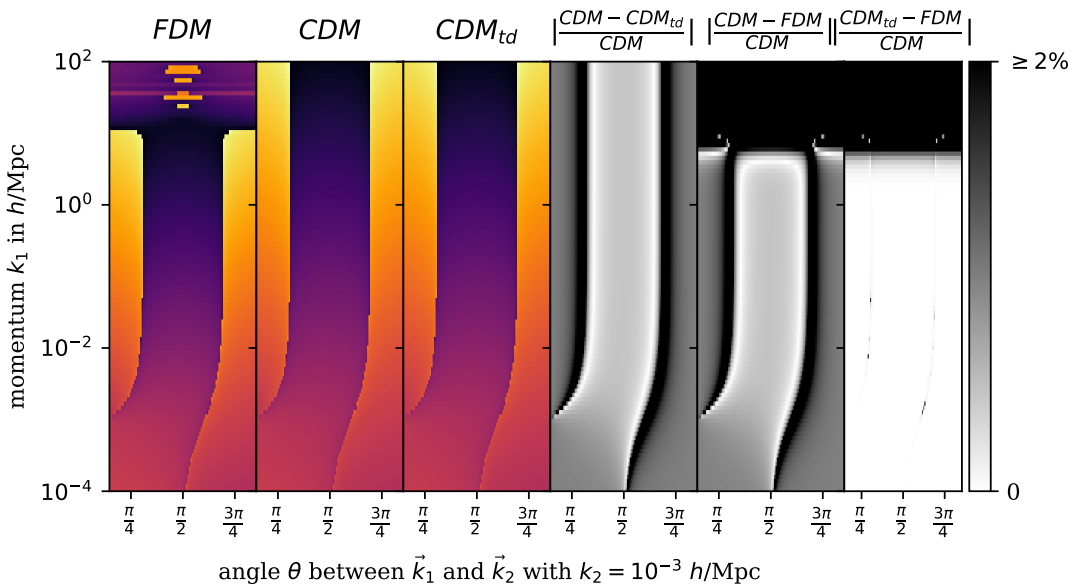


Figure 14: Comparison of symmetrised PT kernels $F_2^{(s)}(\mathbf{k}_1, \mathbf{k}_2)$ obtained via recursion relations and time-dependent PT for EdS. The three plots on the left show the FDM kernel from Eq. (143), the CDM kernel obtained using the recursion relations in Eq. (168) and the CDM kernel obtained using time-dependent PT (CDM_{td}) in Eq. (167). The three plots on the right indicate the relative mismatch between the different kernels. The time-dependent kernels were integrated from $a_0 = 0.01$ to $a = 1$.

more cosmology dependence than the time-independent kernels.

3.2.5 FDM for General Cosmology

One could in theory compute the time-dependent PT kernels in FDM for a general cosmology by numerically integrating two independent solutions to the linear growth equation (89). In practice, we were not able to do so. The reason is that the solutions to Eq. (89) are oscillating below the Jeans scale, that is, for large momenta. Whereas in the CDM case, the two independent solutions D_+ and D_- are distinguished by their growing and decaying behaviour, we could not find a similar criterion for distinguishing the FDM solutions in the oscillating regime. In CDM, we obtain the two independent solutions by integrating numerically from a_0 to a for the growing mode and from a to a_0 for the decaying mode. In this way, the numerical solution is insensitive to initial conditions. This is because when integrating forward in time, i.e. from a_0 to a , any decaying component present in the initial condition quickly decays away. Likewise, when integrating backward in time, any growing component in the initial conditions quickly decays away. The naive approach of integrating forward in time and to use linearly independent initial conditions, for instance $D(a = a_0) = 0, D'(a = a_0) = 1$ for one solution and $D(a = a_0) = 1, D'(a = a_0) = 0$ for the other solution, does not

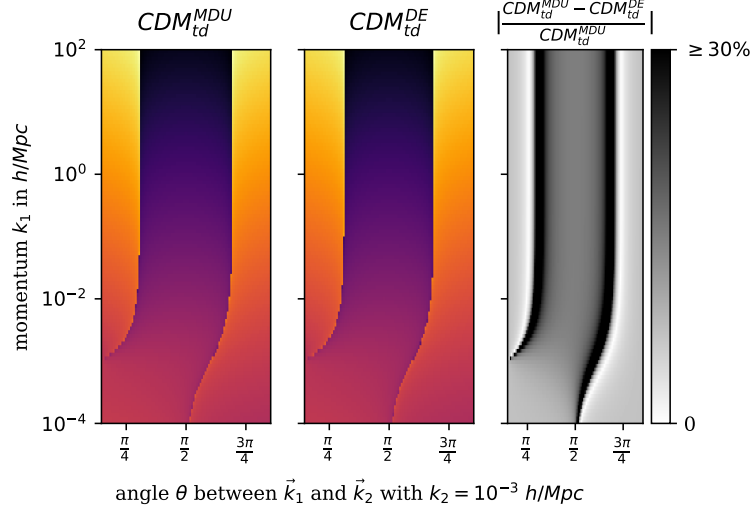


Figure 15: Comparison between time-dependent symmetrised PT kernels $F_2^{(s)}(\mathbf{k}_1, \mathbf{k}_2)$ in EdS and the fiducial cosmology. The relative mismatch plot on the right indicates a mismatch of $\sim 20\%$ across the entire range of scales and angles.

work. This is because integration errors in the form of a growing mode quickly dominate the numerical solution. In FDM, the oscillating regime for $a < a_{osc}$ complicates the numerical integration. In order to capture the CDM growing and decaying mode correctly, one needs to integrate one mode forward and the other mode backward in time. However, if $a_0 < a_{osc}$ the forward integration starts in the oscillating regime where the solution is sensitive to initial conditions. In order to obtain orthogonal solutions in the oscillating regime, we would need to prescribe orthogonal initial conditions at a single time a_0 . Yet, in doing so one does not recover the correct decaying mode if the solution starts growing/decaying somewhere in the integration interval, that is for $a_{osc} \in [a_0, a]$. A more detailed analysis of linear growth in FDM can be found in appendix A.3.

4

A Weak Lensing View on FDM

In this section, we give a *weak lensing view* on FDM. Weak lensing surveys such as *Euclid* measure the galaxy shear power spectrum and allow to infer the shape of the matter power spectrum P_δ thereby giving constraints on cosmological parameters such as the axion mass. They can increase sensitivity significantly compared to galaxy redshift surveys alone. This has the following reason: If one measures the galaxy power spectrum $P_{gal}(k, z) = b^2 P(k, z)$, the survey is biased by the galaxy bias b . The galaxy bias is measured by the galaxy redshift survey itself by letting b be a free parameter. By varying it, one can compensate in a scale-independent manner for suppression of power. Since the preferred values of b and therefore the normalisation of the power spectrum are different for axion cosmologies than for Λ CDM, the constraining power of galaxy surveys is reduced. In contrast, gravitational lensing provides an *unbiased tracer* of dark matter and therefore enables the derivation of stronger constraints on the mass parameter in FDM. In previous weak lensing studies on FDM, Marsh et al. (2011) analysed whether adding a small fraction of axions of mass in the range $m = 10^{-29}$ eV would be detectable via the convergence power spectrum. For modelling nonlinearities, they neglected the quantum pressure entirely and used the CDM halofit model inside CAMB. More recently, Dentler et al. (2021) combine CMB Planck data with shear correlation data from the Dark Energy Survey year 1 to find a 95% C.L. lower limit $m > 10^{-23}$ eV. They model the nonlinear FDM spectra using the adapted halo model HMCODE.

In contrast, we will compute the power spectrum, bispectrum and trispectrum using time-dependent nonlinear Eulerian perturbation in FDM and CDM to derive the corresponding lensing spectra for a *Euclid-like* lensing survey. We estimate the attainable signal-to-noise ratios as well as the χ^2 -functional for distinguishing axions of the masses $m = 10^{-21}$ eV, $m = 10^{-22}$ eV and $m = 10^{-23}$

eV from standard CDM. Unlike the above studies, we do not give constraints on the mass parameter but estimate whether future weak lensing surveys have the constraining power to distinguish FDM from CDM for the currently debated FDM models.

We start by giving an introduction to the statistical description of cosmic random fields and review the basics of weak lensing. Afterwards, we go on to describe our choice of parameters and initial conditions, especially in terms of the considered axion masses, before discussing the lensing results.

4.1 Statistics of Cosmic Fields

This section introduces the statistical basics required to understand the time evolution of cosmic fields. In particular, we draw on the review paper by Bernardeau et al. (2001, p.40 ff) to introduce the notion of *n-point correlation function* and its counterpart in Fourier-space.

In the following, we will assume that the cosmic density field is *statistically homogeneous*, that is, its moments are translation invariant. Moreover, we assume it to be *statistically isotropic*, that is, the joint multi point probability distribution functions $p(\delta_1, \delta_2, \dots)$ are invariant under spatial rotations. These two properties reflect the cosmological principle. The *two-point correlation function* is defined as the joint ensemble average of the density at two different locations

$$\xi(r) = \langle \delta(\mathbf{x})\delta(\mathbf{x} + \mathbf{r}) \rangle, \quad (169)$$

which depends only on the norm of \mathbf{r} due to statistical isotropy. Fourier transforming the two point-correlation function, we find

$$\langle \delta(\mathbf{k}_1)\delta(\mathbf{k}_2) \rangle = \delta_D(\mathbf{k}_1 + \mathbf{k}_2) \int \frac{d^3\mathbf{r}}{(2\pi)^3} \xi(r) e^{i\mathbf{k}\cdot\mathbf{r}} \quad (170)$$

$$\equiv \delta_D(\mathbf{k}_1 + \mathbf{k}_2) P(k_1, t), \quad (171)$$

where we defined the density *power spectrum* $P(k_1)$. Because of the cosmological principle it only depends on the modulus of \mathbf{k}_1 . Higher-order correlation functions are defined as the connected part (denoted with subscript *c*) of the joint ensemble average of the density in an arbitrary number of locations. The notion of *connected* parts is best explained by introducing a diagrammatic representation of the moments of a statistical distribution. Figure 16 depicts the third-order moment of the cosmic density field. It shows how higher-order moments can be decomposed into sums of products of connected parts. Higher-order spectra can

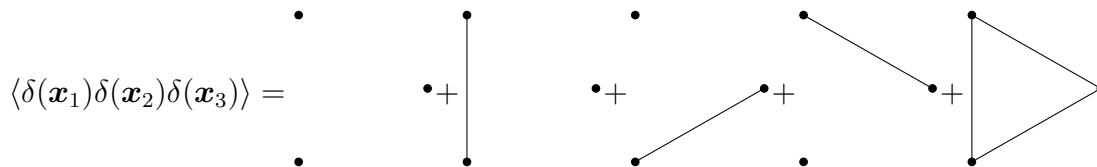


Figure 16: Diagrammatic representation of the third-order moment of the cosmic density field δ . The rightmost diagram represents the connected three-point correlation function.

be defined as higher-order correlation functions in Fourier space

$$\langle \delta(\mathbf{k}_1), \mathbf{k}_2, \dots, \delta(\mathbf{k}_n) \rangle_c =: \delta_D(\mathbf{k}_1 + \mathbf{k}_2 + \dots + \mathbf{k}_n) P_n(\mathbf{k}_1, \mathbf{k}_2, \dots, \mathbf{k}_n), \quad (172)$$

where P_n is the n^{th} -order spectrum and the sum of momenta is always zero because of homogeneity of space. In the following, we will be interested in the cases $n = 3$ and $n = 4$. The matter three-point correlation function in Fourier space is called the matter bispectrum $B(\mathbf{k}_1, \mathbf{k}_2, \mathbf{k}_3)$. The bispectrum depends on the length of two wave vectors as well as the angle enclosed by them. The matter four-point correlation function in Fourier space is called the matter trispectrum $T(\mathbf{k}_1, \mathbf{k}_2, \mathbf{k}_3, \mathbf{k}_4)$ and depends on the length of three wave vectors as well as the two angles enclosed by them. Most inflationary models predict the primordial density perturbation to be a Gaussian random field. This means that all possible joint multi point probability distribution functions are given by multivariate Gaussian distributions. Gaussian random fields are completely determined by the two-point correlation function. As long as the primordial density perturbations evolve according to linear evolution equations, they stay Gaussian. *Wick's theorem* now states that all their statistical properties are already encapsulated in the power spectrum:

$$\langle \delta(k_1) \dots \delta(k_{2p+1}) \rangle = 0, \quad (173)$$

$$\langle \delta(k_1) \dots \delta(k_{2p}) \rangle = \sum_{\text{all pair associations p}} \prod_{\text{pairs}(i,j)} \langle \delta(k_i) \delta(k_j) \rangle. \quad (174)$$

With the help of Wick's theorem, any ensemble average of product of variables can be recast as products of ensemble averages of pairs. In other words, higher-order correlations functions of Gaussian random fields either vanish or can be expressed as products of two-point correlation functions. Thus, we can follow the time evolution of the power spectrum in order to study the cosmic density field in the linear regime. However, the dynamics of gravitational instability is nonlinear and therefore nonlinear evolution inevitably leads to the develop-

ment of non-Gaussian features. Accordingly, we need to understand the evolution of higher-order moments. Fortunately, Eulerian PT gives us a way to describe how non-Gaussian features arise for gravitational clustering from Gaussian initial conditions. This is because the nonlinearities in the equations of motion are quadratic in CDM. Therefore, gravitational instability generates connected higher-order correlation functions that scale as $\xi_n \propto \xi_2^{n-1}$ at large scales, where $|\xi_2| \ll 1$. As a consequence, PT applies (Fry 1984). The quantum pressure term in FDM does not alter this conclusion since it only acts on small scales.

4.1.1 Power Spectrum

We start by considering the evolution of the evolution of the power spectrum and expand it as a perturbation series

$$P(k, a) = P^{(0)}(k, a) + P^{(1)}(k, a) + \dots \quad (175)$$

In linear PT, the time evolution of linear density fluctuations can be approximated by $\delta(\mathbf{x}, a) = D_+(a)\delta(\mathbf{x})$. The time evolution of the linear power spectrum $P^{(0)}$ can therefore be expressed as linear scaling of the initial power spectrum:

$$P^{(0)}(k, a) = \frac{D_+(a)^2}{D_+(a_0)^2} P^{(0)}(k, a_0). \quad (176)$$

For the nonlinear discussion, we need to consider two-point correlations of higher-order perturbations. The basic idea of computing higher-order corrections to the connected n -point correlation functions is as follows: We make use of the PT kernels F_n defined in Eq. (106) to express the n -point correlations of non-Gaussian perturbations as integrals over higher-order correlations of Gaussian perturbations. We then apply Wick's theorem to express higher-order correlations of Gaussian perturbations as two-point correlations of Gaussian perturbations. The latter are completely specified by the initial conditions. This process allows for a diagrammatic representation that we will make use of in the following. Figure 17 shows the diagrammatic representation of the power spectrum at tree-level. A diagram with n vertices represents an n -point correlation function. Every

$$\langle \delta(1)\delta(2) \rangle_c^{(0)} = \bullet \xrightarrow{k} \bullet$$

Figure 17: Tree diagram for the power spectrum.

line with momentum label k corresponds to a linear power spectrum $P^{(0)}(k)$. The PT kernels $F_n(\mathbf{k}_1, \dots, \mathbf{k}_n)$ represent the vertex couplings. We distinguish between

tree and *loop* diagrams. Tree diagrams are trees in a topological sense which does not imply that they correspond to first-order PT. Loop diagrams involve at least one vertex connected to itself through a closed path. Loops in diagrams correspond to momentum integrals. The first higher-order contribution $P^{(1)}$ to the power spectrum comes at loop-level. The two loop-level contributions to the 1-loop matter power spectrum $P^{(1)}$ are often written as

$$P^{(1)}(k, a) = P_{22}(k, a) + P_{13}(k, a), \quad (177)$$

where P_{22} corresponds to the left diagram and P_{13} to the right diagram in Figure 18. The two contributions are explicitly given by:

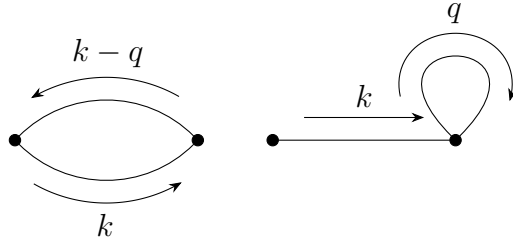


Figure 18: Loop diagrams for the two-point function or power spectrum. The diagram on the left admits one additional permutation. The diagram on the right admits five additional permutations because of the symmetry of $F_3^{(s)}$.

$$P_{22}(k, a) = 2 \int d^3 q [F_2^{(s)}(\mathbf{k} - \mathbf{q}, \mathbf{q})]^2 P^{(0)}(|\mathbf{k} - \mathbf{q}|, a) P^{(0)}(q, a), \quad (178)$$

$$P_{13}(k, a) = 6 \int d^3 q F_3^{(s)}(\mathbf{k}, \mathbf{q}, -\mathbf{q}) P^{(0)}(k, a) P^{(0)}(q, a). \quad (179)$$

The other contribution P_{12} to $P^{(1)}$ vanishes because of Wick's theorem:

$$\begin{aligned} \langle \delta^{(1)}(\mathbf{k}_1), \delta^{(2)}(\mathbf{k}_2) \rangle &= \delta_D(\mathbf{k}_1 + \mathbf{q}_1 + \mathbf{q}_2) \\ &\quad \times F_2(\mathbf{q}_1, \mathbf{q}_2) \langle \delta^{(1)}(\mathbf{q}_1), \delta^{(1)}(\mathbf{q}_2), \delta^{(1)}(\mathbf{k}_2) \rangle \\ &= 0. \end{aligned} \quad (180)$$

4.1.2 Bispectrum

Next, we study the perturbative expansion of the bispectrum

$$B(\mathbf{k}_1, \mathbf{k}_2, \mathbf{k}_3, a) = B^{(0)}(\mathbf{k}_1, \mathbf{k}_2, \mathbf{k}_3, a) + B^{(1)}(\mathbf{k}_1, \mathbf{k}_2, \mathbf{k}_3, a) + \dots, \quad (181)$$

where $B^{(0)}$ is the tree-level part as shown in Figure 19. The diagrams for the bispectrum involve vertices connecting two lines, in other words the PT kernel F_2 . That is why they correspond to second-order PT. $B^{(1)}$ is the corresponding

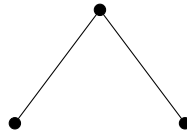
$$\langle \delta^{(2)}(\mathbf{k}_1) \delta^{(1)}(\mathbf{k}_1) \delta^{(1)}(\mathbf{k}_3) \rangle_c =$$


Figure 19: Tree diagram for the bispectrum admitting two additional permutations $\mathbf{k}_1 \leftrightarrow \mathbf{k}_3$ and $\mathbf{k}_2 \leftrightarrow \mathbf{k}_3$.

one-loop correction given by fourth-order perturbation theory. Wick's theorem implies that odd-order correlations functions vanish for Gaussian correlations. Since we assume inflation to only generate Gaussian correlations for the density field, the bispectrum vanishes if we only consider linear-order density fluctuations. The tree diagram for the bispectrum encodes the expression

$$\begin{aligned} \langle \delta^{(2)}(\mathbf{k}_1) \delta^{(1)}(\mathbf{k}_1) \delta^{(1)}(\mathbf{k}_3) \rangle_c \\ = 2F_2^{(s)}(\mathbf{k}_1, \mathbf{k}_1 - \mathbf{k}_2) P_L(\mathbf{k}_1) P_L(\mathbf{k}_2) + 2 \text{ permutations.} \end{aligned} \quad (182)$$

The one-loop contribution to the bispectrum consists of four distinct diagram involving up to fourth-order PT kernels:

$$B^{(1)} = B_{222} + B_{321}^I + B_{321}^{II} + B_{411}, \quad (183)$$

depicted in Figure 20 (from left to right). The explicit expressions are given by:

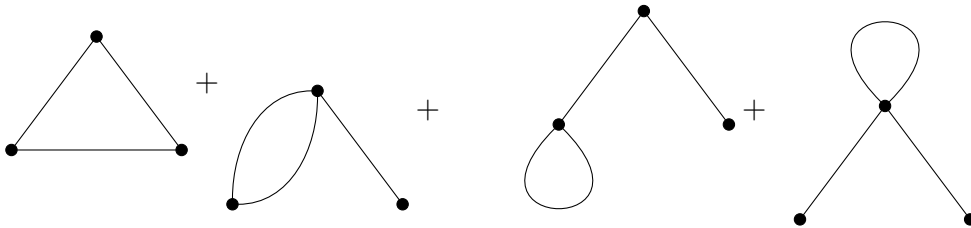


Figure 20: Loop-level corrections for the three-point function or bispectrum.

$$\begin{aligned}
B_{222} &= 8 \int d^3 \mathbf{q} P_L(q, a) P_L(|\mathbf{q} + \mathbf{k}_1|, a) P_L(|\mathbf{q} - \mathbf{k}_2|, a) \\
&\quad \times F_2^{(s)}(-\mathbf{q}, -\mathbf{q} + \mathbf{k}_1) F_2^{(s)}(-\mathbf{q} - \mathbf{k}_1, -\mathbf{q} + \mathbf{k}_2) F_2^{(s)}(\mathbf{k}_2 - \mathbf{q}, \mathbf{q}), \\
B_{321}^I &= 6 \int d^3 \mathbf{q} P_L(k_3, a) P_L(q, a) P_L(|\mathbf{q} - \mathbf{k}_2|, a) \\
&\quad \times F_2^{(s)}(\mathbf{q}, \mathbf{k}_2 - \mathbf{q}) F_3^{(s)}(-\mathbf{q}, \mathbf{q} - \mathbf{k}_2, -\mathbf{k}_2) \\
&\quad + 5 \text{ permutations,} \\
B_{321}^{II} &= 6 \int d^3 \mathbf{q} P_L(k_2, a) P_L(k_3, a) P_L(q, a) \\
&\quad \times F_2^{(s)}(\mathbf{k}_2, \mathbf{k}_3) F_3^{(s)}(\mathbf{k}_3, \mathbf{q}, -\mathbf{q}) \\
&\quad + 5 \text{ permutations,} \\
B_{411} &= 12 \int d^3 \mathbf{q} P_L(k_2, a) P_L(k_3, a) P_L(q, a) \\
&\quad \times F_4^{(s)}(\mathbf{q}, -\mathbf{q}, -\mathbf{k}_2, -\mathbf{k}_3) \\
&\quad + 2 \text{ cyclic permutations.}
\end{aligned} \tag{184}$$

It is useful to define the *reduced bispectrum* as

$$Q(\mathbf{k}_1, \mathbf{k}_2, \mathbf{k}_3) = \frac{B(\mathbf{k}_1, \mathbf{k}_2, \mathbf{k}_3)}{P(k_1)P(k_2) + P(k_2)P(k_3) + P(k_3)P(k_1)}. \tag{185}$$

The loop expansion of the numerator and denominator yields

$$Q(\mathbf{k}_1, \mathbf{k}_2, \mathbf{k}_3) = \frac{B^{(0)}(\mathbf{k}_1, \mathbf{k}_2, \mathbf{k}_3) + B^{(1)}(\mathbf{k}_1, \mathbf{k}_2, \mathbf{k}_3) + \dots}{\Sigma^{(0)}(\mathbf{k}_1, \mathbf{k}_2, \mathbf{k}_3)\Sigma^{(1)}(\mathbf{k}_1, \mathbf{k}_2, \mathbf{k}_3) + \dots}, \tag{186}$$

where

$$\begin{aligned}
\Sigma^{(0)}(\mathbf{k}_1, \mathbf{k}_2, \mathbf{k}_3) &= P^{(0)}(k_1)P^{(0)}(k_2) + P^{(0)}(k_2)P^{(0)}(k_3) + P^{(0)}(k_3)P^{(0)}(k_1), \\
\Sigma^{(1)}(\mathbf{k}_1, \mathbf{k}_2, \mathbf{k}_3) &= P^{(0)}(k_1)P^{(1)}(k_2) + P^{(0)}(k_2)P^{(1)}(k_3) + P^{(0)}(k_3)P^{(1)}(k_1) \\
&\quad + P^{(1)}(k_1)P^{(0)}(k_2) + P^{(1)}(k_2)P^{(0)}(k_3) + P^{(1)}(k_3)P^{(0)}(k_1).
\end{aligned} \tag{187}$$

Expanding Q perturbatively as $Q = Q^{(0)} + Q^{(1)} + \dots$ gives

$$Q^{(0)}(\mathbf{k}_1, \mathbf{k}_2, \mathbf{k}_3) = \frac{B^{(0)}}{\Sigma^{(0)}}, \tag{188}$$

$$Q^{(1)}(\mathbf{k}_1, \mathbf{k}_2, \mathbf{k}_3) = \frac{B^{(1)}}{\Sigma^{(0)}} - \frac{Q^{(0)}\Sigma^{(1)}}{\Sigma^{(0)}}. \tag{189}$$

The reduced bispectrum $Q^{(0)}$ at tree-level is independent of time and normalisation. For scale-free initial conditions $P^{(0)}$, i.e. $P^{(0)} \propto k^n$ with the spectral index n , $Q^{(0)}$ is also independent of overall scale and for equilateral configurations it is also independent of the spectral index. At loop-level, $Q^{(1)}$ depends on the

normalisation of the linear spectrum and its amplitude increases with time.

4.1.3 Trispectrum

Finally, the diagrams for the trispectrum involve vertices connecting two and three lines and therefore correspond to second- and third-order PT. One can decompose the tree-level trispectrum into the contributions

$$T^{(0)}(\mathbf{k}_1, \mathbf{k}_2, \mathbf{k}_3, \mathbf{k}_4, a) = T_{1221}(\mathbf{k}_1, \mathbf{k}_2, \mathbf{k}_3, \mathbf{k}_4, a) + T_{3111}(\mathbf{k}_1, \mathbf{k}_2, \mathbf{k}_3, \mathbf{k}_4, a), \quad (190)$$

depicted in Figure 21 (from left to right).

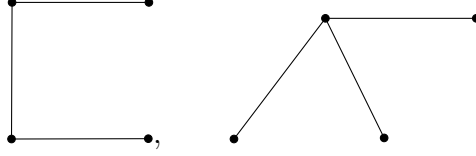


Figure 21: Tree diagrams for trispectrum.

The explicit expression for the contributions to the tree-level trispectrum in terms of the tree-level spectra are given by:

$$\begin{aligned} T_{1221}(\mathbf{k}_1, \mathbf{k}_2, \mathbf{k}_3, \mathbf{k}_4) = & 4P^{(0)}(k_3)P^{(0)}(k_4) \\ & \left(F_2^{(s)}(\mathbf{k}_{13}, -\mathbf{k}_3)F_2^{(s)}(\mathbf{k}_{24}, -\mathbf{k}_4)P^{(0)}(k_{13}) \right. \\ & \left. + F_2^{(s)}(\mathbf{k}_{14}, -\mathbf{k}_4)F_2^{(s)}(\mathbf{k}_{23}, -\mathbf{k}_3)P^{(0)}(k_{14}) \right), \end{aligned} \quad (191)$$

$$T_{3111}(\mathbf{k}_1, \mathbf{k}_2, \mathbf{k}_3, \mathbf{k}_4) = 6P^{(0)}(k_1)P^{(0)}(k_2)P^{(0)}(k_3)F_3^{(s)}(\mathbf{k}_1, \mathbf{k}_2, \mathbf{k}_3). \quad (192)$$

4.2 Weak Lensing

This section introduces the foundations of weak lensing and heavily draws on (Bartelmann and Schneider 1999) and (Bartelmann and Maturi 2016). We start with the geodesic deviation equation that describes the propagation of a light bundle in a general space time

$$\frac{d^2\xi}{d\lambda^2} = \mathcal{T}\xi, \quad (193)$$

where \mathcal{T} is the optical tidal matrix, λ parameterises the curve and ξ is the transverse separation of neighbouring geodesics. In a perturbed spatially flat FLRW background, the local deflection \mathbf{D} is given by:

$$\frac{d^2\mathbf{D}}{d\chi^2} = -\frac{2}{c^2}\delta_{grad}(\nabla_{\perp}\phi(\mathbf{D}(\boldsymbol{\theta}, \chi), \chi)), \quad (194)$$

where δ_{grad} is the difference in the gradients perpendicular to the line of sight ∇_{\perp} , ϕ is the Newtonian gravitational potential and $\boldsymbol{\theta}$ the observed position. The factor of two comes from the fact that the perturbed FLRW metric has equal perturbations in both its temporal and spatial components. The local deflection equation is solved by the Green's function

$$G(\chi, \chi') = \begin{cases} \chi - \chi' & \text{if } \chi > \chi' \\ 0 & \text{else} \end{cases}. \quad (195)$$

One can now integrate the gravitational potential along the line of sight to find the deflection \boldsymbol{D} . However, the integral over the actual light path is quite complicated. The calculation can be significantly simplified with the *Born approximation*. Since typical deflection angles for weak lensing are on the order of arc seconds or smaller, the integration path can be approximated by a straight line. We further assume that corrections can be calculated relative to the fiducial ray. The comoving separation of two light rays propagating through the unperturbed background is then given by $D = \chi\theta$ and we can express the reduced deflection angle as gradient of the *lensing potential* of an extended lens acting on a source at distance χ_S :

$$\boldsymbol{\alpha} = \nabla_{\perp}\psi, \quad \psi(\boldsymbol{\theta}) = \frac{2}{c^2} \int_0^{\chi_S} d\chi \frac{\chi_S - \chi}{\chi_S \chi} \phi(\chi\boldsymbol{\theta}, \chi), \quad (196)$$

where the potential is evaluated at the position $\chi\boldsymbol{\theta}$ perpendicular to and χ parallel to the line of sight. The lensing potential is of fundamental importance in weak lensing and encodes all properties of the gravitational lens. Angles are given as two component-vectors because they are characterised by both a magnitude and a direction. For the further analysis, we want to describe quantities as functions on the sky, i.e. the angular position $\boldsymbol{\theta}$ on the celestial sphere. Consequently, gradients need to be taken w.r.t. angles rather than perpendicular distances and the perpendicular gradient ∇_{\perp} from Eq. (196) is replaced by a gradient w.r.t. $\boldsymbol{\theta}$ $\nabla_{\boldsymbol{\theta}}$. On small angular scales, we can Taylor expand the trigonometric function and write

$$\nabla_{\perp} = \chi^{-1} \nabla_{\boldsymbol{\theta}}. \quad (197)$$

All gradients in the following are to be understood as w.r.t. $\boldsymbol{\theta}$ and we introduce the common short-hand notation

$$\psi_{ij} \equiv \frac{\partial^2 \psi}{\partial \theta_i \partial \theta_j}. \quad (198)$$

The lensing potential can be characterised by the *convergence* κ and the *shear* γ

$$\kappa = \frac{1}{2}\Delta\psi, \quad \gamma_1 = \frac{1}{2}(\psi_{11} - \psi_{22}), \quad \gamma_2 = \psi_{12}. \quad (199)$$

Intuitively, the convergence and the shear describes how gravitational lenses respectively magnify and distort source images. Using the Poisson equation on the expression for the convergence, we find

$$\kappa(\theta, \chi) = \frac{3}{2} \frac{H_0^2}{c^2} \Omega_{m,0} \int_0^\chi d\chi' \frac{(\chi_S - \chi)\chi'}{\chi_S} \frac{\delta(\chi')}{a}. \quad (200)$$

Equation (200) shows that the convergence is directly proportional to a line-of-sight integration over the density contrast. The weight function in the integral W is also called *weak lensing efficiency* and can be modelled as

$$W_\kappa(\chi) = \frac{2\Omega_m}{2a} \frac{1}{\chi_H^2} G(\chi)\chi, \quad (201)$$

with the weighted distance distribution $G(\chi)$ of the lensed galaxies,

$$G(\chi) = \int_\chi^{\chi_H} d\chi' q(z) \frac{dz}{d\chi'} \frac{\chi' - \chi}{\chi'}, \quad (202)$$

where $q(z)$ is the galaxy-redshift distribution measured in a weak lensing survey. Schematically, the relationship between the density contrast and the effective convergence is represented in Figure 22. Measuring correlation functions of the

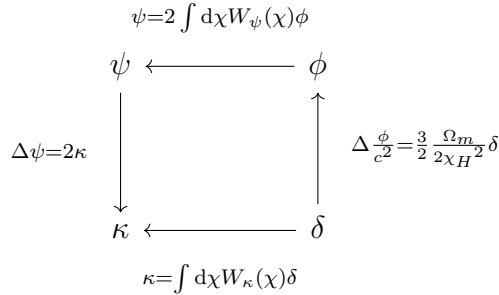


Figure 22: Relationship between density contrast, gravitational potential, lensing potential and effective convergence.

convergence will give us a way to infer correlation functions of the density contrast. The angular correlation function for a quantity $x(\boldsymbol{\theta})$ measured on the sky is given by

$$\xi_x(\boldsymbol{\varphi}) \equiv \langle x(\boldsymbol{\theta}) x(\boldsymbol{\theta} + \boldsymbol{\varphi}) \rangle. \quad (203)$$

This average is one over all positions $\boldsymbol{\theta}$ with an average over all orientations of the separation vector $\boldsymbol{\varphi}$ on the sky and therefore rather complicated. We take the Fourier transform to obtain the angular power spectrum

$$C(\boldsymbol{\ell}) = \int d^2\varphi \xi(\boldsymbol{\varphi}) e^{-i\boldsymbol{\ell}\cdot\boldsymbol{\varphi}}. \quad (204)$$

In order to simplify the computation of angular correlation functions we employ *Limber's approximation* (Limber 1953). It asserts that if the quantity $x(\boldsymbol{\theta})$ defined in two dimensions is a projection

$$x(\boldsymbol{\theta}) = \int_0^{\chi_S} d\chi w(\chi) y(\chi\boldsymbol{\theta}, \chi) \quad (205)$$

of a quantity $y(\mathbf{r})$ defined in three dimensions with a weight function $w(\chi)$, then the angular power spectrum of x is given by

$$C_x(\boldsymbol{\ell}) = \int_0^{\chi_S} d\chi \frac{w^2(\chi)}{\chi^2} P_y\left(\frac{\boldsymbol{\ell}}{\chi}\right), \quad (206)$$

where $P_y(k)$ is the power spectrum of y , evaluated at the three-dimensional wave number $k = \ell/\chi$. This approximation is applicable if y varies on length scales much smaller than the typical length scale of the weight function w . Intuitively, we divide χ by ℓ such that we can compare different scales for a given angle. In other words, $\frac{1}{\ell}$ acts like a weighting function. From the Limber approximation, it immediately follows that the convergence spectrum $C_\kappa(l)$ is determined by a weighted line-of-sight integral over the power spectrum $P_\delta(k)$ of the density contrast. Likewise, we can express the convergence bi- and trispectrum as appropriately weighted line-of-sight integrals over the bi- and trispectra. All in all, we find

$$P_\kappa(\ell_1) = \int_0^{\chi_\infty} \frac{d\chi}{\chi^2} W_\kappa^2(\chi) P_\delta\left(\frac{\ell_1}{\chi}\right), \quad (207)$$

$$B_\kappa(\ell_1, \ell_2, \ell_3) = \int_0^{\chi_\infty} \frac{d\chi}{\chi^4} W_\kappa^3(\chi) B_\delta\left(\frac{\ell_1}{\chi}, \frac{\ell_2}{\chi}, \frac{\ell_3}{\chi}\right), \quad (208)$$

$$T_\kappa(\ell_1, \ell_2, \ell_3, \ell_4) = \int_0^{\chi_\infty} \frac{d\chi}{\chi^6} W_\kappa^4(\chi) T_\delta\left(\frac{\ell_1}{\chi}, \frac{\ell_2}{\chi}, \frac{\ell_3}{\chi}, \frac{\ell_4}{\chi}\right), \quad (209)$$

where we introduced the subscripts δ to denote the matter spectra as opposed to the convergence spectra denoted by the subscript κ . We now assume a simple model for the galaxy redshift distribution $q(z)$

$$q(z) = q_0 \left(\frac{z}{z_0}\right)^2 \exp\left(-\left(\frac{z}{z_0}\right)^\beta\right) dz \quad \text{with} \quad q_0^{-1} = \frac{z_0}{\beta} \Gamma\left(\frac{3}{\beta}\right), \quad (210)$$

used in the *Planck Euclid* survey (Laureijs et al. 2011) with a median redshift $z_0 = 0.9$ and $\beta = 1.5$. This enables us to calculate the convergence spectra using the perturbation theory developed in the last chapter. However, we are still missing one crucial piece of information for better understanding weak lensing surveys: How do we measure convergence spectra and which uncertainties are involved in the measurement process? The convergence κ alone can only be accessed through the magnification of images of distant galaxies. Measuring the magnification is possible, but difficult. In turn, it is more feasible to measure the shear γ by studying the surface brightness of images of distant galaxies. One can either fit models for the surface brightness of elliptical sources to the images and obtain their ellipticity as fit parameters or measure the quadrupole moments of the surface brightness in a model-free approach. Transforming the defining equations for κ and γ into Fourier space

$$2\kappa = -\ell^2\psi, \quad 2\gamma_1 = -(\ell_1^2 - \ell_2^2)\psi, \quad \gamma_2 = -\ell_1\ell_2\psi, \quad (211)$$

we conclude that $|\gamma|^2 = |\kappa|^2$ in Fourier space. Therefore, the shear power spectrum equals the convergence power spectrum. For this reason, we will use the terms *shear spectra*, *convergence spectra* and *lensing spectra* interchangeably in the following. To sum up, we learned that we do not actually measure the cosmic convergence, but the cosmic shear. Yet, there is still a problem with this approach: Individual galaxies cannot be used to determine the cosmic shear because they are intrinsically elliptical. What we can do, however, is measure an ensemble of galaxies. Together with the crucial assumption that the intrinsic ellipticities ϵ_S approach zero when averaged over sufficiently large samples $\langle \epsilon_S \rangle = 0$, one can distinguish intrinsic ellipticities and the ellipticity caused by lensing. Parametrising the latter by the reduced shear $g = \frac{\gamma}{1-\kappa}$, we approximately find that the total measured ellipticity ϵ is

$$\epsilon \sim g + \epsilon_S. \quad (212)$$

Averaging over N faint galaxy images, the scatter of the intrinsic ellipticity is reduced to

$$\Delta\langle \epsilon_S \rangle \approx \frac{\sigma_\epsilon}{\sqrt{N}}, \quad (213)$$

where σ_ϵ is the standard deviation of the intrinsic ellipticity. The angular resolution of this measurement is limited by

$$\Delta\theta = \frac{N^{-\frac{1}{2}}}{n\pi} \quad (214)$$

where \bar{n} is the average number of source galaxies per squared arc minute. As a result, the observed convergence spectrum, denoted by the superscript obs , can be modelled as the true spectrum with an additional shot noise contribution:

$$C_{\kappa}^{(obs)}(\ell) = C_{\kappa}(\ell) + \frac{\sigma_{\epsilon}^2}{\bar{n}}. \quad (215)$$

Assuming that the estimates for the spectra can be approximated by a Gaussian distribution, we can estimate the covariance matrices for the lensing spectra, bispectra and trispectra. The covariance of the lensing spectrum is given by

$$\text{cov}(\ell_1, \ell_2) = \delta_D(\ell_1 - \ell_2) \frac{2}{(2\ell + 1)f_{sky}} C_{\kappa}^{(obs)}(\ell_1) C_{\kappa}^{(obs)}(\ell_2), \quad (216)$$

where f_{sky} denotes the fraction of the observed sky and we neglect a contribution proportional to the lensing trispectrum due to the non-Gaussianity of the weak lensing field (Kaiser 1996; Scoccimarro, Zaldarriaga and Hui 1999). Takada and Jain (2003) give an expression for the covariance of the weak lensing bispectrum:

$$\text{cov}(\ell_1, \ell_2, \ell_3) = \frac{\Delta(\ell_1, \ell_2, \ell_3)}{f_{sky}} C_{\kappa}^{(obs)}(\ell_1) C_{\kappa}^{(obs)}(\ell_2) C_{\kappa}^{(obs)}(\ell_3), \quad (217)$$

where $\ell_1 \leq \ell_2 \leq \ell_3 \leq \ell_4$ in the following in order to count every triangle/rectangle configuration only once. $\Delta(\ell_1, \ell_2, \ell_3)$ counts the multiplicity of triangle configurations and is defined as

$$\Delta(\ell_1, \ell_2, \ell_3) = \begin{cases} 6, & \text{if } \ell_1 = \ell_2 = \ell_3, \\ 2, & \text{if } \ell_i = \ell_j \text{ for } i \neq j, \\ 1, & \text{otherwise.} \end{cases} \quad (218)$$

Similarly, we have

$$\text{cov}(\ell_1, \ell_2, \ell_3, \ell_4) = \frac{\Delta(\ell_1, \ell_2, \ell_3, \ell_4)}{f_{sky}} C_{\kappa}^{(obs)}(\ell_1) C_{\kappa}^{(obs)}(\ell_2) C_{\kappa}^{(obs)}(\ell_3) C_{\kappa}^{(obs)}(\ell_4), \quad (219)$$

for the covariance of the weak lensing trispectrum where $\Delta(\ell_1, \ell_2, \ell_3, \ell_4)$ counts the multiplicity of rectangle configurations. These covariance matrices allow us to understand the statistical uncertainties on the power spectrum measurement. With their help, we can calculate the expected cumulative signal-to-noise ratio $\Sigma(\ell)$ for weak lensing measurements of the different spectra up to multipole order

ℓ ¹³:

$$\Sigma_P^2(\ell) = \sum_{\ell_1=\ell_{min}}^{\ell} \frac{P_{\kappa}^2(\ell_1)}{\text{cov}(\ell_1, \ell_1)}, \quad (220)$$

$$\Sigma_B^2(\ell) = \sum_{\ell_1, \ell_2, \ell_3=\ell_{min}}^{\ell} \frac{B_{\kappa}^2(\ell_1, \ell_2, \ell_3)}{\text{cov}(\ell_1, \ell_2, \ell_3)}, \quad (221)$$

$$\Sigma_T^2(\ell) = \sum_{\ell_1, \ell_2, \ell_3, \ell_4=\ell_{min}}^{\ell} \frac{T_{\kappa}^2(\ell_1, \ell_2, \ell_3, \ell_4)}{\text{cov}(\ell_1, \ell_2, \ell_3, \ell_4)}. \quad (222)$$

We can also give an estimate of whether we can distinguish CDM and FDM experimentally via a weak lensing survey. We assume that the true spectra are given by the CDM spectra and compute the χ^2 -functionals for measuring the noise-weighted mismatch between the true CDM and the wrongly assumed FDM spectra:

$$\chi_P^2(\ell) = \sum_{\ell_1=\ell_{min}}^{\ell} \frac{(P_{\kappa}^{CDM} - P_{\kappa}^{FDM})^2(\ell_1)}{\text{cov}(P_{\kappa}^{CDM})(\ell_1, \ell_1)}, \quad (223)$$

$$\chi_B^2(\ell) = \sum_{\ell_1, \ell_2, \ell_3=\ell_{min}}^{\ell} \frac{(B_{\kappa}^{CDM} - B_{\kappa}^{FDM})^2(\ell_1, \ell_2, \ell_3)}{\text{cov}(B_{\kappa}^{CDM})(\ell_1, \ell_2, \ell_3)}, \quad (224)$$

$$\chi_T^2(\ell) = \sum_{\ell_1, \ell_2, \ell_3, \ell_4=\ell_{min}}^{\ell} \frac{(T_{\kappa}^{CDM} - T_{\kappa}^{FDM})^2(\ell_1, \ell_2, \ell_3, \ell_4)}{\text{cov}(T_{\kappa}^{CDM})(\ell_1, \ell_2, \ell_3, \ell_4)}. \quad (225)$$

4.3 Experimental Setup

At this point, we are almost in a position to compute weak lensing observables in FDM and CDM. The remaining ingredients that we will discuss in this section are the following: Choice of FDM masses, choice of lensing survey parameters and generation of initial conditions.

4.3.1 Choice of FDM Masses

One of the current popular FDM models is one where all of DM is composed of axions with $m = 10^{-22}$ eV (Hu, Barkana and Gruzinov 2000; Marsh 2016; Hui et al. 2017). This mass has also been suggested by Schive, Chiueh and Broadhurst (2014) who fitted the ground state density of a halo obtained in a numerical simulation of FDM to the mass distribution of the dwarf spherical

¹³Note that unlike for the lensing bispectrum where a configuration is uniquely specified by the three multipole moments ℓ_1, ℓ_2, ℓ_3 up to spatial orientation, a lensing trispectrum configuration is not uniquely specified by ℓ_1, \dots, ℓ_4 . In our code, we sum over all configurations by varying three sides and the two enclosed angles.

galaxy Fornax. Comparing galaxy formation in CDM and FDM models, Schive et al. (2015) found the bound $m \geq 1.2 \cdot 10^{-22}$ eV in the 2σ -range. Hložek, Marsh and Grin (2018) study the possible mass range for FDM via CMB lensing based on the full Planck data set and find no evidence for an ULA component in the mass range $10^{-33}\text{eV} \leq m \leq 10^{-24}$ eV. Constraints from the Lyman- α forest have larger uncertainties than the constraints from the CMB because of the need to model the temperature evolution of the intergalactic medium. Nevertheless, the Lyman- α forest can be used to place the strongest constraints on deviations from CDM on small scales. Kobayashi et al. (2017) studied how measurements of the Lyman- α forest flux power spectrum by the XQ-100 survey constrain a multicomponent axion DM model. They claimed that FDM models with $m < 10^{-21}$ eV were ruled out. However, they make use of hydrodynamical CDM simulations using FDM initial conditions, thereby neglecting FDM dynamics at late times. Zhang, Liu and Chu (2019) carefully examine the Lyman- α forest constraints on FDM and conclude that simulations with quantum pressure are required for reliable constraints based on the Lyman- α forest. They also point out that the simulation uncertainties of hydrodynamic simulations may have been underestimated in previous studies. Therefore, strong Lyman- α bounds such as the 95% C.L. lower limit $m > 2 \cdot 10^{20}$ eV given by Rogers and Peiris (2021) based on pure CDM dynamics with FDM initial conditions need to be taken with a pinch of salt. In fact, many other, often complementary cosmological probes can be used to constrain FDM models. For instance, González-Morales et al. (2017) found the upper bound of $m > 4 \cdot 10^{23}$ eV by fitting the luminosity-averaged velocity dispersion of dwarf spherical galaxies; Sarkar, Pandey and Sethi (2021) use the Lyman- α effective opacity to find $m > 10^{-23}$ eV and Maleki, Baghran and Rahvar (2019) find $m > 7 \cdot 10^{-23}$ eV by studying the X-ray emissions during solitons mergers. The above-mentioned mass bounds motivate us to perform our computations for three different FDM masses $m = 10^{-21}$, $m = 10^{-22}$ and $m = 10^{-23}$ eV that are all within or near the range of FDM masses still currently debated.

4.3.2 Lensing Survey Parameters

Our lensing survey parameters are these of a *Euclid-like* survey and listed in table 7. Perhaps most importantly, we list results up to a maximum multipole moment of $\ell_{max} = 10000$. Such a high multipole moment is not accessible in a weak lensing survey. In order to see the effect of axion DM in the considered mass range, we need to resolve scales at the order of $k = 1$ h/Mpc which roughly corresponds to multipole orders $\ell \gtrsim 1000$. In practice, the highest multipole

moment measurable in a weak lensing survey is limited by the shape noise. The signal-to-noise ratio of a single multipole moment drops below 1 at $\ell \sim 3000$. However, we may still gain information by summing over these noise-dominated multipole moments. We expect our results to be reliable in this range because we make a relatively conservative estimate for the shape noise and tree- and even loop-level PT underestimate the power on small scales in the nonlinear regime. At even higher multipole moments of around $\ell = 5000$, baryonic feedback becomes an important, a process which we neglect entirely in PT. At this point, our results become unreliable. We still show the plots for multipole moments $\ell \gtrsim 5000$ in order visually compare the different masses.

4.3.3 Initial Power Spectra

In the section on linear perturbation theory, we derived how the CDM and FDM power spectrum evolve in linear approximation. However, the linear growth equations (73) and (89) are only valid in a radiation-free universe, on subhorizon-scales and where matter can be approximated as a non-relativistic fluid. In order to obtain the initial matter power spectrum at a redshift before nonlinear evolution becomes dominant, one is required to solve a coupled system of relativistic Boltzmann equations for baryons, dark matter and radiation under space-time expansion. Codes such as CAMB (Lewis, Challinor and Lasenby 1999) for CDM and AXIONCAMB (Hlozek et al. 2014) for FDM, also known as *Boltzmann solvers*, perform exactly this task. They return the power spectrum at the desired time in the form of a *transfer function* $T(k, a)$ that encodes all the nonlinear modifications that the primordial power spectrum undergoes while evolving to intermediate redshift:

$$P^{(0)}(k, a) = \mathcal{N} D^2(a, a_0) T^2(k, a) P_{\text{prim}}(k). \quad (226)$$

The norm of the norm of the power spectrum \mathcal{N} as well as the primordial power spectrum P_{prim} have to be determined separately. We assume the primordial spectrum after inflation to be the *Harrison-Zeldovich spectrum* with $P_{\text{prim}} \propto k$ because of scale-invariance of the perturbations in the gravitational potential. As for the initial FDM spectrum, it can in fact be obtained from the CDM spectrum with the help of yet another transfer $T_{\text{FDM}}(k, a)$ that encodes how FDM dynamics differ from CDM dynamics. Hu, Barkana and Gruzinov (2000) gave a semi-analytic expression for the FDM transfer function that is valid for $m \gtrsim 10^{-24}$ eV

$$P_{\text{FDM}}(k, a) = T_{\text{F}}^2(k, a) P_{\text{CDM}}(k, a), \quad T_{\text{F}}(k, a) \approx \frac{\cos x(k, a)^3}{1 + x(k, a)^8}, \quad (227)$$

where $x(k, a) = 1.61 \left(\frac{m}{1e-22} \right)^{\frac{1}{18}} \frac{k}{k_J(a)}$, leading to a drop of power by a factor of 2 at

$$k_{\frac{1}{2}} \approx \frac{1}{2} k_J \left(\frac{m}{10^{-22} \text{eV}} \right)^{\frac{1}{18}}. \quad (228)$$

For lower masses, scale-dependent growth remains relevant at late times and the transfer function becomes redshift-dependent. However, in the following, we shall rely on the transfer functions provided by the CAMB and AXIONCAMB codes shown in Figure 23. We can justify that at the time $a_0 = 0.01$ corresponding

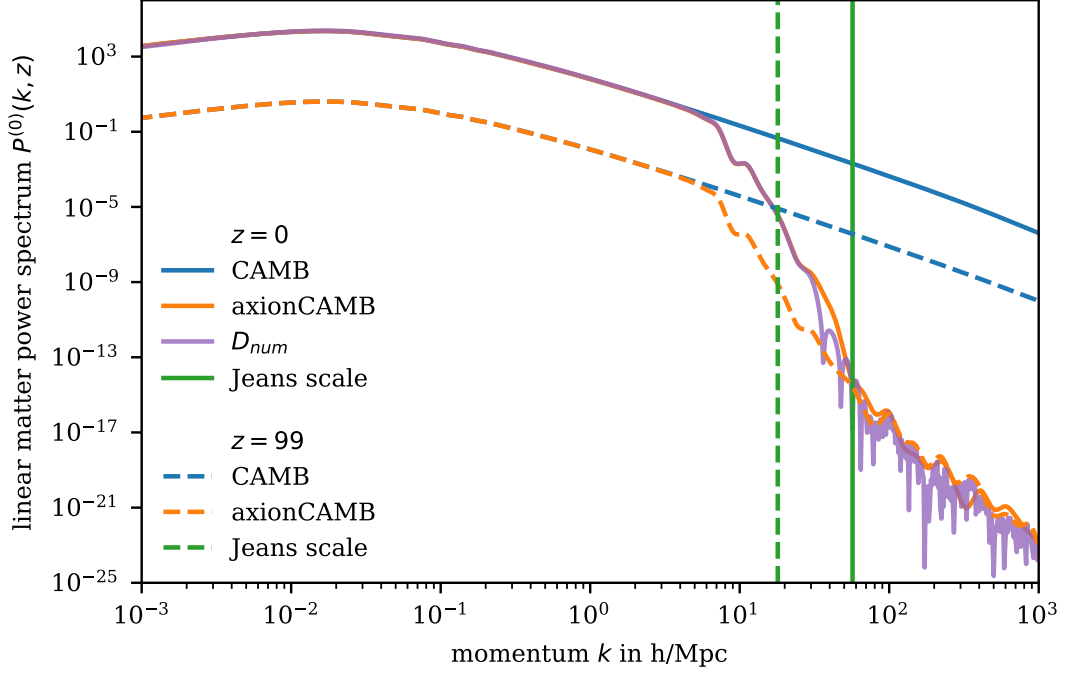


Figure 23: Linear matter power spectra at redshifts $z = 0$ and $z = 99$ with respective Jeans scales from Eq. (86) at $m = 10^{-22}$ eV. The purple line D_{num} denotes the axionCAMB initial power spectrum evolved from $z = 99$ to $z = 0$ using the FDM growth factor obtained by numerical Integration of Eq. (89).

to a redshift $z = 99$, all scales of interest are still in the fully linear regime by computing the scale $\lambda_{NL} = \frac{2\pi}{k_{NL}}$ at which nonlinearities becomes relevant. This scale can be estimated as the scale where the linear variance of δ is unity:

$$1 \stackrel{!}{=} \sigma^2 = \frac{1}{2\pi^2} \int_0^\infty dk P(k) k^2. \quad (229)$$

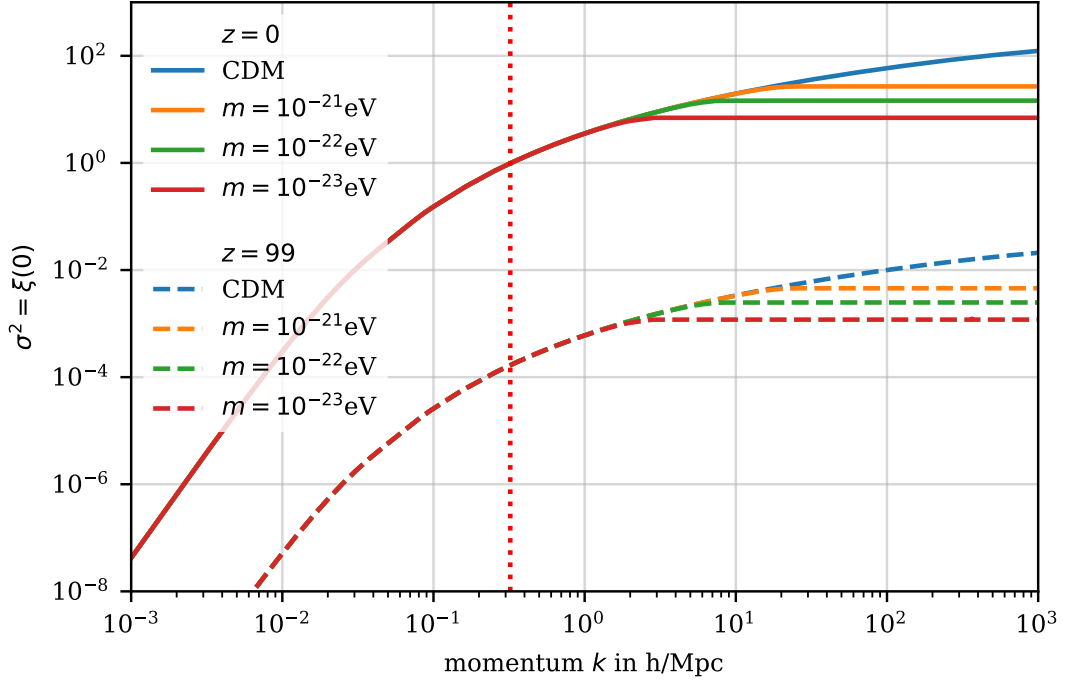


Figure 24: Linear CDM and FDM fluctuation variance as function of the scale k . At $z = 99$, integration of the spectrum yields a variance of $\sigma^2 \propto 10^{-3}$ implying that linear theory is still applicable. The red, dotted, vertical line denotes the scale k_{NL} which the fluctuation variance at $z = 0$ is unity: $k_{NL} \approx 0.3 h/\text{Mpc}$.

4.4 Results

All of the following results were calculated in the [fiducial cosmology](#) at $z = 0$. Unless indicated otherwise, we used the equations for nonlinear Eulerian perturbation theory in the last chapter for all nonlinear quantities. The code that computes the matter spectra, bispectra and trispectra in CDM and FDM is available under <https://github.com/KunkelAlexander/fdm-eulerpt>.

4.4.1 Spectra

Figure 25 shows the CDM and FDM power spectra at tree-level and with loop-level corrections. Below the respective Jeans scales, power is strongly suppressed in the FDM model. Nonlinear corrections at loop-level transfer power to small scales, but suppression is still dominant. Figure 26 shows the respective convergence spectra. Nonlinear corrections significantly increase the magnitude of the dimensionless spectra for multipole moments $\ell \gtrsim 100$. Whereas the CDM and FDM spectra for $1000 \leq \ell \leq 3000$ can be visibly distinguished at $m = 10^{-23}$ eV, a mass of $m = 10^{-22}$ eV already requires an angular resolution of up to $\ell = 10000$ and a mass of $m = 10^{-21}$ eV leads to only marginal, visual differences with CDM up to $\ell = 10000$. This can also be explained by translating the

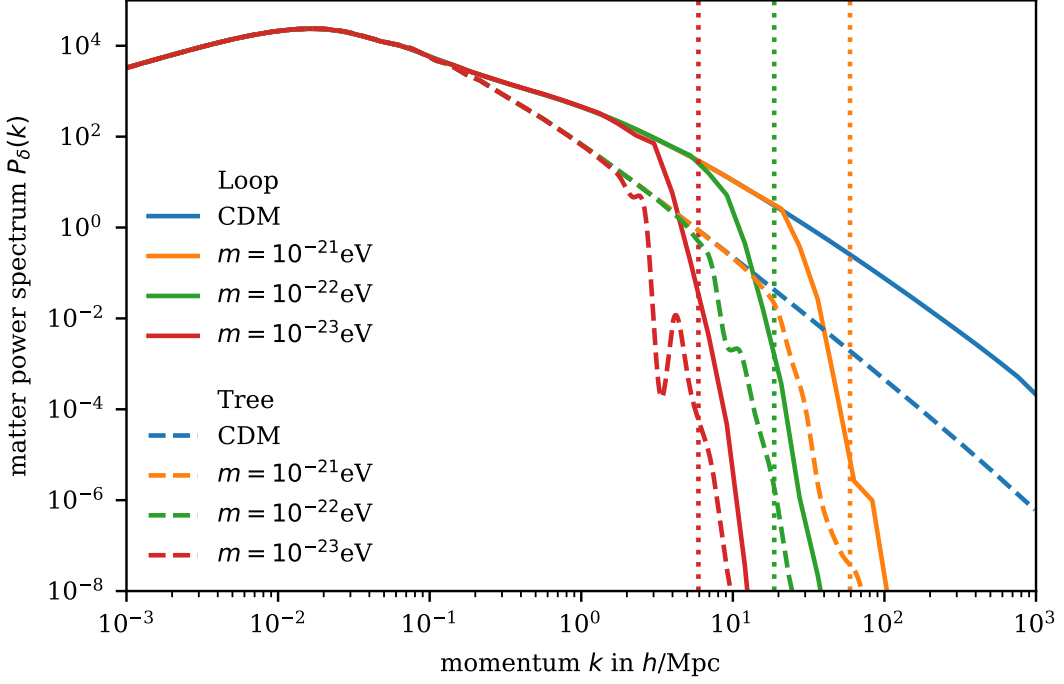


Figure 25: Matter power spectra at $z = 0$ at tree-level and with loop-level corrections. The dotted, vertical lines denote the respective Jeans scales from Eq. (86) at $z = 99$.

comoving quantum Jeans scale into a corresponding multipole order by an order-of-magnitude estimate. We define the *quantum Jeans multipole order* $\ell_J(m)$ via

$$\ell_J(m) \equiv \frac{\pi}{\arctan\left(\frac{k_J(m)}{\chi(z=z_0)}\right)}, \quad (230)$$

where $\chi(z = z_0)$ is the comoving distance at the redshift z_0 and k_J is as defined in Eq. (86) at $z = 99$. For the mean redshift $z_0 = 0.9$ of the redshift distribution defined in Eq. (210), we obtain $\ell_J(m = 10^{-21}\text{eV}) \approx 88000$, $\ell_J(m = 10^{-22}\text{eV}) \approx 28000$ and $\ell_J(m = 10^{-23}\text{eV}) \approx 8800$. Since these quantum Jeans multipole orders are too high to be measurable in a weak lensing survey, the vertical lines in Fig. 26 display $0.1 \cdot \ell_J$ which roughly describes the multipole order where the CDM and FDM lensing spectra start to differ. Figures 27 and 29 show the equilateral matter bispectra and equilateral square matter trispectra and Figures 28 and 30 the respective convergence spectra. As in the case of the power spectrum, loop-level corrections for the bispectrum have the effect of adding power on small angular scales in both CDM and FDM. At both tree- and loop-level, suppression below the Jeans scale is still the dominant effect in FDM, however.

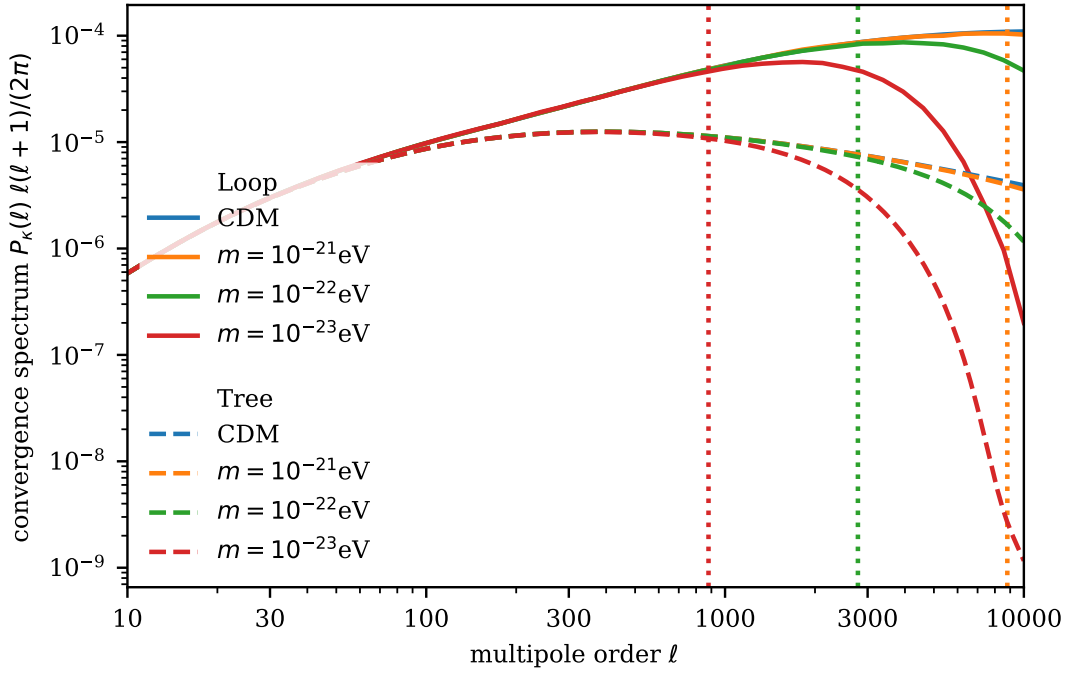


Figure 26: Dimensionless convergence spectra at tree-level and with loop-level corrections at $z = 0$. The vertical, dotted lines correspond to $0.1 \cdot \ell_J$, where the quantum Jeans multipole order ℓ_J is defined in Eq. (230).

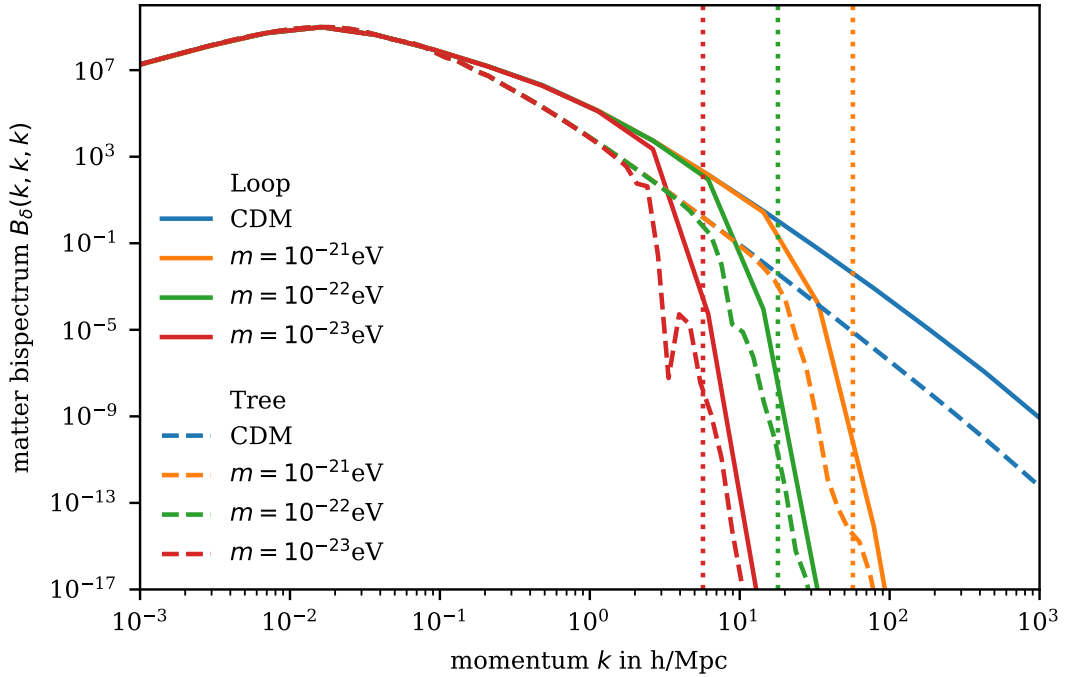


Figure 27: Equilateral matter bispectra at $z = 0$ at tree-level and with loop-level corrections. The dotted, vertical lines denote the respective Jeans scales from Eq. (86) at $z = 99$.

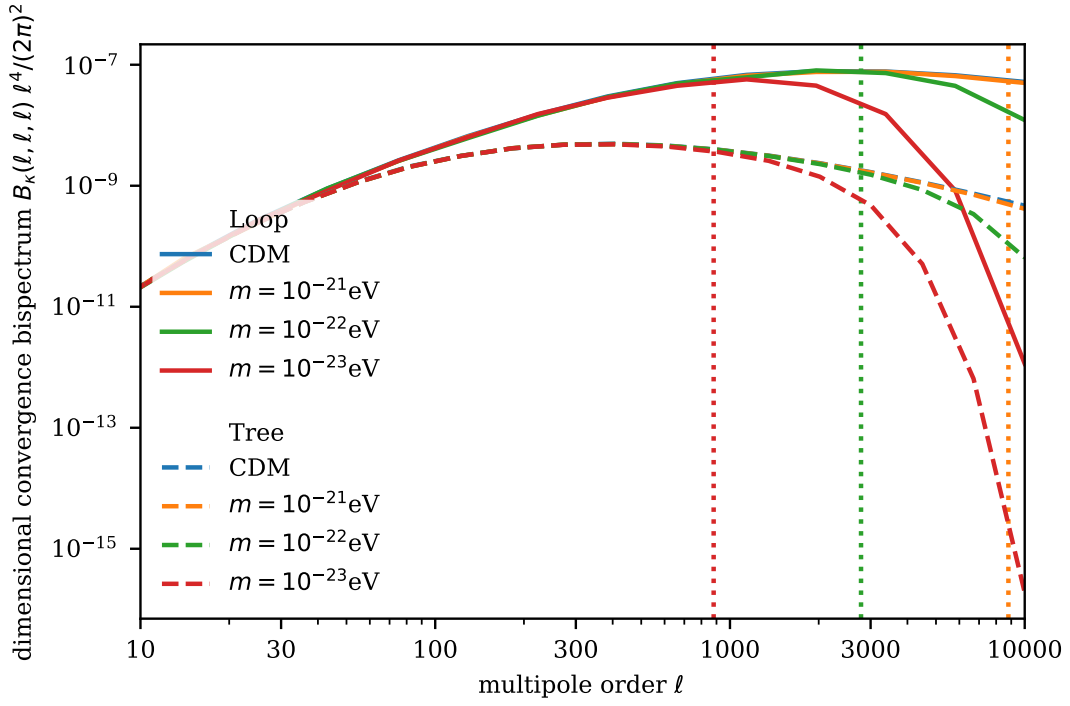


Figure 28: Dimensionless equilateral convergence bispectrum configurations at $z = 0$. The vertical, dotted lines correspond to $0.1 \cdot \ell_J$, where the quantum Jeans multipole order ℓ_J is defined in Eq. (230).

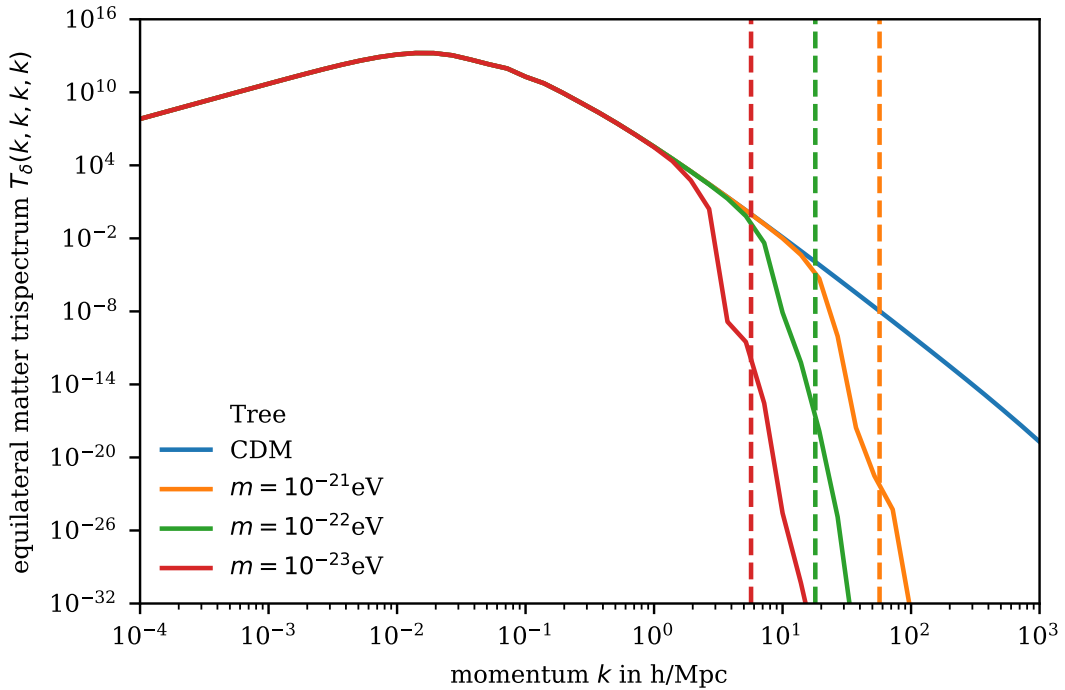


Figure 29: Equilateral square tree-level matter trispectrum configurations at $z = 0$. Dashed lines indicate respective Jeans scales from Eq. (86) at $z = 99$.

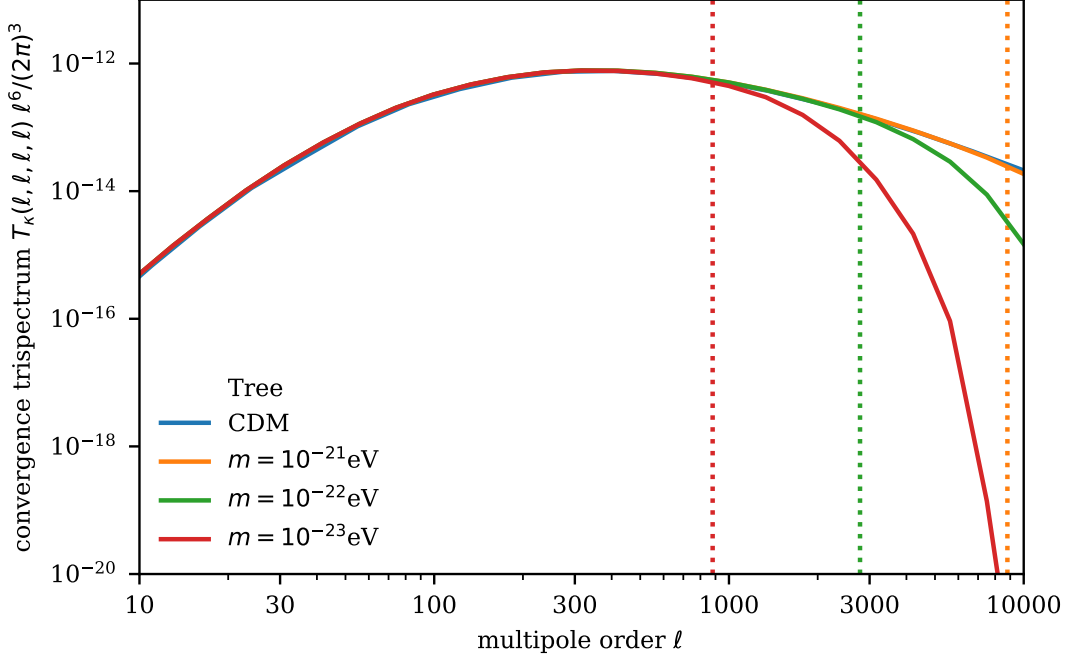


Figure 30: Dimensionless equilateral square convergence trispectrum configurations at $z = 0$. The vertical, dotted lines correspond to $0.1 \cdot \ell_J$, where the quantum Jeans multipole order ℓ_J is defined in Eq. (230).

The loop-level corrections given by Eq. (177) were computed in a form free of infrared divergences using the CUBA-library (Hahn 2004). Details of the numerical integration can be found in appendix A.4. All loop lensing quantities have numerical errors of up to 10 % as a result of the computational challenges involved in computing FDM quantities. We also computed the lensing spectra using CDM PT with FDM initial conditions. The respective figures can be found in appendix A.5. CDM dynamics give loop-level corrections to the lensing spectra and bispectra that are, within the numerical errors, indistinguishable from the ones computed using FDM PT. They indicate that the influence of late-time nonlinear FDM dynamics is negligible for weak lensing observables. We conclude that the suppression of the spectra below the Jeans scale is mainly prescribed by the initial power spectra at high redshift in PT.

Figure 31 shows the angular dependence of the reduced matter bispectrum $Q^{(0)}$ defined in Eq. (188) at tree-level. The fact that $Q^{(0)}$ is enhanced for $\theta = 0, \pi$ reflects the fact that large scale flows generated by gravitational instability are mostly parallel to density gradients. As discussed earlier, the kernel $F_2^{(s)}$ includes the first higher-order correction from the quantum pressure term. Therefore it does not only counteract gravitational collapse but can also enhance it as exemplified by the graphs for $m = 10^{-21}$ eV and $m = 10^{-22}$ eV at scales k around or below the Jeans scale for the respective masses.

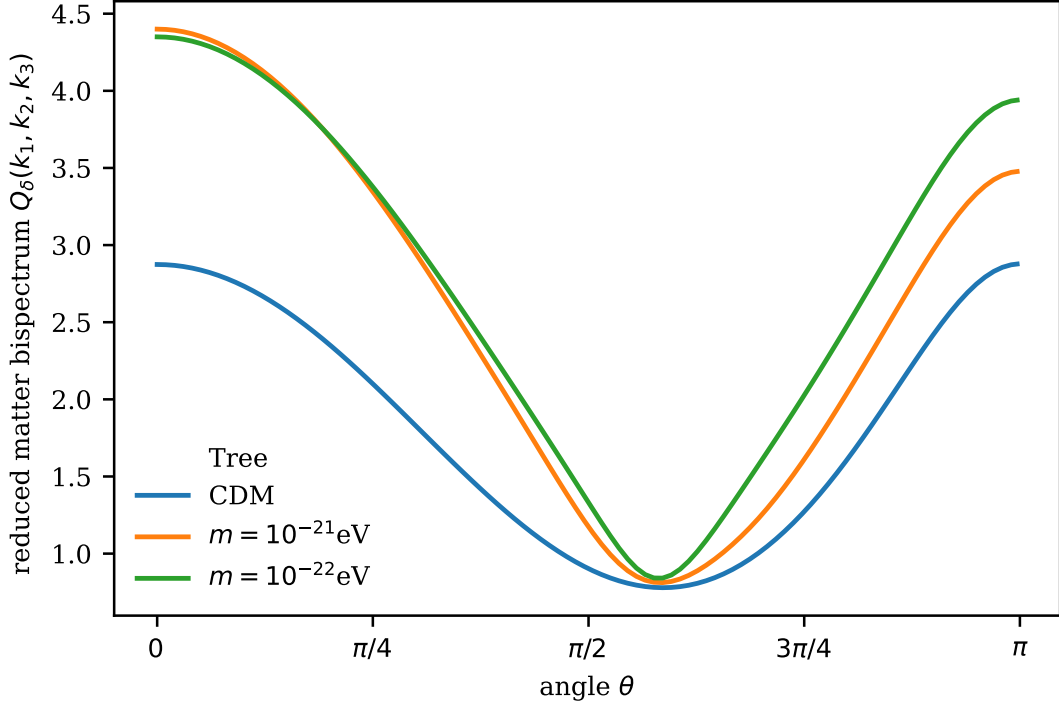


Figure 31: Angular dependence of reduced bispectrum at tree-level with $\theta = \angle(\mathbf{k}_1, -\mathbf{k}_2)$ with $k_1 = 10 h/\text{Mpc}$ and $k_2 = 0.1 h/\text{Mpc}$ at $z = 0$. The graph for $m = 10^{-23} \text{ eV}$ is not shown because it is in the oscillating regime and depends on how the growth factors and the initial spectra approximate oscillations.

4.4.2 Signal-To-Noise Ratios and χ^2 -Functionals

Figure 32 shows the signal-to-noise ratios obtained in CDM according to Eqs. (220), (221) and (222). We compute the respective covariance matrices using the convergence spectrum with loop-level corrections. This is because the non-vanishing bi- and trispectrum themselves are generated by nonlinear dynamics. Using the tree-level convergence spectrum would therefore underestimate the covariance and overestimate the attainable signal-to-noise ratio. Since the bulk of the cumulative signal comes from the modes with low ℓ , there are no significant differences for the attainable signal-to-noise ratios in CDM and FDM weak lensing surveys for the considered masses. The sums in Eqs. (220), (221) and (222) were expressed as integrals and integrated using the CUBA-library (Hahn 2004). We could not compute the respective signal-to-noise ratios for the weak lensing bispectra at loop-level for FDM since the integrals involved proved computationally intractable. We did compare against the signal-to-noise ratios of the loop-level lensing bispectra computed with CDM PT for FDM IC. Yet, these results are also subject to substantial numerical uncertainty since the Monte Carlo-integration routine fails to give error estimates.

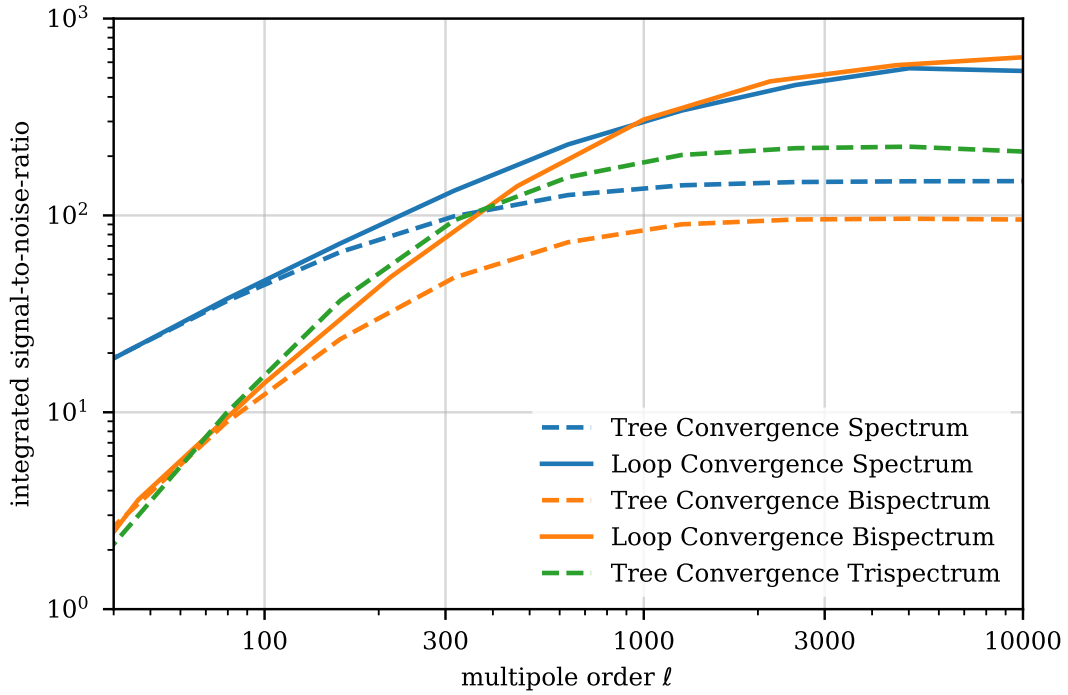


Figure 32: Attainable cumulative signal-to-noise ratio in weak lensing survey.

Figure 33 visualises the angular dependence of the lensing bispectrum at tree-level for $m = 10^{-23}$ eV. The bottom plots reflect that the small-angular scales where the CDM and FDM models actually differ only have a comparatively small signal-to-noise ratio in a weak lensing survey. In contrast, Figure 34 shows the corresponding loop-level results approximated by CDM PT with FDM IC. We observe that the loop-level corrections significantly enhance the signal-to-noise ratio for multipole orders where CDM and FDM at $m = 10^{-23}$ eV can be distinguished.

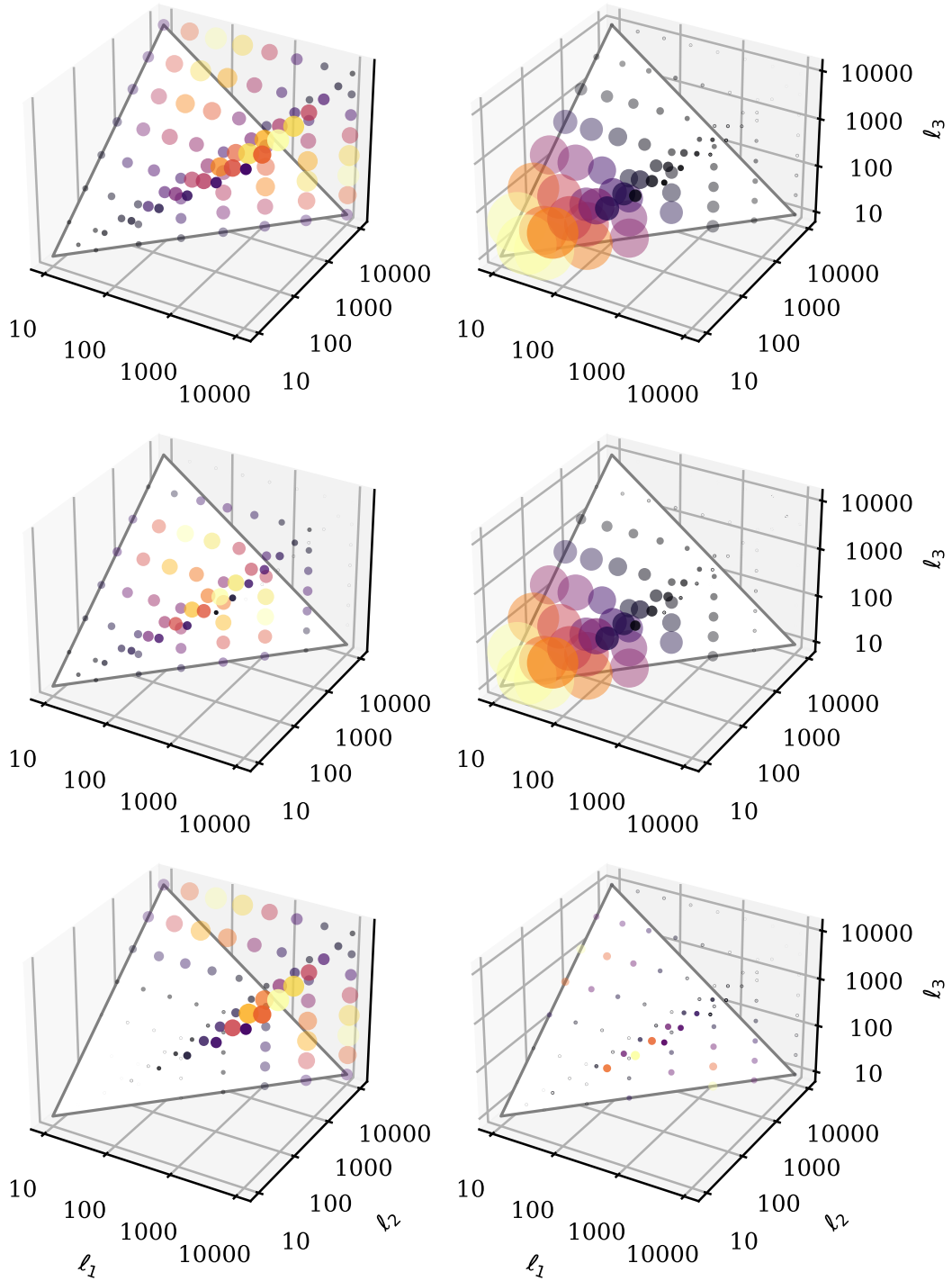


Figure 33: Configuration dependence (first column) and signal-to-noise ratio (second column) of weak lensing bispectrum at tree-level.

Color and size both represent magnitudes; Same, arbitrary normalisation across rows.

Top to bottom: CDM, FDM for $m = 10^{-23}$ and difference between the two.

Left column: Dimensionless lensing bispectrum $(\ell_1 \ell_2 \ell_3)^{\frac{3}{2}} B_\kappa(\ell_1, \ell_2, \ell_3)$ at $z = 0$.

Right column: signal-to-noise ratio $B_\kappa(\ell_1, \ell_2, \ell_3) / \sqrt{\text{cov}(\ell_1, \ell_2, \ell_3)}$ at $z = 0$.

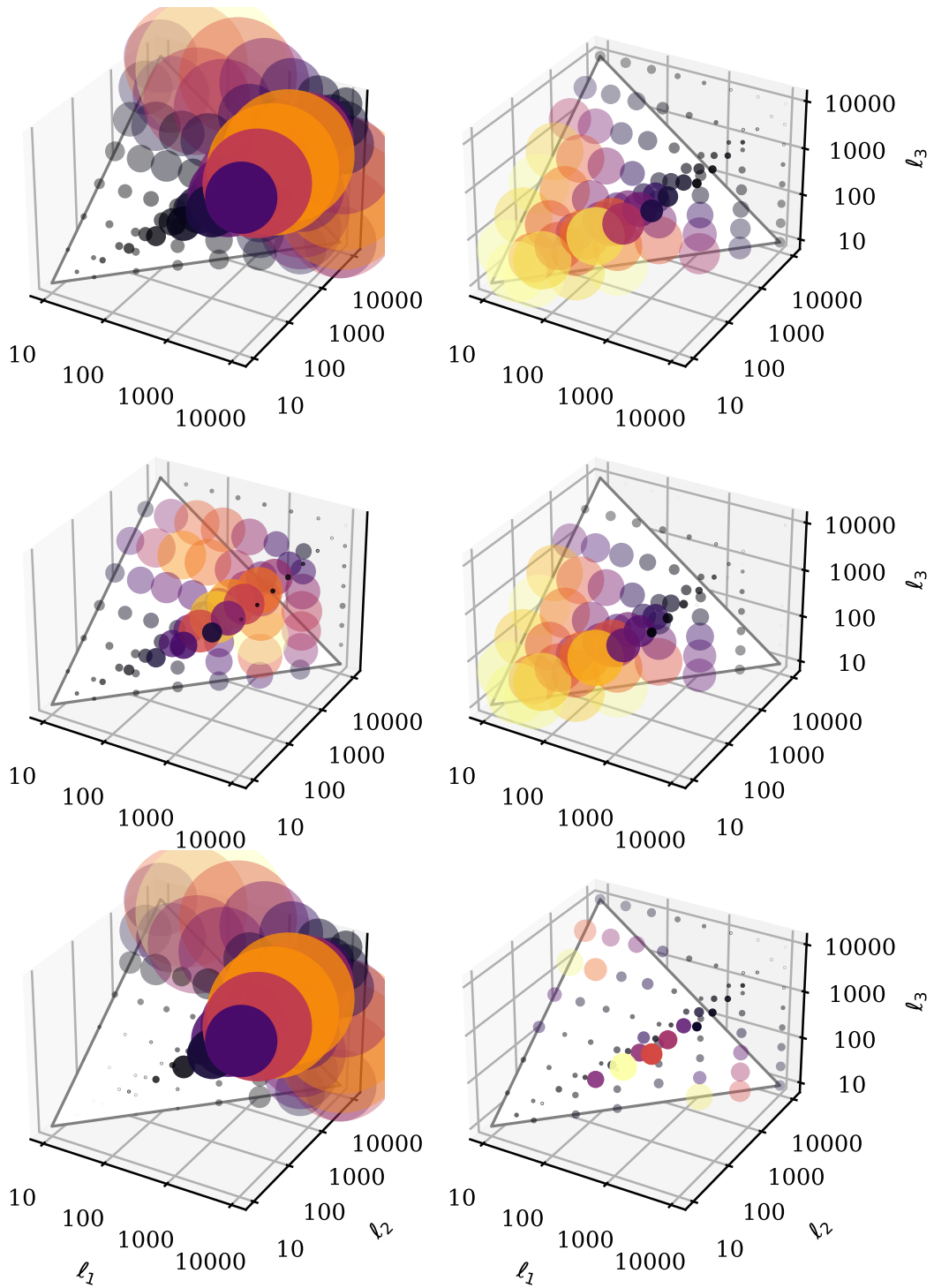


Figure 34: Configuration dependence (first column) and signal-to-noise ratio (second column) of weak lensing bispectrum at loop-level where FDM dynamics are approximated by CDM PT with FDM IC.

Color and size both represent magnitudes; Same normalisation as in Fig. 33.

Top to bottom: CDM, CDM with FDM IC for $m = 10^{-23}$ and difference between the two.

Left column: Dimensionless lensing bispectrum $(\ell_1 \ell_2 \ell_3)^{\frac{3}{2}} B_\kappa(\ell_1, \ell_2, \ell_3)$ at $z = 0$.

Right column: signal-to-noise ratio $B_\kappa(\ell_1, \ell_2, \ell_3) / \sqrt{\text{cov}(\ell_1, \ell_2, \ell_3)}$ at $z = 0$.

Finally, Figure 35 shows the χ^2 -functionals for distinguishing CDM and FDM computed according to Eqs. (223), (224) and (225) where all sums are again expressed as integrals and calculated using the CUBA-library (Hahn 2004).

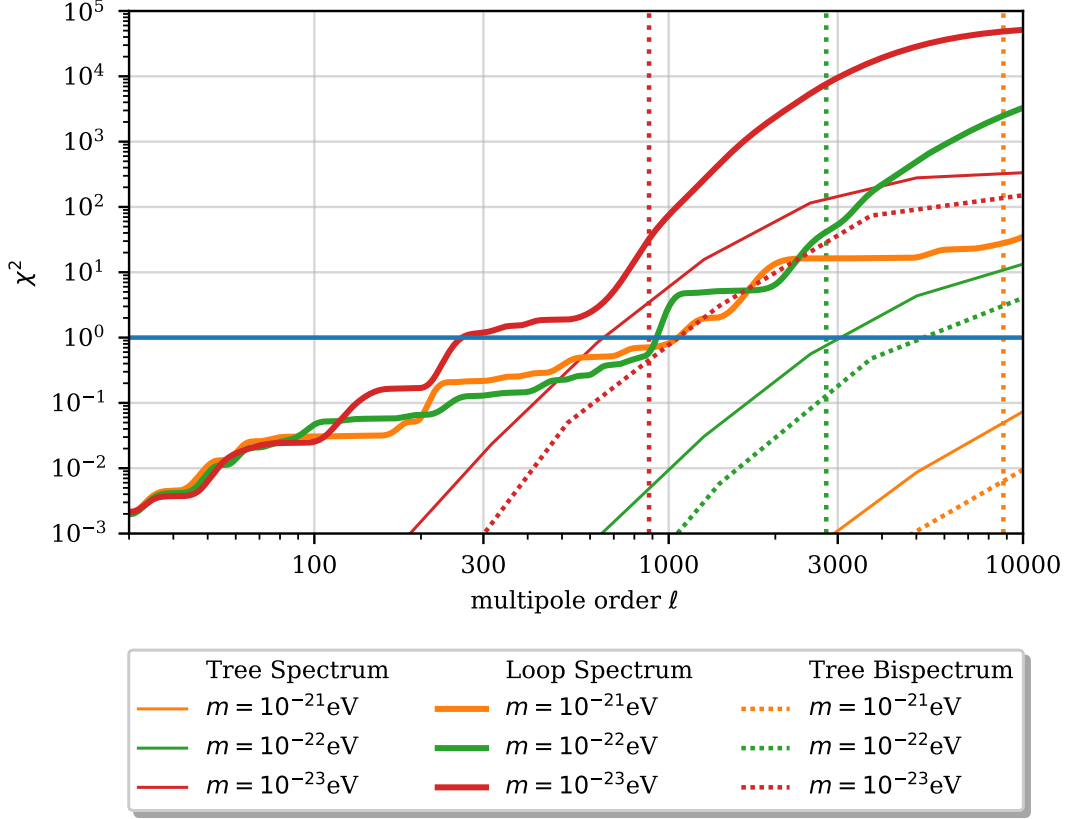


Figure 35: χ^2 -functional to distinguish CDM and FDM as a function of the maximum multipole order ℓ according to Eqs. (223), (224) and (225). The vertical, dotted lines correspond to $0.1 \cdot \ell_J$, where the quantum Jeans multipole order ℓ_J is defined in Eq. (230). The horizontal blue line corresponds to $\chi^2 = 1$.

The loop-level χ^2 -functionals are dominated by noise for low ℓ since they are computed by interpolating the loop-level lensing spectra depicted in Fig. 26 using cubic splines. They suggest that we may be able to distinguish CDM and FDM at $m = 10^{-21}$ eV for a maximum multipole order of $\ell = 2000$. This is not the case as shown by Figure 36 which compares the χ^2 -functionals computed via FDM PT and CDM PT with FDM IC, where the latter were calculated without the use of splines using high-dimensional MC integrations. We expect CDM PT with FDM IC to underestimate the suppression of power w.r.t. the FDM model. Therefore, it should give a lower bound on the attainable χ^2 -values. At large ℓ , the loop-level lensing spectrum results agree well for $m = 10^{-22}$ eV and $m = 10^{-23}$ eV. At $m = 10^{-21}$ eV however, CDM PT with FDM PT predicts much smaller χ^2 -values for high ℓ . We conclude that the respective FDM PT χ^2 functional is dominated by noise up to high ℓ . Figure 37 underlines this conclusion. It displays the tree-

level χ^2 -functionals for FDM PT and CDM PT with FDM IC that agree very well.

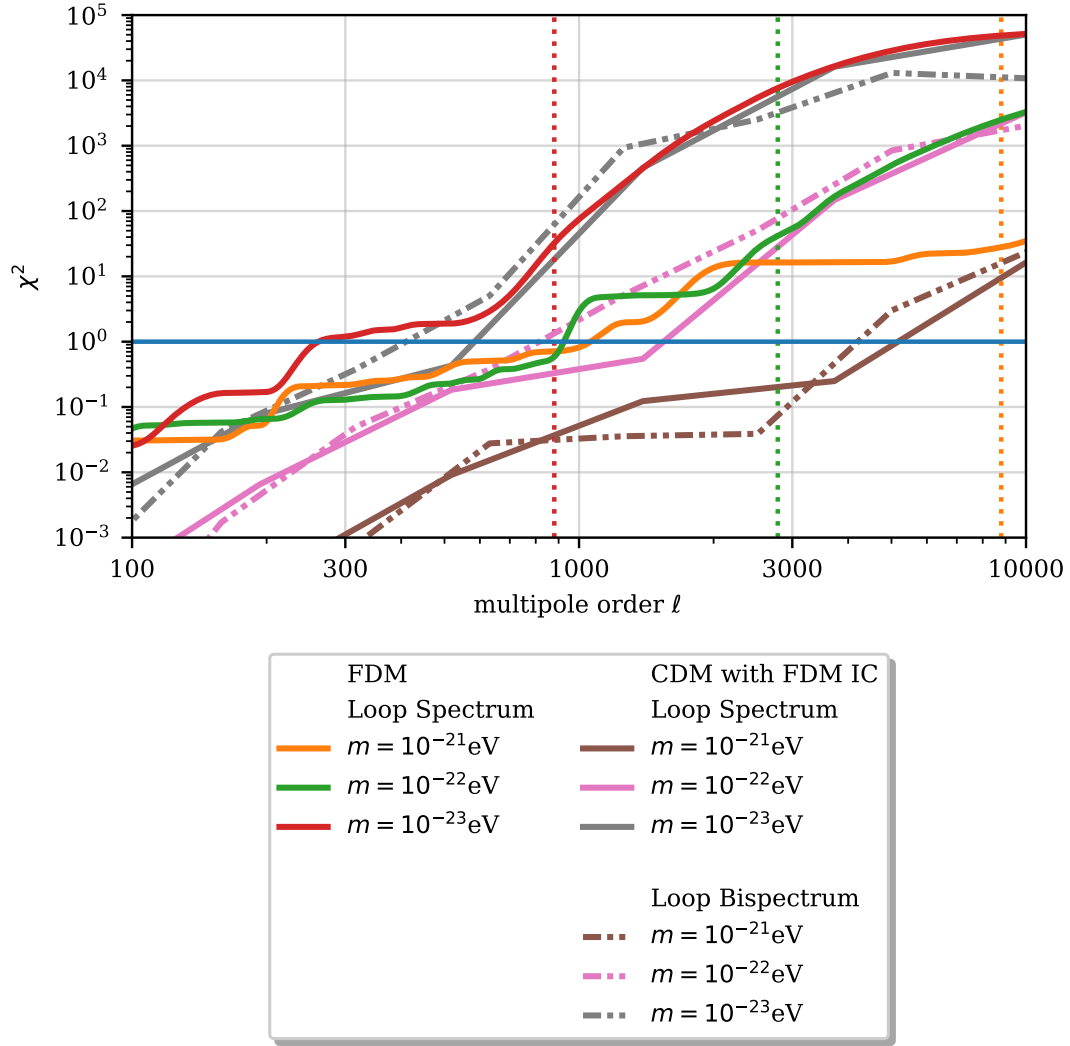


Figure 36: χ^2 -functional to distinguish CDM and FDM as a function of the maximum multipole order ℓ according to Eqs. (223), (224) and (225). Both FDM dynamics and FDM dynamics approximated by CDM PT with FDM initial conditions are shown. The vertical, dotted lines correspond to $0.1 \cdot \ell_J$, where the quantum Jeans multipole order ℓ_J is defined in Eq. (230).

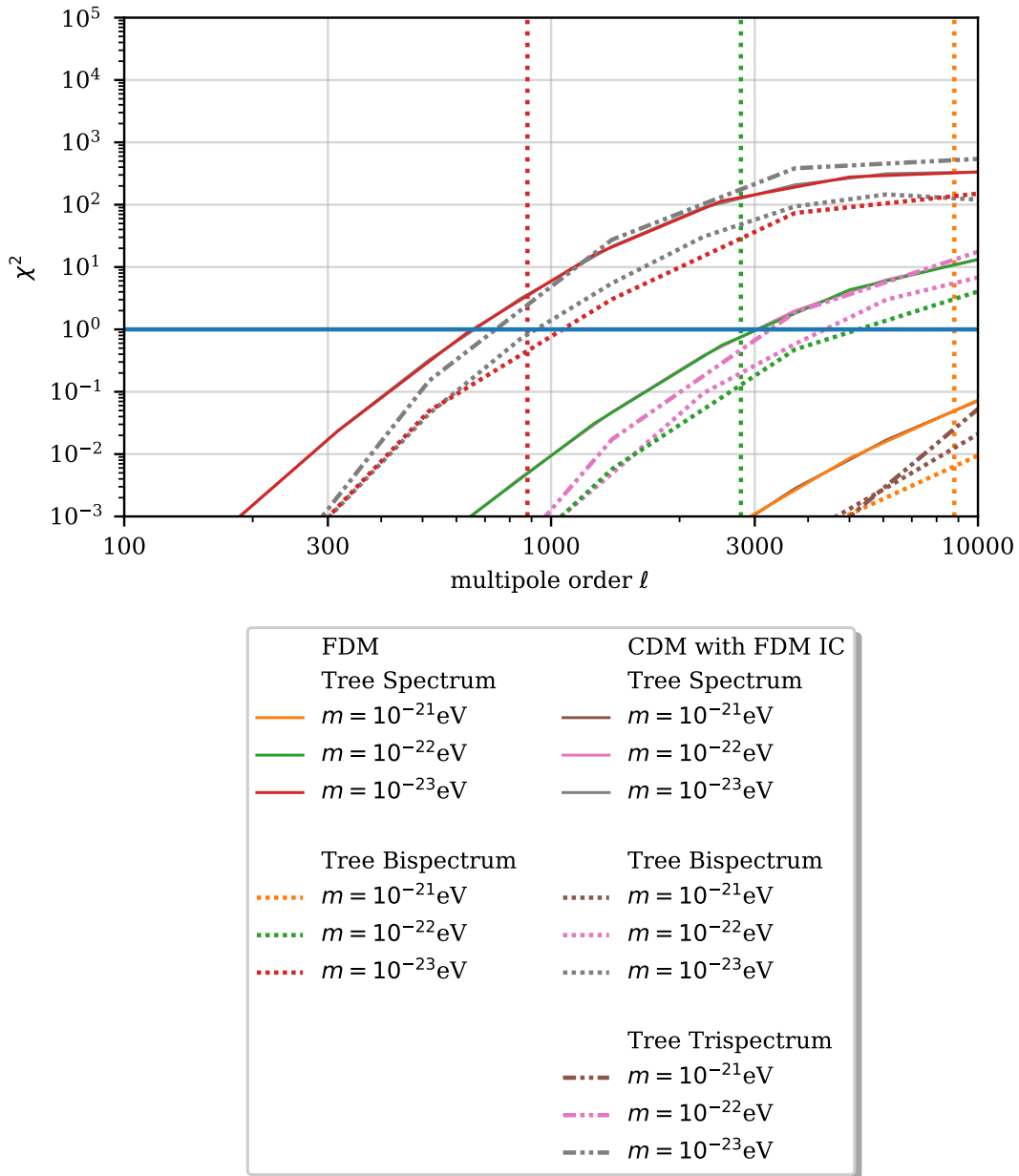


Figure 37: χ^2 -functional to distinguish CDM and FDM as a function of the maximum multipole order ℓ according to Eqs. (223), (224) and (225). FDM dynamics are approximated by CDM PT with FDM initial conditions. The vertical, dotted lines correspond to $0.1 \cdot \ell_J$, where the quantum Jeans multipole order ℓ_J is defined in Eq. (230).

4.5 Discussion

In this chapter, we have seen how Eulerian perturbation theory can be used to compute weak lensing observables. We derived the attainable signal-to-noise ratios and χ^2 -functionals for distinguishing CDM and FDM in a Euclid-like weak-lensing survey. The tree-level lensing spectrum results imply $\chi^2 = 1$, i.e. an uncertainty of 1σ , for FDM with $m = 10^{-23}$ eV at $\ell \sim 700$. At the masses

$m = 10^{-22}$ and $m = 10^{-21}$, the respective signals are too weak to distinguish CDM and FDM in our weak lensing survey up to $\ell = 3000$. The lensing bispectrum gives a lower χ^2 -functional than the lensing spectrum at tree-level. Assuming that the loop-level CDM PT results with FDM IC underestimate the true χ^2 -functionals, we find $\chi^2 = 1$ at $\ell \sim 600$ and $\ell \sim 1500$ for $m = 10^{-23}$ eV and $m = 10^{-22}$ eV using the loop-level lensing spectra. The signal for $m = 10^{-21}$ eV is still too weak to be measurable in a realistic weak lensing survey. At loop-level, the lensing bispectrum gives slightly higher χ^2 -values than the lensing spectrum. The main uncertainty in our approach stems from the modelling of nonlinear structure formation via PT. The signal-to-noise ratios for the tree- and loop-level spectra and bispectra indicate that loop-level corrections lead to higher signal-to-noise ratios. Since PT underestimates the magnitude of the nonlinear corrections on small scales, the tree-level-only results for the χ^2 -functionals therefore give a conservative lower bound for the χ^2 -values in a weak lensing survey. The comparison of FDM PT and CDM PT with FDM initial conditions shows that late-time nonlinear FDM dynamics only marginally affect the considered weak lensing observables compared to CDM dynamics. The additional suppression of power in nonlinear FDM dynamics do not lead to a measurable difference in our weak lensing survey.

5

Hybrid Simulation of FDM

Much of the recent progress in understanding FDM dynamics comes from numerical simulations, often in the ultra-light regime for $m = 10^{-22}$ eV. In the literature, there are numerical studies of structure formation in the FDM model using both the wave and the fluid formulation. They employ a number of different algorithms, including spectral methods (Mocz et al. 2017; Edwards et al. 2018; Du et al. 2018), finite difference methods (Schive, Chiueh and Broadhurst 2014), finite volume methods (Schwabe, Niemeyer and Engels 2016; Li, Hui and Bryan 2018; Hopkins 2018) and smoothed particle hydrodynamics algorithms (Mocz and Succi 2015; Nori and Baldi 2018).

The first high-resolution cosmological simulation of the wave formulation of FDM was carried out by Woo and Chiueh (2008). They used a spectral method to simulate FDM with a uniform mesh resolution of 1024^3 grid points, but even such a high spatial resolution is inadequate for the innermost regions of halos. One of the key requirements of cosmological simulations is the ability to resolve a large dynamical range in scale. To form sufficiently many objects with the size of dwarf galaxies, the simulation volume must span a few cubic megaparsecs. On the lower end, the simulation must resolve scales at the order of ten parsecs leading to a range in scale of $\sim 10^5$. Schive, Chiueh and Broadhurst (2014) first addressed this issue with the code GAMER. It uses an adaptive mesh refinement (AMR) framework to solve the wave formulation of the SPS. The drawback of solving the wave formulation is the need to resolve the de Broglie wavelength of the matter wave even in regions where the density is low and smooth. The reason is that the velocity is related to the gradient of the phase of the wave function, i.e. a given velocity translates into a phase that varies on the scale of the de Broglie wavelength $\lambda_{dB} = \frac{2\pi}{mv}$. If the latter is not resolved, the velocity field is not represented correctly (Li, Hui and Bryan 2018). This is in contrast to conventional

CDM simulations with AMR that only require higher spatial resolution in regions with higher density. In an FDM simulation with $m = 10^{-22}$ eV and a velocity of $v = 100$ km/s, the de Broglie wavelength $\lambda_{dB} \sim 1.2$ kpc is much smaller than the box size required for a large cosmological simulation. Because of their high computational demands, existing wave simulations are therefore usually limited to small box sizes ¹⁴. In contrast to wave simulations, simulations of the fluid formulation do not need to resolve the de Broglie wavelength to correctly capture large-scale dynamics. In fact, they even allow the adoption of a Lagrangian picture via smoothed-particle hydrodynamics methods incorporating the quantum pressure. The possible simulation volumes are much closer to those attainable in traditional N -body and smoothed-particle hydrodynamics approaches for CDM. This is why hydrodynamical methods have been extensively used to study structure formation in FDM (Veltmaat and Niemeyer 2016; Schwabe, Niemeyer and Engels 2016; Schive et al. 2015; Hopkins 2018; Mocz et al. 2017; Nori and Baldi 2018; Nori et al. 2018). Their biggest drawback, however, is that they fail to correctly resolve regions of interference because the quantum pressure is ill-defined in regions of vanishing density. Therefore, fluid simulations of the SPS are generally not trustworthy. Ideally, one could create a hybrid AMR scheme that solves the fluid formulation of the SPS on a coarse grid on large-scales and the wave formulation on a refined grid on small scales thereby combining the advantages of both approaches: The coarse grid on large scales need not resolve the de Broglie wavelength while the wave formulation on small scales correctly describes interference effects. Such a hybrid approach will enable zoom-in simulations on dwarf galaxies with the correct FDM dynamics on all scales. A first step in this direction has been taken by Veltmaat, Niemeyer and Schwabe (2018) and Schwabe and Niemeyer (2021). They developed a hybrid code that employs a Lagrangian N -body solver on large scales and a finite difference wave solver with AMR on small scales. The critical part in such a hybrid scheme is the reconstruction of the wave function from particle information at the N -body-Schrödinger-boundaries. In this chapter, we develop a hybrid code on a static grid that solves the phase equations (21) and (22) on large scales and switches to a wave solver when it detects interference. We start by discussing the issue of reconstruction of the wave function at the boundary between the fluid and wave simulations, hereafter referred to as *boundary matching*. We then go on to give an introduction into different simulation methods for the different formulations of the SPS. Finally, we

¹⁴Recently, a number of simulations (Mina, Mota and Winther 2020; Mocz et al. 2020) reached larger box sizes in the wave formulation. May and Springel (2021) computed a de Broglie scale-resolved FDM simulation in a $10 h/\text{Mpc}$ box on a very large static grid with 8640^3 points. This simulation was enabled by a newly-developed highly parallelised FFT algorithm.

describe our phase and hybrid algorithms and validate their numerical properties using a number of one-, two- and three-dimensional test cases.

5.1 Boundary Matching Problem

The crucial issue in developing a hybrid code combining a fluid solver with a wave solver lies in reconstructing the wave function from the Madelung formulation of the SPS. Remember the Madelung transform from Eq. (20)

$$\psi(\mathbf{x}, t) \equiv \sqrt{\frac{\rho(\mathbf{x}, t)}{m}} e^{iS(\mathbf{x}, t)}. \quad (231)$$

The wave function is split up into its norm and its phase. We then take the gradient of the phase to derive the velocity (see. Eq. (25)):

$$\mathbf{v} = \frac{\hbar}{ma} \nabla S. \quad (232)$$

5.1.1 Evolution of the Velocity Field

Let us first suppose that we evolve the density and velocity fields $\rho(\mathbf{x}, t)$ and $\mathbf{v}(\mathbf{x}, t)$. At the matching boundary between the fluid and the wave simulation, we need to reconstruct $\psi(\mathbf{x}, t)$ and therefore the phase $S(\mathbf{x}, t)$ from the density $\rho(\mathbf{x}, t)$ and the velocity $\mathbf{v}(\mathbf{x}, t)$. We can reconstruct the phase field $S(\mathbf{x}, t)$ by integrating the velocity field according to

$$S(\mathbf{x}, t) - S(\mathbf{x}_0, t) = \int_{\mathcal{C}} \mathbf{v}(\mathbf{x}, t) \cdot d\mathbf{x}, \quad (233)$$

where \mathcal{C} is a piecewise differentiable curve from \mathbf{x}_0 to \mathbf{x} . The integral is independent of the choice of curve since the velocity field is conservative. Eq. (233) highlights an important difficulty arising when integrating the velocity field. The integration constant $S(\mathbf{x}_0, t)$ is itself time-dependent. In order to obtain the phase at an arbitrary point \mathbf{x} , we need to evolve the phase in time at at least one point \mathbf{x}_0 ¹⁵. The choice of this point is arbitrary and numerical errors might depend on its position. Moreover, it always needs to be located in a region where the fluid formulation is valid. In other words, it will need to be moved away from regions

¹⁵This problem also occurs if we recast the integration problem in the form of a Poisson equation

$$\Delta S = \nabla \cdot \mathbf{v}, \quad (234)$$

with von Neumann boundary conditions at the matching boundary. Since we cannot provide Dirichlet boundary conditions, the solution will only be determined up to a time-dependent constant. This constant is necessary to reconstruct the wave function $\psi(\mathbf{x}, t)$.

of vanishing density dynamically. Further, the integration path \mathcal{C} will connect all points in the simulation where we employ the fluid formulation with \mathbf{x}_0 . As a result, distant regions in the simulation will need to communicate at every time step. This communication can potentially have a large computational overhead.

5.1.2 Parallel Evolution of the Velocity and Phase Fields

In order to avoid the integration of the velocity field, we can evolve the phase field $S(\mathbf{x}, t)$ in addition to the velocity field. If we treat the velocity field as fundamental and evolve it by a time step Δt , the velocity fields at the times t and $t + \Delta t$ can be used to update the phase field by treating the Hamilton-Jacobi equation (22) as an ODE. This approach has the advantage that no integration of the velocity field is necessary. Further, existing hydrodynamics codes and ODE solvers can be used for updating both the velocity and density fields. The disadvantages of this method are the computational and memory overhead of evolving an additional field as well as the fact that the time evolution of the phase field at different points decouples. Neighbouring points on a grid are updated via the velocities at the respective grid points but never communicate directly. Hence, numerical errors at neighbouring points decouple.

5.1.3 Evolution of the Phase Field

A third approach consists in treating the density and phase fields $\rho(\mathbf{x}, t)$ and $S(\mathbf{x}, t)$ as fundamental fields and in evolving them using the Hamilton-Jacobi-Madelung equations (21) and (22). This allows the unique reconstruction of the wave function $\psi(\mathbf{x}, t)$ without additional computational overhead. At the same time, it leads to what we call the *reverse boundary matching problem* in the following. The velocity \mathbf{v} can be easily obtained from the wave function via differentiation. Yet, the phase is only determined by the wave function up to a multiple of 2π :

$$S(\mathbf{x}, t) = \arctan \left(\frac{\Im(\psi(\mathbf{x}, t))}{\Re(\psi(\mathbf{x}, t))} \right). \quad (235)$$

We must therefore determine the correct phase by requiring continuity at the matching boundary. On a discrete grid, this translates into the requirement that the phase field $S(\mathbf{x}, t)$ must not change by more than 2π between neighbouring grid points at the matching boundary. In other words, we must resolve the de Broglie wavelength at the matching boundary in order for the reverse boundary matching problem to admit a unique solution. This immediately shows that a useful hybrid scheme based on this approach necessarily requires an AMR-algorithm with at least two refinement levels for the phase equation: An outer

refinement level where the grid need not resolve the de Broglie wavelength and an second refinement level where the de Broglie wavelength is resolved and the reverse boundary matching problem has a unique solution. This concludes our discussion of the boundary matching problem and sets the stage for the development of the hybrid scheme. We first review the basics of computational fluid dynamics (CFD) and then construct a numerical scheme to solve the Hamilton-Jacobi Madelung equations.

5.2 Introduction to CFD

The following section introduces the basics of computational fluid dynamics (CFD) and heavily draws on (Hirsch 2007). There are three main methods for the discretisation of spatial derivatives in partial differential equations (PDEs): *Finite difference*, *finite volume* and *finite element* methods. Finite difference methods work on structured grids by replacing spatial derivatives by discrete difference expressions between neighbouring grid points. Finite volume methods discretise the integral form of conservation laws. Lastly, there are finite element methods that are especially important for unstructured grids. In the following, we will be concerned with finite difference and finite volume methods. Jupyter notebooks that can be used to reproduce and interact with many of the figures in the following sections can be found on github under <https://github.com/KunkelAlexander/fdm-hybrid-scheme/>. The easiest way to access them is via this [Binder repository](#). The notebook accompanying the following section on the linear advection equation is called `advection_widget.ipynb`. The notebook on the SPS is called `sps_widget.ipynb`.

5.2.1 Finite Difference Method

In this section, we introduce the finite difference method (FDM) by considering the one-dimensional linear convection equation

$$u_t + au_x = 0, \quad (236)$$

with initial conditions and boundary conditions

$$u(x, t = 0) = u_0(x), \quad 0 \leq x \leq L, \quad (237)$$

$$u(x = 0, t) = u(x = L, t), \quad t \geq 0, \quad (238)$$

as a model equation for linear conservation laws. It admits the solution $u(x, t) = u_0(x - at)$ that is constant along any curve in the x - t -plane¹⁶. We start by discretising the space and time dimensions. We choose a uniform grid with N points and constant grid spacing Δx for the spatial dimension and subdivide the time axis into time intervals Δt :

$$x_i \equiv i\Delta, \quad t^n = n\Delta t, \quad u_i^n = u(i\Delta x, n\Delta t), \quad (239)$$

where space positions are denoted by the subscript i and time levels by the superscript n . Numerical schemes for differential equations as well as the solutions they produce must be assessed on the basis of three main concepts: consistency, stability and convergence. *Consistent numerical schemes* must tend to the differential equation when time and space steps tend to zero. The numerical errors of a *stable numerical solutions* are bounded for finite Δt and Δx when the number of iterations n tends to infinity. A convergent numerical solution tends to the exact mathematical model when time and space steps tend to zero. The *equivalence theorem of Lax* then states that for a well-posed initial value problem and a consistent discretisation scheme, stability is a necessary and sufficient condition for convergence. In the following, we shall therefore always check numerical schemes for consistency as well as stability. Let us discretise the spatial derivatives in Eq. (236) via the finite difference

$$\partial_x = \frac{u(x + \Delta x) - u(x)}{\Delta x}. \quad (240)$$

Taylor expanding $u(x + \Delta x)$, we find

$$\frac{u(x + \Delta x) - u(x)}{\Delta x} = u_x(x) + \frac{\Delta x}{2} u_{xx}(x) = u_x(x) + \Delta x. \quad (241)$$

This shows that the introduction of the finite difference leads to a *truncation error*, that is, a difference between the numerical scheme and the underlying differential equation. This truncation error is proportional to the term $\frac{\Delta x}{2} u_{xx}(x)$ to lowest order in Δx . This tells us that the result numerical scheme is consistent and first-order accurate in space¹⁷. Taylor expansion analysis shows the following expressions for the forward, backward and central differences ∂_x^f , ∂_x^b are first-

¹⁶In fact, first-order PDEs can be reduced to ODEs on curves on which their solutions are constant. The so-called *method of characteristics* permits the solution of nonlinear first-order PDEs. For a discussion see appendix A.6.

¹⁷Apart from the truncation error, numerical schemes exhibit other discretisation errors, iteration errors from the solution of linear or nonlinear systems of equations as well as floating point errors.

first- and second-order respectively:

$$\partial_x^f u_i^n \equiv \frac{u_{i+1}^n - u_i^n}{\Delta x}, \quad \partial_x^b u_i^n \equiv \frac{u_i^n - u_{i-1}^n}{\Delta x}, \quad \partial_x^c u_i^n \equiv \frac{u_{i+1}^n - u_{i-1}^n}{2\Delta x}. \quad (242)$$

Replacing the spatial derivative in the linear advection equation by the second-order central discretisation ∂_x^c , we find the ODE

$$\partial_t u = a \frac{u_{i+1} - u_{i-1}}{2\Delta x}. \quad (243)$$

This separation of temporal and spatial discretisation of a PDE is called *method of lines*. In the next step, we replace the time derivative by a suitable finite difference. If we evaluate the right-hand side (RHS) of Eq. (243) at the time level n , we find the *explicit* Euler method:

$$u_i^{n+1} = u_i^n + a\Delta t \frac{u_{i+1}^n - u_{i-1}^n}{2\Delta x}. \quad (244)$$

In explicit methods, the matrix of the unknown variables at the new time is a diagonal matrix while the RHS of the system depends only on the variables at previous times. Explicit methods for the linear advection equation require a condition on the maximum time step size of the form

$$C_{CFL} = \left| \frac{a\Delta t}{\Delta x} \right| \leq 1, \quad (245)$$

that is called Courant-Friedrichs-Lewy (CFL) condition. The CFL condition ensures that the domain of dependence of the numerical discretisation of an *explicit* time discretisation contains the true physical domain of dependence by reflecting the finite propagation speed a of solutions to the linear advection equation. More generally, it can be shown that CFL conditions ensure that numerical causality corresponds to physical causality as Δx tends to zero (Ajaib 2013). Instead of evaluating the RHS of Eq. (243) at the time level n , we can evaluate it at the time level $n + 1$ to obtain the *implicit* Euler method

$$u_i^{n+1} = u_i^n + a\Delta t \frac{u_{i+1}^{n+1} - u_{i-1}^{n+1}}{2\Delta x}. \quad (246)$$

In *implicit methods*, the matrix to be inverted is not diagonal since more than one set of variables is unknown at the same time level. Implicit methods therefore require the solution of potentially nonlinear systems of equations at every time step. Their advantage is that they circumvent the CFL condition by using the entire numerical domain of dependence thereby including the true limited physical

domain of dependence. In the following, we shall mostly consider explicit methods because implicit methods have a high computational cost in cosmological simulations. Fig. 38 compares the numerical evolution of a top hat propagating into positive x -direction according to the explicit Euler method in Eq. (244) with its analytical time evolution. The numerical solution does clearly not describe

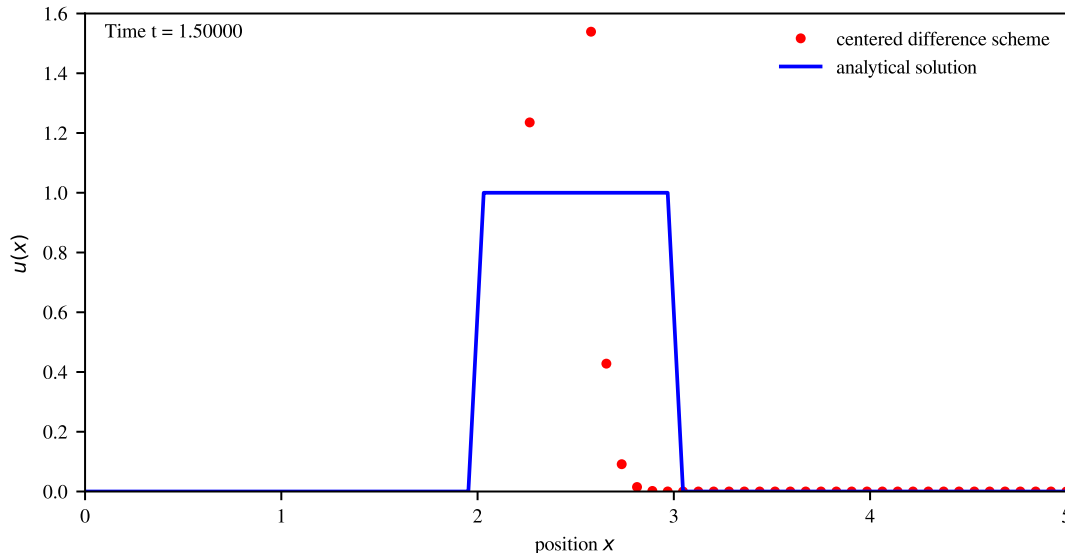


Figure 38: Central difference scheme (Eq. (244)) for the time evolution of a top hat according to the linear advection equation (236) with $a = 1$. The simulation uses the simulation parameters $L = 5$ and $\Delta x = 5/64$. The time step Δt is set according to the CFL condition Eq. (245). The initial conditions are taken as $u(x, t = 0) = 1$ for $0.5 < x < 1.5$ and 0 otherwise.

the analytical solution well. What went wrong? Clearly, the scheme Eq. (244) is not convergent, hence not stable. We know that the analytical solution to the linear advection equations travels at a finite propagation speed a . One reason for the failure of the central difference method is that the information needed to update u_i^n is derived from values of u in both *upstream* and *downstream* directions. The upstream direction is $x < x_i$ for $a > 0$ since that is the direction from which the flow comes. The downstream direction is $x > x_i$, that is, the direction where the steam goes. Anything that happens to the flow downstream from x_i should never affect the value of $q(x_i)$ since information flows downstream. One can also show that the central difference method is not stable by performing a *von Neumann analysis*: One Fourier transforms the truncation error assuming periodic boundary conditions and then studies the time evolution of the Fourier modes. Fortunately, we can obtain a stable scheme by using forward and backward derivatives to discretise the linear advection equation as

$$u_i^{n+1} = u_i^n + \Delta t \left(\min(a, 0) \partial_x^b u_i^n + \max(a, 0) \partial_x^f u_i^n \right). \quad (247)$$

Such a form of discretisation is called *upwind* discretisation and lets the numerical scheme reflect the physical domain of dependence of the wave-like solutions of the advection equation. Fig. 39 compares the upwind discretisation of the linear advection equation with its numerical solution. We observe that the upwind scheme

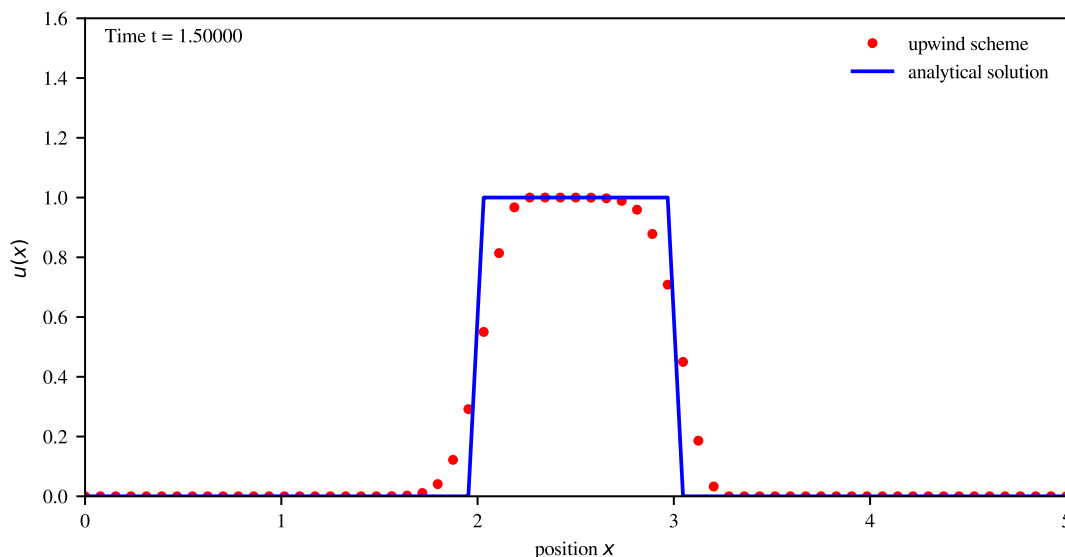


Figure 39: Upwind scheme (Eq. (247)) for the time evolution of a Gaussian wave packet according to the linear advection equation (236) with $a = 1$. The simulation parameters are set as in Fig. 38.

describes the propagation of the top hat well. However, it is rather diffusive at the discontinuities of the top hat. This is because the upwind discretisation Eq. (247) is only first-order in space and time. As a general rule, first-order schemes tend to be very diffusive and are therefore often unacceptable for practical applications. We shall always seek methods of at least second order in the following. A possible option for a higher-order scheme for the linear advection equation is the *Lax-Wendroff scheme*:

$$u_i^{n+1} = u_i^n - \frac{\Delta t}{2\Delta x} a(u_{i+1}^n - u_{i-1}^n) + \frac{\Delta t^2}{2\Delta x^2} a^2(u_{i+1}^n - 2u_i^n + u_{i-1}^n) \quad (248)$$

Truncation error analysis shows that it is second-order in both time and space. Further, it stabilises the central difference scheme given in Eq. (244) by adding additional *artificial viscosity* in the form of a diffusion term:

$$\Delta u = \frac{1}{\Delta x^2} (u_{i+1}^n - 2u_i^n + u_{i-1}^n) + \mathcal{O}(\Delta x^2). \quad (249)$$

In fact, we observe that the truncation error in the Taylor expansion of $u(x + \Delta x)$ Eq. (241) at order Δx was also proportional to a diffusion term. Diffusion generally tends to stabilise numerical schemes as can be shown by von Neumann

analysis. This explains why the upwind scheme works so well: The upwind discretisation of the derivative in the linear advection equation has the effect of adding artificial diffusion to the central discretisation and therefore stabilises the scheme. Fig. 40 shows the evolution of the top hat according to the Lax-Wendroff scheme. Compared to the upwind scheme, it is less diffusive, but exhibits unphysical wiggles at the discontinuities of the top hat. This demonstrates a fundamental

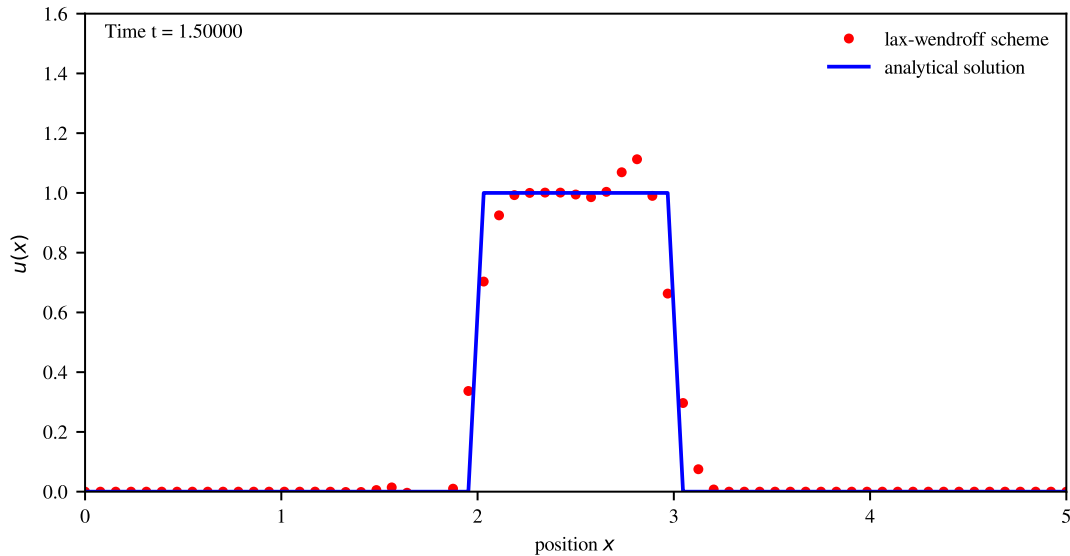


Figure 40: Lax-Wendroff scheme (Eq. (248)) for the time evolution of a Gaussian wave packet according to the linear advection equation (236) with $a = 1$. The simulation parameters are set as in Fig. 38.

problem of linear higher-order schemes: They introduce unphysical oscillations at discontinuities. The absence of unphysical oscillations can be characterised by the notion of *monotonicity* for linear differential equations and the *Total Variation* (TVD) property in the nonlinear case. The total variation quantifies the oscillations in a function

$$TV(u(t)) = \int_{-\infty}^{\infty} |u'(x, t)| dx. \quad (250)$$

For scalar, possibly nonlinear conservation laws, the total variation of the exact solution is a non-increasing function of time

$$TV(u(t_2)) \leq TV(u(t_1)), \quad \forall t_2 \geq t_1. \quad (251)$$

This implies that the solution u does not develop any new local extrema over time and that the magnitude of existing extrema does not increase¹⁸. This excludes

¹⁸The TVD theory only applies to scalar conservation laws in one spatial dimension. Empirically, however, it has been shown to be very successful even for systems of nonlinear conservation

the formation of local instabilities such as unphysical oscillations because they increase the total variation. Therefore, numerical schemes aim to implement the TVD condition described by Eq. (251) in the discrete case. We call a numerical scheme TVD iff

$$TV(u^{n+1}) \leq TV(u^n), \quad \forall n, \quad (252)$$

where

$$TV(u^n) = \sum_{i=-\infty}^{\infty} |u_{i+1}^n - u_i^n|. \quad (253)$$

Godunov's theorem now states that all linear TVD schemes for the convection equation are necessarily first-order accurate. The only way out is to create non-linear higher-order schemes, even for linear conservation laws. This leads to the introduction of *slope limiters* that control the process of generation of over- and undershoots preventing gradients from exceeding certain limits. Let us explain this at the example of a second-order backward difference discretisation of the linear advection equation for $a > 0$:

$$\partial_t u = -\frac{a}{2\Delta x}(3u_i - 4u_{i-1} + u_{i-2}) = -\frac{a}{2\Delta x}[-4(u_{i-1} - u_i) + (u_{i-2} - u_i)]. \quad (254)$$

We can express a general linear explicit scheme with two time-levels as

$$u_i^{n+1} = u_i^n + \sum_j b_j (u_{i+j}^n - u_i^n), \quad (255)$$

and the TVD condition is satisfied if $b_j \geq 0$ for all j . Hence Eq. (254) is clearly not TVD because of the negative coefficient in front of u_{i-1} . We can rewrite Eq. (254) as

$$\partial_t u = -\frac{a}{\Delta x} \left[u_i - u_{i-1} + \frac{1}{2}(u_i - u_{i-1}) - \frac{1}{2}(u_{i-1} - u_{i-2}) \right], \quad (256)$$

and multiply the non-monotone terms by the slope limiter ψ

$$\partial_t u = -\frac{a}{\Delta x} \left[u_i - u_{i-1} + \frac{1}{2}\psi(r_i)(u_i - u_{i-1}) - \frac{1}{2}\psi(r_{i-1})(u_{i-1} - u_{i-2}) \right], \quad (257)$$

where

$$r_i = \frac{u_{i+1} - u_i}{u_i - u_{i-1}} \quad (258)$$

denotes the ratio of subsequent gradients. The spatial part of the scheme (257) can be shown to be monotone if $\psi(r) \geq 0$ for $r \geq 0$, $\psi(r) = 0$ for $r \leq 0$ and $0 \leq \psi(r) \leq 2r$. Additionally, one demands $\frac{\psi(r)}{r} = \psi\left(\frac{1}{r}\right)$ which implies that

laws.

forward and backward gradients are treated the same way. Moreover $\psi(1) = 1$ which is a necessary requirement for second-order accuracy on smooth solutions. Intuitively, limiter functions prevent unphysical oscillations by limiting sharp gradients thereby reducing higher-order schemes to first-order accuracy locally. At the same time, their effect on smooth parts of the solution should be as small as possible. Three often-used limiters are the Van Albada limiter, the minmod and the Superbee limiter:

$$\psi_{\text{vanAlbada}}(r) = \frac{r^2 + r}{1 + r^2}, \quad (259)$$

$$\psi_{\text{minmod}} = \begin{cases} \min(r, 1) & \text{if } r \geq 0 \\ 0 & \text{if } r \leq 0 \end{cases}, \quad (260)$$

$$\psi_{\text{Superbee}} = \max(0, \min(2r, 1), \min(r, 2)). \quad (261)$$

Fig. 41 shows the evolution of the top hat according to the second-order upwind scheme with the Superbee limiter. The discontinuity is sharply resolved and the schemes is not dispersive ¹⁹ As for the time discretisation in the method of

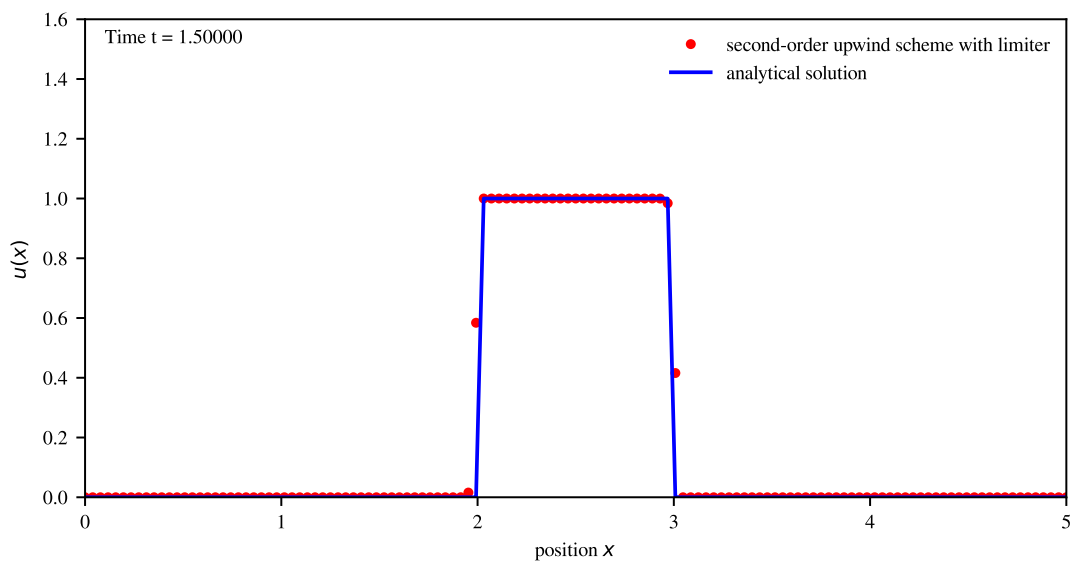


Figure 41: Second-order upwind scheme defined in Eq. (257) with the Superbee limiter defined in Eq. (261) for the time evolution of a Gaussian wave packet according to the linear advection equation (236) with $a = 1$. The simulation parameters are set as in Fig. 38.

lines, a popular choice is the class of TVD, high-order Runge-Kutta (RK) time discretisations. Their derivation starts with the assumption that the first-order forward Euler time discretisation is stable with a suitable time step restriction

¹⁹Note, however, that in general slope limiting can introduce unwanted artifacts into numerical solutions turning sine waves into square wave forms. This can be seen in the interactive notebook accompanying this chapter.

$t < t_0$, given by the CFL condition Eq. (245) in the above case (Shu 2007). They then require a time step restriction of the form

$$\Delta t \leq c\Delta t_0, \quad (262)$$

where c is the CFL coefficient of the TVD method. Shu (2007) lists a number of higher-order TVD RK-methods. In the following, we shall use the second-order method

$$\begin{aligned} u^{(1)} &= u^n + \Delta t L(u^n, t^n), \\ u^{n+1} &= \frac{1}{2}u^n + \frac{1}{2}u^{(1)} + \frac{1}{2}\Delta t L(u^{(1)}, t^n + \Delta t), \end{aligned} \quad (263)$$

and the fourth-order method found by Spiteri and Ruuth (2002) using numerical optimisation for a large CFL coefficient

$$\begin{aligned} u^{(1)} &= u^n + 0.39175222700392\Delta t L(u^n, t^n) \\ u^{(2)} &= 0.44437049406734u^n + 0.55562950593266u^{(1)} \\ &\quad + 0.36841059262959\Delta t L(u^{(1)}, t^n + 0.39175222700392\Delta t) \\ u^{(3)} &= 0.62010185138540u^n + 0.37989814861460u^{(2)} \\ &\quad + 0.25189177424738\Delta t L(u^{(2)}, t^n + 0.58607968896780\Delta t) \\ u^{(4)} &= 0.17807995410773u^n + 0.82192004589227u^{(3)} \\ &\quad + 0.54497475021237\Delta t L(u^{(3)}, t^n + 0.47454236302687\Delta t) \\ u^{n+1} &= 0.00683325884039u + 0.51723167208978u^{(2)} \\ &\quad + 0.12759831133288u^{(3)} \\ &\quad + 0.08460416338212\Delta t L(u^{(3)}, t^n + 0.47454236302687\Delta t) \\ &\quad + 0.34833675773694u^{(4)} \\ &\quad + 0.22600748319395\Delta t L(u^{(4)}, t^n + 0.93501063100924\Delta t). \end{aligned} \quad (264)$$

They have the respective CFL coefficients $c = 1$ and $c = 1.508$ in Eq. (262). The latter is remarkable since it implies that the fourth-order RK scheme allows a more lenient time step condition than the forward Euler method which partly offsets the cost of having a five-stage integrator. In the above examples, we always assumed periodic boundary conditions. One way to boundary conditions in finite difference methods is the use of *ghost cells*. Ghost cells extend the regular simulation grid by additional cells that provide the boundary conditions for the finite difference stencils at the edge of the simulation volume or of different simulation patches. This concludes our discussion of finite difference schemes and

we will now turn towards finite volume schemes.

5.2.2 Finite Volume Method

This discusses the finite volume method (FVM). It allows the numerical solution of nonlinear conservation laws of the form

$$\partial_t u + \nabla \cdot \mathbf{F}(u) = 0, \quad (265)$$

where u is a scalar field. This section heavily draws on the lecture notes by Dullemond and Wang (2009) and the introductions to FVM by LeVeque (2002) and Hirsch (2007). Finite volume schemes divide the spatial domain into small control volumes Ω known as *cells*. They go on to solve the integral version of the conservation law

$$\partial_t \int_{\Omega} u \, d\mathbf{x} + \oint_S \mathbf{F} \cdot d\mathbf{S} = 0. \quad (266)$$

The time variation of the average of u inside the control volume only depends on the surface value of the fluxes. Each cell exchanges the conserved quantity with neighbouring cells via fluxes at the cell boundaries. Finite volume schemes mimic this behaviour on a discrete level. This makes finite volume schemes manifestly conservative which has the advantage that they yield the unique physical solution of a PDE even in the presence of shocks.

In the following we will only consider the case of one-dimensional scalar laws, but the discussion can be easily extended to systems of nonlinear conservation laws in an arbitrary number of spatial dimensions. As in the finite difference case, we start by discretising the time and space dimensions on a uniform grid with N points per spatial dimension and subdivide the time axis into constant time intervals Δt . In addition, we define the cells $\Omega_i = [x_{i-\frac{1}{2}}, x_{i+\frac{1}{2}}]$ at every grid point. The cell centres are located on the grid and the respective cell faces S_i are located between the grid points at $x_{i-\frac{1}{2}}$ and $x_{i+\frac{1}{2}}$. We define the numerical approximation \bar{u}_i to the cell-averages in the cell Ω_i as

$$\bar{u}_i(t) = \frac{1}{\Delta x} \int_{\Omega_i} dx u(x, t) = \frac{1}{\Delta x} \int_{x_{i-\frac{1}{2}}}^{x_{i+\frac{1}{2}}} u(x, t) dx. \quad (267)$$

The conservation law can now be expressed in terms of the cell averages as

$$\partial_t \bar{u}_i(t) = \frac{F(u(x_{i-\frac{1}{2}}, t)) - F(u(x_{i+\frac{1}{2}}, t))}{\Delta x}. \quad (268)$$

Using a suitable time discretisation, we obtain an explicit numerical scheme for

the cell averages

$$\bar{u}_{i+1} = \bar{u}_i - \frac{\Delta t}{\Delta x} (F_{i-\frac{1}{2}}^{n+\frac{1}{2}} - F_{i-\frac{1}{2}}^{n+\frac{1}{2}}), \quad (269)$$

where we evaluate the fluxes at the time $t = (n + \frac{1}{2})\Delta t$. Eq. (269) can in fact conserve the quantity u if the flux approximations at the cell-faces are *consistent*. A consistent flux discretisation at a given cell-face must be independent of the cell considered²⁰. For a consistent flux approximation, a theorem of Lax and Wendroff implies that if the solution u_i of the discretised equation (269) converges boundedly to some function $u(x, t)$ when $\Delta x, \Delta t$ tend to zero, then $u(x, t)$ is a weak solution of Eq. (265) (Hirsch 2007, p.209). The properties of a given finite volume scheme now depend on how we approximate the fluxes $F_{i-\frac{1}{2}}^n$ at the cell faces. In the following, we give explicit flux approximation for the advection equation with non-constant advection velocity

$$\partial_t u + \partial_x (v(x) \cdot u) = 0, \quad (270)$$

where $F(u) = v(x) \cdot u$. As a first approximation, we can assume the exact solution $u(x)$ in the cell Ω_i to coincide with its average \bar{u}_i . This approach is called *Godunov's method*. The simplest flux-conserving scheme based on Godunov's method is the *donor-cell scheme*. The average interface state is simply

$$\bar{u}_{i+\frac{1}{2}}^{n+\frac{1}{2}} = \begin{cases} \bar{u}_i^n, & \text{for } v_{i+\frac{1}{2}} > 0, \\ \bar{u}_{i+1}^n, & \text{for } v_{i+\frac{1}{2}} < 0, \end{cases} \quad (271)$$

and the donor-cell interface flux is given by

$$F_{i+\frac{1}{2}}^{n+\frac{1}{2}} = v_{i+\frac{1}{2}} \begin{cases} \bar{u}_i^n, & \text{for } v_{i+\frac{1}{2}} > 0, \\ \bar{u}_{i+1}^n, & \text{for } v_{i+\frac{1}{2}} < 0. \end{cases} \quad (272)$$

The *image behind this scheme* is as follows: For positive velocities the quantity at the cell center u_i is carried to the cell edge by the velocity at the left cell edge $v_{i-\frac{1}{2}}$. For negative velocities, it is the velocity at the right cell edge $v_{i+\frac{1}{2}}$ that carries u_i away. Evaluating the flux as a product of the advected quantity u and the velocity v at the cell edge, $F_{i+\frac{1}{2}} = v_{i+\frac{1}{2}} u_{i+\frac{1}{2}}$, does not conserve the advected quantity. For a constant velocity field, the donor-cell scheme just reduces to the upwind scheme defined in Eq. (247).

²⁰In practice, this requirement can be violated in subtle ways, for instance, if a higher-order flux discretisation gives different approximation polynomials in neighbouring cells.

Remark 2: Riemann problem

Godunov's method defines a so-called *Riemann problem* at the cell faces. A Riemann problem is an initial value problem where the initial conditions are prescribed by a piecewise constant function with a single discontinuity. At the cell face $S_{i+\frac{1}{2}}$ at the time level n it can be stated as

$$\partial_t u + \partial_x F(u) = 0, \quad (273)$$

$$u_0(x) = \begin{cases} \bar{u}_{i+1}, & x < x_{i+\frac{1}{2}}, \\ \bar{u}_i, & x \geq x_{i+\frac{1}{2}}. \end{cases} \quad (274)$$

For a sufficiently small time step, the Riemann problems at each cell face become independent and one can derive an expression for the cell face flux by solving them. In the case of the linear advection equation, we can easily find an analytical solution to the cell face Riemann problem. In general, its solution is either complicated, as for the ideal fluid equations, or impossible, as in the case of magneto-hydrodynamics. We will therefore settle with approximating the cell-interface fluxes.

Godunov's method yields a first-order method in space and time: We assume the solutions to be constant in each cell and the fluxes to be constant over each time step. We can improve Godunov's method by employing better approximations of the solution within the cell. We can assume that the state within each cell is a linear function of position. Such a state is called *piecewise linear*. More generally, the way one approximates the state inside the cell is called *subgrid model*. An important class of higher-order versions of Godunov's method that commonly use linear or parabolic subgrid models are *Monotone Upstream Schemes for Conservation Laws* (MUSCL), named after the original method of this kind proposed by Leer (1979). Within each cell, the state at the beginning of the time step is given by

$$u(x, t = t_n) = \bar{u}_i^n + \sigma_i^n (x - x_i) \quad \text{for } x_{i-\frac{1}{2}} < x < x_{i+\frac{1}{2}}, \quad (275)$$

where σ_i^n is a suitably chosen slope. The flux at the cell-interface is then given by

$$F_{i+\frac{1}{2}}(t) = \max(0, v_{i+\frac{1}{2}}) \bar{u}_i^n + \min(v_{i+\frac{1}{2}}, 0) \bar{u}_{i+1}^n + v_{i+\frac{1}{2}} \sigma_i^n \left(\frac{1}{2} \Delta x - v_{i+\frac{1}{2}} (t - t_n) \right), \quad (276)$$

which after averaging over a time step Δt reads

$$F_{i+\frac{1}{2}}^{n+\frac{1}{2}} \approx \langle F_{i+\frac{1}{2}}(t) \rangle = \max(0, v_{i+\frac{1}{2}}) \bar{u}_i^n + \min(v_{i+\frac{1}{2}}, 0) \bar{u}_{i+1}^n + \frac{1}{2} v_{i+\frac{1}{2}} \sigma_i^n (\Delta x - v_{i+\frac{1}{2}} \Delta t). \quad (277)$$

If we now choose a central difference approximation $\sigma_i^n = \frac{\bar{u}_{i+1}^n - \bar{u}_{i-1}^n}{2\Delta x}$ for the slope, we obtain a method that is second-order in space. But as in the finite difference case, such a scheme leads to unphysical oscillations. We need to introduce limiters to avoid these unphysical oscillations. This time, instead of limiting the slopes σ_i^n , we limit the corresponding time-averaged fluxes and obtain

$$F_{i+\frac{1}{2}}^{n+\frac{1}{2}} = \max(0, v_{i+\frac{1}{2}}) \bar{u}_i^n + \min(v_{i+\frac{1}{2}}, 0) \bar{u}_{i+1}^n + \frac{1}{2} |v_{i+\frac{1}{2}}| \left(1 - \left| \frac{v_{i+\frac{1}{2}} \Delta t}{\Delta x} \right| \right) \psi(r_{i+\frac{1}{2}}^n) (\bar{u}_{i+1}^n - \bar{u}_i^n), \quad (278)$$

where ψ is a slope limiter (i.e. the limiters defined in Eqs. (261), (260) or (259)) and

$$r_{i+\frac{1}{2}}^n = \begin{cases} \frac{\bar{u}_i^n - \bar{u}_{i-1}^n}{\bar{u}_{i+1}^n - \bar{u}_i^n}, & \text{for } v_{i+\frac{1}{2}} \geq 0, \\ \frac{\bar{u}_{i+2}^n - \bar{u}_i^n}{\bar{u}_{i+1}^n - \bar{u}_i^n}, & \text{for } v_{i+\frac{1}{2}} \leq 0. \end{cases} \quad (279)$$

The resulting scheme is the donor-cell scheme with an additional correction that makes it second-order. The MUSCL-type schemes together with higher order TVD RK time discretisations will be our method of choice for solving the continuity equation because they are higher-order, easy to implement and do not require the formal solution of the Riemann-problem at the cell interfaces. This concludes our discussion of finite volume schemes as well as the brief introduction into some important concepts in CFD.

5.3 Simulating the Hamilton-Jacobi Equation

This section is based on (Shu 2007) and discusses numerical strategies for the solution of Hamilton-Jacobi (HJ) equations of the form

$$\frac{\partial S(\mathbf{x}, t)}{\partial t} + H(S_{x_1}, S_{x_2}, \dots, S_{x_d}) = 0, \quad (280)$$

$$S(x, 0) = S_0(x), \quad (281)$$

where S_{x_i} denotes a partial derivative of S w.r.t. to the coordinate x_i and h is a Lipschitz continuous function. We introduce $v_i := S_{x_i}$ and take the gradient of

the Hamilton-Jacobi equation to see that the dynamics of \mathbf{v} are governed by the conservation law

$$\mathbf{v}_t + H(\mathbf{v})_x = 0, \quad (282)$$

$$\mathbf{v}(\mathbf{x}, 0) = \mathbf{v}^0(\mathbf{x}). \quad (283)$$

This connection between HJ equations and conservation laws can be used to develop strategies for the numerical solution of the HJ equation and leads from the HJ-Madelung equation (22) to the fluid equations (26). In general, the solutions \mathbf{v} of the conservation law Eq. (282) will be bounded and have a bounded total variation, but develop discontinuities. These discontinuities translate into kinks for solutions of the HJ equation. The unique, physical (in the context of classical mechanics) weak solution of the HJ equation is called viscosity solution and can be singled out by certain inequalities. In the following, we consider numerical schemes that are guaranteed to converge to the viscosity solution for $\Delta x, \Delta t \rightarrow 0$. Let us consider a uniform, one-dimensional grid with constant grid spacing Δx . We further introduce the forward and backward velocities

$$v_{i+\frac{1}{2}} = \frac{S_{i+1} - S_i}{\Delta x}, \quad v_{i-\frac{1}{2}} = \frac{S_i - S_{i-1}}{\Delta x}. \quad (284)$$

First-order monotone schemes are defined as schemes of the form

$$\partial_t S_i = -F\left(v_{i+\frac{1}{2}}, v_{i-\frac{1}{2}}\right). \quad (285)$$

The argument function $F(a, b)$ is a *monotone flux* that is characterised by the following properties:

- Lipschitz continuity in both arguments;
- It is a non-decreasing function in a and non-increasing function in b ;
- Consistency with the physical flux: $F(a, a) = H(a)$.

Monotone schemes are guaranteed to converge to the viscosity solution of the HJ equation and are numerically stable. They are our method of choice for discretising the convective term in the HJ-Madelung equation Eq. (22). Note, however, that the latter is not an HJ equation in the sense of Eq. (282) because of the coupling to the continuity equation and the quantum pressure and potential terms. This has the advantage that we do not worry too much about discontinuous derivatives of S (shocks in the Madelung fluid) because of the diffusive nature of the quantum pressure term. At the same time, we have no theoretical

convergence guarantees for the resulting numerical scheme and need to rely on numerical experimentation to assess its properties. Examples of monotone fluxes include the Godunov flux

$$F(a, b) = \begin{cases} \min_{a \leq x \leq b} H(x) & a \leq b \\ \max_{b \leq x \leq a} H(x) & a > b, \end{cases} \quad (286)$$

as well as the Lax-Friedrichs flux

$$F(a, b) = \frac{1}{2}[H(a) + H(b) - \alpha(b - a)], \quad (287)$$

where $\alpha = \max_x |H'(x)|$. They both apply to a general Hamiltonian. There are other simple monotone fluxes which only apply to Hamiltonians of a certain form. If the Hamiltonian is of the form $H(v_1, \dots, v_n) = f(v_1^2, \dots, v_n^2)$ where f is a monotone function of each argument, one can use the Osher-Sethian flux

$$\hat{H}^{OS}(v_{1,i-\frac{1}{2}}, v_{1,i+\frac{1}{2}}, \dots, v_{n,i-\frac{1}{2}}, v_{n,i+\frac{1}{2}}) = F(\bar{v}_{1,i}^2, \dots, \bar{v}_{n,i}^2), \quad (288)$$

where \bar{v}_i^2 are implemented as

$$\bar{v}_i^2 = \begin{cases} (\min(v_{i-\frac{1}{2}}, 0))^2 + (\max(v_{i+\frac{1}{2}}, 0))^2, & \text{if } f \text{ non-increasing in } \bar{v}_i^2 \\ (\min(v_{i+\frac{1}{2}}, 0))^2 + (\max(v_{i-\frac{1}{2}}, 0))^2, & \text{if } f \text{ non-decreasing in } \bar{v}_i^2. \end{cases} \quad (289)$$

The Osher-Sethian-flux applies to the convective term in the HJ-Madelung equation and will be used in the following since it is purely upwind and easy to implement. Note that the resulting scheme for a regular HJ equation requires a CFL condition of the form (Osher and Shu 1991):

$$\Delta t \leq \frac{\Delta x}{2 \sum_i |\partial_i H|}, \quad (290)$$

where $\Delta t \leq \frac{\Delta x}{2 \sum_i |v_i|}$ for $H = \sum v_i^2/2$.

5.4 Simulating Gravity

By now, we have almost all ingredients to describe numerical schemes for solving the HJ-Madelung equations. We know how to solve the continuity and a generic HJ equation. However, the HJ equation (22) involves two additional terms: the quantum pressure term and the potential term. In this section, we discuss how to best describe time evolution with the gravitational potential and

draw on (Zimmermann 2020, p. 62ff) and Mocz et al. (2017). We start by going back to the wave formulation of the SPS and consider it in the form given in Eqs. (18) and (19):

$$i\hbar\partial_t\psi(\mathbf{x},t) = \left(-\frac{\hbar^2}{2m}\Delta + m\phi(\mathbf{x},t)\right)\psi(\mathbf{x},t), \quad (291)$$

$$\Delta\phi(\mathbf{x},t) = 4\pi G a \rho_b \delta(\mathbf{x},t), \quad (292)$$

If we wanted to explicitly evolve the wave equation, we would have to compute the time-ordered evolution operator $\hat{U}(t,t')$

$$\hat{U}(t,t') = \hat{T} e^{\frac{i}{\hbar} \int_t^{t'} ds \hat{H}(s)}, \quad (293)$$

where \hat{T} is the time-ordering symbol. The explicit time-dependence of the Hamiltonian via the gravitational potential makes the action of the time-ordering symbol non-trivial even for small time steps Δt . Therefore, one has to find an efficient approximation for the time-ordered evolution operator \hat{U} .

What we can find are the time evolution operators \hat{U}_K and \hat{U}_V for the kinetic sub-Hamiltonian

$$\hat{H}_K = -\frac{\hbar^2}{2m}\Delta, \quad (294)$$

and the potential sub-Hamiltonian

$$\hat{H}_V = m\phi(\mathbf{x},t), \quad (295)$$

where $\hat{H} = \hat{H}_K + \hat{H}_V$:

$$\hat{U}_K(\Delta t) = \exp\left(-i\frac{\hbar^2}{2m}k^2\Delta t\right), \quad (296)$$

$$\hat{U}_V(\Delta t) = \exp(-im\phi\Delta t). \quad (297)$$

The operator \hat{U}_K is exact because the kinetic Hamiltonian naturally does not have an explicit time dependence. The operator \hat{U}_V also is exact even though the potential Hamiltonian seemingly explicitly depends on time via the gravitational potential. The reason is that the action of the gravitational potential only rotates the phase, but conserves the density. Hence, the potential Hamiltonian is also time-independent as long as we can ignore the action of the kinetic sub-Hamiltonian for small time steps Δt . We can therefore use \hat{U}_K and \hat{U}_V to find approximations of the exact time evolution operator. The time evolution of the

wave function for a small time step Δt is given by

$$\psi(\mathbf{x}, t + \Delta t) = \exp \left[\frac{i\Delta t}{\hbar} \left(\frac{\hbar^2}{2m} \Delta - \frac{m}{2} \phi(\mathbf{x}, t + \Delta t) - \frac{m}{2} \phi(\mathbf{x}, t) \right) \right] \psi(\mathbf{x}, t). \quad (298)$$

The exponential can be simplified using the Baker-Hausdorff-Campbell formula

$$\begin{aligned} \psi(\mathbf{x}, t + \Delta t) &= \exp \left(-\frac{im\Delta t}{2\hbar} \Phi(\mathbf{x}, t + \Delta t) \right) \\ &\times \exp \left(\frac{i\hbar\Delta t}{2m} \Delta \right) \\ &\times \exp \left(-\frac{im\Delta t}{2\hbar} \Phi(\mathbf{x}, t) \right) \psi(\mathbf{x}, t) \\ &+ \mathcal{O}(\Delta t)^3. \end{aligned} \quad (299)$$

We can read off a second-order time-accurate approximation of the exact time evolution operator as

$$\hat{U}_{K+V}(\Delta t) = \hat{U}_K \left(\frac{1}{2} \Delta t \right) \circ \hat{U}_V(\Delta t) \circ \hat{U}_K \left(\frac{1}{2} \Delta t \right) + \mathcal{O}(\Delta t^3). \quad (300)$$

Because of the close resemblance to the kick-drift-kick time evolution in N -Body simulations, we will refer to this scheme as kick-drift-kick scheme in the following. The kick corresponds to the application of the potential operator and the drift is the application of the kinetic operator. The kick-drift-kick scheme is time-symmetric and norm-preserving as it is the composition of unitary maps. In fact, we can further simplify the time evolution operator by recognising that the kicks leave the density and therefore the gravitational potential unchanged. They can be combined as

$$\hat{U}_{K+V}(\Delta t) = \hat{U}_K(\Delta t) \circ \hat{U}_V(\Delta t) + \mathcal{O}(\Delta t^3), \quad (301)$$

after we initialise the algorithm with an initial kick by half a time step. As a result, one needs to solve the Poisson equation only once per time step. In the context of the HJ-Madelung equations, the kinetic term in the Schrödinger equation corresponds to the combined evolution of the continuity and HJ equations including the quantum pressure but excluding the potential term. Including the quantum pressure term in the kick step as in (Li, Hui and Bryan 2018, p. 18) does not lead to a second-order time-accurate scheme since the quantum pressure is part of the drift operator.

5.5 Simulating the Schrödinger Equation

This section reviews the two main approaches for solving the Schrödinger equation in the context of the SPS: finite difference and pseudospectral methods. The code presented in (Schive, Chiueh and Broadhurst 2014) uses a modification of an explicit finite difference method known in the literature as *forward-in-time-centered-in-space* (FTCS). The kinetic operator is discretised using a central finite difference such as

$$\Delta\psi = \frac{\psi_{i+1} - 2\psi_i + \psi_{i-1}}{\Delta x^2}, \quad (302)$$

and the discretisation in time is performed using a second-order leapfrog integrator. One can easily choose arbitrarily high-order central differences in this method. In practice, one is limited by several factors: Higher-order differences increase the number of required floating point operators and need bigger ghost boundaries thereby also increasing the memory requirements of the scheme. In addition, they need a stricter CFL-condition of the form

$$\Delta t \leq \min \left(C_{CFL,K} \frac{ma^2}{\hbar} \Delta x^2, C_{CFL,V} \frac{\hbar}{a|\phi_{max}|} \right), \quad (303)$$

where $C_{CFL,K}$ and $C_{CFL,V}$ are constants of order unity constant that depend on the details of the discretisation (Schwabe, Niemeyer and Engels 2016). This condition on the time step ensures that the phase rotation of the wave function in one time step is smaller than 2π . Another way to look at the relation between the temporal and spatial step sizes is to realise that the SPS depends on higher-order derivatives and admits whistler-type waves with $\omega = \nu k^2$. This generally implies a time step condition of the form $\Delta t \propto \Delta x^2$ (Hopkins 2018).

Apart from finite differences, the pseudospectral approach is a well established and highly accurate method of discretising the Schrödinger equation in the spatial domain. It is suitable for periodic boundary conditions and applications for solving the SPS can be found in (Mocz et al. 2017) or (May and Springel 2021), for instance. The basic idea of this method is very simple: We take the discrete Fourier-transform of ψ , apply the Laplace operator by multiplying with k^2 in Fourier space and take the inverse Fourier transform. For smooth $\psi(x, t)$ we achieve spectral convergence, that is, faster than any polynomial. This is possible because unlike finite difference methods which only use neighbouring grid points, the Fourier transform uses the entire computation domain at once. The overall computational work is still of order $\mathcal{O}(N \log N)$ thanks to the fast Fourier transform algorithm. This method, of course, only works for the wave formulation of the SPS and does not integrate well with other finite difference or finite

volume methods. Using a Fourier transform, we can similarly solve the Poisson equation for periodic boundary conditions ²¹. Combining the solution of the Poisson equation and the Schrödinger equation via a fast Fourier transform with the kick-drift-kick scheme for time evolution, we obtain the algorithm presented by Mocz et al. (2017). We will refer to it as *reference wave scheme* in the following and use it to compute reference solutions in all simulations with gravity where no analytical solutions to the SPS exist.

5.6 The Phase Scheme

At this point, we are ready to present the scheme that we use to solve the HJ-Madelung equations (22) and (21) in the hybrid scheme. In the following, we will simply refer to this higher-order scheme as *phase scheme*. In order to account for cosmological expansion, we perform the substitutions $dt \rightarrow a^2 dt \equiv d\tau$ and $\rho \rightarrow a^{-3}\rho$ and normalise the comoving mass density ρ to the comoving background density ρ_b :

$$\frac{m}{\hbar} \partial_\tau \rho + \nabla \cdot (\rho \nabla S) = 0, \quad (304)$$

$$\frac{m}{\hbar} \partial_\tau S + \frac{1}{2} (\nabla S)^2 + \phi S - \frac{1}{2} \frac{\Delta \sqrt{\rho}}{\sqrt{\rho}} = 0, \quad (305)$$

$$\Delta \phi - 4\pi G a (\rho - 1) = 0. \quad (306)$$

The system of equations consists of a continuity equation coupled to a HJ equation with additional quantum pressure and potential terms. Because of the dispersive nature of the quantum pressure term, the continuity equation does not develop shocks in theory. Neither does the HJ equation develop kinks. Yet, the quantum pressure term is not positive-definite and can lead to negative densities. Moreover, limited resolution and phase jumps by multiples of 2π can lead to shock-like solutions in practice. In our numerical experiments, the only way to achieve a stable higher-order scheme was to use shock-capturing schemes for evolving the continuity equation and the convective term of the HJ ²². We start by describing the design of the phase scheme and then go on to study its stability, accuracy and limitations using a series of test cases.

²¹Different boundary conditions can in fact be implemented by computing the convolution with a modified Green's function.

²²An alternative approach to evolve the phase field $S(\mathbf{x}, t)$ consist in solving the convective equations (52). A simple central finite difference discretisation for the diffusion terms and upwinding for the convection terms did, however, not yield a stable scheme for high Peclet numbers. In cosmological simulations, the scheme tended to fail once the formation of halos set in.

5.6.1 Design

We evolve the continuity equation using a MUSCL scheme with linear subgrid model according to Eq. (278) together with the VAN ALBADA limiter

$$\psi(r) = \frac{r^2 + r}{1 + r^2}, \quad (307)$$

where r is the ratio of subsequent gradients. As for the HJ scheme, we use a finite difference scheme. The convection term is discretised according to Eq. (289) with the Sethian-Osher flux. The velocities at the cell faces are then computed as slope-limited finite differences using the VAN ALBADA limiter. A more detailed analysis of the impact of different limiters can be found in appendix A.7. We treat the cell averages $\bar{\rho}$ in the finite volume scheme as point values ρ in the discretisation of the quantum pressure term. Technically, we use the MUSCL scheme as conservative finite difference method and not as finite volume scheme. This has the consequence that the maximum order of accuracy we can reach with the linear subgrid MUSCL scheme is second order (Nishikawa 2020). The quantum pressure term is discretised as

$$\frac{\Delta\sqrt{\rho}}{\sqrt{\rho}} = \left(\frac{1}{2}\Delta\log(\rho) + \frac{1}{4}(\nabla\log(\rho))^2 \right), \quad (308)$$

with second-order central finite differences for both the gradient operator and the Laplacian. Fourth-order central differences did not improve the behaviour of the scheme in most test cases and actually required smaller time steps in some. The resulting semi-discrete scheme is discretised with the fourth-order RK method described in Eq. (264). The second-order discretisation described in Eq. (263) also works well, but required a more stringent CFL condition in some test cases. For including the effect of the gravitational potential, we adopt the kick-drift-kick approach described in Eq. (300) together with a pseudospectral method for solving the Poisson equation. In all runs, the time steps were chosen such that they fulfill the CFL condition

$$\Delta\tau \leq \min \left[C_D \frac{m}{\hbar} \Delta x^2, C_K \Delta x \frac{m}{2\hbar \sum_{i=1}^3 |\partial_i S|}, C_V \frac{\hbar}{|\phi_{max}|} \right], \quad (309)$$

where $C_D = \frac{1}{6}$, $C_K = 0.5$ and $C_V = 2\pi \cdot 0.3$ as in the Madelung fluid simulations in (Schwabe, Niemeyer and Engels 2016) and the wave simulation in (Schive, Chiueh and Broadhurst 2014). The exact value of C_D depends on the time discretisation used. Note that these values are purely empirical because the HJ-Madelung equations are nonlinear and one can, in general, not derive analytical conditions

on the time steps in the nonlinear case.

5.6.2 Testing and Validation

In this section, we verify the PYTHON-implementation of the phase scheme that can be found in the github repository accompanying this chapter. It heavily relies on the excellent SCIPY- and NUMPY-libraries (Harris et al. 2020; Virtanen et al. 2020). We conduct a series of one- and two-dimensional tests against analytical solutions of the Schrödinger equation and compare the phase scheme to numerical solutions of the SPS computed with the reference wave scheme. In addition to mass conservation, which is guaranteed up to machine precision by the finite volume scheme, we monitor conservation of the energy as given in Eq. (47):

$$E = \int \left[\frac{\hbar^2}{2m^2} [\nabla\psi]^2 + \frac{1}{2}\phi[\psi]^2 \right] d^3x \quad (310)$$

$$= \int \frac{\hbar^2}{2m^2} (\nabla\sqrt{\rho})^2 d^3x + \int \frac{\rho}{2} v^2 d^3x + \int \frac{\rho}{2} \phi d^3x. \quad (311)$$

Moreover, we numerically assess the accuracy of the resulting scheme by studying the truncation error of the density field in the L1-norm. For comparison, we also implemented a first-order version of the phase scheme without slope limiters. It uses the donor-cell scheme described in Eq. (272) to evolve the continuity equation and the Osher-Sethian-flux with first-order finite differences to evolve the phase equation. Apart from this difference, the first-order and higher-order phase schemes are identical. We assume periodic boundary conditions, set $\frac{\hbar}{m} = 1$ and turn off gravity $G = 0$ and cosmological expansion $a = 1$ unless denoted otherwise. The tests 1, 2 and 4 are taken from (Li, Hui and Bryan 2018).

Animations of the 1D and 2D tests are available on [github](#). They are also linked with the figures in the following section. Simply *click on the figures* to view the animations.

Test 1: Standing Gaussian Wave Packet (1D)

In the first test, we initialise the simulation with a solution to the free 1D Schrödinger equation: the stationary Gaussian wave packet described in Eq. (60)

$$\psi(x, t) = \sqrt{\frac{1}{\alpha + i\frac{\hbar t}{m}}} \exp\left(-\frac{(x - x_0)^2}{2(\alpha + i\frac{\hbar t}{m})}\right). \quad (312)$$

Fig. 42 compares the numerical solution obtained using the phase scheme with the analytical solution. The phase S correctly evolves into the parabola described

by

$$S_0(x, t) = \frac{x^2 \frac{\hbar t}{m}}{2(\alpha^2 + \frac{\hbar^2 t^2}{m^2})} - \arctan\left(\frac{\hbar t}{m\alpha}\right) / 2. \quad (313)$$

The low-density regions at the simulation boundaries do not cause the phase scheme to fail.

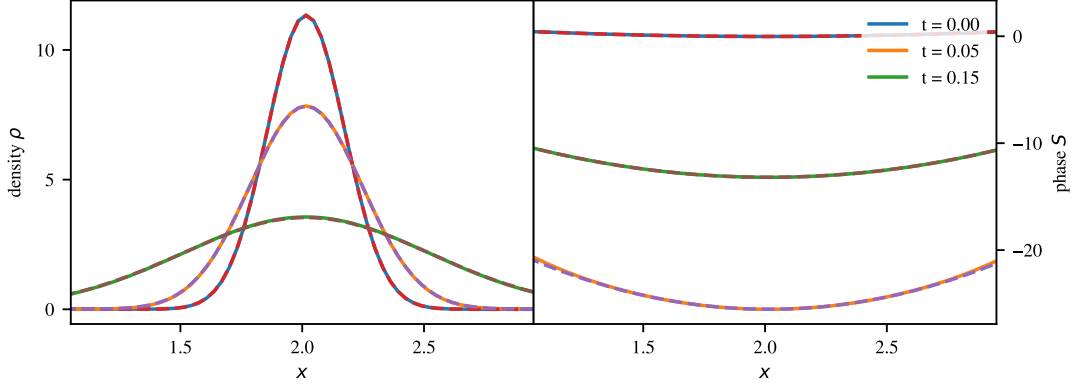


Figure 42: Evolution of wave function at three different times. Solid lines represent the numerical solution using the phase scheme. Dashed lines represent analytical solution. Parameters in Eq. (312) set as $\alpha = \frac{1}{10}$, $x_0 = 2$ with a domain size $L = 10$ and a resolution $\Delta x = 10/128$.

Test 2: Quasi-Shock (1D)

The SPS in a static universe exhibits an important symmetry that we have not yet mentioned: the *scaling symmetry*. If a wave function ψ solves the SPS, then so does another wave function ψ' with

$$\psi(\mathbf{x}, t)' = \lambda^2 \psi(\lambda \mathbf{x}, \lambda^2 t), \quad \lambda \in \mathbb{R}_{>0}. \quad (314)$$

This suggests that we look for solutions to the free Schrödinger equation that only depend on the ratio x/\sqrt{t} . One such self-similar solution is given by

$$\psi(x, t) = \frac{A}{2} + B - \frac{1}{2}(1 \mp i)C\left(x\sqrt{\frac{m}{\pi\hbar|t|}}\right) - \frac{A}{2}(1 \pm i)S\left(x\sqrt{\frac{m}{\pi\hbar|t|}}\right), \quad (315)$$

where the upper/lower sign is for a positive/negative t , A and B are constants and C and S are the Fresnel integrals

$$C(\theta) = \int_0^\theta \cos\left(\frac{\pi\xi^2}{2}\right) d\xi, \quad S(\theta) = \int_0^\theta \sin\left(\frac{\pi\xi^2}{2}\right) d\xi. \quad (316)$$

The asymptotic behaviour of the density ρ is $\rho \rightarrow (A + B)^2$ as $x \rightarrow -\infty$ and $\rho \rightarrow B^2$ as $x \rightarrow \infty$. The density jump becomes increasingly sharp as $t \rightarrow 0$

and resembles what one expects for shock formation in a normal fluid. But this resemblance is superficial because a normal shocks irreversibly produce entropy whereas FDM dynamics are time-reversible (Hui et al. 2017, p.27). This test case is interesting because the density profile exhibits characteristic oscillations on the scale $x \sim \sqrt{\hbar t/m}$. Fig. 43 compares the numerical solution using the phase scheme with the analytical solution of Eq. (315) for $t_0 = 0.0025$ in code units. The phase scheme agrees well with the analytical solution which demonstrates the phase scheme's ability to capture intricate interference patterns as long as the density is sufficiently high.

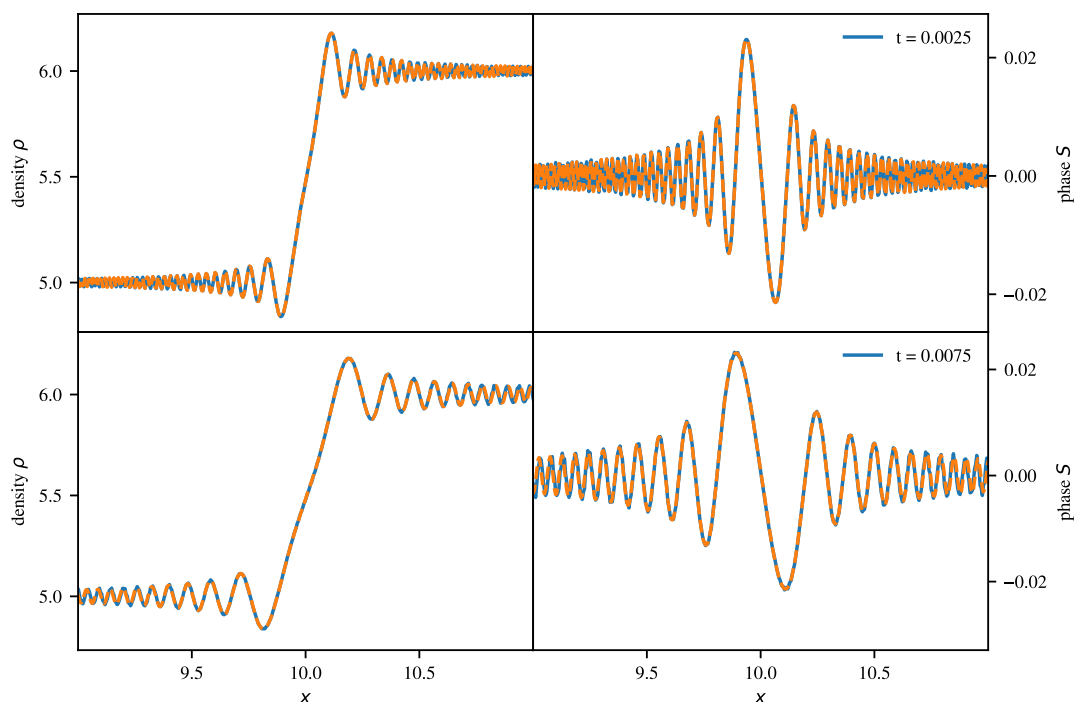


Figure 43: Snapshots of evolution of wave function for Eq. (315). Solid, blue lines represent the numerical solution using the phase scheme. Dashed, orange lines represent analytical solution. Parameters set as $A = \sqrt{5} - \sqrt{6}$, $B = \sqrt{6}$, $x_0 = 10$, domain size $L = 20$ and $\Delta x = 20/4096$. The boundaries of the simulation are cut off since they are polluted by the periodic boundary conditions of the simulation.

Test 3: Expansion Wave (1D)

This test case demonstrates one of the limitations of the phase scheme. The phase scheme may develop discontinuities in the phase field S starting from smooth initial conditions. We consider the Gaussian wave packet described in Eq. (60) with a small background density ϵ :

$$\psi(x, t) = \epsilon + \sqrt{\frac{1}{\alpha + i\frac{\hbar t}{m}}} \exp\left(-\frac{(x - x_0)^2}{2(\alpha + i\frac{\hbar t}{m})}\right), \quad (317)$$

where $\epsilon \in \mathbb{R}$. The phase of this wave function is given by

$$S(x, t) = \arctan \left(\frac{\sin(S_0(x, t))}{\cos(S_0(x, t) + \epsilon)} \right), \quad (318)$$

where S_0 is the phase of the Gaussian wave packet without background density as given in Eq. (313). For $\epsilon > 0$, S has roots x_{0n} when $S_0(x, t) = \pi n$ for $n \in \mathbb{Z}$ at a given time t :

$$x_{0n}(t) = \pm \sqrt{\left(\pi n + \arctan \left(\frac{\hbar t}{m\alpha} \right) / 2 \right) \left(\alpha^2 + \frac{\hbar^2 t^2}{m^2} \right) \frac{2m}{\hbar t}}. \quad (319)$$

If we assume that $\frac{\hbar t}{\alpha m}$ is small, we can expand the inverse tangent function to obtain

$$x_{0n}(t) = \pm \sqrt{2\pi n \alpha^2 \left(\frac{\hbar t}{m} \right)^{-1} + \alpha \left(\frac{\hbar t}{m} \right)^0 + 2\pi n \left(\frac{\hbar t}{m} \right)^1}, \quad (320)$$

where we neglect higher-order terms. The first term under the root is large for small times and the roots for larger n move with higher velocities. It turns out that Eq. (320) roughly describes how a sharp jump in the phase field S propagates. Fig. 44 shows the numerical and analytical evolution of Eq. (317) for four different times. The analytical solution for the phase field is computed by adding multiples of 2π to Eq. (318) until the phase field is continuous. We start with smooth initial conditions and the phase field evolves into a parabola where the density is large. The second panel shows that a discontinuity in the phase field S develops from smooth initial conditions. The third panel shows why this is not an issue for the wave scheme: Whereas the analytical solution of the Schrödinger equation is oblivious to jumps of 2π , the phase scheme cannot easily adjust for them. Fluid schemes for the Madelung equations do not share this problem because the velocity field also does not *see* the 2π jumps. The fourth panel shows that the phase front propagates with a delay compared to the analytical solution and exhibits unphysical oscillations. It does not capture the long-term evolution of the wave packet correctly. A solution to this problem could be the

The p - q -Scheme

We compute the finite differences for the phase field in terms of the variables p and q defined as

$$p = \sin(S/f), \quad q = \cos(S/f). \quad (321)$$

for $f \in \mathbb{R}_{>0}$. The spatial derivatives of S can then be expressed as

$$\partial_x S = (q\partial_x p - p\partial_x q)f. \quad (322)$$

The finite differences computed in this way are insensitive to jumps of $f \cdot 2\pi$. The drawback of this approach is that one needs to resolve f times the de Broglie wavelength. This partly offsets the advantage of using the phase scheme in the first place.

A value of $f = 2$ was sufficient in order for the phase scheme to correctly describe long-term evolution of the wave packet in this test case. In general, we did not observe such a pathological situation occurring in our cosmological model simulations and therefore decided against the p - q -scheme. We believe that it could occur if the flow of the phase field was opposite to the large-scale density gradients at late time. If larger high-resolution simulations reveal that such a situation occurs generically, the p - q -scheme represents a potential remedy.

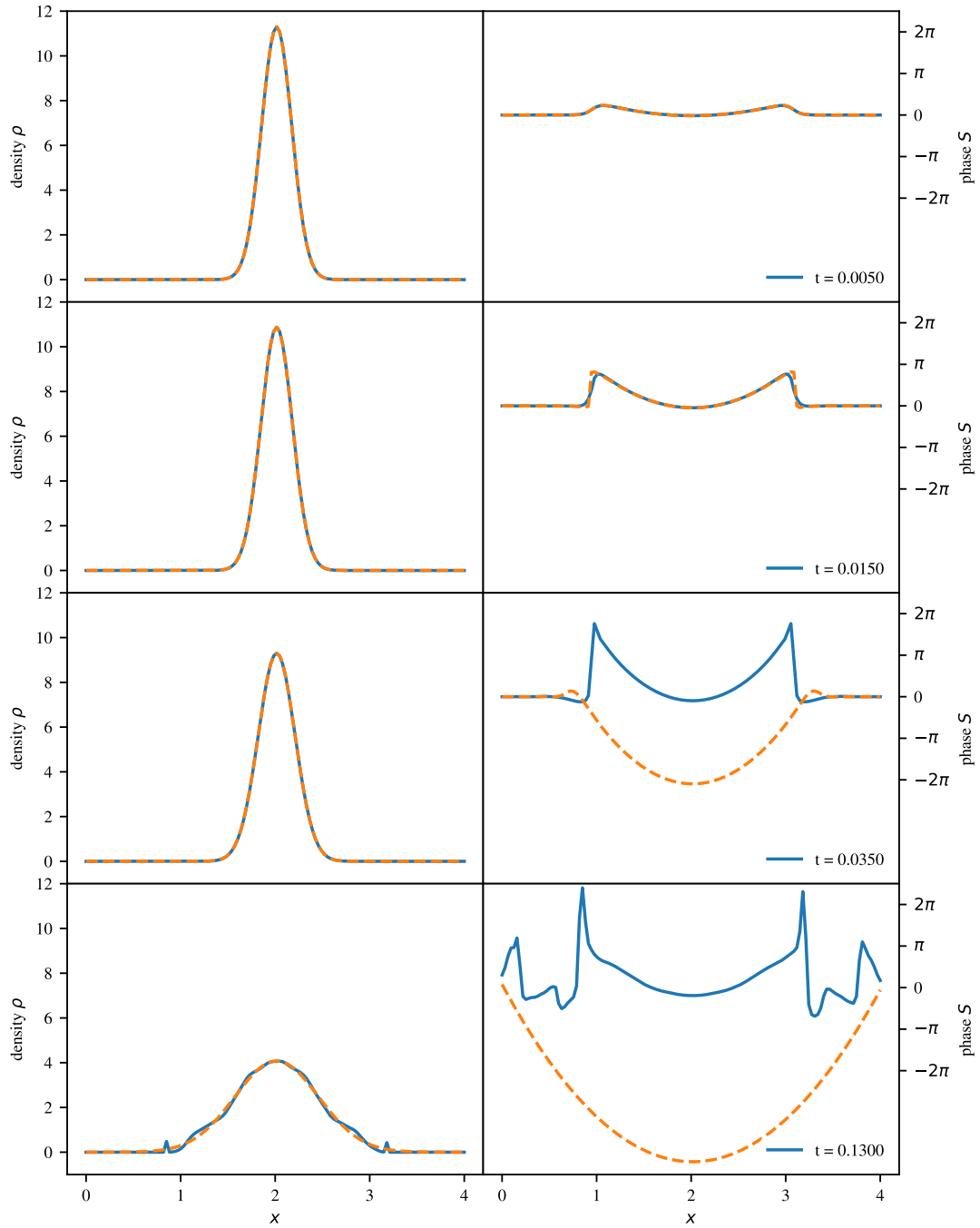


Figure 44: Snapshots of evolution of wave function for Eq. (317). Solid, blue lines represent the numerical solution using the phase scheme. Dashed, orange lines represent analytical solution. $\epsilon = 10^{-4}$ and other parameters are set as in Fig. 42.

Colliding Gaussian Wave Packet (1D)

In this section, we consider two travelling Gaussian wave packets meeting each other. This test highlights another difficulty of the phase scheme: It fails if regions of vanishing density occur.

The wave function of a single packet is given by Eq. (62) and the linear

superposition reads:

$$\begin{aligned} \psi(x, t) = & \sqrt{\frac{\alpha}{\alpha + i\frac{\hbar}{m}t}} \exp\left(-\frac{(x + x_0 - ik\alpha)^2}{2(\alpha + i\frac{\hbar}{m}t)}\right) \exp\left(-\frac{\alpha k^2}{2}\right) \\ & + \sqrt{\frac{\alpha}{\alpha + i\frac{\hbar}{m}t}} \exp\left(-\frac{(x + x_0 + ik\alpha)^2}{2(\alpha + i\frac{\hbar}{m}t)}\right) \exp\left(-\frac{\alpha k^2}{2}\right). \end{aligned} \quad (323)$$

Fig. 45 shows the numerical and analytical evolution of this situation. The numerically computed density field describes the analytical solution well up to $t = 0.0012$ in code units where destructive interference leads to regions of vanishing density. Numerically, the density does not exactly vanish, but as Li, Hui and Bryan (2018) pointed out the true quantum pressure and hence the numerical error still diverge. Correspondingly the numerical solution deviates from the analytical solution at later times. We also observe that the phase field in the middle panels exhibits unphysical oscillations in regions of very low density. The density in these regions is at the order of 10^{-32} in code units and we expect the numerical errors associated with the quantum pressure to be very large. We conclude that the phase scheme performs worse than existing fluid solvers for the Madelung equations, i.e. (Hopkins 2018), that manage to evolve past some of the regions of vanishing density.

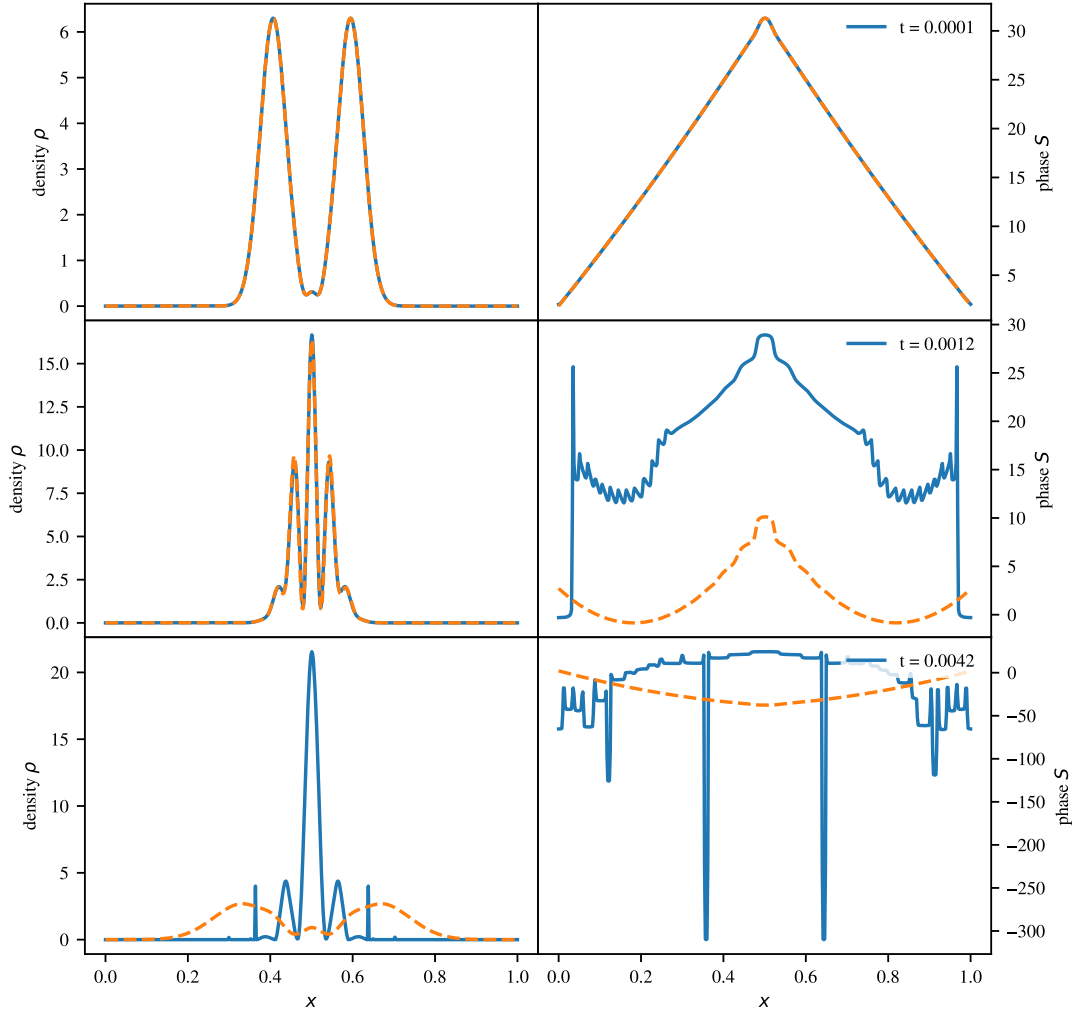


Figure 45: Snapshots of evolution of wave function for Eq. (323). Solid, blue lines represent the numerical solution using the phase scheme. Dashed, orange lines represent analytical solution. Parameters are set as $\alpha = \frac{1}{500}$, $k = 20\pi$, $x_0 = 0.5$, $x_1 = 0.1$, $L = 1$, $\Delta x = 1/512$.

Gravity (2D)

In this section, we test the phase scheme for a slightly more realistic setup in the context of cosmological simulations. We set the gravitational constant $G = 1$, but still leave cosmological expansion turned off. The simulation is initialised with the two-dimensional analogue of Eq. (63):

$$\begin{aligned}
 \psi(x, y) = & \sqrt{\rho_b} + \sum_{n=0}^N \sum_{m=0}^N \\
 & \times \left(\alpha_{n,m} \cos(2\pi nx/L_x) \cos(2\pi my/L_y) \right. \\
 & + \beta_{n,m} \cos(2\pi nx/L_x) \sin(2\pi my/L_y) \\
 & + \gamma_{n,m} \sin(2\pi nx/L_x) \cos(2\pi my/L_y) \\
 & \left. + \delta_{n,m} \sin(2\pi nx/L_x) \sin(2\pi my/L_y) \right), \tag{324}
 \end{aligned}$$

where $\alpha_{n,m}$, $\beta_{n,m}$, $\gamma_{n,m}$ and $\delta_{n,m}$ are small uniform, random numbers and L_x and L_y the extents of the simulation box in the x - and y -directions. These initial conditions correspond to a power spectrum with a sharp cutoff for high k and we will refer to them as *cosmological IC* in the following. Fig. 46 shows the evolution of cosmological IC under the influence of gravity at two different times. The left columns show the density and phase field as computed with the phase scheme, the center columns show their evolution computed using the reference wave scheme and the right column shows the relative differences of the fields. We observe that the two schemes agree well up to $t = 1.0$ in code units. The phase field stays continuous and no low-density regions have formed. Further evolution reveals that the wave and phase schemes disagree at the filaments and halos. The mismatch in the density fields remains limited to these regions and does not propagate into the rest of the simulation. Whereas the phase field remains smooth for the phase scheme, the wave scheme has developed 2π -discontinuities. As a result, the naive algorithm which adds multiples of 2π to make the quantity

$$\tilde{S} = \arctan \left(\frac{\Im(\psi_{wave})}{\Re(\psi_{wave})} \right) \quad (325)$$

continuous fail. This is shown in the bottom plot in the center column of the lower panel. The phase scheme remains stable at later times, but disagrees with the wave scheme. A plot can be found in appendix A.7.

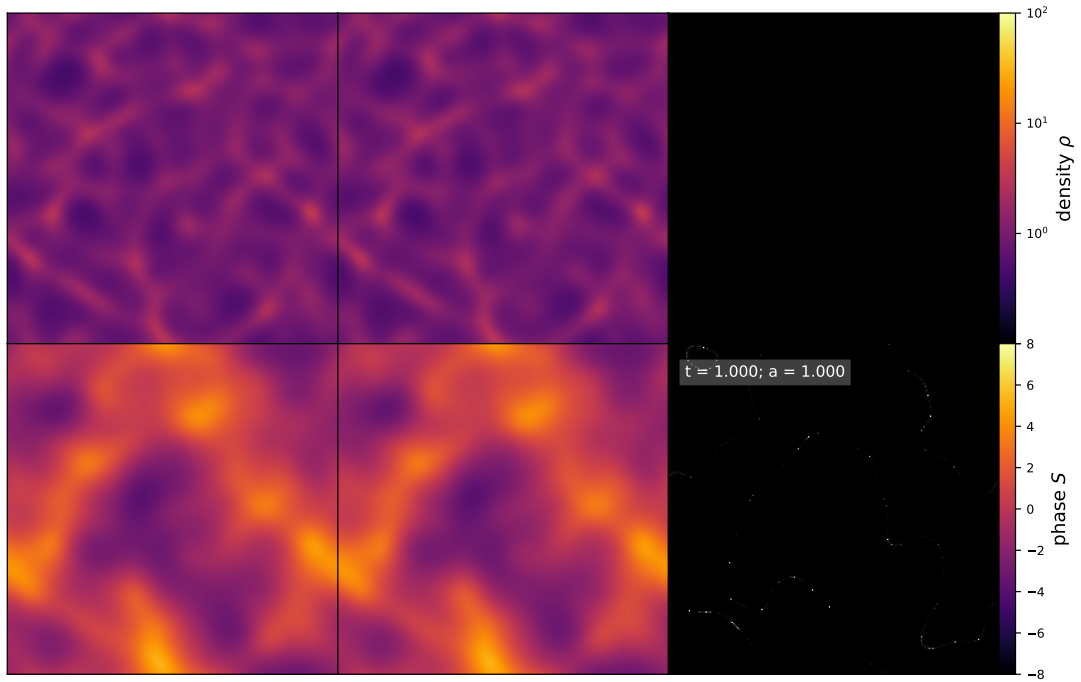
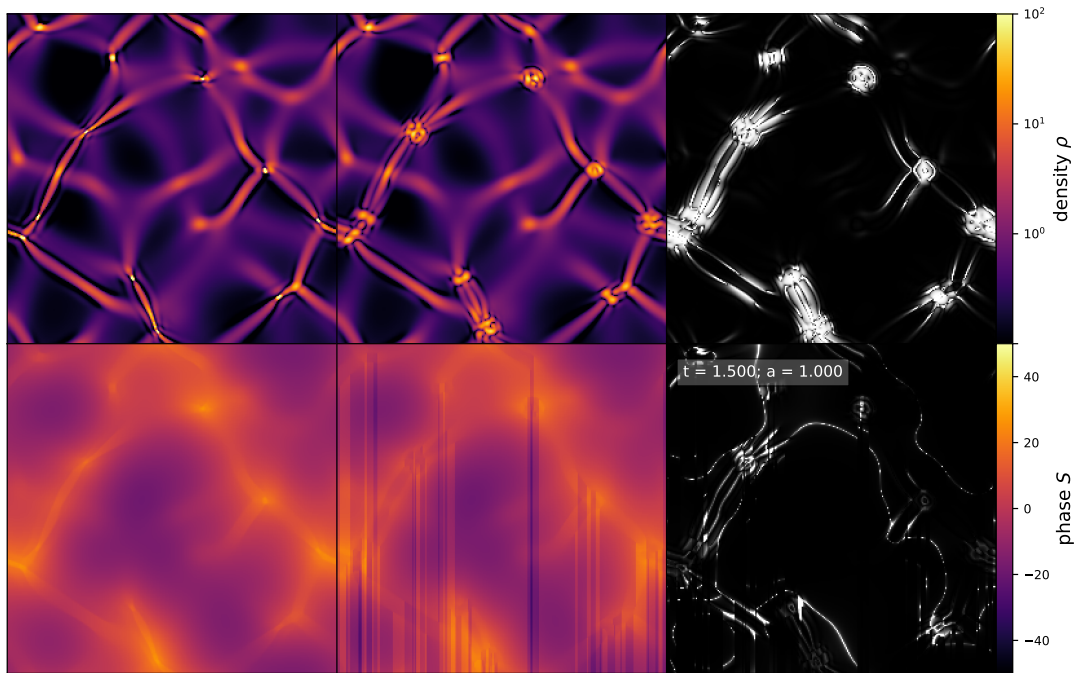
(a) $t = 1.0$ (b) $t = 1.5$

Figure 46: Snapshots of evolution of wave function for Eq. (324) at times $t = 1.0$ and $t = 1.5$ in code units. The left columns show the phase scheme, the center columns show the reference wave scheme and the right columns their relative mismatch. Black regions correspond to zero relative error, whereas white regions correspond to 100% relative error. Parameters are set as $N = 10$, $L = 25$, $\Delta x = 25/256$, $G = 1$ and $a = 1$ with the initial perturbations between 0 and $5 \cdot 10^{-3}$.

Accuracy Test

We measure the accuracy of the phase scheme by computing its truncation error E in the L1-norm. In the one-dimensional case it reads:

$$E(t) = \frac{\sum_{i=1}^N |\rho_i(t) - \rho_{ana}(x_i, t)|}{N}, \quad (326)$$

where $\rho_{ana}(x, t)$ is the density of an analytical solution to the Schrödinger equation. If a numerical scheme has order of accuracy s , we expect the error to behave like

$$E(t) = C(t)(\Delta x)^s + \text{higher-order terms}. \quad (327)$$

The constant $C(t)$ depends on the particular solution computed as well as on the time t . Higher-order terms are asymptotically negligible as $\Delta x \rightarrow 0$. Often, the quality of a numerical method is summarised by the order of accuracy s , but this can be misleading (LeVeque 2002, p.150). The higher-order terms can be dominant on the grids one uses in practice. Similarly, a lower-order method with low C for a given problem can outperform higher-order methods. Fig. 47 shows the truncation error for a number of different test cases as a function of the grid size for solutions to the one-dimensional Schrödinger equation. We visualise them on a double-logarithmic scale because Eq. (327) then takes the form

$$\log E \approx \log |C| + s \log |\Delta x|. \quad (328)$$

Accordingly, we can read off the order of accuracy as slope of the graphs.

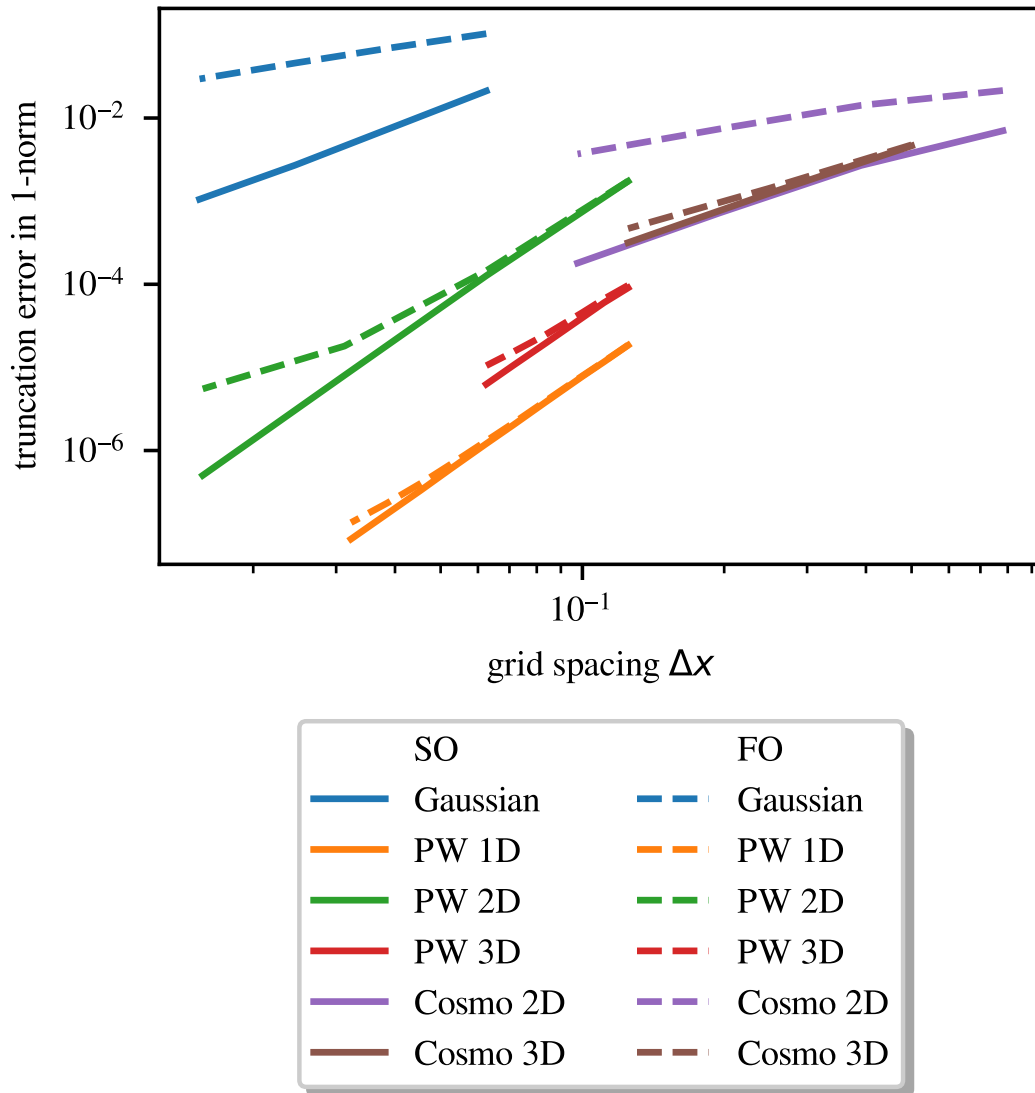


Figure 47: Log-log plot of the L1-truncation error vs. grid size for the higher-order phase scheme (SO, solid lines) and the first-order phase scheme (FO, dashed line) for the HJ-Madelung equations on different test problems: The test *Gaussian* correspond to Eq. (60); the tests *PW 1D*, *PW 2D* and *PW 3D* correspond to solutions of the free Schrödinger equation for cosmological IC without gravity in 1D, 2D and 3D; the tests *Cosmo 2D* and *Cosmo 3D* corresponds to tests with cosmological IC and gravity in 2D and 3D. For the *Cosmo 2D* and *Cosmo 3D* tests, the reference solution was computed using the reference wave scheme.

The higher-order phase scheme is approximately of order two in all tests considered and always outperforms the first-order phase scheme. Appendix A.7 provides a discussion of the effect of choosing different limiters on the accuracy of the phase scheme. It turns out that the choice of limiter can have a large impact on the constant C depending on the test problem, but that for the tests with gravity and cosmological IC all limiters considered perform equally well.

Stability test

In order to assess the stability of the phase scheme, we evolved Eq. (63) for $N = 10$, $L = 25$, $\Delta x = 25/64$, $G = 1$ and $a = 1$ up to $t = 25$. The algorithm remains stable and conserves the density remains positive. Because of interference, energy is not conserved, however. In addition, we also experimented with different time discretisations and the allowed maximum time step conditions, especially in terms of the condition

$$\Delta t \leq C_D \frac{m}{\hbar} \Delta x^2. \quad (329)$$

Fig. 48 shows the truncation error as a function of the time step condition C_D for a number of two-dimensional test cases with gravity. The truncation error starts to increase rapidly once the time steps become too large. For these tests, we found that the phase scheme is stable up to $C_D \sim 0.06$ for the second-order TVD RK method given in Eq. (263), up to $C_D \sim 0.4$ for a third-order TVD RK method and up to $C_D \sim 0.7$ for the fourth-order TVD RK method given in Eq. (264). This result suggests that one should use a higher-than-second-order time discretisation for the phase scheme.

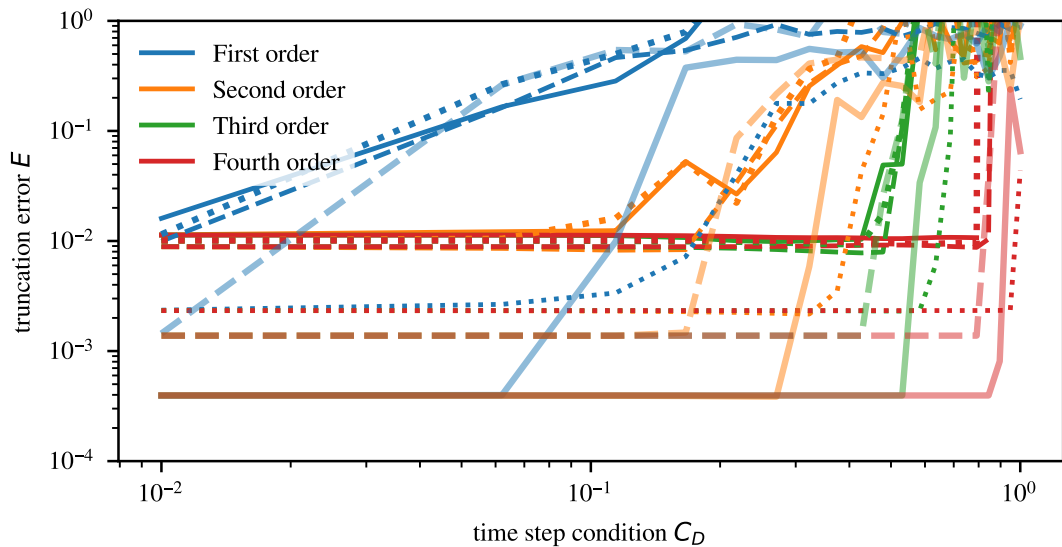


Figure 48: Truncation error E as a function of the time step condition defined in Eq. (329) for a variety of different of different two-dimensional tests with gravity for resolutions between $\Delta x \sim 10^{-2}$ and $\Delta x \sim 10^{-4}$ in code units. The four colours denote the order of the respective time discretisations used.

5.7 The Hybrid Scheme

This section explains how the interplay of the phase scheme and the wave scheme works to produce a hybrid scheme on a static, uniform grid. We have seen that the phase scheme fails in regions of destructive interference where the density vanishes, i.e. the filaments and halos in a cosmological simulation. In these regions, we want to employ a wave scheme. In the following, we will describe the wave scheme and explain how we detect regions of interference and perform the boundary matching.

5.7.1 Design

As wave scheme, we choose a fourth order FTCS method with a second-order RK time discretisation because it is explicit, accurate, integrates well with the phase scheme, is easy to implement and very similar to the scheme used in the GAMER-code. Gravity is also handled with a kick-drift-kick scheme. As criterion for detecting interference, we use the magnitude of the quantum pressure term. Our numerical experiments show that it can reliably indicate where the phase scheme fails. This is because the quantum pressure diverges in regions of vanishing density. Moreover, the quantum pressure is responsible for interference in the HJ-Madelung equations and its magnitude therefore naturally quantifies the importance of interference effects. As an alternative, we considered using the Peclet number of the convective equations (52) as criterion. The Peclet numbers P_{S_r} and P_{S_i} defined via the coefficients F of the convective terms and D of the diffusive terms measure the relative strength between convection and diffusion:

$$D_{S_r} = \frac{\hbar}{2m\Delta x}, \quad D_{S_i} = -\frac{\hbar}{2m\Delta x}, \quad F_{S_r} = v_r, \quad F_{S_i} = v_i, \quad (330)$$

$$P_{S_r} = F_{S_r}/D_{S_r}, \quad P_{S_i} = F_{S_i}/D_{S_i}. \quad (331)$$

In our experiments, P_{S_r} can also be used to reliably determine where the phase scheme fails. Still, we decided to base the *switching criterion* on the dimensionless quantity \mathcal{M}_{int} :

$$\mathcal{M}_{int} = (\Delta x)^2 \frac{1}{N_{dim}} \frac{\Delta\sqrt{\rho}}{\sqrt{\rho}}, \quad (332)$$

where N_{dim} is the number of dimensions. We discretise it according to Eq. (308) with a second-order central difference. \mathcal{M}_{int} has the advantage that it is easy to compute (we compute it anyway for evolving the phase scheme) and that it is independent of the constants G and $\frac{\hbar}{m}$. It proved robust and fairly universal in

our tests. In one dimension, it reads

$$\mathcal{M}_{int} = \left| \frac{\sqrt{\bar{\rho}_{i+1}} - 2\sqrt{\bar{\rho}_i} + \sqrt{\bar{\rho}_{i-1}}}{\sqrt{\bar{\rho}_i}} \right|. \quad (333)$$

If \mathcal{M}_{int} crosses a fixed threshold, we switch to the wave scheme. We empirically found a threshold of around $\mathcal{M}_{int} \sim 0.05$ by experimenting with 2D simulations. It works well for the wave expansion and colliding wave packet tests in 1D as well as for simulations with gravity over a range of different resolutions Δx in 2D and 3D. Yet, it is resolution-dependent and will certainly need improving before it can be used in a large-scale cosmological simulation. Fig. 49 shows which regions it flags for the use of the wave scheme in a 2D simulation with gravity.

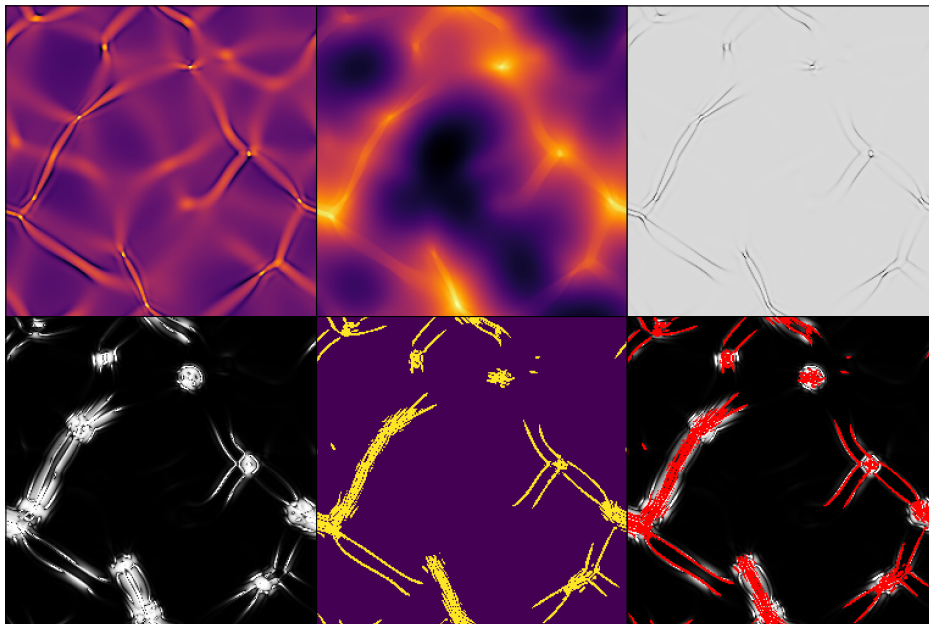


Figure 49: Visualisation of the switching criterion.

In first row from left to right: density, phase, \mathcal{M}_{int} .

In second row from left to right: relative density mismatch between phase scheme and reference wave scheme, regions where \mathcal{M}_{int} defined in Eq. (333) is greater than 0.05, overlay of density mismatch (bw) and regions where switching criterion requires wave scheme (red).

The complete algorithm for the phase scheme reads as follows: We divide the simulation volume into patches that are managed via a binary tree in 1D, a quadtree in 2D and an octree in 3D. We start with a root patch covering the entire simulation. At the beginning of every N_{update} time steps, we check which subregions require the wave scheme. If a subregion requires the wave scheme, the simulation volume is subdivided accordingly and the tree structure updated.

The tree stores where to use the wave and where to use the phase scheme. Next, the phase of the wave function and the phase field are both advanced by half a time step. Then, the ghost boundaries are populated. If a patch using the wave scheme provides boundary information for a patch using the phase scheme, the phase is made continuous by adding multiples of 2π at every point. Since we use a uniform grid, the grid needs to be fine enough to resolve the de Broglie wavelength everywhere. Only then will the reverse boundary problem have a unique solution. The patches using the phase scheme naturally provide boundary conditions for the patches using the wave scheme. Once the boundaries are populated, we perform a drift step with the respective FTCS and phase schemes. We then compute the updated density field from the updated wave functions and compute the gravitational field by solving the Poisson equation with a Fourier transform across the whole computational domain. The gravitational field is then used to kick the phase fields by half a time step once again. This completes one time step.

5.7.2 Testing and Validation

In the following, we validate the hybrid scheme with the one-dimensional colliding wave packet test given by Eq. (323) and with 2D and 3D test cases using gravity and cosmological IC.

1D

Fig. 50 demonstrates the hybrid scheme's ability to detect regions where the phase scheme fails and to automatically switch to the wave scheme when necessary. Note that the hybrid scheme also switches to the wave scheme in regions of very low, but non-vanishing density where the phase scheme would otherwise accumulate large errors. In this example, we run an additional smoothing step over the phase field to ensure its continuity when switching back from the wave to the phase scheme. In an AMR simulation, one would need to make sure to resolve the de Broglie wavelength in such a case.

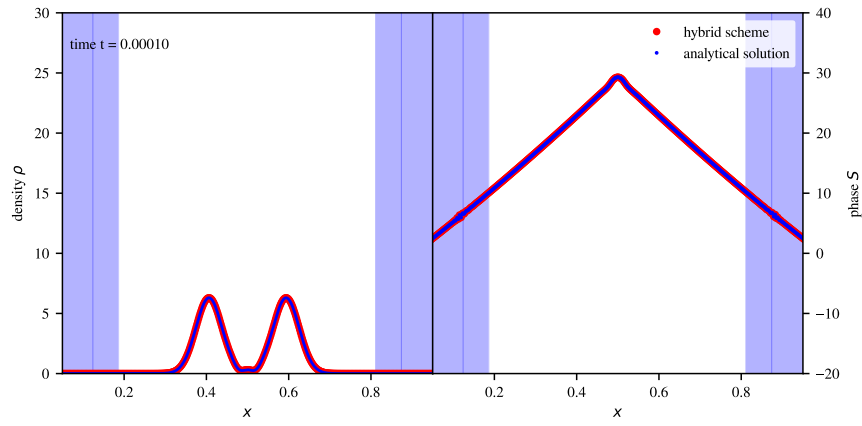
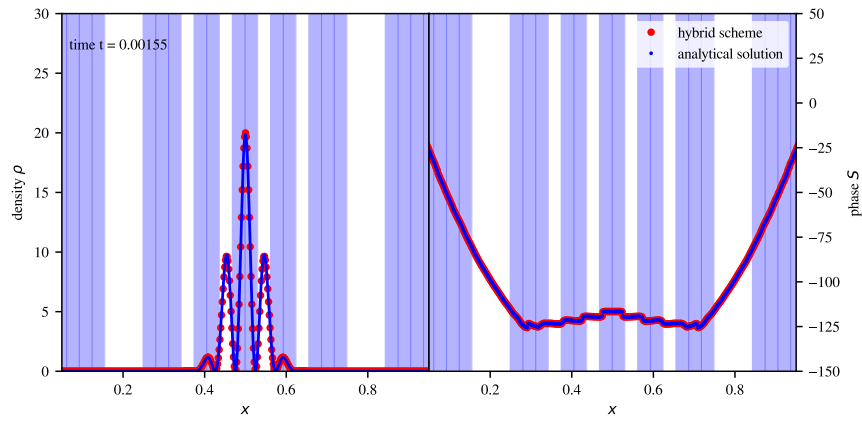
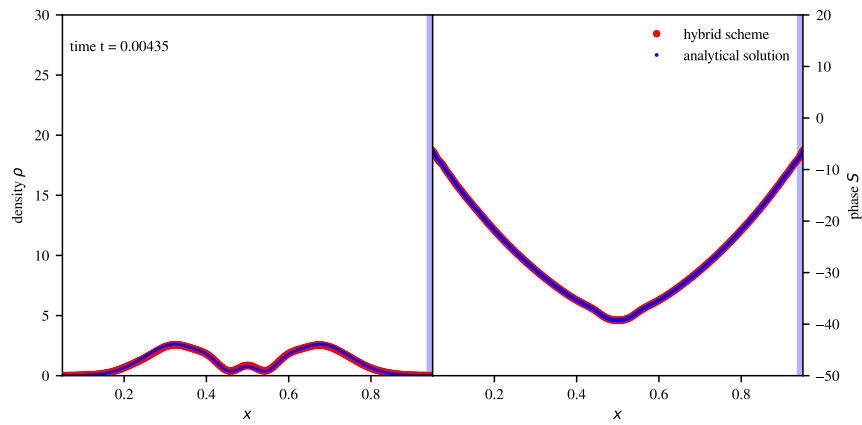
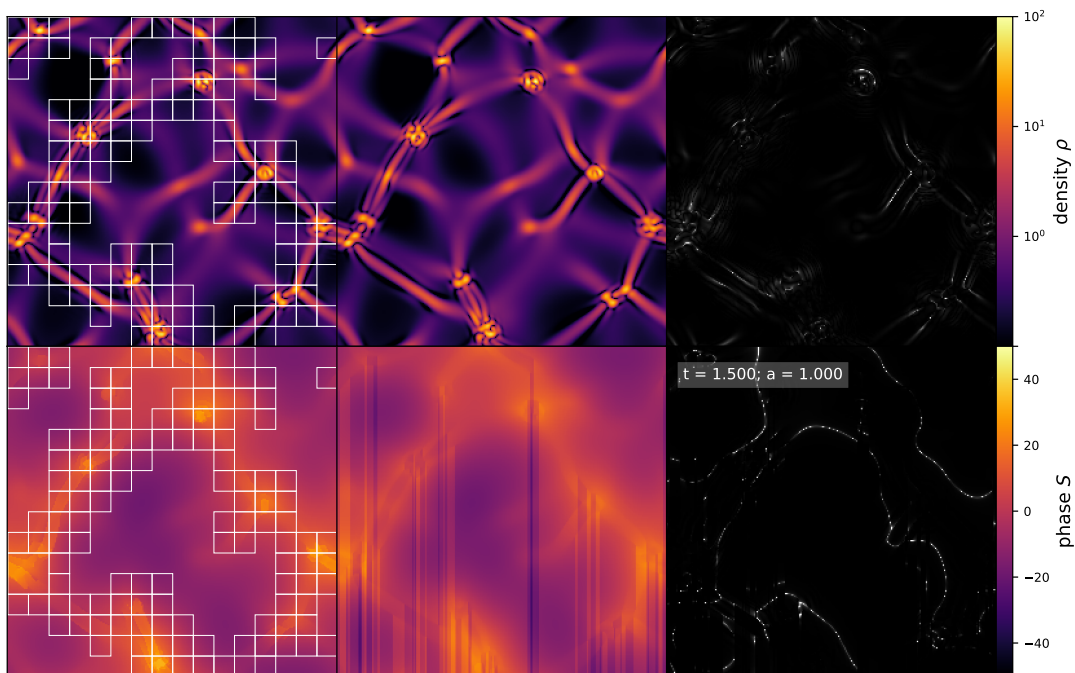
(a) $t = 0.0001$ (b) $t = 0.00155$ (c) $t = 0.00435$

Figure 50: Snapshots of 1D simulation from according to Eq. (323) using the hybrid scheme. Wave scheme is employed within the subregions that are shaded in blue. Parameters are set as in Fig. 45.

2D

We now consider a two-dimensional test case with gravity and cosmological IC that demonstrates the hybrid scheme's ability to resolve interference around halos and filaments correctly. Fig. 51 shows the output of the hybrid scheme at time $t = 1.5$ in code units for the same initial conditions as in Fig. 46. The wave scheme is used in subregions denoted by a white rectangle. The first subregions using the wave scheme are required at $t = 1.2$ and at $t = 1.5$, the wave scheme is used for around 50% of the simulation volume. We observe the hybrid scheme performs much better than the phase scheme and large relative errors only remain where the phase and density are very small.



(a) $t = 1.5$

Figure 51: Snapshot of 2D simulation from cosmological initial conditions on a grid with 256^2 points using the hybrid scheme. Wave scheme is employed within the subregions indicated by a white rectangle. Parameters are set as in Fig. 46.

3D

Finally, we present a three-dimensional test case with gravity and cosmological IC. It demonstrates that all methods developed in the previous sections also work in a three-dimensional simulation. Fig. 52 shows density slices from a 3D simulation with cosmological IC at time $t = 1.6$. The wave scheme is required for around 10 % of the simulation volume in this three-dimensional test. Halos and filaments form and show the correct interference patterns. Finally, Fig. 53 shows

a volume rendering of the same simulation also visualising the regions where the wave scheme is employed. The overdense region in the left part of the figure corresponds to the overdense region with concentric interference rings in the left column in Fig. 52.

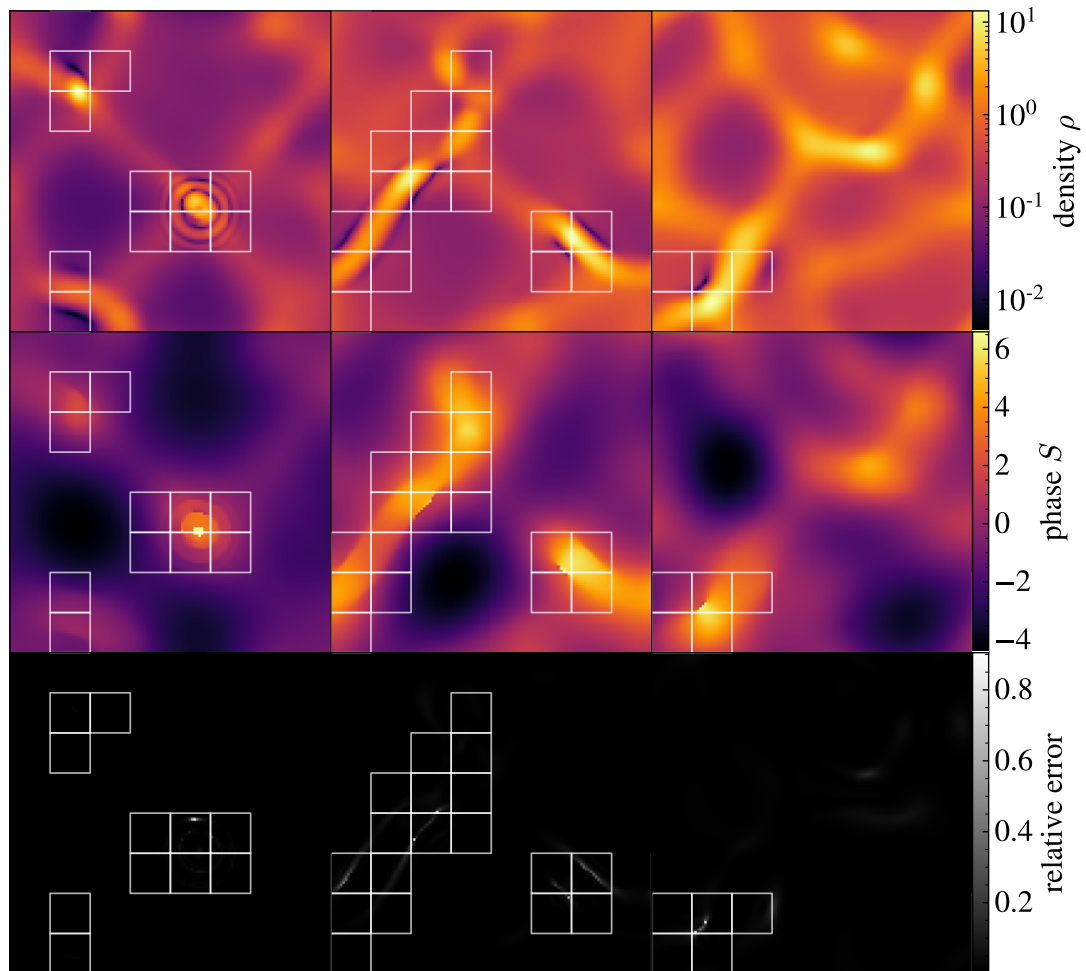


Figure 52: Density and phase slices from 3D simulation using the hybrid scheme on a grid with 128^3 points at time $t = 1.6$. Wave scheme is employed within the subregions shown by a white rectangle. Third row shows relative mismatch between densities of reference wave scheme and hybrid scheme. Slices from left to right are at the following positions (units in grid cells): in y - z -plane at $x = 38$, in x - z -plane at $y = 26$ and in x - y -plane at $z = 13$. Simulation parameters are set as $N = 10$, $L = 12$, $\Delta x = 12/128$, $G = 1$ and $a = 1$.

5.8 Discussion

This chapter presented a hybrid algorithm for simulating FDM on a uniform static grid in 1D, 2D and 3D. It evolves the HJ-Madelung equations on large scales and dynamically switches to a wave scheme for the SPS in regions of interference. We numerically assessed the stability and accuracy of the phase scheme. It turned out to be important to use a shock-capturing scheme for evolving both the density

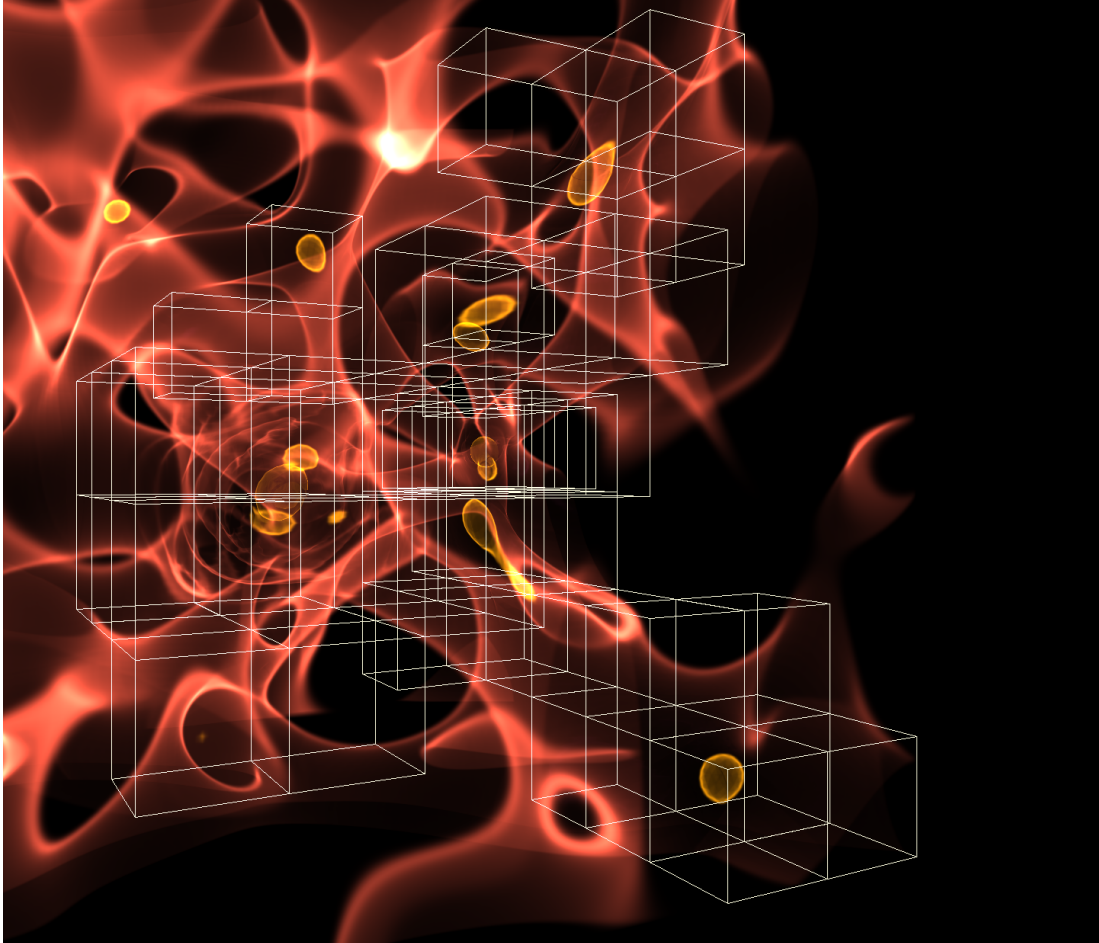


Figure 53: Volumetric rendering of 3D simulation using hybrid scheme on a grid with 128^3 points at time $t = 1.6$ in code units. Wave scheme is employed within the subregions shown by white mesh. Regions with higher density are visualised with lighter shades of red. The black, right edge of the rendering corresponds to the edge of the simulation volume. The overdense region in the left part of the figure corresponds to the overdense region with concentric interference rings depicted in the left column in Fig. 52. The rendering was created using the YT-library (Turk et al. 2011).

and phase fields. Further, stability remains an issue because the quantum pressure term can introduce negative densities. That is why we advocate for third- or fourth-order TVD RK time discretisations that also allow for relatively large time steps. Next steps in the development of the hybrid scheme include implementing it in an AMR code and determining criteria from when to refine the phase equation. Standard criteria for fluid AMR codes can provide guidance here. Further, a third-order scheme with a parabolic subgrid model might be desirable. Lastly, the scheme needs to be assessed on the basis of a large-scale cosmological simulation in order to verify that phase jumps do not introduce large errors.

6

Conclusions and Outlook

In this thesis, we compared the CDM and FDM models in the context of a Euclid-like weak lensing survey using non-linear Eulerian PT and developed a proof-of-concept code for a hybrid scheme that solves the Hamilton-Jacobi-Madelung equations on large scales and the wave formulation of the SPS in regions of interference.

In the first part of the thesis, we presented a general framework for time-dependent Eulerian PT based on Scoccimarro's method. It requires few assumptions and can easily be applied to other dark matter models that use a set of (modified) Euler equations. We used it to demonstrate the cosmology dependence of standard time-independent Eulerian PT in CDM and applied it to FDM to compute matter spectra and bispectra at tree- and loop-level and matter trispectra at tree-level. We went on to compute the lensing spectra and bispectra at tree- and loop-level as well as the lensing trispectra at tree-level for the FDM masses $m = 10^{-21}$ eV, $m = 10^{-22}$ eV and $m = 10^{-23}$ eV. We gave estimates of the attainable cumulative signal-to-noise ratios in a weak lensing survey. Further, we have computed the χ^2 -functionals expressing whether we could distinguish the CDM and FDM models if the universe was described by the CDM model and we wrongly assumed an FDM model. According to FDM PT, which we expect to give a lower bound on the attainable χ^2 values, we can distinguish FDM from CDM for masses up to $m = 10^{-23}$ eV at tree-level and for masses up to $m = 10^{-22}$ eV if we include loop-level corrections. A weak lensing signal from FDM with a mass higher than $m \sim 10^{-21}$ eV is not measurable according to PT in our model survey. A comparison of the predictions of FDM PT with the predictions of CDM PT with FDM initial conditions lets us conclude that the impact of the FDM model on the considered weak lensing observables lies mainly in the initial conditions in the form of the initial power spectra at high redshift and not in the

late time power suppression through FDM dynamics.

In the second part of the thesis, we have combined a newly developed second-order scheme for solving the Hamilton-Jacobi-Madelung equations with a wave scheme to create a hybrid scheme for simulating structure formation in the FDM model. We opted for solving the Hamilton-Jacobi equation and not the Madelung equations because this approach is better suited for reconstructing the wave function at the boundaries between the wave and fluid simulations. The hybrid scheme uses a MUSCL conservative finite difference scheme for the continuity equation and a monotone, upwind finite difference scheme for the Hamilton-Jacobi equation. It turned out necessary to use shock-capturing schemes for evolving both the density and phase fields. Otherwise, the simulation fails once the formation of halos and solitons sets in. We have performed a series of one-, two- and three-dimensional test to validate the correctness of the implementation and the stability of the hybrid scheme. A three-dimensional simulation mimicking a cosmological simulation demonstrates the hybrid scheme's ability to correctly recover small-scale FDM dynamics while solving the Hamilton-Jacobi-Madelung equation in a large fraction of the simulation volume.

Beyond the scope of this thesis is the implementation of the hybrid scheme in an existing code for cosmological simulations that uses adaptive mesh refinement and could actually benefit from the hybrid scheme. Potentially, the hybrid scheme can push the range simulation volumes for the allowed range of FDM masses significantly closer to those relevant for studying galaxy evolution in an FDM simulation.

References

- Ajaib, Muhammad Adeel (Feb. 2013). ‘Numerical Methods and Causality in Physics’. In: arXiv: [1302.5601 \[physics.comp-ph\]](#).
- Bahcall, Neta A., Lori M. Lubin and Victoria Dorman (July 1995). ‘Where Is the Dark Matter?’ In: *The Astrophysical Journal* 447.2. DOI: [10.1086/309577](#).
- Baldauf, Tobias et al. (June 2014). ‘The Bispectrum in the Effective Field Theory of Large Scale Structure’. In: DOI: [10.1088/1475-7516/2015/05/007](#). arXiv: [1406.4135v3 \[astro-ph.CO\]](#).
- Bartelmann, Matthias and Matteo Maturi (Dec. 2016). ‘Weak gravitational lensing’. In: arXiv: [1612.06535 \[astro-ph.CO\]](#).
- Bartelmann, Matthias and Peter Schneider (Dec. 1999). ‘Weak Gravitational Lensing’. In: *Phys.Rept.*340:291-472,2001. DOI: [10.1016/S0370-1573\(00\)00082-X](#). arXiv: [astro-ph/9912508 \[astro-ph\]](#).
- Bernardeau, F. et al. (Dec. 2001). ‘Large-Scale Structure of the Universe and Cosmological Perturbation Theory’. In: *Phys.Rept.*367:1-248,2002. DOI: [10.1016/S0370-1573\(02\)00135-7](#). arXiv: [astro-ph/0112551 \[astro-ph\]](#).
- Bohm, David (Jan. 1952). ‘A Suggested Interpretation of the Quantum Theory in Terms of "Hidden" Variables. I’. In: *Physical Review* 85.2, pp. 166–179. DOI: [10.1103/physrev.85.166](#).
- Bullock, James S. and Michael Boylan-Kolchin (July 2017). ‘Small-Scale Challenges to the CDM Paradigm’. In: *Annual Review of Astronomy and Astrophysics, vol. 55, pp. 343-387 (2017)*. DOI: [10.1146/annurev-astro-091916-055313](#). arXiv: [1707.04256 \[astro-ph.CO\]](#).
- Carrasco, John Joseph M. et al. (Apr. 2013). ‘The 2-loop matter power spectrum and the IR-safe integrand’. In: DOI: [10.1088/1475-7516/2014/07/056](#). arXiv: [1304.4946v2 \[astro-ph.CO\]](#).
- Chavanis, Pierre-Henri (Sept. 2011). ‘BEC dark matter, Zeldovich approximation, and generalized Burgers equation’. In: *Phys. Rev. D* 84, 063518 (2011) 84.6. DOI: [10.1103/physrevd.84.063518](#). arXiv: [1103.3219 \[astro-ph.CO\]](#).
- Cheng, Dalong, M.-C. Chu and Jiayu Tang (July 2015). ‘Cosmological structure formation in Decaying Dark Matter models’. In: *Journal of Cosmology and Astroparticle Physics* 2015.07, pp. 009–009. DOI: [10.1088/1475-7516/2015/07/009](#).
- Clowe, Douglas et al. (Aug. 2006). ‘A Direct Empirical Proof of the Existence of Dark Matter’. In: *The Astrophysical Journal* 648.2, pp. L109–L113. DOI: [10.1086/508162](#).

- Coles, Peter and Bernard Jones (Jan. 1991). ‘A lognormal model for the cosmological mass distribution’. In: *Monthly Notices of the Royal Astronomical Society* 248.1, pp. 1–13. DOI: [10.1093/mnras/248.1.1](https://doi.org/10.1093/mnras/248.1.1).
- Colin, Pedro, Vladimir Avila-Reese and Octavio Valenzuela (Oct. 2000). ‘Substructure and Halo Density Profiles in a Warm Dark Matter Cosmology’. In: *The Astrophysical Journal* 542.2, pp. 622–630. DOI: [10.1086/317057](https://doi.org/10.1086/317057).
- Collaboration, Planck et al. (July 2018). ‘Planck 2018 results. VI. Cosmological parameters’. In: *A&A* 641, A6 (2020). DOI: [10.1051/0004-6361/201833910](https://doi.org/10.1051/0004-6361/201833910). arXiv: [1807.06209](https://arxiv.org/abs/1807.06209) [[astro-ph.CO](https://arxiv.org/archive/astro-ph)].
- Dennis, Glen, Maurice de Gosson and Basil Hiley (Dec. 2014). ‘Bohm’s Quantum Potential as an Internal Energy’. In: DOI: [10.1016/j.physleta.2015.02.038](https://doi.org/10.1016/j.physleta.2015.02.038). arXiv: [1412.5133](https://arxiv.org/abs/1412.5133) [[quant-ph](https://arxiv.org/archive/quant)].
- Dentler, Mona et al. (Nov. 2021). ‘Fuzzy Dark Matter and the Dark Energy Survey Year 1 Data’. In: arXiv: [2111.01199](https://arxiv.org/abs/2111.01199) [[astro-ph.CO](https://arxiv.org/archive/astro-ph)].
- Du, Xiaolong et al. (Mar. 2018). ‘Tidal disruption of fuzzy dark matter subhalo cores’. In: *Physical Review D* 97.6, p. 063507. DOI: [10.1103/physrevd.97.063507](https://doi.org/10.1103/physrevd.97.063507).
- Dullemond, C.P. and H.H. Wang (Apr. 2009). ‘Lecture Numerical Fluid Dynamics’. In: URL: https://www.ita.uni-heidelberg.de/~dullemond/lectures/num_fluid_2009/.
- Edwards, Faber et al. (Oct. 2018). ‘PyUltraLight: a pseudo-spectral solver for ultralight dark matter dynamics’. In: *Journal of Cosmology and Astroparticle Physics* 2018.10, pp. 027–027. DOI: [10.1088/1475-7516/2018/10/027](https://doi.org/10.1088/1475-7516/2018/10/027).
- Einasto, Jaan, Ants Kaasik and Enn Saar (July 1974). ‘Dynamic evidence on massive coronas of galaxies’. In: *Nature* 250.5464, pp. 309–310. DOI: [10.1038/250309a0](https://doi.org/10.1038/250309a0).
- Fry, J. N. (Apr. 1984). ‘The Galaxy correlation hierarchy in perturbation theory’. In: *The Astrophysical Journal* 279, p. 499. DOI: [10.1086/161913](https://doi.org/10.1086/161913).
- González-Morales, Alma X. et al. (Aug. 2017). ‘Unbiased constraints on ultralight axion mass from dwarf spheroidal galaxies’. In: *Monthly Notices of the Royal Astronomical Society* 472.2, pp. 1346–1360. DOI: [10.1093/mnras/stx1941](https://doi.org/10.1093/mnras/stx1941).
- Goroff, M. H. et al. (Dec. 1986). ‘Coupling of modes of cosmological mass density fluctuations’. In: *The Astrophysical Journal* 311, p. 6. DOI: [10.1086/164749](https://doi.org/10.1086/164749).
- Hahn, T. (Apr. 2004). ‘Cuba - a library for multidimensional numerical integration’. In: *Comput.Phys.Commun.* 168 (2005) 78-95. DOI: [10.1016/j.cpc.2005.01.010](https://doi.org/10.1016/j.cpc.2005.01.010). arXiv: [hep-ph/0404043](https://arxiv.org/abs/hep-ph/0404043) [[hep-ph](https://arxiv.org/archive/hep)].

- Harris, Charles R. et al. (Sept. 2020). ‘Array programming with NumPy’. In: *Nature* 585.7825, pp. 357–362. DOI: [10.1038/s41586-020-2649-2](https://doi.org/10.1038/s41586-020-2649-2). URL: <https://doi.org/10.1038/s41586-020-2649-2>.
- Heifetz, Eyal and Eliahu Cohen (Jan. 2015). ‘Toward a thermo-hydrodynamic like description of Schrodinger equation via the Madelung formulation and Fisher information’. In: *Found. Phys.* 45 (11), 1514-1525 (2015). DOI: [10.1007/s10701-015-9926-1](https://doi.org/10.1007/s10701-015-9926-1). arXiv: [1501.00944](https://arxiv.org/abs/1501.00944) [quant-ph].
- Hirsch (2007). *Numerical Computation of Internal and External Flows*. Ed. by Butterworth-Heinemann. Elsevier. ISBN: 978-0-7506-6594-0. DOI: [10.1016/b978-0-7506-6594-0.x5037-1](https://doi.org/10.1016/b978-0-7506-6594-0.x5037-1).
- Hložek, Renée, David J E Marsh and Daniel Grin (Feb. 2018). ‘Using the full power of the cosmic microwave background to probe axion dark matter’. In: *Monthly Notices of the Royal Astronomical Society* 476.3, pp. 3063–3085. DOI: [10.1093/mnras/sty271](https://doi.org/10.1093/mnras/sty271).
- Hlozek, Renée et al. (Oct. 2014). ‘A search for ultra-light axions using precision cosmological data’. In: *Phys. Rev. D* 91, 103512 (2015). DOI: [10.1103/PhysRevD.91.103512](https://doi.org/10.1103/PhysRevD.91.103512). arXiv: [1410.2896](https://arxiv.org/abs/1410.2896) [astro-ph.CO].
- Hopkins, Philip F. (Nov. 2018). ‘A Stable Finite-Volume Method for Scalar-Field Dark Matter’. In: *MNRAS*, 2019, 489, 2367. DOI: [10.1093/mnras/stz1922](https://doi.org/10.1093/mnras/stz1922). arXiv: [1811.05583](https://arxiv.org/abs/1811.05583) [astro-ph.CO].
- Hu, Wayne, Rennan Barkana and Andrei Gruzinov (Mar. 2000). ‘Cold and Fuzzy Dark Matter’. In: *Phys.Rev.Lett.* 85 (2000) 1158-1161. DOI: [10.1103/PhysRevLett.85.1158](https://doi.org/10.1103/PhysRevLett.85.1158). arXiv: [astro-ph/0003365](https://arxiv.org/abs/astro-ph/0003365) [astro-ph].
- Hui, Lam et al. (Feb. 2017). ‘Ultralight scalars as cosmological dark matter’. In: *Physical Review D* 95.4. DOI: [10.1103/physrevd.95.043541](https://doi.org/10.1103/physrevd.95.043541).
- Hunter, J. D. (2007). ‘Matplotlib: A 2D graphics environment’. In: *Computing in Science & Engineering* 9.3, pp. 90–95. DOI: [10.1109/MCSE.2007.55](https://doi.org/10.1109/MCSE.2007.55).
- Jain, Bhuvnesh and Edmund Bertschinger (Nov. 1993). ‘Second Order Power Spectrum and Nonlinear Evolution at High Redshift’. In: *Astrophys.J.* 431 (1994) 495. DOI: [10.1086/174502](https://doi.org/10.1086/174502). arXiv: [astro-ph/9311070](https://arxiv.org/abs/astro-ph/9311070) [astro-ph].
- (Mar. 1995). ‘Self-Similar Evolution of Cosmological Density Fluctuations’. In: *Astrophys.J.* 456 (1996) 43. DOI: [10.1086/176625](https://doi.org/10.1086/176625). arXiv: [astro-ph/9503025](https://arxiv.org/abs/astro-ph/9503025) [astro-ph].
- Kaiser, Nick (Oct. 1996). ‘Weak Lensing and Cosmology’. In: *Astrophys.J.* 498 (1998) 26. DOI: [10.1086/305515](https://doi.org/10.1086/305515). arXiv: [astro-ph/9610120](https://arxiv.org/abs/astro-ph/9610120) [astro-ph].
- Kobayashi, Takeshi et al. (July 2017). ‘Lyman-alpha Constraints on Ultralight Scalar Dark Matter: Implications for the Early and Late Universe’. In: *Phys.*

- Rev. D* 96, 123514 (2017). DOI: [10.1103/PhysRevD.96.123514](https://doi.org/10.1103/PhysRevD.96.123514). arXiv: [1708.00015](https://arxiv.org/abs/1708.00015) [astro-ph.CO].
- Laguë, Alex et al. (Apr. 2020). ‘Evolving Ultralight Scalars into Non-Linearity with Lagrangian Perturbation Theory’. In: DOI: [10.1093/mnras/stab601](https://doi.org/10.1093/mnras/stab601). arXiv: [2004.08482](https://arxiv.org/abs/2004.08482) [astro-ph.CO].
- Laureijs, R. et al. (Oct. 2011). ‘Euclid Definition Study Report’. In: arXiv: [1110.3193](https://arxiv.org/abs/1110.3193) [astro-ph.CO].
- Leer, Bram van (July 1979). ‘Towards the ultimate conservative difference scheme. V. A second-order sequel to Godunov's method’. In: *Journal of Computational Physics* 32.1, pp. 101–136. DOI: [10.1016/0021-9991\(79\)90145-1](https://doi.org/10.1016/0021-9991(79)90145-1).
- LeVeque, Randall J. (Aug. 2002). *Finite Volume Methods for Hyperbolic Problems*. Cambridge University Press. DOI: [10.1017/cbo9780511791253](https://doi.org/10.1017/cbo9780511791253).
- Lewis, Antony, Anthony Challinor and Anthony Lasenby (Nov. 1999). ‘Efficient Computation of CMB anisotropies in closed FRW models’. In: *Astrophys.J.* 538:473–476,2000. DOI: [10.1086/309179](https://doi.org/10.1086/309179). arXiv: [astro-ph/9911177](https://arxiv.org/abs/astro-ph/9911177) [astro-ph].
- Li, Xinyu, Lam Hui and Greg L. Bryan (Oct. 2018). ‘Numerical and Perturbative Computations of the Fuzzy Dark Matter Model’. In: *Phys. Rev. D* 99, 063509 (2019). DOI: [10.1103/PhysRevD.99.063509](https://doi.org/10.1103/PhysRevD.99.063509). arXiv: [1810.01915](https://arxiv.org/abs/1810.01915) [astro-ph.CO].
- Limber, D. Nelson (Jan. 1953). ‘The Analysis of Counts of the Extragalactic Nebulae in Terms of a Fluctuating Density Field’. In: *The Astrophysical Journal* 117, p. 134. DOI: [10.1086/145672](https://doi.org/10.1086/145672).
- Madelung, E. (Mar. 1927). ‘Quantentheorie in hydrodynamischer Form’. In: *Zeitschrift für Physik* 40.3-4, pp. 322–326. DOI: [10.1007/bf01400372](https://doi.org/10.1007/bf01400372).
- Makino, Nobuyoshi, Misao Sasaki and Yasushi Suto (July 1992). ‘Analytic approach to the perturbative expansion of nonlinear gravitational fluctuations in cosmological density and velocity fields’. In: *Physical Review D* 46.2, pp. 585–602. DOI: [10.1103/physrevd.46.585](https://doi.org/10.1103/physrevd.46.585).
- Maleki, Alireza, Shant Baghran and Sohrab Rahvar (Nov. 2019). ‘Investigation of two colliding solitonic cores in Fuzzy Dark Matter models’. In: *Phys. Rev. D* 101, 023508 (2020). DOI: [10.1103/PhysRevD.101.023508](https://doi.org/10.1103/PhysRevD.101.023508). arXiv: [1911.00486](https://arxiv.org/abs/1911.00486) [astro-ph.CO].
- Marsh, David J. E. et al. (Oct. 2011). ‘Ultra-light Axions: Degeneracies with Massive Neutrinos and Forecasts for Future Cosmological Observations’. In: *Phys.Rev. D* 86 (2012) 023508. DOI: [10.1103/PhysRevD.85.103514](https://doi.org/10.1103/PhysRevD.85.103514). arXiv: [1110.0502](https://arxiv.org/abs/1110.0502) [astro-ph.CO].
- Marsh, David J.E. (July 2016). ‘Axion cosmology’. In: *Physics Reports* 643, pp. 1–79. DOI: [10.1016/j.physrep.2016.06.005](https://doi.org/10.1016/j.physrep.2016.06.005).

- May, Simon and Volker Springel (Jan. 2021). ‘Structure formation in large-volume cosmological simulations of fuzzy dark matter: Impact of the non-linear dynamics’. In: DOI: [10.1093/mnras/stab1764](https://doi.org/10.1093/mnras/stab1764). arXiv: [2101.01828](https://arxiv.org/abs/2101.01828) [[astro-ph.CO](#)].
- Mina, Mattia, David F. Mota and Hans A. Winther (July 2020). ‘Solitons in the dark: non-linear structure formation with fuzzy dark matter’. In: arXiv: [2007.04119](https://arxiv.org/abs/2007.04119) [[astro-ph.CO](#)].
- Mocz, Philip and Sauro Succi (May 2015). ‘Numerical solution of the nonlinear Schrödinger equation using smoothed-particle hydrodynamics’. In: *Physical Review E* 91.5. DOI: [10.1103/physreve.91.053304](https://doi.org/10.1103/physreve.91.053304).
- Mocz, Philip et al. (July 2017). ‘Galaxy formation with BECDM – I. Turbulence and relaxation of idealized haloes’. In: *Monthly Notices of the Royal Astronomical Society* 471.4, pp. 4559–4570. DOI: [10.1093/mnras/stx1887](https://doi.org/10.1093/mnras/stx1887).
- Mocz, Philip et al. (Apr. 2020). ‘Galaxy formation with BECDM – II. Cosmic filaments and first galaxies’. In: *Monthly Notices of the Royal Astronomical Society* 494.2, pp. 2027–2044. DOI: [10.1093/mnras/staa738](https://doi.org/10.1093/mnras/staa738).
- Navarro, Julio F., Carlos S. Frenk and Simon D. M. White (Aug. 1995). ‘The Structure of Cold Dark Matter Halos’. In: *Astrophys.J.* 462:563-575, 1996. DOI: [10.1086/177173](https://doi.org/10.1086/177173). arXiv: [astro-ph/9508025](https://arxiv.org/abs/astro-ph/9508025) [[astro-ph](#)].
- Nishikawa, Hiroaki (June 2020). ‘A Truncation Error Analysis of Third-Order MUSCL Scheme for Nonlinear Conservation Laws’. In: *International Journal for Numerical Methods in Fluids, Vol.93, Issue 4, April 2021*. DOI: [10.1002/flid.4918](https://doi.org/10.1002/flid.4918). arXiv: [2006.08268](https://arxiv.org/abs/2006.08268) [[physics.comp-ph](#)].
- Nori, M. and M. Baldi (Jan. 2018). ‘AX-GADGET: a new code for cosmological simulations of Fuzzy Dark Matter and Axion models’. In: *Nori M., Baldi M., 2018, Monthly Notices of the Royal Astronomical Society, 478, 3935*. DOI: [10.1093/mnras/sty1224](https://doi.org/10.1093/mnras/sty1224). arXiv: [1801.08144](https://arxiv.org/abs/1801.08144) [[astro-ph.CO](#)].
- Nori, Matteo et al. (Oct. 2018). ‘Lyman α forest and non-linear structure characterization in Fuzzy Dark Matter cosmologies’. In: *Monthly Notices of the Royal Astronomical Society* 482.3, pp. 3227–3243. DOI: [10.1093/mnras/sty2888](https://doi.org/10.1093/mnras/sty2888).
- Osher, Stanley and Chi-Wang Shu (Aug. 1991). ‘High-Order Essentially Nonoscillatory Schemes for Hamilton–Jacobi Equations’. In: *SIAM Journal on Numerical Analysis* 28.4, pp. 907–922. DOI: [10.1137/0728049](https://doi.org/10.1137/0728049).
- Peccei, R. D. (June 1996). ‘QCD, Strong CP and Axions’. In: *J.Korean Phys.Soc.*, pp. 199–208. arXiv: [hep-ph/9606475](https://arxiv.org/abs/hep-ph/9606475) [[hep-ph](#)].
- Peebles, P. J. E. (Dec. 1981). *The Large-Scale Structure of the Universe*. Princeton University Press. DOI: [10.1515/9780691206714](https://doi.org/10.1515/9780691206714).

- Recami, Erasmo and Giovanni Salesi (Jan. 1998). ‘Kinematics and hydrodynamics of spinning particles’. In: *Physical Review A* 57.1, pp. 98–105. DOI: [10.1103/physreva.57.98](https://doi.org/10.1103/physreva.57.98).
- Reimberg, Paulo (Oct. 2016). ‘On the symmetry properties of the PT kernels and recurrence relations’. In: arXiv: [1610.07455](https://arxiv.org/abs/1610.07455) [[astro-ph.CO](https://arxiv.org/archive/ph)].
- Rogers, Keir K. and Hiranya V. Peiris (Feb. 2021). ‘Strong Bound on Canonical Ultralight Axion Dark Matter from the Lyman-Alpha Forest’. In: *Physical Review Letters* 126.7, p. 071302. DOI: [10.1103/physrevlett.126.071302](https://doi.org/10.1103/physrevlett.126.071302).
- Sarkar, Anjan Kumar, Kanhaiya L. Pandey and Shiv K. Sethi (Jan. 2021). ‘Using the redshift evolution of the Lyman- effective opacity as a probe of dark matter models’. In: DOI: [10.1088/1475-7516/2021/10/077](https://doi.org/10.1088/1475-7516/2021/10/077). arXiv: [2101.09917](https://arxiv.org/abs/2101.09917) [[astro-ph.CO](https://arxiv.org/archive/ph)].
- Schive, Hsi-Yu, Tzihong Chiueh and Tom Broadhurst (June 2014). ‘Cosmic structure as the quantum interference of a coherent dark wave’. In: *Nature Physics* 10.7, pp. 496–499. DOI: [10.1038/nphys2996](https://doi.org/10.1038/nphys2996).
- Schive, Hsi-Yu et al. (Aug. 2015). ‘Contrasting Galaxy Formation from Quantum Wave Dark Matter, DM, with CDM, using Planck and Hubble Data’. In: DOI: [10.3847/0004-637X/818/1/89](https://doi.org/10.3847/0004-637X/818/1/89). arXiv: [1508.04621](https://arxiv.org/abs/1508.04621) [[astro-ph.GA](https://arxiv.org/archive/ph)].
- Schwabe, Bodo and Jens C. Niemeyer (Oct. 2021). ‘Deep zoom-in simulation of a fuzzy dark matter galactic halo’. In: arXiv: [2110.09145](https://arxiv.org/abs/2110.09145) [[astro-ph.CO](https://arxiv.org/archive/ph)].
- Schwabe, Bodo, Jens C. Niemeyer and Jan F. Engels (Aug. 2016). ‘Simulations of solitonic core mergers in ultralight axion dark matter cosmologies’. In: *Physical Review D* 94.4. DOI: [10.1103/physrevd.94.043513](https://doi.org/10.1103/physrevd.94.043513).
- Scoccimarro, R. (Oct. 1998). ‘Transients from initial conditions: a perturbative analysis’. In: *Monthly Notices of the Royal Astronomical Society* 299.4, pp. 1097–1118. DOI: [10.1046/j.1365-8711.1998.01845.x](https://doi.org/10.1046/j.1365-8711.1998.01845.x).
- Scoccimarro, Román (Jan. 2006). ‘A New Angle on Gravitational Clustering’. In: *Annals of the New York Academy of Sciences* 927.1, pp. 13–23. DOI: [10.1111/j.1749-6632.2001.tb05618.x](https://doi.org/10.1111/j.1749-6632.2001.tb05618.x).
- Scoccimarro, Roman and Joshua Frieman (Sept. 1995). ‘Loop Corrections in Non-Linear Cosmological Perturbation Theory’. In: *Astrophys.J.Suppl.*105:37,1996. DOI: [10.1086/192306](https://doi.org/10.1086/192306). arXiv: [astro-ph/9509047](https://arxiv.org/abs/astro-ph/9509047) [[astro-ph](https://arxiv.org/archive/ph)].
- Scoccimarro, Roman, Matias Zaldarriaga and Lam Hui (Jan. 1999). ‘Power Spectrum Correlations Induced by Non-Linear Clustering’. In: *Astrophys.J.*527:1,1999. DOI: [10.1086/308059](https://doi.org/10.1086/308059). arXiv: [astro-ph/9901099](https://arxiv.org/abs/astro-ph/9901099) [[astro-ph](https://arxiv.org/archive/ph)].
- Shu, Chi-Wang (Oct. 2007). ‘High-order Numerical Methods for the Time-dependent Hamilton-Jacobi Equations’. In: *Lecture Notes Series, Institute for Mathem-*

- atical Sciences, National University of Singapore.* WORLD SCIENTIFIC, pp. 47–91. DOI: [10.1142/9789812709066_0002](https://doi.org/10.1142/9789812709066_0002).
- Spergel, David N. and Paul J. Steinhardt (Apr. 2000). ‘Observational Evidence for Self-Interacting Cold Dark Matter’. In: *Physical Review Letters* 84.17, pp. 3760–3763. DOI: [10.1103/physrevlett.84.3760](https://doi.org/10.1103/physrevlett.84.3760).
- Spiteri, Raymond J. and Steven J. Ruuth (Jan. 2002). ‘A New Class of Optimal High-Order Strong-Stability-Preserving Time Discretization Methods’. In: *SIAM Journal on Numerical Analysis* 40.2, pp. 469–491. DOI: [10.1137/s0036142901389025](https://doi.org/10.1137/s0036142901389025).
- Szapudi, István and Nick Kaiser (Jan. 2003). ‘Cosmological Perturbation Theory Using the Schrödinger Equation’. In: *The Astrophysical Journal* 583.1, pp. L1–L4. DOI: [10.1086/368013](https://doi.org/10.1086/368013).
- Takada, Masahiro and Bhuvnesh Jain (Oct. 2003). ‘Cosmological parameters from lensing power spectrum and bispectrum tomography’. In: *Mon.Not.Roy.Astron.Soc.* 348:897,2004. DOI: [10.1111/j.1365-2966.2004.07410.x](https://doi.org/10.1111/j.1365-2966.2004.07410.x). arXiv: [astro-ph/0310125](https://arxiv.org/abs/astro-ph/0310125) [astro-ph].
- Tegmark, Max et al. (May 2004). ‘The Three-Dimensional Power Spectrum of Galaxies from the Sloan Digital Sky Survey’. In: *The Astrophysical Journal* 606.2, pp. 702–740. DOI: [10.1086/382125](https://doi.org/10.1086/382125).
- Tsekov, R. (Apr. 2009). ‘Bohmian mechanics versus Madelung quantum hydrodynamics’. In: *Ann. Univ. Sofia, Fac. Phys. SE (2012)* 112-119. DOI: [10.13140/RG.2.1.3663.8245](https://doi.org/10.13140/RG.2.1.3663.8245). arXiv: [0904.0723v10](https://arxiv.org/abs/0904.0723v10) [quant-ph].
- Turk, M. J. et al. (Jan. 2011). ‘yt: A Multi-code Analysis Toolkit for Astrophysical Simulation Data’. In: *The Astrophysical Journal Supplement Series* 192, 9, p. 9. DOI: [10.1088/0067-0049/192/1/9](https://doi.org/10.1088/0067-0049/192/1/9). arXiv: [1011.3514](https://arxiv.org/abs/1011.3514) [astro-ph.IM].
- Veltmaat, Jan and Jens C. Niemeyer (Dec. 2016). ‘Cosmological particle-in-cell simulations with ultralight axion dark matter’. In: *Physical Review D* 94.12. DOI: [10.1103/physrevd.94.123523](https://doi.org/10.1103/physrevd.94.123523).
- Veltmaat, Jan, Jens C. Niemeyer and Bodo Schwabe (Aug. 2018). ‘Formation and structure of ultralight bosonic dark matter halos’. In: *Physical Review D* 98.4, p. 043509. DOI: [10.1103/physrevd.98.043509](https://doi.org/10.1103/physrevd.98.043509).
- Virtanen, Pauli et al. (2020). ‘SciPy 1.0: Fundamental Algorithms for Scientific Computing in Python’. In: *Nature Methods* 17, pp. 261–272. DOI: [10.1038/s41592-019-0686-2](https://doi.org/10.1038/s41592-019-0686-2).
- Wallstrom, Timothy C. (Mar. 1994). ‘Inequivalence between the Schrödinger equation and the Madelung hydrodynamic equations’. In: *Physical Review A* 49.3, pp. 1613–1617. DOI: [10.1103/physreva.49.1613](https://doi.org/10.1103/physreva.49.1613).

- Weinberg, David H. et al. (June 2013). ‘Cold dark matter: controversies on small scales’. In: DOI: [10.1073/pnas.1308716112](https://doi.org/10.1073/pnas.1308716112). arXiv: [1306.0913](https://arxiv.org/abs/1306.0913) [[astro-ph.CO](https://arxiv.org/archive/astro-ph)].
- Widrow, Lawrence M. and Nick Kaiser (Oct. 1993). ‘Using the Schroedinger Equation to Simulate Collisionless Matter’. In: *The Astrophysical Journal* 416, p. L71. DOI: [10.1086/187073](https://doi.org/10.1086/187073).
- Wolfram Research, Inc. (2021). *Mathematica, Version 12.3.1*. Champaign, IL, 2021. URL: <https://www.wolfram.com/mathematica>.
- Woo, Tak-Pong and Tzihong Chiueh (June 2008). ‘High-Resolution Simulation on Structure Formation with Extremely Light Bosonic Dark Matter’. In: *Astrophys.J.* 697:850-861, 2009. DOI: [10.1088/0004-637X/697/1/850](https://doi.org/10.1088/0004-637X/697/1/850). arXiv: [0806.0232](https://arxiv.org/abs/0806.0232) [[astro-ph](https://arxiv.org/archive/astro-ph)].
- Zhang, Jiajun, Hantao Liu and Ming-Chung Chu (Jan. 2019). ‘Cosmological Simulation for Fuzzy Dark Matter Model’. In: *Frontiers in Astronomy and Space Sciences* 5. DOI: [10.3389/fspas.2018.00048](https://doi.org/10.3389/fspas.2018.00048).
- Zimmermann, Tim (2020). ‘An Investigation of the Lower-Dimensional Dynamics of Fuzzy Dark Matter’. In: URL: https://www.thphys.uni-heidelberg.de/~wimberger/ma_tim.pdf.



Appendix

A.1 Newtonian Cosmology

In this section, we give a reminder on Newtonian cosmology based on the classical reference (Peebles 1981, pp. 41-43). We introduce the Friedmann equations and derive the Poisson equation in comoving coordinates. Note that while the derivation of the SPS in chapter 2 is based on the linear perturbation of the Robertson-Walker line element, the SPS and all related equations can be understood purely in terms of Newtonian cosmology.

The position of particles in Newtonian cosmology is described in terms of comoving coordinates \mathbf{x} that are related to the proper separation \mathbf{r} of two particles via the relation $\mathbf{r} = a\mathbf{x}$, where $a(t)$ is the scale factor. Accordingly, the velocity is given by $\dot{\mathbf{r}} = \dot{a}(t)\mathbf{x} + a(t)\dot{\mathbf{x}}$ and differentials transform as $(\frac{\partial}{\partial t})_r = (\frac{\partial}{\partial t})_x - H\mathbf{x} \cdot \nabla_x$ and $\nabla_r = \frac{1}{a}\nabla_x$. In a homogeneous and isotropic background universe, the scale factor evolves according to the *Friedmann equations*:

$$\frac{\ddot{a}}{a} = -\frac{4}{3}\pi G \left(\rho_b + 3\frac{p_b}{c^2} \right) + \frac{\Lambda}{3}, \quad (334)$$

$$\frac{\dot{a}^2}{a^2} = \frac{8}{3}\pi G \rho_b + \frac{\Lambda}{3} - \frac{R^{-2}}{a^2}, \quad (335)$$

where Λ is the cosmological constant and $a|R|c$ is the radius of curvature of the hypersurface at $t = \text{const.}$ and $\frac{d}{dt}x \equiv \dot{x}$. In terms of the conformal time τ defined via $dt = a(\tau)d\tau$ and the conformal Hubble function $\mathcal{H} = \frac{d \ln(a)}{d\tau} = Ha$, the Friedmann equations read

$$\begin{aligned} \mathcal{H}' &= -\frac{\Omega_m(\tau)}{2}\mathcal{H}^2(\tau) + \frac{\Lambda}{3}a^2(\tau) = \left(\Omega_{\Lambda(\tau)} - \frac{\Omega_m(\tau)}{2} \right) \mathcal{H}^2(\tau), \\ R^{-2} &= (\Omega_{tot}(\tau) - 1)\mathcal{H}^2(\tau), \end{aligned} \quad (336)$$

where $\frac{d}{d\tau}x \equiv x'$. In a closed model $R^{-2} > 0$ and in an open model $R^{-2} < 0$. The Einstein-de Sitter model has $R^{-2} = \Lambda = 0$ with $p = 0$. The density parameter is the ratio of the mean mass density $\rho_b(t)$ to the density in an Einstein-de Sitter model with the same Hubble constant,

$$\Omega(t) = \frac{8}{3}\pi G\rho_b/H_0^2. \quad (337)$$

Alternatively, we can use the Friedmann equation to obtain

$$\Delta\Phi(\mathbf{x}, \tau) = \frac{3}{2}\Omega_m(\tau)\mathcal{H}(\tau)\delta(\mathbf{x}, \tau) \quad (338)$$

In the Newtonian limit the zero-zero component of the field equations for an ideal fluid with mass density ρ , pressure p and velocity $v \ll c$ becomes

$$\Delta_r\Phi = 4\pi G\left(\rho + \frac{3p}{c^2}\right) - \Lambda, \quad (339)$$

and in the limit where $p \ll \rho c^2$, we find that an observer in the background model measures the potential

$$\Phi_b = \frac{2}{3}\pi G\rho_b(t)r^2 - \Lambda, \quad (340)$$

where $\rho_b(t)$ is the mean mass density. The geodesic equations become

$$\ddot{r} = -\nabla\Phi. \quad (341)$$

Rewriting them in comoving coordinates yields the cosmological equation

$$\frac{\ddot{a}}{a} = -\frac{4\pi G}{3}\left(\rho + \frac{3p}{c^2}\right) + \frac{\Lambda}{3}. \quad (342)$$

The proper velocity of a particle relative to the origin expressed in comoving coordinates is given by

$$\mathbf{u} = a\dot{\mathbf{x}} + \mathbf{x}\dot{a}, \quad (343)$$

and its Lagrangian reads

$$\mathcal{L} = \frac{1}{2}m(a\dot{\mathbf{x}} + \dot{a}\mathbf{x})^2 - m\Phi(\mathbf{x}, t). \quad (344)$$

Under the canonical transformation

$$\mathcal{L} \rightarrow \mathcal{L} - \frac{d\psi}{dt}, \quad \psi = \frac{1}{2}ma\dot{x}^2, \quad (345)$$

the Lagrangian reduces to

$$\mathcal{L} = \frac{1}{2}ma^2\dot{x}^2 - m\phi, \quad (346)$$

where $\phi = \Phi + \frac{1}{2}a\ddot{a}x^2$. The field equation for the new potential ϕ is

$$\Delta_x\phi(\mathbf{x}, t) = 4\pi Ga^2(\rho(\mathbf{x}, t) - \rho_b(t)). \quad (347)$$

A.2 Explicit Symmetrisation of FDM PT Kernels

In this section, we explicitly derive the symmetrised PT kernels $F_3^{(s)}$ and $F_4^{(s)}$ by making use of the symmetries of the vertex couplings in FDM. We start with the third-order kernel explicitly given in Eqs. (145) and (146) for $a = 1$ and the corresponding diagram given in Fig. 9. Since $\Gamma_{1bc} = \Gamma_{1cb}$, as follows from Eq. (154), Eq. (145) reduces to

$$\begin{aligned} I_1^{(3)}(\mathbf{k}_1, \mathbf{k}_2, \mathbf{k}_3, \eta) &= 2 \int_{\eta_0}^{\eta} ds \Gamma_{1bc}^{(2)}(\mathbf{k}, \mathbf{k}_1, \mathbf{k}_{23}, s, \eta) \int_{\eta_0}^s ds_1 \Gamma_{cde}^{(2)}(\mathbf{k}_{23}, \mathbf{k}_2, \mathbf{k}_3, s_1, s) \\ &\quad f_b(\mathbf{k}_1, s, \eta) f_d(\mathbf{k}_2, s_1, s) f_e(\mathbf{k}_3, s_1, s). \end{aligned} \quad (348)$$

Since $I_1^{(3)}$ already enjoys symmetry under $\mathbf{k}_2 \leftrightarrow \mathbf{k}_3$ and $\mathbf{k}_{23} \leftrightarrow \mathbf{k}_1$, it can be symmetrised as

$$I_1^{(3,s)}(\mathbf{k}_1, \mathbf{k}_2, \mathbf{k}_3, \eta) = \frac{1}{3}(I_1^{(3)}(\mathbf{k}_1, \mathbf{k}_2, \mathbf{k}_3, \eta) + I_1^{(3)}(\mathbf{k}_2, \mathbf{k}_1, \mathbf{k}_3, \eta) + I_1^{(3)}(\mathbf{k}_3, \mathbf{k}_2, \mathbf{k}_1, \eta)), \quad (349)$$

Further, $J_1^{(3)}$ is already symmetric under exchange of momenta because the only nonvanishing element of the vertex coupling Γ at fourth order is the (1111)-component given in Eq. (155) that stems from the quantum pressure term and is already symmetric under exchange of momenta:

$$\begin{aligned} J_1^{(3,s)}(\mathbf{k}_1, \mathbf{k}_2, \mathbf{k}_3, \eta) &= J_1^{(3)}(\mathbf{k}_1, \mathbf{k}_2, \mathbf{k}_3, \eta) \\ &= \int_{\eta_0}^{\eta} \Gamma_{1111}^{(3)}(\mathbf{k}, \mathbf{k}_1, \mathbf{k}_2, \mathbf{k}_3, s, \eta) f_1(\mathbf{k}_1, s, \eta) f_1(\mathbf{k}_2, s, \eta) f_1(\mathbf{k}_3, s, \eta) \end{aligned} \quad (350)$$

We conclude

$$F_3^{(s)} = J_1^{(3,s)}(\mathbf{k}_1, \mathbf{k}_2, \mathbf{k}_3, \eta) + I_1^{(3,s)}(\mathbf{k}_1, \mathbf{k}_2, \mathbf{k}_3, \eta). \quad (351)$$

At fourth order, we distinguish five contributions to the coupling kernel:

$$\begin{aligned}
\Psi_2^{(4)}(\mathbf{k}, \eta) &= \delta(\mathbf{k}_1, \eta)\delta(\mathbf{k}_2, \eta)\delta(\mathbf{k}_3, \eta)\delta(\mathbf{k}_4, \eta)\delta_D(\mathbf{k} - \mathbf{k}_{1234}) \\
&\quad (J_4(\mathbf{k}_1, \mathbf{k}_2, \mathbf{k}_3, \mathbf{k}_4, \eta) \\
&\quad + K_4(\mathbf{k}_1, \mathbf{k}_2, \mathbf{k}_3, \mathbf{k}_4, \eta) \\
&\quad + H_4(\mathbf{k}_1, \mathbf{k}_2, \mathbf{k}_3, \mathbf{k}_4, \eta) \\
&\quad + W_4(\mathbf{k}_1, \mathbf{k}_2, \mathbf{k}_3, \mathbf{k}_4, \eta) \\
&\quad + I_4(\mathbf{k}_1, \mathbf{k}_2, \mathbf{k}_3, \mathbf{k}_4, \eta)).
\end{aligned} \tag{352}$$

The contribution W_4 corresponds to the diagram in Fig. 10 and takes the simple form:

$$\begin{aligned}
W_4(\mathbf{k}_1, \mathbf{k}_2, \mathbf{k}_3, \mathbf{k}_4, \eta) &= \int_{\eta_0}^{\eta} \Gamma_{11111}^{(4)}(\mathbf{k}_{1234}, \mathbf{k}_1, \mathbf{k}_2, \mathbf{k}_3, \mathbf{k}_4, s, \eta) \\
&\quad f_1(\mathbf{k}_1, s, \eta)f_1(\mathbf{k}_2, s, \eta)f_1(\mathbf{k}_3, s, \eta)f_1(\mathbf{k}_4, s, \eta).
\end{aligned} \tag{353}$$

As at third order, $\Gamma_{11111}^{(4)}$ stems from the quantum pressure term and is therefore symmetric under exchange momenta from which it follows that W_4 is symmetric under exchange of momenta. The contribution I_4 corresponds to the left diagram in Fig. 11:

$$\begin{aligned}
I_4(\mathbf{k}_1, \mathbf{k}_2, \mathbf{k}_3, \mathbf{k}_4, \eta) &= \int_{\eta_0}^{\eta} ds \Gamma_{1bc}^{(2)}(\mathbf{k}_{1234}, \mathbf{k}_{12}, \mathbf{k}_{34}, s, \eta) \\
&\quad \int_{\eta_0}^s ds_1 \int_{\eta_0}^s ds_2 \Gamma_{bde}^{(2)}(\mathbf{k}_{12}, \mathbf{k}_1, \mathbf{k}_2, s_1, s) \Gamma_{cfg}^{(2)}(\mathbf{k}_{34}, \mathbf{k}_3, \mathbf{k}_4, s_2, s) \\
&\quad f_d(\mathbf{k}_1, s_1, s)f(\mathbf{k}_2, s_1, s)f_f(\mathbf{k}_3, s_2, s)f_g(\mathbf{k}_4, s_2, s),
\end{aligned} \tag{354}$$

which can be symmetrised by using the fact that it is already invariant under $\mathbf{k}_1 \leftrightarrow \mathbf{k}_2$; $\mathbf{k}_3 \leftrightarrow \mathbf{k}_4$; $\mathbf{k}_1, \mathbf{k}_2 \leftrightarrow \mathbf{k}_3, \mathbf{k}_4$:

$$\begin{aligned}
I_4^s(\mathbf{k}_1, \mathbf{k}_2, \mathbf{k}_3, \mathbf{k}_4, \eta) &= \\
&\quad \frac{1}{3}(I_4(\mathbf{k}_1, \mathbf{k}_2, \mathbf{k}_3, \mathbf{k}_4, \eta) + I_4(\mathbf{k}_1, \mathbf{k}_3, \mathbf{k}_2, \mathbf{k}_4, \eta) + I_4(\mathbf{k}_1, \mathbf{k}_4, \mathbf{k}_3, \mathbf{k}_2, \eta)).
\end{aligned} \tag{355}$$

The contribution J_4 corresponds to the right diagram in Fig. 11:

$$\begin{aligned}
J_4(\mathbf{k}_1, \mathbf{k}_2, \mathbf{k}_3, \mathbf{k}_4, \eta) = & \\
& 4 \int_{\eta_0}^{\eta} ds W_{2bc}(\mathbf{k}_{1234}, \mathbf{k}_1, \mathbf{k}_{234}, s, \eta) f_b(\mathbf{k}_1, s) \\
& \times \int_{\eta_0}^s ds_1 W_{cde}(\mathbf{k}_{234}, \mathbf{k}_2, \mathbf{k}_{34}, s_1, s) \int_{\eta_0}^{s_1} ds_2 W_{efg}(\mathbf{k}_{34}, \mathbf{k}_3, \mathbf{k}_4, s_2, s_1) \\
& \times f_d(\mathbf{k}_2, s_1, s) f_f(\mathbf{k}_3, s_2, s_1) f_g(\mathbf{k}_4, s_2, s_1),
\end{aligned} \tag{356}$$

and enjoys symmetry under $\mathbf{k}_1 \leftrightarrow \mathbf{k}_{234}$; $\mathbf{k}_2 \leftrightarrow \mathbf{k}_{34}$; $\mathbf{k}_3 \leftrightarrow \mathbf{k}_4$. The factor 4 follows from the three additional permutations of the diagram. Its fully symmetric form is given by

$$\begin{aligned}
J_4^s(\mathbf{k}_1, \mathbf{k}_2, \mathbf{k}_3, \mathbf{k}_4, \eta) = & \frac{1}{12} (J_4(\mathbf{k}_1, \mathbf{k}_2, \mathbf{k}_3, \mathbf{k}_4, \eta) + J_4(\mathbf{k}_1, \mathbf{k}_3, \mathbf{k}_2, \mathbf{k}_4, \eta) \\
& + J_4(\mathbf{k}_1, \mathbf{k}_4, \mathbf{k}_3, \mathbf{k}_2, \eta) + J_4(\mathbf{k}_2, \mathbf{k}_3, \mathbf{k}_1, \mathbf{k}_4, \eta) \\
& + J_4(\mathbf{k}_2, \mathbf{k}_4, \mathbf{k}_1, \mathbf{k}_3, \eta) + J_4(\mathbf{k}_3, \mathbf{k}_4, \mathbf{k}_1, \mathbf{k}_2, \eta) \\
& + J_4(\mathbf{k}_2, \mathbf{k}_1, \mathbf{k}_3, \mathbf{k}_4, \eta) + J_4(\mathbf{k}_3, \mathbf{k}_1, \mathbf{k}_2, \mathbf{k}_4, \eta) \\
& + J_4(\mathbf{k}_4, \mathbf{k}_1, \mathbf{k}_3, \mathbf{k}_2, \eta) + J_4(\mathbf{k}_3, \mathbf{k}_2, \mathbf{k}_1, \mathbf{k}_4, \eta) \\
& + J_4(\mathbf{k}_4, \mathbf{k}_2, \mathbf{k}_1, \mathbf{k}_3, \eta) + J_4(\mathbf{k}_4, \mathbf{k}_3, \mathbf{k}_1, \mathbf{k}_2, \eta)).
\end{aligned} \tag{357}$$

The contribution K_4 corresponds to the left diagram in Fig. 12:

$$\begin{aligned}
K_4(\mathbf{k}_1, \mathbf{k}_2, \mathbf{k}_3, \mathbf{k}_4, \eta) = & \\
& 2 \int_{\eta_0}^{\eta} ds \Gamma_{1b2}^{(2)}(\mathbf{k}_{1234}, \mathbf{k}_1, \mathbf{k}_{234}, s, \eta) f_b(\mathbf{k}_1, s, \eta) \\
& \times \int_{\eta_0}^s ds_1 (\Gamma_{1111}^{(3)}(\mathbf{k}_{234}, \mathbf{k}_2, \mathbf{k}_3, \mathbf{k}_4, s_1, s) \\
& \times f_1(\mathbf{k}_2, s_1, \eta) f_1(\mathbf{k}_3, s_1, s) f_1(\mathbf{k}_4, s_1, s)).
\end{aligned} \tag{358}$$

where the additional permutation together with the symmetry properties of $\Gamma_{abc}^{(2)}$ give the factor of 2. Again, we recognise that the expression is invariant under permutations of $\mathbf{k}_2, \mathbf{k}_3$ and \mathbf{k}_4 . Its symmetric form is given by

$$\begin{aligned}
K_4^{(s)}(\mathbf{k}_1, \mathbf{k}_2, \mathbf{k}_3, \mathbf{k}_4, \eta) = & \\
& \frac{1}{4} \left[K_4(\mathbf{k}_1, \mathbf{k}_2, \mathbf{k}_3, \mathbf{k}_4, \eta) + K_4(\mathbf{k}_2, \mathbf{k}_1, \mathbf{k}_3, \mathbf{k}_4, \eta) \right. \\
& \left. + K_4(\mathbf{k}_3, \mathbf{k}_2, \mathbf{k}_1, \mathbf{k}_4, \eta) + K_4(\mathbf{k}_4, \mathbf{k}_2, \mathbf{k}_3, \mathbf{k}_1, \eta) \right]
\end{aligned} \tag{359}$$

The last remaining contribution H_4 corresponds to the right diagram in Fig. 12:

$$\begin{aligned}
H_4(\mathbf{k}_1, \mathbf{k}_2, \mathbf{k}_3, \mathbf{k}_4, \eta) = & \\
& \int_{\eta_0}^{\eta} \Gamma_{1111}^{(3)}(\mathbf{k}_{1234}, \mathbf{k}_{14}, \mathbf{k}_2, \mathbf{k}_3, s, \eta) f_1(\mathbf{k}_2, s, \eta) f_1(\mathbf{k}_3, s, \eta) \\
& \times \int_{\eta_0}^s ds_1 \Gamma_{1ef}^{(2)}(\mathbf{k}_{14}, \mathbf{k}_1, \mathbf{k}_4, s_1, \eta) f_e(\mathbf{k}_1, s_1, s) f_f(\mathbf{k}_4, s_1, s) \\
& + \text{permutations with } \mathbf{k}_1 \leftrightarrow \mathbf{k}_2, \mathbf{k}_1 \leftrightarrow \mathbf{k}_3.
\end{aligned} \tag{360}$$

A symmetrised form of H_4 is given by

$$\begin{aligned}
H_4^{(s)}(\mathbf{k}_1, \mathbf{k}_2, \mathbf{k}_3, \mathbf{k}_4, \eta) = & \\
& \frac{1}{6} \left[(H_4(\mathbf{k}_1, \mathbf{k}_2, \mathbf{k}_3, \mathbf{k}_4, \eta) + H_4(\mathbf{k}_1, \mathbf{k}_3, \mathbf{k}_2, \mathbf{k}_4, \eta) \right. \\
& + H_4(\mathbf{k}_1, \mathbf{k}_4, \mathbf{k}_3, \mathbf{k}_2, \eta) + H_4(\mathbf{k}_2, \mathbf{k}_3, \mathbf{k}_1, \mathbf{k}_4, \eta) \\
& \left. + H_4(\mathbf{k}_2, \mathbf{k}_4, \mathbf{k}_1, \mathbf{k}_3, \eta) + H_4(\mathbf{k}_3, \mathbf{k}_4, \mathbf{k}_1, \mathbf{k}_2, \eta) \right].
\end{aligned} \tag{361}$$

It follows that

$$\begin{aligned}
F_4^{(s)}(\mathbf{k}_1, \mathbf{k}_2, \mathbf{k}_3, \mathbf{k}_4, \eta) = & \left[J_4^{(s)}(\mathbf{k}_1, \mathbf{k}_2, \mathbf{k}_3, \mathbf{k}_4, \eta) + H_4^{(s)}(\mathbf{k}_1, \mathbf{k}_2, \mathbf{k}_3, \mathbf{k}_4, \eta) \right. \\
& \left. + W_4^{(s)}(\mathbf{k}_1, \mathbf{k}_2, \mathbf{k}_3, \mathbf{k}_4, \eta) + I_4^{(s)}(\mathbf{k}_1, \mathbf{k}_2, \mathbf{k}_3, \mathbf{k}_4, \eta) + K_4^{(s)}(\mathbf{k}_1, \mathbf{k}_2, \mathbf{k}_3, \mathbf{k}_4, \eta) \right].
\end{aligned} \tag{362}$$

A.3 Linear Growth in FDM

This section describes in detail how we compute the linear growth factors $D(k, a)$ as solutions to the linear growth equation (89) in FDM. The linear growth factors describe how linear density fluctuations grow

$$\delta(\mathbf{x}, a) = \delta(\mathbf{x}, a = 0) D(a). \tag{363}$$

In a FDM-dominated EdS universe there are known analytical solutions of the linear growth equation in terms of Bessel functions given by Eq. (93). If we naively use them evolve a linear density fluctuation from the time a_0 to the time a we find

$$D_{\pm}(k, a, a_0) = \left(\frac{a_0}{a} \right)^{\frac{1}{4}} \frac{J_{\mp 5/2} \left(\frac{b(k)}{2\sqrt{a}} \right)}{J_{\mp 5/2} \left(\frac{b(k)}{2\sqrt{a_0}} \right)}. \tag{364}$$

We immediately notice that Eq. (364) exhibits unphysical divergences at the roots of the Bessel function. Laguë et al. (2020) argue that this is simply a matter of choice of normalisation, but this is not quite true. Eq. (364) is obviously not

a solution of the linear growth equation (89) since it is divergent. We conclude that Eq. (93) only describes the evolution of linear fluctuations for initial conditions where $D_{\pm}(k, a_{in}) = 1$. For different initial conditions, we are not aware of an analytical solution to Eq. (89), even in the EdS case. Laguë et al. (2020) suggest two ways to remedy this issue: One way is to approximate the denominator of Eq. (364) by a fifth-order Taylor expansion of the Bessel function

$$J_{-n}(x) = x^{-n} \left[\frac{2^n}{\Gamma(1-n)} + \frac{2^{n-2}x^2}{(n-1)\Gamma(1-n)} + \frac{2^{n-5}x^4}{(n-2)(n-1)\Gamma(1-n)} + \mathcal{O}(x^6) \right], \quad (365)$$

where $\Gamma(x) = \int_0^{\infty} dy y^{x-1} e^{-y}$ is the Euler Gamma function. This normalisation removes divergences from Eq. (364) and gives little oscillations. In contrast, a different number of terms in the Taylor expansion leads to fast oscillations and/or divergences. At the same time, renormalising the growth function with this prescription has the disadvantage that $D_+(k, a_0, a_0) \neq 1$ in the oscillating regime. The alternative that Laguë et al. (2020) adopt is to use a model for the mean growth of the FDM growth function. They describe the growing mode D_+ in terms of a smoothed Heaviside step function:

$$D(k, a) \approx \left(1 - \left[1 + e^{-2\alpha(k-k_0)} \right]^{-8} \right) D_{\text{CDM}}(a), \quad (366)$$

where $k_0 \propto k_J$ and α are free parameters determined via a fit to the AXION-CAMB transfer function. For large scales, this approach exactly recovers the CDM growth function, but has the disadvantage that oscillations are entirely neglected. Moreover, the smoothed Heaviside step function falls off exponentially for large k which is not a correct description of the asymptotic behaviour of D_+ . For large k , the Bessel function behaves as

$$D_+(k, a) \propto J_{-\frac{5}{2}} \left(\frac{b(k)}{2\sqrt{a}} \right) \propto \frac{1}{k} \cos \left(\frac{b(k)}{2\sqrt{a}} \right). \quad (367)$$

For this reason, we opted for a different mean growth model of the form:

$$D(k, a) \approx \left(1 + \alpha \left(\frac{k}{k_J} \right)^{\beta} \right) D_{\text{CDM}}(a), \quad (368)$$

Fig. 54 shows a numerical fit of this model to the growing solution of Eq. (89) for $m = 10^{-23} eV$. It turns out that the asymptotic behaviour of this average growth

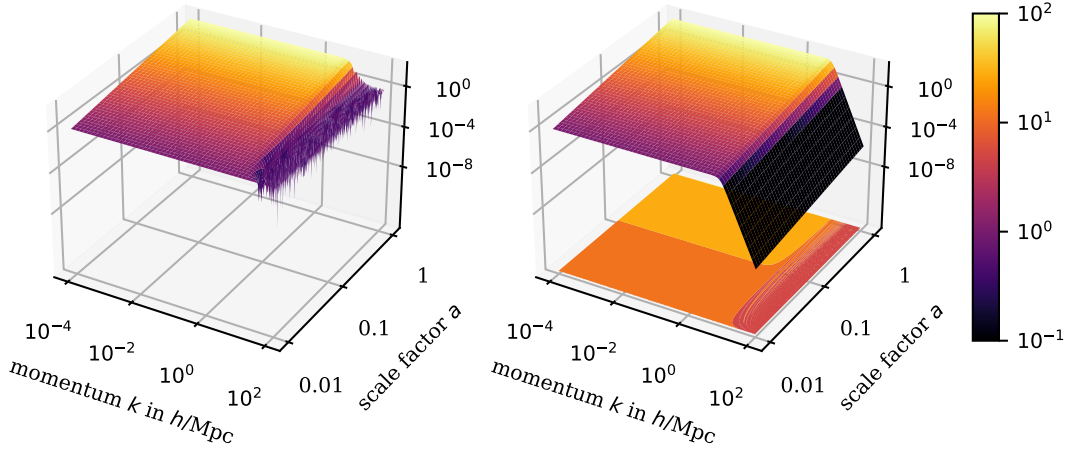


Figure 54: Depiction of fit of the mean growth model defined in Eq. (368). The left plot shows the numerical solution of Eq. (89) in the fiducial cosmology for $m = 10^{-23}$ eV. The right plot shows the fitted model for with fit parameters $\alpha = 1.11$ and $\beta = 7.38$. The z -axis as well as the colour scheme depict the quantity $D_+(k, a)$. The input data are normalised to $D_+(k, a_0) = 1$.

model is $D(k) \sim k^{-7}$ in both EdS and the fiducial cosmology and therefore still fails to describe the correct asymptotic behaviour of the FDM growth factor. In this thesis, we therefore opt for integrating Eq. (89) numerically. As initial conditions, we choose

$$D(a_0) = 1, \quad D'(a_0) = D'_{\text{CDM}}(a_0), \quad (369)$$

where $D'_{\text{CDM}}(a_0)$ is obtained via numerical integration of the linear CDM growth equation (73) starting from a scale factor $a'_0 \ll a_0$, i.e. $a'_0 = 10^{-6}$ and $a_0 = 10^{-2}$. This approach has several advantages: We ensure $D(k, a_0, a_0) = 1$ via the initial conditions and obtain the correct CDM evolution in a general cosmology in the limit $k \rightarrow 0$. Further and most importantly, the growth factor obtained in this way is in fact a solution to the linear growth equation (89) up to numerical accuracy. It does not exhibit unphysical divergences as shown in Fig. 55. We see that the growth factor renormalised via the prescription in Eq. (365), the mean growth model defined in Eq. (368) and the numerical solution of the growth equation also exhibit the correct asymptotic behaviour

$$\lim_{k \rightarrow \infty} \frac{D_{\text{FDM}}(k, a)}{D_{\text{CDM}}(a)} = 0. \quad (370)$$

In addition, the numerical solution captures the oscillatory behaviour of the analytical solution for high k as shown in Fig. 56. Unfortunately, there are also several disadvantages to numerically integrating the linear growth equation in

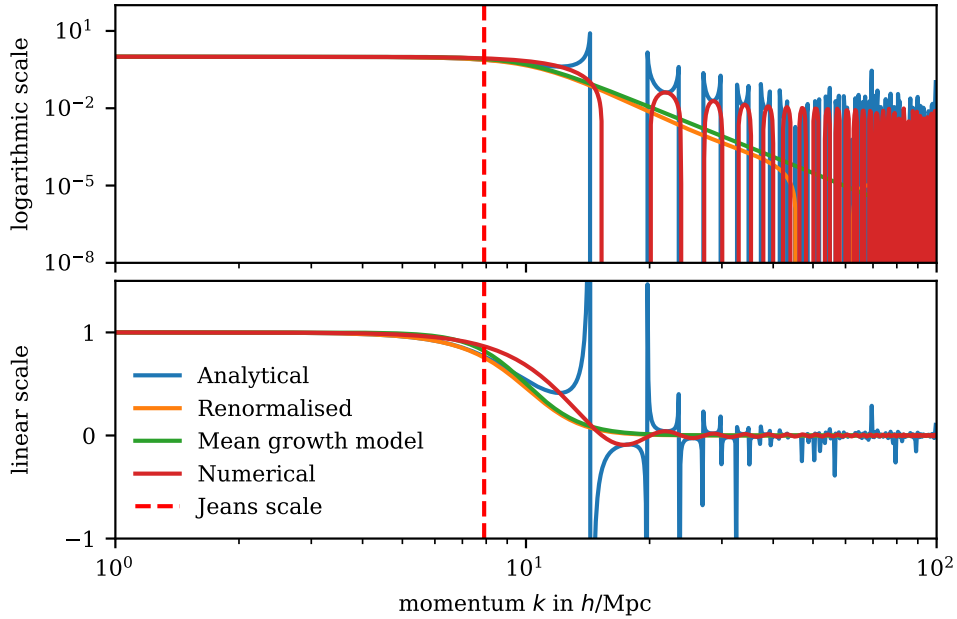


Figure 55: Asymptotic behaviour of growing modes represented via the quotient of FDM and CDM growth factors $D_{+,FDM}(k, a)/D_{+,CDM}(a)$ in an FDM-dominated EdS universe for $m = 10^{-23}$ eV. The graphs show the analytical, divergent expression (364), the renormalised expression using Eq. (365), the mean growth model defined in Eq. (368) with the fit parameters $\alpha = 0.61$, $\beta = 6.46$, as well as the numerical solution obtained by integrating the linear growth equation with initial conditions given by Eq. (369).

FDM. Firstly, we do not actually capture the growing mode in the oscillating regime. This is because we do not know the correct initial conditions for the growing mode. Therefore, the numerical solution in the oscillating regime will in general be a linear combination of the two modes D_+ and D_- . However, since the correct initial conditions for the linear fluctuation fields are unknown too, this does not add any uncertainty to the linear growth model in terms of initial conditions. In any case, we recover the correct modes for $a > a_{osc}$. This is because any component proportional to D_- in the initial conditions quickly decays away for $a > a_{osc}$.

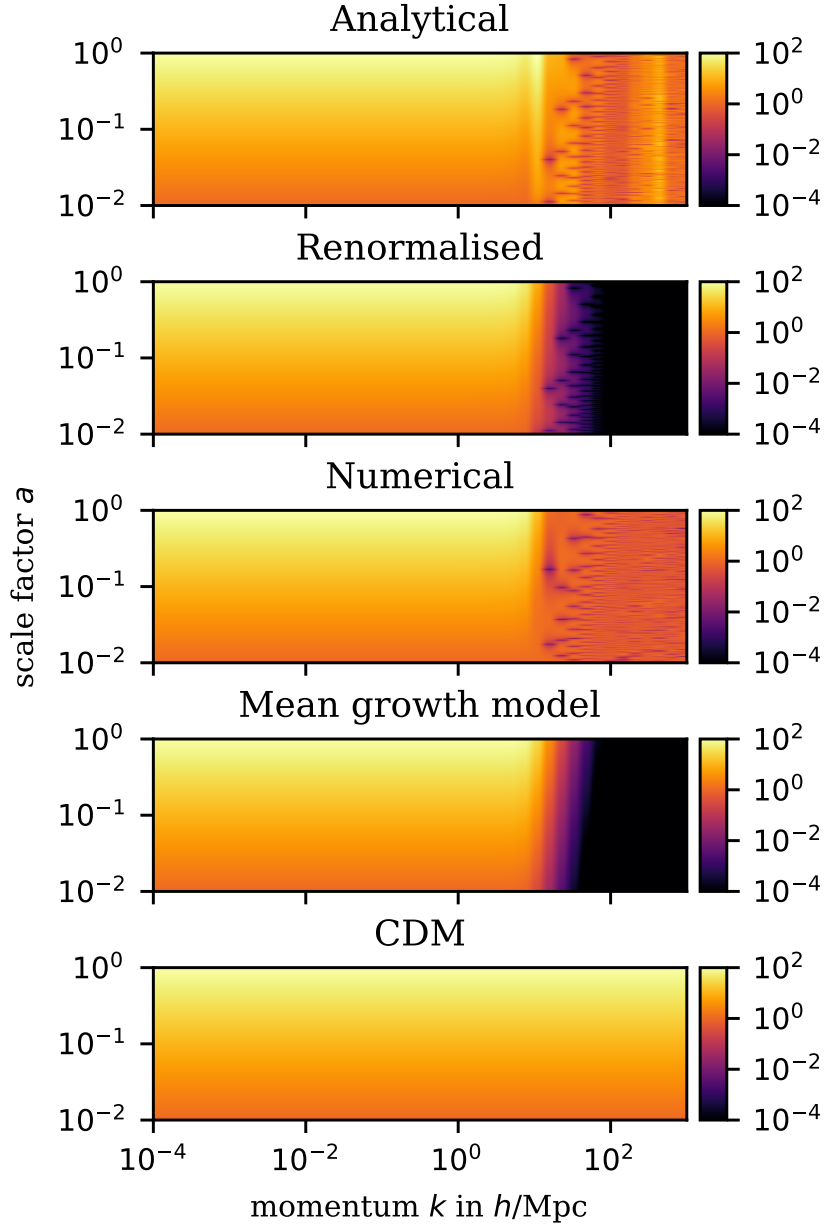


Figure 56: Comparison of different models for growth factor $D_+^{(FDM)}$ in an FDM-dominated EdS universe for $m = 10^{-23}$ eV. From top to bottom, the maps show the analytical, divergent expression (364), the renormalised expression using Eq. (365), the mean growth model defined in Eq. (368) with the fit parameters $\alpha = 0.61$, $\beta = 6.46$, the numerical solution obtained by integrating the linear growth equation with initial conditions given by Eq. (369) as well as the analytical CDM solution from Eq. (78).

Another disadvantage of the numerical integration of the linear growth equation is that it requires interpolation for different momenta. We solve this problem by using a two-dimensional cubic spline to describe the growth factor. The time dimension is resolved with 1000 points in the range $a \in [0.01, 1]$ and the momentum dimension is resolved with 2000 points in the range $k \in [10^{-6}, 10^3] \text{ Mpc}^{-1}$. For $k > 10^3 \text{ Mpc}^{-1}$, the spline is extrapolated as $D(k, a) \propto k^{-4}$. We numerically

verified that increasing the resolution of the spline and increasing k_{max} to higher values does not change any of our results. The biggest disadvantage of numerically integrating the growth equation Eq. (89) is, however, that we are unable to obtain two linearly independent solutions. Integrating the growing mode forward and the decaying mode backward in time, we could not find a prescription to ensure that we obtain orthogonal solutions in the oscillating regime. Figs. 57 and 58 illustrate this issue.

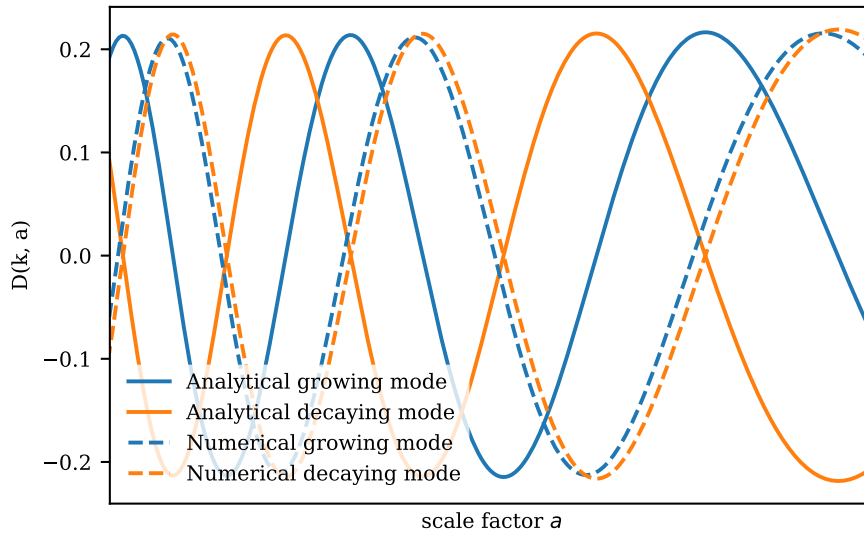


Figure 57: Comparison of analytical and numerical solutions of Eq. (89) in oscillating regime. The analytical solutions are given by (93) and have arbitrary normalisation. As opposed to the analytical solutions, the numerical solutions are not orthogonal.

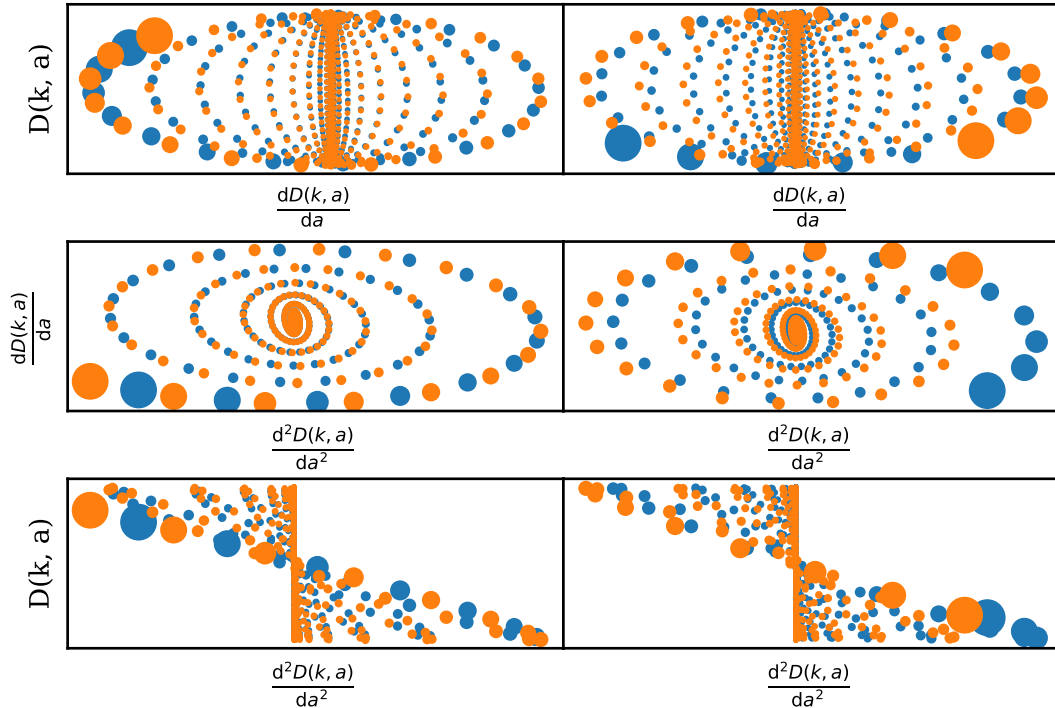


Figure 58: Comparison of analytical and numerical solutions of Eq. (89) in the oscillating regime. The colours denote the growing mode (blue) and the decaying mode (orange). The size of the data points denote the time a , where earlier times are denoted by bigger dots. The variable range depicted is from $a_0 = 0.01$ to $a = 1$ for $k = 50 h/\text{Mpc}$ and $m = 10^{-23} \text{ eV}$.

Consequently, we were unable to calculate the Green’s function of the growth equation in a general cosmology for FDM. Tests with the the mean growth model for both the growing and decaying mode in order to compute the Green’s function were also not successful. Instead, we rely on the analytical solution of the FDM growth function in EdS to carry out time-dependent PT in FDM. The Green’s function calculated in this way does not exhibit any unphysical divergences because the denominators cancel.

A.4 Lensing Integrals

In the following, we describe how to perform the loop-level, line-of-sight, signal-to-noise and χ^2 integrations in chapter 4. Let us begin with integrating the loop-level integrations to the matter spectra. The task amounts to numerically integrating Eqs. (177) and (183). Both integrands exhibit IR divergences. If we find a way to rewrite the integrands s.t. the leading IR divergences cancel, all subleading IR divergences are guaranteed to cancel as well (Scoccimarro and Frieman 1995; Jain and Bertschinger 1995). Carrasco et al. (2013) give such an

expression:

$$\begin{aligned}
P_{IR-safe}^{(1)} = \int \frac{d^3q}{(2\pi)^3} & \left[6F_3^{(s)}(\mathbf{k}, \mathbf{q}, -\mathbf{q})P^{(0)}(k)P^{(0)}(q) \right. \\
& + 2[F_2^{(s)}(\mathbf{k} - \mathbf{q}, \mathbf{q})]^2 P^{(0)}(|\mathbf{k} - \mathbf{q}|)P^{(0)}(q)\theta(|\mathbf{k} - \mathbf{q}| - q) \\
& \left. + 2[F_2^{(s)}(\mathbf{k} + \mathbf{q}, -\mathbf{q})]^2 P^{(0)}(|\mathbf{k} + \mathbf{q}|)P^{(0)}(q)\theta(|\mathbf{k} + \mathbf{q}| - q) \right], \tag{371}
\end{aligned}$$

Eq. (371) can be applied to the FDM case since the momentum dependence of the FDM mode coupling functions does not introduce any additional divergences compared to the CDM case. The same holds true for the IR safe version of the bispectrum corrections that are divergent just as in the case of the one-loop power spectrum. Baldauf et al. (2014) provide an IR-safe expression for the bispectrum contributions: The integrands of the contributions B_{321}^{II} and B_{411} , as defined in Eq. (183) only exhibit divergences at $q = 0$. The integrand of B_{321}^{II} exhibits a divergence at $\mathbf{q} = \mathbf{k}_2$ which can be mapped to a divergence at $q = 0$ by writing

$$\begin{aligned}
\int_q \tilde{b}_{321}^I &= \int_{q < |\mathbf{k}_2 - \mathbf{q}|} d^3q b_{321}^I(\mathbf{q}, \mathbf{k}_2, \mathbf{k}_3) + \int_{q \geq |\mathbf{k}_2 - \mathbf{q}|} d^3q b_{321}^I(\mathbf{q}, \mathbf{k}_2, \mathbf{k}_3) \\
&+ 5 \text{ permutations} \\
&= 6 \int d^3q b_{321}^I(\mathbf{q}, \mathbf{k}_2, \mathbf{k}_3)\theta(|\mathbf{k}_2 - \mathbf{q}| - q) + b_{321}^I(-\mathbf{q}, \mathbf{k}_2, \mathbf{k}_3)\theta(|\mathbf{k}_2 + \mathbf{q}| - q) \\
&+ 5 \text{ permutations.} \tag{372}
\end{aligned}$$

Similarly, one finds the following expression for the integrand of B_{222} :

$$\begin{aligned}
\int_q \tilde{b}_{222} &= \frac{1}{2} \int d^3q \{ [b_{222}(\mathbf{q}, \mathbf{k}_1, \mathbf{k}_2)\theta(|\mathbf{k}_1 + \mathbf{q}| - q)\theta(|\mathbf{k}_2 - \mathbf{q}| - q) \\
&+ b_{222}(-\mathbf{q}, \mathbf{k}_1, \mathbf{k}_2)\theta(|\mathbf{k}_1 - \mathbf{q}| - q)\theta(|\mathbf{k}_2 + \mathbf{q}| - q)] \\
&+ [\mathbf{k}_1 \leftrightarrow \mathbf{k}_3] + [\mathbf{k}_2 \leftrightarrow \mathbf{k}_3] \}. \tag{373}
\end{aligned}$$

The full one-loop bispectrum in a form where all IR-divergences cancel is then given by

$$B_{SPT} = B_{112} + \int_q \tilde{b}_{222} + \tilde{b}_{321}^I + [b_{321}^{II} + 5 \text{ perm.}] + [b_{411} + 2 \text{ cyclic perm.}]. \tag{374}$$

We integrate the above expressions using the CUBA-library (Hahn 2004). For the loop-corrections to the CDM power spectrum, the four integration algorithms Vegas, Cuhre, Divonne and Suave all provide consistently good results. The FDM integrations are much more problematic because they involve time integrations

for the PT kernels in addition to the the momentum integrations. In addition, the PT kernels and the growth factor both exhibit strong oscillations for large k . Integrations become very time-consuming and take as much 5 CPU hours for the Monte Carlo integration of the one-loop contribution to the FDM bispectrum at a single triangle configuration with a relative error of 10 %. For computing the power spectrum loop corrections, we used the Vegas algorithm that stores the integrand structure between different integration runs and thus accelerates integration for different k values. For the bispectrum loop corrections, we used the Divonne algorithm. We tested our integration routines by comparison against analytical solutions in the CDM case derived by Makino, Sasaki and Suto (1992). Further, we numerically verified that the FDM PT kernels reduced to the correct analytical CDM expressions for small k . Moreover, we implemented the PT code independently in Python and C++ and cross-checked results. For the numerical integration of the *line-of-sight integrals*, we combined the PT kernel integrations, the loop integrations and the line-of-sight integrations into higher-dimensional integrals that we integrated using the CUBA-library. This proved advantageous since the line-of-sight integrations smooth oscillations and make the loop integrations more numerically tractable. The *signal-to-noise sums* and χ^2 -*functionals* were also computed as integrals using the CUBA-library. This led to problems for the FDM loop-level bispectrum integrals. They are six-dimensional and the line-of-sight integral to compute the lensing bispectra makes them seven-dimensional. The computation of the loop-level signal-to-noise-ratio therefore requires a three-dimensional integral over a seven-dimensional integral which did not compute. Alternatively, we tested combining the signal-to-noise integrals and the perturbative integrals to obtain a seventeen-dimensional integral which again proved computationally intractable. In the CDM case, this approach yielded an eleven-dimensional integral that we managed to integrate. We used this approach to predict the loop-level bispectrum signal-to-noise ratios and χ^2 -functionals.

A.5 CDM PT with FDM IC

Figs. 59, 60 and 61 compare the lensing spectra computed using FDM PT with their counterparts computed in CDM PT with FDM IC. For the latter, we use the CDM coupling kernels obtained from the EdS recursion relations as well as the CDM growth factors in the fiducial cosmology. The figures clearly show that the difference of the lensing spectra computed with the two methods is very small. We conclude that the suppression of the lensing spectra below the quantum Jeans multipole order in PT lies mainly in the initial conditions and is

not the result of the approximation of late-time FDM dynamics through FDM PT.

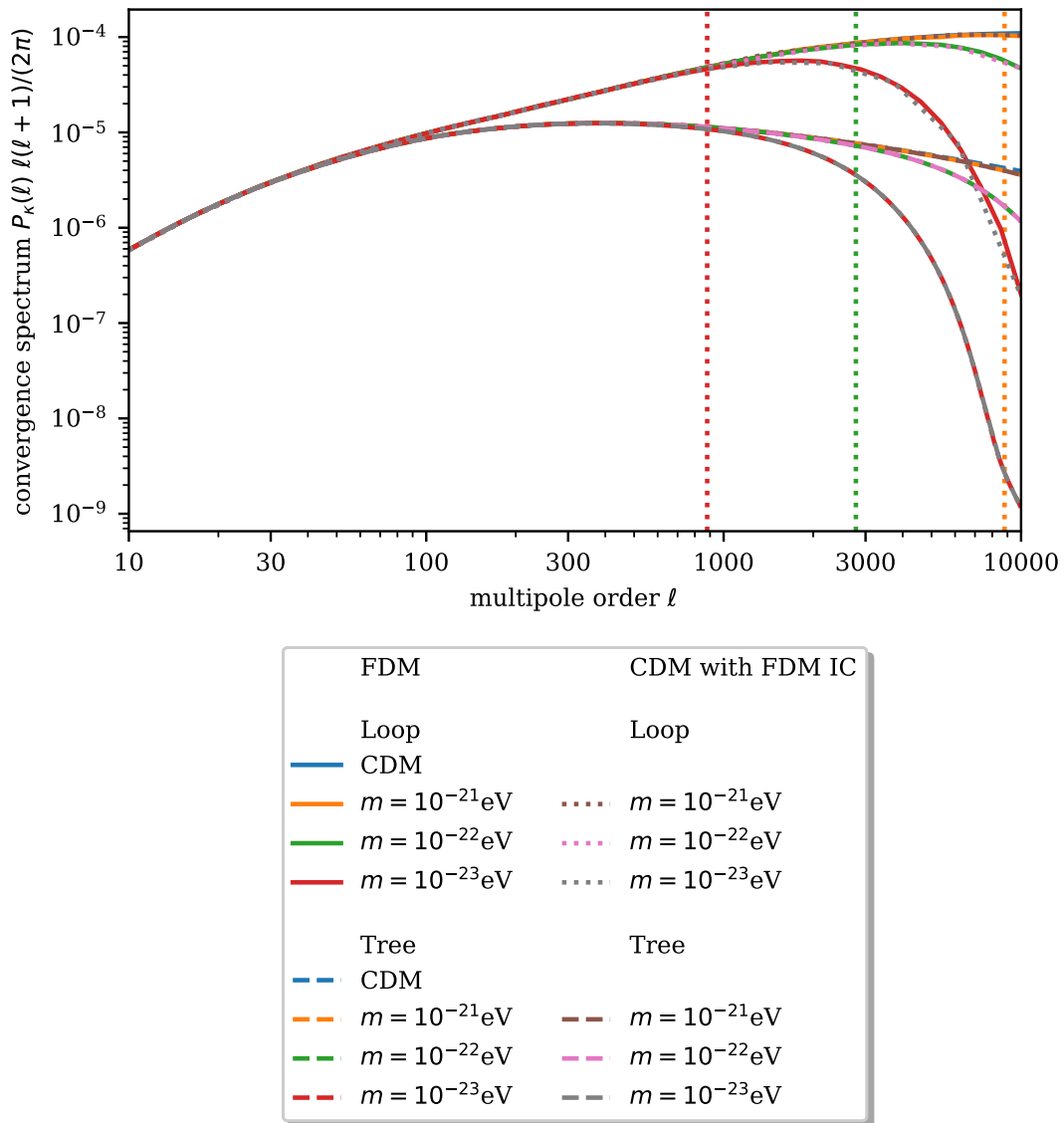


Figure 59: Dimensionless equilateral convergence spectrum configurations at $z = 0$. The vertical, dotted lines correspond to $0.1 \cdot \ell_J$, where the quantum Jeans multipole order ℓ_J is defined in Eq. (230). FDM dynamics approximated by CDM PT with FDM IC.

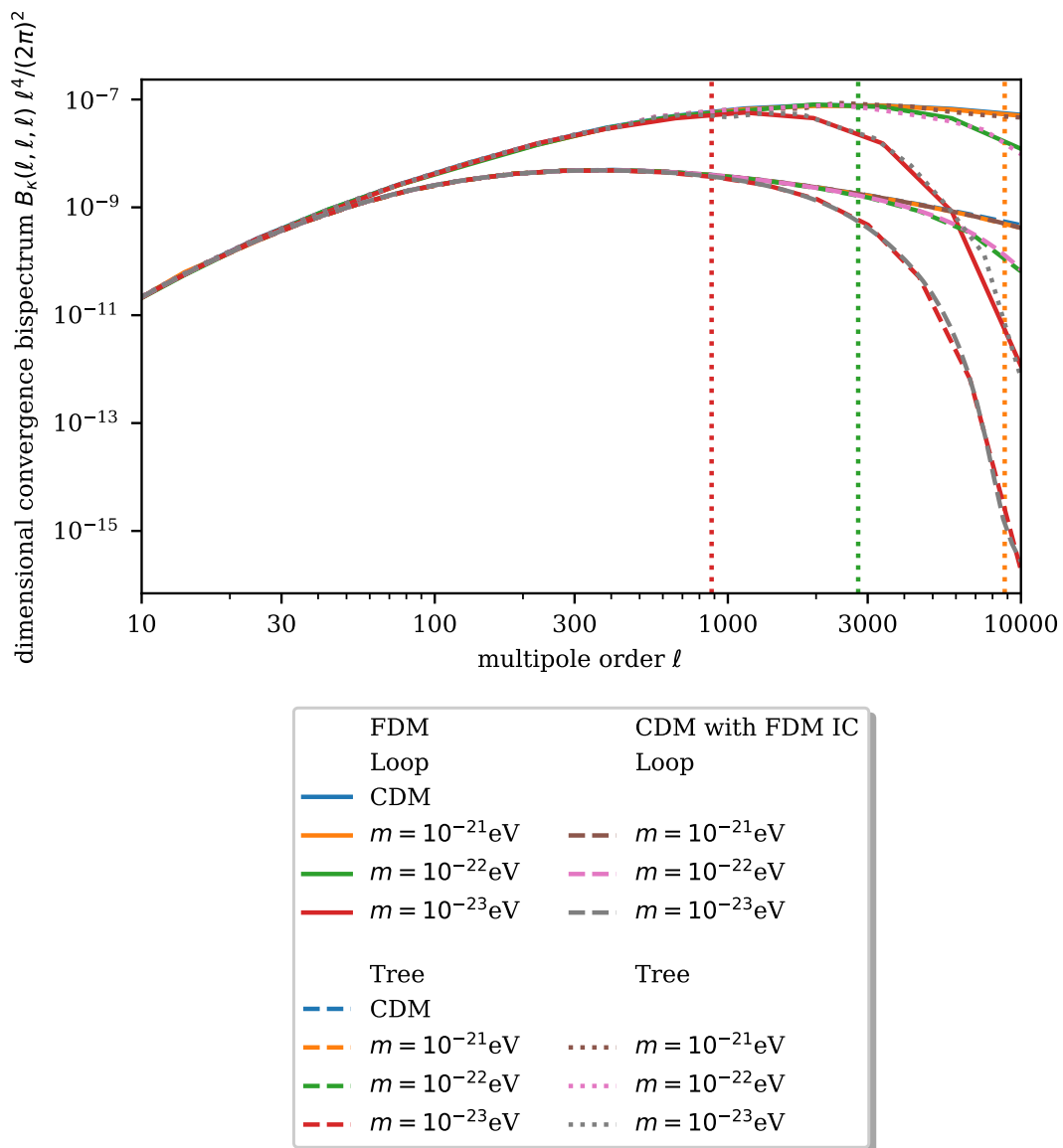


Figure 60: Dimensionless equilateral convergence bispectrum configurations at $z = 0$. The vertical, dotted lines correspond to $0.1 \cdot \ell_J$, where the quantum Jeans multipole order ℓ_J is defined in Eq. (230). FDM dynamics approximated by CDM PT with FDM IC.

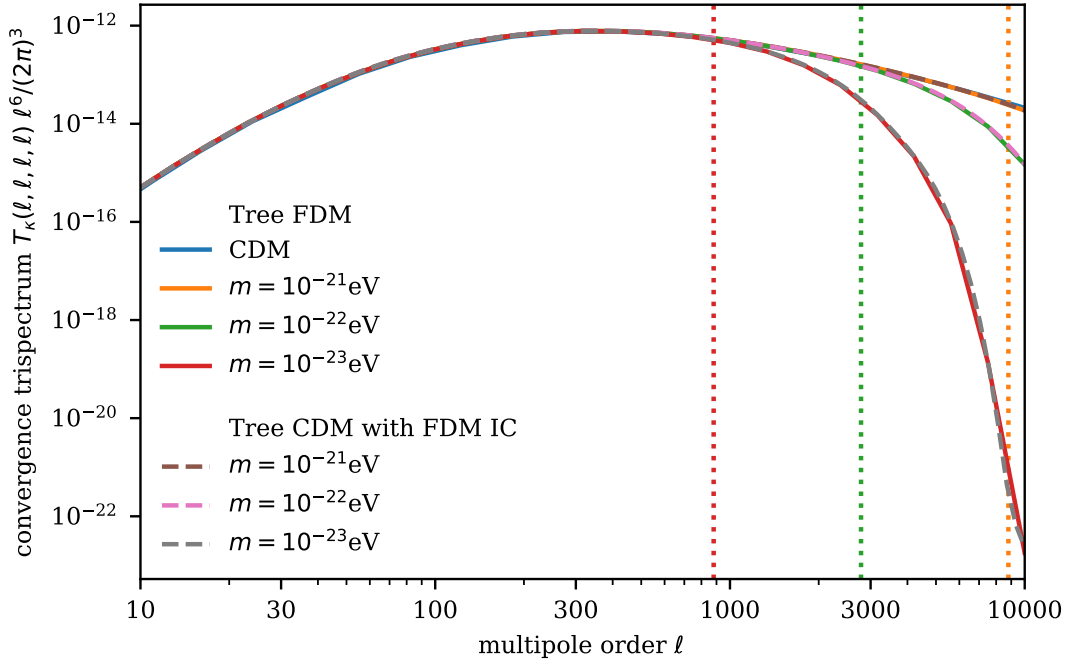


Figure 61: Dimensionless equilateral square convergence trispectrum configurations at $z = 0$. The vertical, dotted lines correspond to $0.1 \cdot \ell_J$, where the quantum Jeans multipole order ℓ_J is defined in Eq. (230). FDM dynamics approximated by CDM PT with FDM IC.

A.6 Method of Characteristics

The fact that solutions to the linear advection equation have a finite, constant propagation speed hints at a fundamental property of first-order PDEs: They admit *characteristic curves* on which solutions are constant. We denote a curve in the x - y -plane by $\Gamma(s) = (x(s), t(s))$. Such a curve is called characteristic if

$$\frac{d}{ds}u(\Gamma(s)) = 0. \quad (375)$$

Substituting this condition into the linear advection equation (236) yields

$$\frac{d}{ds}u(\Gamma(s)) = \frac{\partial u}{\partial x} \frac{dx}{ds} + \frac{\partial u}{\partial t} \frac{dt}{ds} \stackrel{!}{=} 0, \quad (376)$$

and we find that the PDE reduces to the following system of ODEs:

$$\frac{dx}{ds} = a, \quad \frac{dt}{ds} = 1. \quad (377)$$

The characteristic curves of the linear advection equation are straight parallel lines given by

$$x(t) = x_0 + at. \quad (378)$$

The unique solution at a point (x, t) is obtained by tracing back the characteristics passing through the point (x, t) back to the point (x_0, t_0) . Since the solution to the PDE is constant along the characteristic, we find

$$u(x, t) = u(x_0, t_0) = u(x - a(t - t_0), t_0) = u_0(x - a(t - t_0), t_0). \quad (379)$$

The quantity u at the point (x_0, t_0) travels to the point (x, t) along the characteristic with finite propagation speed a . This consideration also applies to a linear system of first-order PDEs of the form

$$\mathbf{u}_t + \mathbf{A}\mathbf{u}_x = 0, \quad (380)$$

with a vector \mathbf{u} and a constant matrix \mathbf{A} . The linear conservation law is called hyperbolic if \mathbf{A} is diagonalisable with real eigenvalues. In this case, diagonalisation gives

$$\mathbf{v}_t + \mathbf{D}\mathbf{v}_x = 0, \quad (381)$$

with n independent advection equations where the eigenvalues of \mathbf{A} are the characteristic velocities.

We can also apply the method of characteristic to non-linear first-order PDE's. For instance, *Burger's equation* serves as prototype of a non-linear conservation law

$$\partial_t u + \partial_x f(u) = 0. \quad (382)$$

For $f(u) = \frac{1}{2}u^2$, it reduces to the so-called inviscid Burger's equation that describes the advection of a quantity u with the characteristic velocity u :

$$\partial_t u + u\partial_x u = 0. \quad (383)$$

Its characteristic curves are given by

$$x(t) = x_0 + u_0(x_0)t, \quad (384)$$

and we note that their slope depends on the initial value $u_0(x_0)$. Crucially, this implies that unlike in the linear case, the advection velocity is position-dependent and characteristic curves can intersect. Such intersections correspond to shocks, that is, discontinuities in the solution of PDEs. At these points, there are no classical solutions, but infinitely many weak solutions to the PDE. This can be intuitively seen because multiple characteristics lead from one intermediate state to many initial states. In other words, there are infinitely many weak solutions to

Burger's equation for smooth initial conditions.

A.7 Slope Limiters in Phase Scheme

In designing, the phase scheme it turned out necessary to employ slope limiters for both the density and phase fields. Fig. 62 shows a situation that would typically become unstable if we use a naive higher-order discretisation of the HJ-Madelung equations. While we expect interference at the filaments and halos physically, the phase scheme fails and produces structures that look CDM-like. The resulting filaments have a very high density and large gradients leading to numerical instabilities without the use of a monotone, shock-capturing scheme for evolving the continuity equation.

We therefore compared different slope limiters using different analytical solutions to the Schrödinger equation. Fig. 63 shows the truncation errors for the Gaussian wave packet test given by Eq. (60) for a number of different limiters. They all produce a nearly second-order scheme, but the VAN ALBADA-limiter gave a truncation error that is around one order of magnitude smaller than the SMART-limiter in this test case. The difference was less severe for small density perturbations and eigen- and coherent states of the harmonic oscillator, but we still opt for the VAN ALBADA-limiter because its smooth behaviour reflects the underlying physics of the Schrödinger equation well.

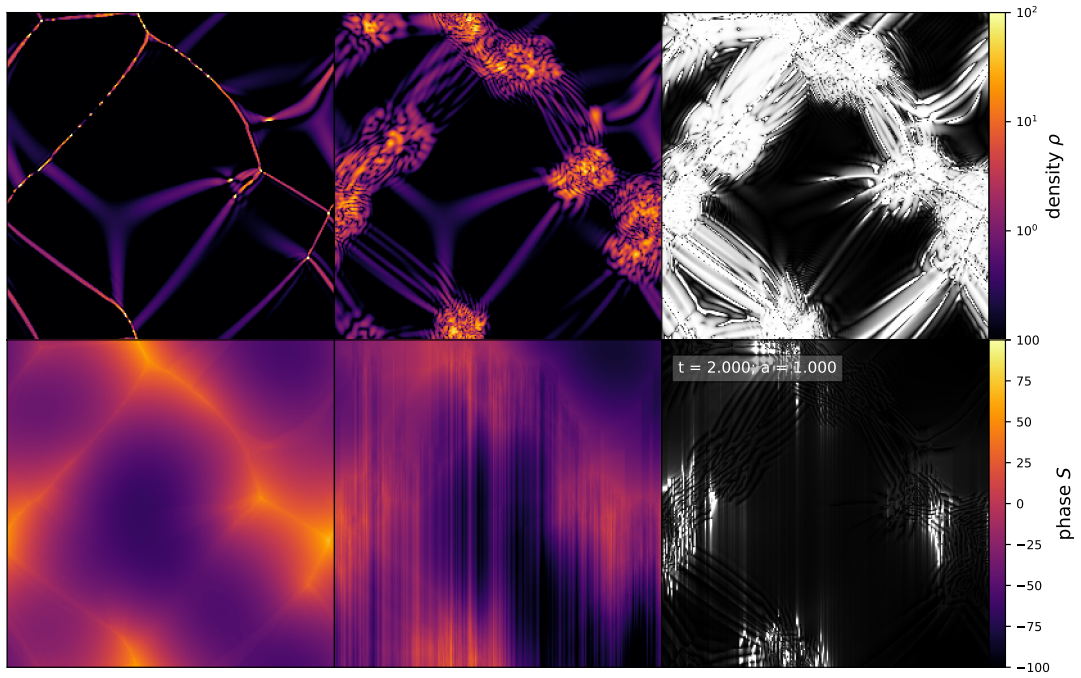
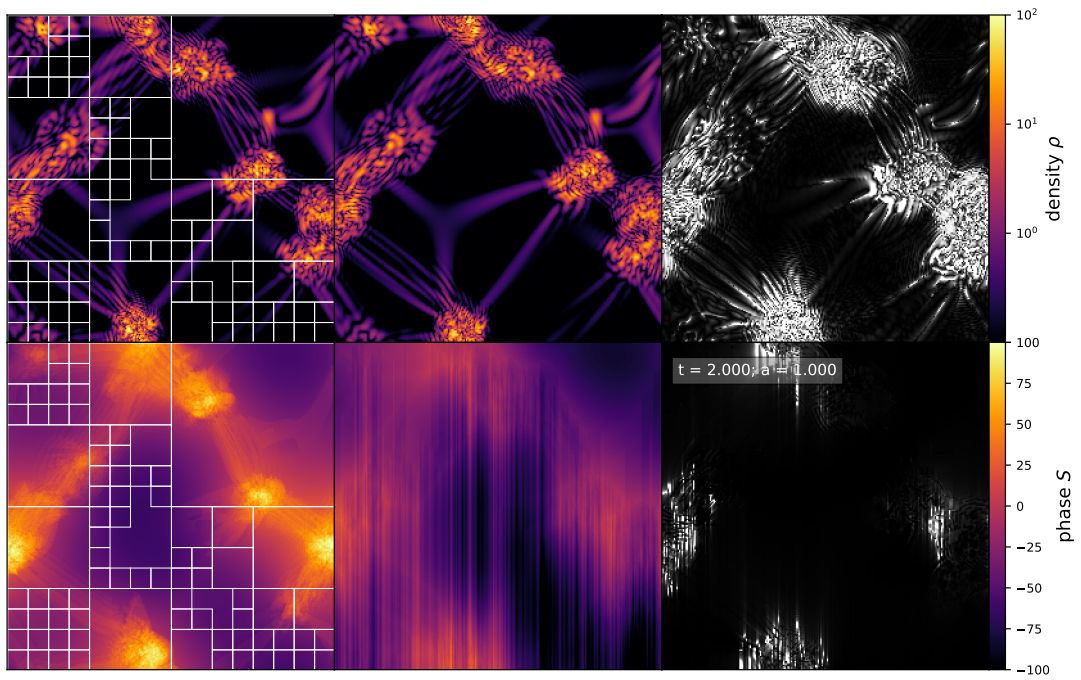
(a) *phase – only*(b) *hybrid*

Figure 62: Snapshots of evolution of wave function for Eq. (324) for phase and hybrid scheme at time $t = 2.0$. Wave scheme is employed within the subregions shown by a red rectangle. Parameters set as in Fig. 46.

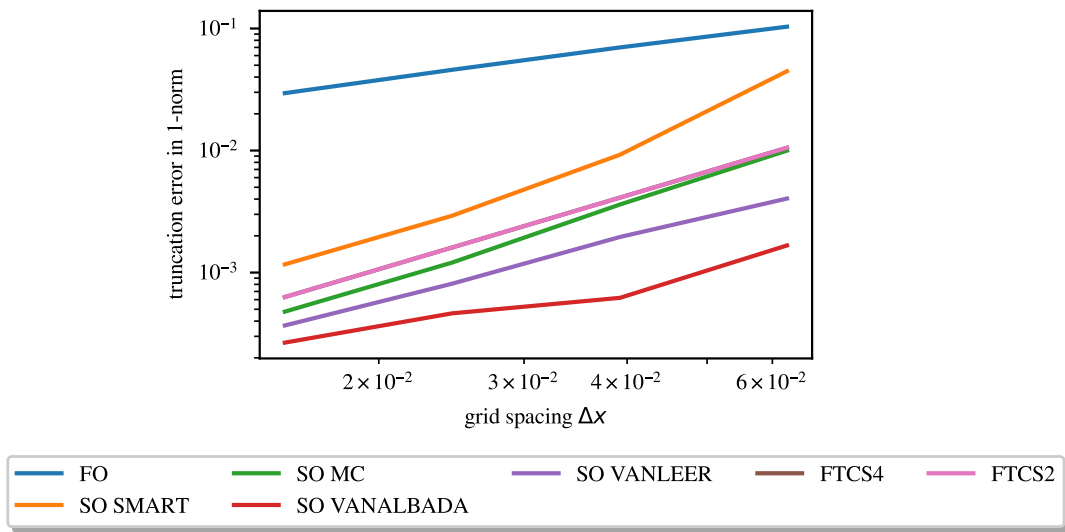


Figure 63: Comparison of truncation errors for Gaussian wave packet (60) evolved to $t = 0.25$ for first order phase scheme (FO), higher-order phase scheme (SO) with different limiters (MC, SMART, van Albada, van Leer) and FTCS wave scheme with second- and fourth-order finite difference stencils.

Erklärung

Ich versichere, dass ich diese Arbeit selbstständig verfasst und keine anderen als die angegebenen Quellen und Hilfsmittel benutzt habe.

Bobritsch-Hilbersdorf, den 20.05.22,

Alexander Kunkel